Particle Confinement in Axisymmetric Poloidal Magnetic Field Configurations with Zeros of *B*: Methodological Note

V. V. Arsenin and A. A. Skovoroda

Nuclear Fusion Institute, Russian Research Centre Kurchatov Institute, pl. Kurchatova 1, Moscow, 123182 Russia

Received June 23, 2005

Abstract—Collisionless particle confinement in axisymmetric configurations with magnetic field nulls is analyzed. The existence of an invariant of motion—the generalized azimuthal momentum—makes it possible to determine in which of the spatial regions separated by magnetic separatrices passing through the magnetic null lines the particle occurs after it leaves the vicinity of a magnetic null line. In particular, it is possible to formulate a sufficient condition for the particle not to escape through the separatrix from the confinement region to the external region. In the configuration under analysis, the particles can be lost from a separatrix layer with a thickness on the order of the Larmor radius because of the nonconservation of the magnetic moment μ. In this case, the variations in μ are easier to describe in a coordinate system associated with the magnetic surfaces. An analysis is made of the applicability of expressions for the single-pass change $\Delta\mu$ in the magnetic moment that were obtained in different magnetic field models for a confinement system with a divertor (such that there is a circular null line). © 2005 Pleiades Publishing, Inc.

1. Some types of magnetic confinement systems, both closed and open, are equipped with elements for producing reversed magnetic fields (cusp devices), for instance, systems based on a field reversed configuration (FRC) [1, 2], a bidipole confinement system with an internal conductor [3, 4], the AMBAL-M open system [5, 6], and the EPSILON linked mirror system with divertors [7]. Such elements can function, in particular, as an MHD stabilizer. A separatrix surface, which contains magnetic null lines and/or points, is a natural boundary between the internal region, where hot plasma is confined, and external regions, through which the particles that have escaped from the confinement region move toward the walls and are lost there. Since the adiabatic invariant μ—the magnetic moment of a particle—is not conserved in the vicinity of a zero of the magnetic field, it is relevant to study the question of how the nonadiabatic character of motion influences particle losses from the confinement region. An extensive literature exists concerning various aspects of this problem (see, e.g., review [8]). The aim of the present paper is to give a simple presentation of some results on the effect of magnetic field nulls on plasma confinement in axisymmetric poloidal magnetic field configurations (among which are confinement devices described in [1–6] and a system with a stabilizing divertor described in [7]). The existence of an integral of motion—the generalized azimuthal momentum—makes it possible to easily determine the conditions under which the particle cannot escape through the separatrix from the confinement region into the external region. The effects of the nonconservation of the magnetic moment μ can be accounted for relatively simply by working in a coordinate system associated with a magnetic surface. Also, a comparative analysis is carried out of the formulas describing the change in μ at different magnetic surfaces in different models developed for divertor-equipped confinement systems, which have received little study.

2. In a cylindrical coordinate system (r, ϑ, z), the axisymmetric poloidal magnetic field $\mathbf{B}\{B_r, 0, B_z\}$ is described by only one component of the vector potential A_ϑ:

$$B_r = -\frac{1}{r}\frac{\partial(rA_\vartheta)}{\partial z}, \quad B_z = \frac{1}{r}\frac{\partial(rA_\vartheta)}{\partial r}. \tag{1}$$

For a particle with mass m and charge q that moves in such a field, the generalized azimuthal momentum is conserved,

$$P = mr^2\dot\vartheta + \frac{q}{c}rA_\vartheta. \tag{2}$$

Here, the prime denotes the derivative with respect to time and c is the speed of light. Accordingly, the equations of particle motion have the form (see, e.g., [9])
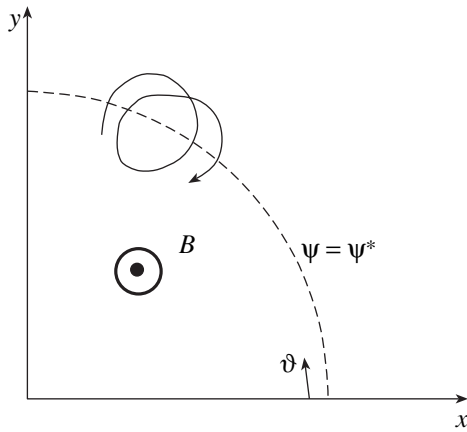
$$m\ddot r = -\frac{\partial u}{\partial r}, \quad m\ddot z = -\frac{\partial u}{\partial z}, \tag{3}$$

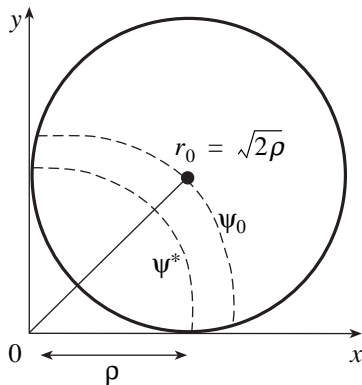where $u = q\Phi + u_0$, with $\Phi(r, z)$ being the electric potential, and

$$u_0 = \frac{1}{2m}\left(\frac{P}{r} - \frac{q}{c}A_\vartheta\right)^2. \tag{4}$$

Equations (3) have the energy integral

$$E = \frac{m}{2}(\dot r^2 + \dot z^2) + u_0 + q\Phi. \tag{5}$$

Fig. 1. Projection of a portion of a particle trajectory onto the (x, y) plane.

Fig. 2. Larmor circle in a uniform magnetic field at $r_0 = \sqrt{2}\,\rho$.

It is convenient to switch from the component A_ϑ to the flux function

$$\psi = rA_\vartheta. \tag{6}$$

The surface $\psi = \mathrm{const}$ is composed of the magnetic field lines. In terms of the flux function, the quantity u in Eqs. (3) is written as

$$u = \frac{1}{2mr^2}\left(P - \frac{q}{c}\psi\right)^2 + q\Phi. \tag{7}$$

Before passing to the analysis of the spatial restrictions on particle motions in one or another magnetic field geometry, we explain the physical meaning of the generalized momentum P in expression (7).

Let us consider a uniform magnetic field $\mathbf{B}\{0, 0, B_z\}$ in a straight solenoid whose axis is the z axis of a Cartesian coordinate system (x, y, z). We set the potential equal to zero, $\Phi = 0$. In particle motion, the coordinates of the centers of the Larmor circles, $x + \omega_B^{-1} v_y$

and $y - \omega_B^{-1} v_x$, remain constant (here, $v_{x, y}$ are the velocity components and $\omega_B = qB_z/mc$ is the gyrofrequency). Consequently, the distance r_0 from the center of a circle to the axis of the solenoid also remains constant,

$$\left(x + \frac{v_y}{\omega_B}\right)^2 + \left(y - \frac{v_x}{\omega_B}\right)^2 = r_0^2 = \mathrm{const.} \tag{8}$$

We rewrite the left-hand side of this equality as $r^2 + \rho^2 + 2r v_\vartheta/\omega_B$ (where the Larmor radius $\rho = |\omega_B|^{-1}(v_x^2 + v_y^2)^{1/2}$ is a conserved quantity) and take into account the equality $r^2 = 2\psi/B_z$ to see that, in the case at hand, the momentum $P = mr v_\vartheta + (q/c)\psi$ is given by the expression

$$P = \frac{qB_z}{2c}(r_0^2 - \rho^2), \tag{9}$$

and, hence, the generalized azimuthal momentum is related to the radial coordinate of the Larmor center. The generalized momentum can also be written in the form

$$P = \frac{q}{c}(\psi_0 - \psi_\rho), \tag{10}$$

where ψ_0 and ψ_ρ are the magnetic fluxes (multiplied by $(2\pi)^{-1}$) through the circle at which the Larmor center is located and through a Larmor circle, respectively. Note that the generalized momenta P of the particles with $r_0 > \rho$ and with $r_0 < \rho$ have opposite signs. This circumstance will be important in analyzing different regions of particle motions in configurations with a field null at the magnetic axis (see below).

In the general case in which the magnetic field is nonuniform and the electric field $\nabla\Phi$ is nonzero, the particle trajectory is more complicated than a helix, but the meaning of the generalized momentum P as a characteristic of a certain surface near which the particles, on the average, move does not change. If the particle trajectory does not encircle the axis of the solenoid during the cyclotron period, so that there exist points where $v_\vartheta = 0$ (Fig. 1), it is convenient to consider the axisymmetric surface which passes through these points. We denote the flux through this surface by ψ^* to rewrite expression (2) as

$$P = \frac{q}{c}\psi^*. \tag{11}$$

Note that the surface $\psi^* = \mathrm{const}$ does not coincide with the surface $\psi_0 = \mathrm{const}$, at which there is the Larmor center. In the case of a uniform magnetic field and for $\Phi = 0$, we have $\psi^* = \psi_0 - \psi_\rho$, as is illustrated in Fig. 2.

The most interesting confinement systems are those whose size across the magnetic field is much greater than the mean ion Larmor radius. In such systems, the total flux ψ is much higher than the characteristic flux
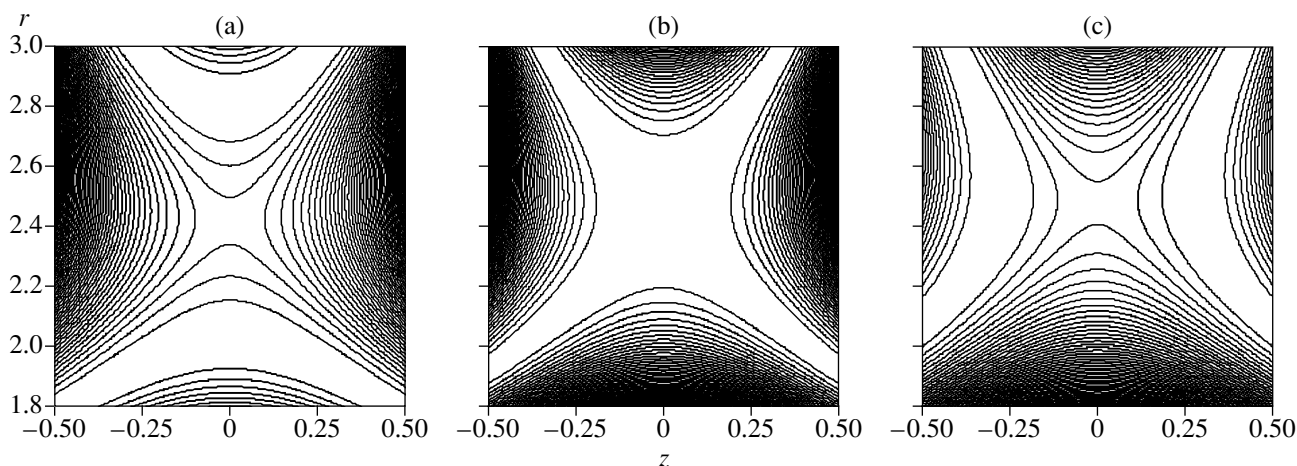
Fig. 3. Contours of the same value of potential (7) with $\Phi = 0$ in a configuration with a divertor (such that there exists a circumference at which the magnetic field vanishes) for $cP/q \equiv \psi^* =$ (a) $0.9\psi_{sep}$, (b) ψ_{sep}, and (c) $1.1\psi_{sep}$. The coordinates are given in units of $L/2\pi$, where L is the distance between the end mirrors (or the period in a periodic sequence of confinement cells with divertors). The white striplike regions are around the value $u_{min} = 0$. The field null is at the radius $r_{sep} = 2.4$.

through a Larmor circle, ψ_ρ. In what follows, we will consider precisely these confinement systems.

3. The region where the particle can move may be determined by considering the relief of the potential $u(r, z)$. For $\Phi = 0$, the potential vanishes at a line along which $\psi = cP/q$ and increases on both sides from it. The "corridor" $u \le E$ at the bottom of the "valley" in the relief has a width of $\delta\psi \sim (c/q)r\sqrt{mE}$; with allowance for the relationship $\delta\psi = Br\delta n$ (where δn is the distance from the magnetic surface along the normal to it), this corresponds to a δn value on the order of the Larmor radius. In the presence of separatrices, the valleys have a branched shape in a certain range of values of the ratio P/q (Fig. 3). Because of this branched shape, the particles can escape from the confinement region along the separatrices. The conditions for the particles not to occur in such channels and, accordingly, not to escape along the separatrices will be discussed below for several types of magnetic configurations.

4. Let us consider a spindle cusp—a configuration with one field null at the axis at $z = 0$. For simplicity, we assume that the $z = 0$ plane is a symmetry plane and that, at sufficiently large distances from it ($|z| > l$), the magnetic field is uniform and its strength is equal to $B = B_0$. An important point for further analysis is that the total flux ψ has opposite signs in the two halves of the confinement system (to be specific, we set $\psi > 0$ to the right from the null). The contours of the same value of $\psi(r, z)$ in the meridional cross section, or equivalently, the magnetic field lines, are shown in Fig. 4.

Let a particle be initially in a uniform magnetic field to the right from the point $z = 0$, and let it move toward the field null to occur in the zone of nonadiabatic motion (in Fig. 4, the boundaries of this zone are shown schematically because now we do not need to know its

exact shape). In order to determine the distance the particle can travel when moving away from the field null after passing its vicinity with, generally, a change in its magnetic moment μ (and, accordingly, in its Larmor radius), we show in Fig. 5 the dependence of P/q on the radial coordinate of the Larmor center, r_0, in the right (subscript plus) and left (subscript minus) regions of a uniform magnetic field. It is important to stress that there are ranges of distances, r_{0+} and r_{0-}, in which the ratio P/q takes on the same values. If

$$r_{0+} > r^* \equiv (\rho_+^2 + \rho_-^2)^{1/2} \tag{12}$$

(where ρ_+ and ρ_- are the Larmor radii in the right and left regions of a uniform magnetic field), then the invariant P/q is larger than $(P/q)^{max}_- = B_0\rho_-^2/2c$. This implies that a particle that has the transverse velocity $\rho_+|\omega_B|$ to the right of the field null cannot occur in the left region and move there with the transverse velocity $\rho_-|\omega_B|$. The particle not only can return back but also
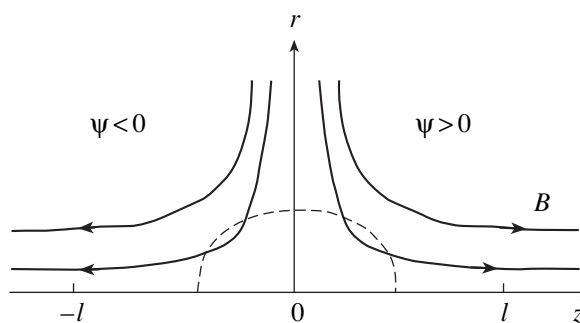
Fig. 4. Meridional cross section of the magnetic surfaces $\psi = $ const in a confinement system with a field null at the axis.
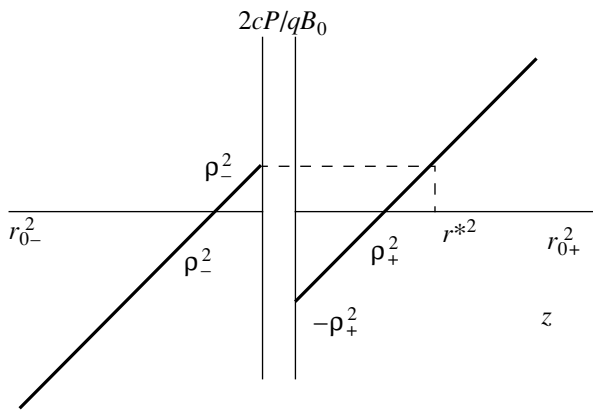
Fig. 5. Dependence of P/q on r_0^2 in the right and left regions of a uniform magnetic field.
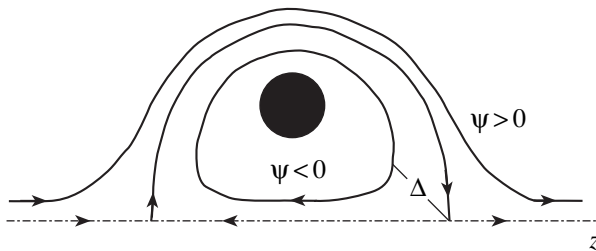

Fig. 6. Contours of ψ in a bidipole confinement system.

can pass into a narrow circular slit around the magnetic null line. Moreover, in both these allowed situations, the particle, acquiring a new value of μ, remains confined to the magnetic surface determined by the initial value of ψ^* (see formula (11)) on the same side of the separatrix $z = 0$, despite the fact that it was able to cross the separatrix because of the nonadiabatic effects in this region. The maximum value of r^* on the right-hand side of inequality (12) is $r_E^* = \sqrt{2}\rho_E$, where ρ_E is the largest possible Larmor radius (calculated in terms of the velocity $\sqrt{2E/m}$). Consequently, for $r_{0+} > r_E^*$, any particle of energy E is forbidden to pass into the region $z < -l$, regardless of the value of the pitch angle.

If the Larmor center of an incident particle is within the cylinder

$$\rho_+ < r_{0+} < r^*, \tag{13}$$

then it can either return back to the axis, or can escape into a circular slit around the separatrix $z = 0$ (in this case, the Larmor center of the particle does not cross the separatrix), or can escape through a region near the axis ($r_{0-} < \rho_-$) into the left region of a uniform magnetic field. Note that, in the latter case, the Larmor orbit of the escaping particle encircles the axis. In all these three situations, we have $P/q > 0$.

Finally, we see from Fig. 5 that, for

$$r_{0+} < \rho_+, \tag{14}$$

when $P/q < 0$ and the Larmor orbit of the incident particle encircles the axis, the following situations are allowed: (i) backward reflection; (ii) escape into the left region of a uniform magnetic field, where the Larmor center will be at a distance from the axis that is greater than ρ_- (the Larmor orbit does not encircle the axis) but is less than r^*; and (iii) return into the circular slit (in this case, the Larmor center will move near the separatrix on the left of it, $\psi < 0$).

Let us now follow the motions of a particle propagating from the circular slit and approaching the field null that are allowed by the conservation law for the generalized azimuthal momentum P. For definiteness, we assume that the particle is confined to the magnetic surface $\psi^* = $ const. For

$$\psi^* > B_0 \frac{\rho_E^2}{2} \tag{15}$$

(the Larmor center is not too close to the separatrix), the particle is forbidden to pass into the left region of a uniform magnetic field. In this case, the particle can return back to the hole or can pass into the right region of a uniform field; moreover, in either case, the particle will eventually occur at its initial magnetic surface ψ^*. If condition (15) is not satisfied, then the particle also can pass into an axial uniform-field region with a radius on the order of ρ_E.

5. In a configuration with closed magnetic field lines and with two magnetic nulls on the axis (such as, e.g., an FRC or a bidipole confinement system), a particle that, by virtue of equality (11), is restricted to move near the closed magnetic surface $\psi^* = $ const that is at a large distance $\Delta \gtrsim \rho_E$ from the separatrix (see Fig. 6) is confined absolutely: without colliding with other plasma particles, it cannot move away from this surface and escape from the region bounded by the separatrix. The only particles that are allowed to cross the separatrix are those in a boundary layer with a thickness of about ~ρ_E. In a region near the field null, the radius ρ_E can be estimated by calculating it in terms of the magnetic field at a distance ρ_E from the null: $\rho_E^2 \sim \sqrt{2E/m}|\nabla\omega_B|^{-1}$, where the gradient is taken at the null point. Detailed calculations of particle trajectories in a configuration in the form of a Hill vortex can be found in [10].

The size of the region of nonadiabatic motion, l_{na}, can be larger than Δ (the results of calculations for some types of magnetic configurations are presented in [8]). The pitch angle of a particle that has visited this region can change, but the particle itself will remain confined, provided that it will move outside the aforementioned boundary layer.

6. In a configuration with a divertor, such that there exists a circular null line at $r = r_{sep}$ and $z = 0$, the point $(r_{sep}, 0)$ is a saddle point of the flux function $\psi(r, z)$. For definiteness, we assume that $B_z > 0$ at the axis. We then see that the flux function ψ in the equatorial cross section, $\psi|_{z=0}$, takes on its maximum value $\psi = \psi_{max}$ at $r = r_{sep}$. For any value of ψ in the half-open interval $[0, \psi_{max})$, there exists a magnetic surface $\psi = const$ with the same value of the flux function in the sector between the "limbs" of the separatrix in the region $r > r_{sep}$. Accordingly, the generalized azimuthal momenta $P = (q/c)\psi^*$ of a particle that resides in the axial region and of a particle that remains in the external sector will be the same. The conservation of P allows the particles to stay in both these regions. However, the potential barrier u given by expression (7) may hinder the passage of the particles from one of these regions into another.

Indeed, let us consider the radial profile of u in the equatorial plane, $u|_{z=0}$, for $\Phi = 0$. Between the minima $u|_{z=0} = 0$ on both sides of the separatrix $r = r_{sep}$, the profile has a maximum, $u|_{z=0} = u_{max}$ (see Fig. 3a), whose magnitude is determined by the difference $\psi_{max} - \psi^*$: the larger the distance from the separatrix at which the particle starts moving, the higher the maximum. The particle can pass through the maximum only when $u_{max} < E$. It is easy to see that this condition can be satisfied only for particles that are within a separatrix layer with a thickness on the order of the Larmor radius. The particles that start moving at distances from the separatrix that exceed the layer thickness cannot cross it.

Let us now consider the motion of the particles that are near such magnetic surfaces $\psi = const$ lying outside the separatrix layer, from which the plasma can be transported in a transverse direction through the magnetic field null, but passing through the region of nonadiabatic motion. We assume that this region is wider than the separatrix layer and is crossed by the magnetic surface $\psi = const$. In such circumstances, the magnetic moment μ of a particle that crosses the nonadiabatic region can change. In particular, it may become smaller, which implies that the particle velocity along a magnetic field line increases. Accordingly, in a configuration with closed magnetic field lines, no particles will be lost, as was already mentioned in Section 5. In a configuration with open field lines, however, the particles will be put into the loss cone. This loss channel can be closed by the ambipolar end plugs.[1]

7. Since a moving particle is confined to a certain magnetic surface $\psi = \psi_S$, its motion can conveniently be described in a coordinate system associated with this

---

[1] In confinement systems in which the straight sections are connected by curvilinear elements, the superbanana losses can be avoided by using curvilinear elements of special geometry with which to ensure the omnigeneity property—the coincidence of the averaged drift surfaces of the particles with the magnetic surfaces.

surface [11, 12]. In this case, the familiar results on variations in the magnetic moment μ can be reproduced in a relatively simple way. The coordinate system in question is introduced as follows: the coordinate δ is reckoned from the reference magnetic surface ψ_S along the normal to it and the role of the coordinate z is played by the longitudinal coordinate s (the length along the magnetic field line). In these coordinates, we have

$$r = r_S(s) + \delta\cos\theta(s), \quad z = z_S(s) + \delta\sin\theta(s), \quad (16)$$

where the functions r_S and z_S are related to the reference surface and $\theta(s)$ is the angle between the normal to it and the radial direction. We also introduce the dimensionless variables by normalizing the time to the reciprocal of the gyrofrequency at a certain fixed point at which the magnetic field strength is equal to $B = B_0$ and the quantities r, δ, and s to a characteristic scale length L, e.g., the period of a periodic sequence of divertors (see below). For brevity, we set $\psi_S = \psi^* = cP/q$. The position of this magnetic surface can easily be determined, e.g., for a particle flying from the uniform field region; in this case, the magnetic surface can be simply described in terms of the radial coordinate of the Larmor center (see Section 2). The Hamiltonian is given by the expression $H = m(L\omega_{B0}/2\pi)^2 \hat{H}$, where the dimensionless Hamiltonian has the form

$$\hat{H} = \frac{1}{2}\left(p_\delta^2 + \frac{p_s^2}{(1 - \delta/R(s))^2} + \frac{(\psi - \psi_S)^2}{(r_S(s) + \delta\cos\theta(s))^2} \right), \quad (17)$$

with $p_\delta = \dot{\delta}$, $p_s = \dot{s}(1 - \delta/R(s))^2$, and $R^{-1} = -d\theta/ds$ being the magnetic field line curvature. The dimensionless Hamiltonian $\hat{H}$ is on the order of $(\rho/L)^2$; it can be conveniently used as a measure of the degree to which the moving particles are magnetized. The magnetization is strong when $\hat{H} \ll 1$.

For $|\delta/r_S| \ll 1$ and $|\delta/R| \ll 1$, we take into account the relationship $\psi - \psi_S \approx r_S b(s)\delta$ and ignore the terms on the order of $O\left(\dfrac{\delta}{R}\right)$ to obtain

$$\hat{H} = \frac{1}{2}(p_\delta^2 + p_s^2 + b^2(s)\delta^2), \quad (18)$$

where $b(s) = B(s)/B_0$ is the dimensionless magnetic field along the field line $\psi = \psi_S$. In accordance with what was said above, expression (18) implies that the deviation δ is no larger than the quantity

$$|\delta|_{max} = \sqrt{2\hat{H}}/b_{min}, \quad (19)$$

which has the meaning of the dimensionless Larmor radius at the point where the magnetic field at the reference magnetic surface ψ^* is minimum.

With dimensionless Hamiltonian (18), the equations of motion read

$$\ddot{\delta} + b^2(s)\delta = 0, \quad \ddot{s} + \delta^2 b \frac{db}{ds} = 0. \tag{20}$$

They describe fast oscillations of δ and far slower (because of the smallness of δ in the second term of the second equation) oscillations of s. The transverse action is an adiabatic invariant,

$$J_\delta = \frac{1}{2\pi} \oint p_\delta d\delta = \frac{b}{2\pi} \oint \sqrt{\frac{2\hat{H} - p_s^2}{b^2} - \delta^2} d\delta$$
$$= \frac{2\hat{H} - p_s^2}{2b} \approx \text{const.} \tag{21}$$

Combining expressions (21) and (18), we find

$$J_\delta = \frac{1}{2}\left(\frac{\dot{\delta}^2}{b} + b\delta^2\right). \tag{22}$$

In order to determine the transverse action invariant J_δ, we can choose the time at which $\dot{\delta} = 0$. This yields

$$J_\delta = b\rho^2/2, \tag{23}$$

where ρ is the dimensionless radius of the Larmor circle. We thus see that, to within a constant factor, the adiabatic invariant J_δ coincides with the magnetic moment μ. Hence, approximate expression (18) for the dimensionless Hamiltonian, which is valid for small values $|\delta/R| \ll 1$, is consistent with the adiabatic invariance of μ.

8. By taking into account the correction to Hamiltonian (18) that is introduced by the magnetic field line curvature, it is possible to describe how the magnetic moment μ changes when the oscillations of δ come into interplay with the motion along the magnetic field line. (That the magnetic moment μ is not converted primarily because of the field line curvature was pointed out in [11] and also in [8].) In expression (17), we keep the term that is linear in δ/R. As a result, we obtain

$$\hat{H} = \frac{1}{2}\left[p_\delta^2 + p_s^2\left(1 + \frac{2\delta}{R}\right) + b^2(s)\delta^2\right], \tag{24}$$

and, instead of the first of equations of motion (20), we arrive at

$$\ddot{\delta} + b^2(s)\delta = -\frac{p_s^2}{R}. \tag{25}$$

Multiplying Eq. (25) by $\dot{\delta}$ yields the following equation for the invariant J_δ defined by equality (22):

$$\dot{J}_\delta = -\frac{p_s^2\dot{\delta}}{Rb} - \frac{\dot{b}}{b}(J_\delta - b\delta^2). \tag{26}$$

We assume that the changes in μ are sufficiently small, so we can substitute the quasiclassical solution to Eq. (25) with a zero curvature (this solution is consistent with the conservation of μ) into the right-hand side of Eq. (26) to obtain $\delta = \sqrt{2J_\delta/b} \cos\varphi$, where $\varphi = \int^t b dt$ is the phase of Larmor rotation. In this case, Eq. (26) takes the form

$$\dot{J}_\delta = \sqrt{\frac{2J_\delta}{b}} \frac{p_s^2}{R} \sin\varphi + \frac{J_\delta p_s}{b} \frac{db}{ds} \cos 2\varphi. \tag{27}$$

The increment in J_δ during the time interval Δt is found by integrating Eq. (27). Both terms on the right-hand side of this equation are oscillating functions; consequently, if there is a need to calculate the increment ΔJ_δ during the half-period of bounce oscillations (or, for transit particles, during the transit time) then it should be noted that the corresponding contributions to ΔJ_δ are exponentially small in the adiabaticity parameter—the ratio of the oscillation frequency to the bounce frequency (or, equivalently, the inverse transit time). Since the oscillation frequency in the second term (namely, $2b$, which corresponds to the dimensional frequency $2\omega_B$) is two times higher than that in the first term, its contribution to ΔJ_δ can be ignored. As a result, we arrive at the following familiar expression:

$$\Delta(\sqrt{2J_\delta}) \approx \text{Im} \int_{\Delta\varphi} \frac{\dot{s}^2}{Rb^{3/2}} e^{i\varphi} d\varphi, \tag{28}$$

where $\Delta\varphi = \int_{\Delta t} b dt$ and $b\Delta t \gg 1$.

Note that, for the solution to the total (with allowance for curvature) equation (25), the δ value averaged over the Larmor period is nonzero. The reasons for this are as follows. The centrifugal force $mv_\parallel^2/R$ gives rise to azimuthal drift. The δ coordinate of the stopping points (with respect to the azimuthal angle ϑ) on the cycloidal trajectory differs from $\delta_0 = (\delta_{\max} + \delta_{\min})/2$ by the amount v_{dr}/ω_B (this difference has been touched on in Section 2). The drift due to the transverse nonuniformity of the magnetic field, proportional to $v_\perp^2$, is taken into account by retaining the quadratic term in the expansion of $\psi - \psi_S$ in powers of δ in expression (17). In this case, Eq. (25) contains a term $\propto\delta^2$ and a term $\propto\delta^2\dot{\delta}$ is added to the right-hand side of Eq. (26). As a result, the right-hand side of Eq. (27) will contain a term with $\sin 3\varphi$ (which introduces merely an exponentially small correction to ΔJ_δ) and also a term proportional to $\propto(J_\delta/l_\perp)\sin\varphi$ (where $l_\perp$ is the dimensionless scale on which the magnetic field varies in the transverse direction). This latter term also makes an insignificant contribution to ΔJ_δ because the power of the quantity b in it is larger than that in the term with the curvature by one unit (an important factor in calculating J_δ is the singularity $1/b(s)$ in the complex plane; see [8], Section 7).

9. The change in the magnetic moment of the moving particles, $\Delta\mu$, was calculated for magnetic configurations of different geometries (see, e.g., [13–17] and also [8]). Here, we present a particular version of expression (28) for a straight periodic sequence of confinement cells with divertors. To be specific, we consider transit particles in the equatorial plane of a divertor and assume that the particle velocity components satisfy the inequality $v_\perp \ll v_\parallel$. Let us estimate the change in the magnetic moment by using the approximate formulas [8] for $\Delta\mu$ that refer to two different regions of magnetic surfaces ψ_S: the axial region and the separatrix region. The aim is to analyze how much the results obtained for these two regions differ from one another.

For the magnetic surfaces ψ_S near the magnetic axis, the function $b(s)$ can be described in terms of only one harmonic in the longitudinal coordinate s,

$$b_S(s) = 1 - \varepsilon_S \cos s. \qquad (29)$$

In this case, the period along the magnetic field lines (contained in the characteristic scale length to which the coordinate s was normalized) and the modulation depth ε_S depend on ψ_S. In particular, for the representation of the magnetic field of a chain of divertors (see Section 10 below), the modulation depth is equal to

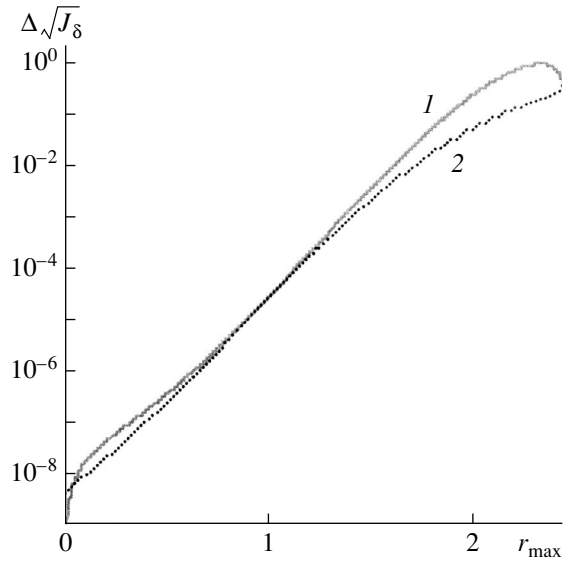$$\varepsilon_S = \left(1 + \frac{r_{max}^2}{4}\right)\varepsilon, \qquad (30)$$

where r_{max} is the dimensionless distance from the axis to the point at which the magnetic field along the magnetic field line is minimum and ε is the modulation depth at the axis. In approximation (29), for a particle in its transit through one period of the system, we have

$$\Delta\sqrt{J_\delta} = C_1 r_{max}\sqrt{1-\varepsilon_S}\, e^{-\frac{2(1-\varepsilon_S)^{3/2}}{3\sqrt{\hat{H}\varepsilon_S}}} \sin\varphi_0, \qquad (31)$$

where C_1 is a numerical factor on the order of unity and φ_0 is the phase of Larmor rotation at the point at which the magnetic field is minimum [8].

Near the separatrix layer, where the dependence $b(s)$ along the magnetic field lines is more pronounced, it is convenient to use the plane cusp approximation, because the layer thickness is much less than r_{sep}. In this approximation, we obtain from [8] the estimate

$$\Delta\sqrt{J_\delta} = C_2\sqrt{\frac{\hat{H}}{1-\varepsilon_S}}\left[\frac{(1-\varepsilon_S)\left(2\sqrt{\frac{1-\varepsilon}{\varepsilon}}-r_{max}\right)}{2\sqrt{2\hat{H}}}\right]^{1/8}$$
$$\times e^{\frac{(1-\varepsilon_S)\left(2\sqrt{\frac{1-\varepsilon}{\varepsilon}}-r_{max}\right)}{2\sqrt{2\hat{H}}}}\sin\varphi_0, \qquad (32)$$

Fig. 7. Dependence of the quantity $\Delta\sqrt{J_\delta}$ on the radius of the magnetic surface for a divertor cell: curves *1* and *2* are calculated from formulas (31) and (32), respectively. The parameter values are $\varepsilon = 0.4$ and $\hat{H} = 0.001$, the dimensionless radius of the separatrix being $2\pi r_{sep}/L = 2.4$.

where $C_2 \sim 1$. In the axial region, where $r_{max} \ll 1$ and $\varepsilon \approx \varepsilon_S$, the argument of the exponential function in relationship (32) is close to that in formula (31) because $2\sqrt{2} = 2.83 \approx 3$. Figure 7 shows how the estimates given by relationships (31) and (32) depend on the radius r_{max} for $\hat{H} = 0.001$ and $\varepsilon = 0.4$ in the model that will be used in Section 10. It is seen that formula (32) provides a fairly good description of nearly the entire confinement region, except for a narrow axial region $r_{max} \lesssim 0.1$, in which the resulting estimates are different because formula (31) contains the small factor r_{max}.

10. Here, we consider one convenient approximation for the magnetic field in a straight periodic confinement system. At a low plasma pressure, $\beta \ll 1$, the magnetic field differs only slightly from that in vacuum; thereby, in the simplest case, it can be represented as a sum of the uniform field and one harmonic in the longitudinal coordinate z,

$$\psi = B_0\frac{r^2}{2} - B_1\frac{r}{k}I_1(kr)\cos(kz). \qquad (33)$$

Here, I_1 is the first-order modified Bessel function; $0 < B_1 < B_0$; and $k = 2\pi/L$, with L being the period of the confinement system along its axis. In the region $r \lesssim L(2\pi)$, we have

$$I_1 \approx \frac{kr}{2}\left(1 + \frac{(kr)^2}{8}\right). \qquad (34)$$
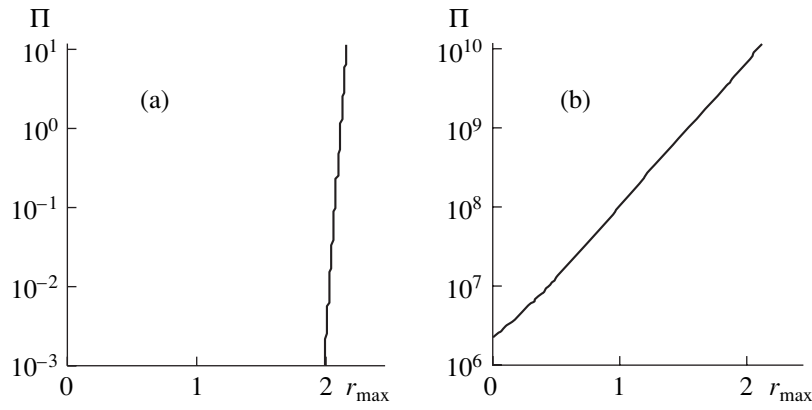
Fig. 8. Radial profiles of Π for (a) deuterium ions with the energy $E = 10$ keV and (b) α particles with the energy $E = 3.5$ MeV. The cell parameters are $L = 3$ m, $B = 5$ T, and $\varepsilon = 0.4$, the radial density profile being parabolic with the maximum value $n = 10^{14}$ cm^{-3} at the axis. The dimensionless Hamiltonian $\hat{H}$ is equal to 2.3×10^{-5} for deuterium ions and to 2×10^{-2} for α particles, the ratio of the characteristic frequencies is $\omega_{pi}/\omega_{B0} = 39$, and the dimensionless plasma density is $\hat{n} = 2.7 \times 10^{21}$. The separatrix radius is $r_{sep} = 2.44(L/2\pi)$.

For $kr \ll 1$, both terms on the right-hand side of representation (33) are written in the paraxial approximation. Since, however, the total magnetic field vanishes at the radius such that

$$kr_{sep} = 2\sqrt{(1-\varepsilon)/\varepsilon} \qquad (35)$$

(where $\varepsilon = B_1/B_0$), representation (33) describes a non-paraxial situation. In order to satisfy the condition $kr_{sep} \approx 1$, the parameter ε should be close to unity. In practice, for $r \approx r_{sep}$, the accuracy of calculation of the components B_z and B_r from the second term of representation (33) in approximation (34) is no worse than 10% even with $\varepsilon > 0.4$.

As an example of how to apply representation (33) and approximation (34), we evaluate the important integral $U = \int_{L_1} B^{-1} dl$ in which the integration is carried out over one period L_1 along a magnetic field line. We begin with the dimensionless expression presented in [9],

$$\hat{U} = 2 \int_{r_{min}}^{r_{max}} \frac{dr}{B_r} = 2 \int_{r_{min}}^{r_{max}} \frac{r\,dr}{\sqrt{\varepsilon^2 r^2 I_1^2 - \left(\frac{r^2}{2} - \hat{\psi}\right)^2}}. \qquad (36)$$

Calculations yield

$$\hat{U} = \frac{8K(w)}{\sqrt{4 - (\xi - \zeta)^2}}, \qquad (37)$$

where K is the elliptic integral of the first kind, $w = \sqrt{\dfrac{4 - (\xi + \zeta)^2}{4 - (\xi - \zeta)^2}}$, $\xi = \sqrt{(1-\varepsilon)^2 - \varepsilon\hat{\psi}}$, $\zeta = \sqrt{(1+\varepsilon)^2 + \varepsilon\hat{\psi}}$, and $\hat{\psi} = 4\pi^2\psi/B_0 L^2$. As ψ increases from zero at the axis to ψ_{sep} at the separatrix, the param-

eter w increases from zero to unity. The function $U = \dfrac{4}{\pi} U_{axis} \sqrt{\dfrac{1 - \varepsilon^2}{4 - (\xi - \zeta)^2}} K(w)$ has a logarithmic singularity at the separatrix:

$$\frac{U}{U_{axis}}(w \longrightarrow 1) = \frac{\sqrt{2}}{\pi} \ln\left(\frac{16}{1-w}\right), \qquad (38)$$

where the subscript "axis" stands for the value of the function at the axis.

11. Here, for the aforementioned confinement system with divertors, we compare the changes in μ due to nonadiabatic effects with those due to Coulomb scattering. Assuming that the Coulomb scattering is weak (the collisions are infrequent), we have $|\Delta v_\perp| \ll v$ for transit time scales. For simplicity, we restrict ourselves to considering only highly transit ions whose velocity components satisfy the inequality $v_\perp \ll v_\parallel$ (we do not consider how the ions return to the divertor cell: whether they are reflected from a strong magnetic mirror or an electrostatic plug or they pass back through the curvilinear connecting elements). The changes in the magnetic moment that are of interest to us will be characterized in terms of the dispersion of the increment in μ in transit through one period of the system.

The dispersion of the increment in the magnetic moment, $\Delta\mu = (mv_\perp/B)\Delta v_\perp$, of a particle that moves along a portion of its trajectory within the time dt and undergoes small-angle scattering is given by the relationship $\langle(\Delta\mu)^2\rangle = (mv_\perp/B)^2\langle(\Delta v_\perp)^2\rangle$, $\langle(\Delta v_\perp)^2\rangle = (v^2/\tau)dt$, $\tau = 2\pi v^3 n/(\lambda\omega_{pi}^4)$, where n is the plasma density, λ is the Coulomb logarithm, and ω_{pi} is the ion

plasma frequency (see, e.g., [18]). The total dispersion during the transit time is

$$\langle (\Delta\mu)^2 \rangle_c = \frac{4\mu E}{\tau} \int\limits_{L_1} \frac{dl}{B|v_\parallel|} \qquad (39)$$

(where $E = mv^2/2$), or, in dimensionless form, which involves the invariant J_δ,

$$\langle (\Delta J_\delta)^2 \rangle_c = 4\pi^2\lambda \left(\frac{\omega_{pi}}{\omega_{B0}}\right)^4 J_\delta \frac{\hat{U}}{\hat{n}\hat{H}}, \qquad (40)$$

where we have introduced the dimensionless plasma density $\hat{n} = nL^3$ and the function $\hat{U}$ is given by formula (37).

Using formula (32) and assuming that the phase φ_0 varies in a random manner (i.e., setting $\langle \sin^2\varphi_0 \rangle = 1/2$), we estimate the dispersion that could be introduced by the nonadiabatic effects:

$$\langle (\Delta J_\delta)^2 \rangle_{na} = \frac{2C_2^2 \hat{H} J_\delta}{1-\varepsilon_S} \left(\frac{\Lambda}{2\sqrt{2\hat{H}}}\right)^{1/4} e^{-\frac{\Lambda}{\sqrt{2\hat{H}}}}, \qquad (41)$$

where $\Lambda = (1 - \varepsilon_S)\left(2\sqrt{\frac{1-\varepsilon}{\varepsilon}} - r_{max}\right)$. The ratio $\langle (\Delta J_\delta)^2 \rangle_{na}/\langle (\Delta J_\delta)^2 \rangle_c$ is equal to

$$\Pi = \frac{\hat{H}^2\hat{n}}{2\pi^2\lambda(1-\varepsilon_S)\hat{U}} \left(\frac{\omega_{B0}}{\omega_{pi}}\right)^4 \left(\frac{\Lambda}{2\sqrt{2\hat{H}}}\right)^{1/4} e^{-\frac{\Lambda}{\sqrt{2\hat{H}}}}. \qquad (42)$$

Figure 8 shows how the quantity Π depends on the radius r_{max} of the magnetic surface for 10-keV D ions and for 3.5-MeV ^{4}He ions in a divertor cell with reactor parameters. We can see that, for the main plasma, the effect of the nonadiabatic nature of the ion motion is small over the entire volume, but for fast particles, this effect can be significant. It should be noted, however, that, even when the dispersion given by formula (41) exceeds that given by formula (40), we cannot speak of the decisive role of nonadiabatic effects in particle losses because, for values of $(\Delta J_\delta)^2$ that are small but are larger than those given by formula (40), it may well be that the magnetic moment μ will not change at all. An excess of the standard mapping parameter (see [8]) over a certain critical value can be considered to serve as a criterion that the magnetic moment does indeed change. This excess takes place in a separatrix layer with a thickness on the order of ρ_E.

12. In summary, we can say that, in the confinement systems under consideration, namely, those with magnetic null lines and/or points near the plasma boundary, transverse losses of particles due to the nonadiabatic nature of their motion can occur only from a separatrix layer with a thickness on the order of the Larmor radius. The depth of the region where the magnetic moment μ changes is of the same order of magnitude, but not all of the particles that enter this region are allowed by the conservation law for the generalized azimuthal momentum to pass through the separatrix, so such particles can be subject to absolute confinement.

REFERENCES

1. M. Tuszewskii, Nucl. Fusion **28**, 2033 (1988).

2. B. L. Wright, Nucl. Fusion **9**, 1739 (1990).

3. A. I. Morozov, V. P. Pastukhov, and A. Yu. Sokolov, in *Proceedings of the Workshop on D-^{3}He Based Reactor Studies, Moscow, 1991*, Paper IC1; in *Proceedings of the International Sherwood Fusion Theory Conference, Santa Fe, 1992*, Paper 2C44.

4. M. M. Berdnikova, S. V. Vaĭtonis, A. M. Vaĭtonene, *et al.*, Vopr. At. Nauki Tekh., Ser. Termoyadernyĭ Sintez, No. 1, 22 (2003).

5. G. I. Dimov, Preprint No. 2-150 (Inst. of Nuclear Physics, Siberian Division, USSR Acad. Sci., Novosibirsk, 1982).

6. T. D. Akhmetov, V. S. Belkin, E. D. Bender, *et al.*, Fiz. Plazmy **23**, 988 (1997) [Plasma Phys. Rep. **23**, 911 (1997)].

7. V. V. Arsenin, E. D. Dlougach, V. M. Kulygin, *et al.*, Nucl. Fusion **41**, 945 (2001).

8. B. V. Chirikov, in *Reviews of Plasma Physics*, Ed. by B. B. Kadomtsev (Énergoatomizdat, Moscow, 1984; Consultants Bureau, New York, 1987), Vol. 13.

9. A. I. Morozov and L. S. Solov'ev, in *Reviews of Plasma Physics*, Ed. by M. A. Leontovich (Gosatomizdat, Moscow, 1963; Consultants Bureau, New York, 1966), Vol. 2.

10. M. Y. Wang and G. H. Miley, Nucl. Fusion **19**, 39 (1979).

11. A. M. Dykhne and A. V. Chaplik, Zh. Éksp. Teor. Fiz. **40**, 666 (1961) [Sov. Phys. JETP **13**, 465 (1961)].

12. J. Lacina, Czech. J. Phys. B **13**, 401 (1963).

13. R. J. Hastie, G. D. Hobbs, and J. B. Taylor, in *Proceedings of the 3rd International Conference on Plasma Physics and Controlled Nuclear Fusion Research, Novosibirsk, 1968* (IAEA, Vienna, 1969), Vol. 1, p. 389.

14. G. E. Howard, Phys. Fluids **14**, 2378 (1971).

15. R. H. Cohen, G. Rowlands, and J. H. Foote, Phys. Fluids **21**, 627 (1978).

16. A. V. Zvonkov and A. V. Timofeev, Fiz. Plazmy **11**, 320 (1985) [Sov. J. Plasma Phys. **11**, 186 (1985)].

17. S. V. Kuz'min and P. B. Lysyanskiĭ, Fiz. Plazmy **15**, 778 (1989) [Sov. J. Plasma Phys. **15**, 449 (1989)].

18. B. A. Trubnikov, *Reviews of Plasma Physics*, Ed. by M. A. Leontovich (Gosatomizdat, Moscow, 1963; Consultants Bureau, New York, 1965), Vol. 1.

Translated by G.V. Shepekina

ICR Heating in Ion Separation Systems

A. V. Timofeev

Russian Research Centre Kurchatov Institute, pl. Kurchatova 1, Moscow, 123182 Russia
Received February 24, 2005; in final form, May 19, 2005

Abstract—A systematic procedure for analyzing the physical processes that govern ICR heating in systems for ion separation is developed. The procedure is based on an analytic model of an rf antenna generating rf fields within a plasma column in a magnetic field and includes such issues as the calculation of rf fields, examination of the ICR interaction of ions with these fields, and determination of the distribution function of the ion flow at the exit from the ICR heating system. It is shown that, even in ICR heating systems with easily achievable parameter values, ions with appreciably different masses can be efficiently separated by energy. © 2005 Pleiades Publishing, Inc.

1. INTRODUCTION

ICR systems for ion separation are based on the possibility of selective heating of ions of one species in a plasma with a complex ion composition (see, e.g., [1]). An analysis of the physical processes occurring in such systems is carried out in several steps: the development of a model of an antenna that excites rf fields within a plasma column; the calculation of rf fields; the examination of the resonant interaction of ions with these fields; and, finally, the determination of the distribution function of the ions produced in the ICR interaction process.

The key problem is that of calculating the fields. There is no general and universal means of solving it. The spatial distributions of the fields and their polarization depend essentially on such parameters as the plasma density, the temperature of the plasma components, the magnetic field strength, etc. For a plasma with several ion species, the important parameters are relative concentrations of the species and also the relationships between their gyrofrequencies, on the one hand, and the rf field frequency, on the other. A rather complicated problem involving a variety of factors is that of the excitation of rf fields in a plasma containing a mixture of isotopes having almost equal masses. In what follows, a study will be made of a simpler case of a plasma with two ion species whose masses, as well as concentrations, are vastly different. Let the mass number of 3% of the ions be equal to $A = 100$, and let the mass number of the remaining ion species be equal to $A = 200$. Numerical estimates will be carried out for the PS-1 plasma separator that is now under construction at the Nuclear Fusion Institute of the Russian Research Centre Kurchatov Institute. The parameters of the separator are as follows: the magnetic field $B_0 \approx 5$ kG, the plasma density $n_0 \approx 10^{12}$ cm^{-3}, the electron temperature $T_e \approx 5$ eV, the ion temperature $T_i \approx 0.5$ eV, the antenna radius $r_A = 15$ cm, the vacuum chamber radius $r_B = 20$ cm, the mean plasma radius $r_{Pl} = 10$ cm, and the

antenna length $2L = 1$ m. The total length $2L_1$ of the heating system along the magnetic field can be several times greater than the antenna length. We will assume that the lighter ion species satisfies the ICR condition $\omega \approx \omega_i \approx 5 \times 10^5$ s^{-1}.

In order to calculate rf fields in a plasma under the above conditions, it is expedient to utilize an approach in which the rf field generated by a current-carrying antenna is represented as a superposition of the TM and TE modes [2, 3], each of which is a superposition of the electric and magnetic fields described by an independent solution to the set of Maxwell's equations. In vacuum, the electric field of the TE modes is perpendicular to the waveguide axis (so the longitudinal electric field component is zero) and the magnetic field of the TM modes is oriented in the same manner. In a plasma waveguide, the polarization of the independent modes is mixed, so the terms TE and TM modes are rather conventional. In what follows, the mode in which the main component of the electric field is the transverse one will be called the TE mode and that in which the main component of the electric field is longitudinal will be referred to as the TM mode.

In vacuum, the electric fields of both of the modes are nearly potential. However, the TE and TM modes generated by the current-carrying antennas are phased in such a way that their potential components cancel one another, leaving a comparatively weak vortex electric field. The TM mode is efficiently screened by the plasma due to the redistribution of the electrons along the main magnetic field under the action of the longitudinal electric field of this mode. On the other hand, the plasma exerts a weaker influence on the TE mode, which thereby can penetrate deep into the plasma column even when the plasma density is high. In this case, there is a strong potential electric field of the TE mode within the plasma because the TM mode is screened by the electric charge. Based on these distinctive features of the excitation of rf fields by current-carrying anten-
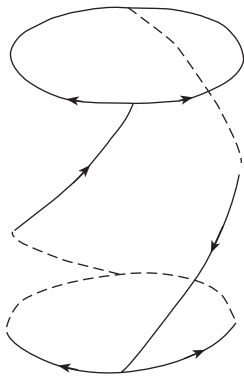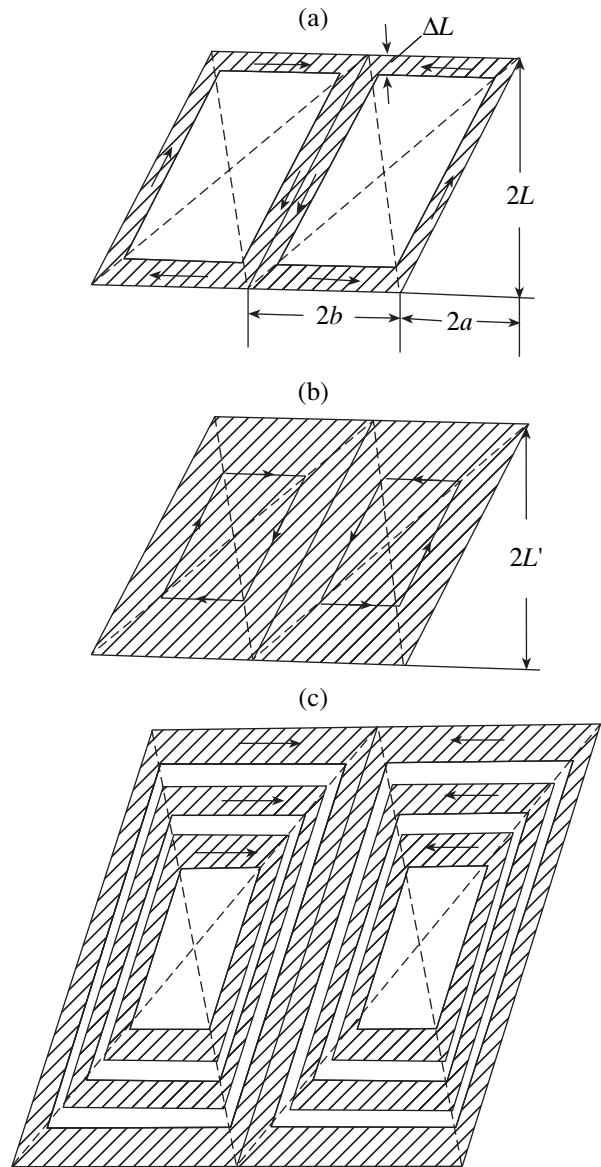
Fig. 1. Helical antenna. The instantaneous directions of the current are indicated by arrows.

Fig. 2. Mappings of antennas onto a plane: (a) helical antenna, (b) an element of a model of a helical and spiral antennas (with a continuous current density distribution), and (c) spiral antenna.

nas, it is possible to obtain an analytic expression for the left-polarized electric field, whose interaction with ions under the ICR conditions is especially intense. The change in the ion energy in this field and the shape of the distribution function of the accelerated ions are quite easy to calculate. As a result, in the present paper, a comparatively simple (essentially analytic) model is proposed that describes the entire ICR heating process. The starting point of the ICR heating model is the model of current-carrying antennas (a helical and a spiral one), which is described in Section 2. In Section 3, the spatial structure of the rf field is analyzed based on the above considerations. It is found that the main contribution to the left-polarized electric field comes from a small number of largest scale axial harmonics. In Section 4, it is shown that, under conditions corresponding to the screening of the TM mode by the plasma, the potential approximation provides a satisfactory description of the rf field in a system stretched along its axis. The boundary conditions at the ends of the plasma column are discussed, as well as their dependence on the electric contact between the plasma and the ends of the vacuum chamber. In Section 5, the ICR heating process is considered and the causes for the broadening of the resonance lines in ICR heating systems are discussed. Finally, Section 6 gives an analysis of how the energy distribution of the ion flow is influenced by such factors as the velocity of the directed ion motion, rf field frequency, and system length.

2. CURRENT-CARRYING ANTENNAS AND CURRENT SPECTRUM

The antennas used for ICR heating of a plasma column are composed of finite-width conductors having the form of a helix wound on a cylindrical surface around the plasma. In order for the ion heating to be efficient, it is necessary that the antenna current have both the azimuthal and longitudinal components (see, e.g., [2, 3]). This requirement can be met, e.g., when the conductor is at least partially wound along a helix. It is

in this way that the conductors are wound in the most widely used helical antennas.

The antennas can conveniently be analyzed by considering their mappings onto a plane. For instance, the mapping of the helical antenna shown in Fig. 1 is given in Fig. 2a, in which the points separated by the distance $4b = 2\pi r_A$ (where r_A is the antenna radius) in the horizontal direction should be identified. The current distribution in a helical antenna can be treated as a superposition of two distributions. One of the distributions is displayed in Fig. 2b. The other distribution is such that each of the parallelograms in Fig. 2b is contracted

toward the point of intersection of the diagonals in a ratio of $1/(1 - \Delta)$. In the contracted parallelograms, the current density is the same as that in the parallelograms in Fig. 2b and the current direction is reversed.

In Fig. 2a, the current lines along the inclined (helical) portion of the antenna rotate in the azimuthal direction. For $a = b$ (where $b = \pi r_A/2$), the outermost current lines, which connect two ends of the antenna ($z = \pm L$), rotate half a turn. Such an antenna is called a half-wave antenna [1]. The turning angle can be arbitrary. Increasing this angle leads to an increase in the θ component of the antenna electric field. It is this component that is responsible for the excitation of the transverse electric field, which heats the ions under ICR conditions. In this situation, however, the longitudinal wavenumber also increases, which can have an undesirable effect.

In a helical antenna, the current flows along narrow strips of width $L\Delta$, so its spectrum in the longitudinal wavenumbers changes insignificantly up to the wavenumbers $k_{\parallel} \approx 1(L\Delta)$. The wider the current-carrying conductors, the narrower the spectrum. In the limit $\Delta = 1$, the current distribution passes over to that shown in Fig. 2b. In practice, such a distribution can be achieved with a spiral antenna—a system of conductors wound along spirals that emerge from the centers of the parallelograms (see [2]). An approximate analysis of a spiral antenna can be carried out by modeling it as a set of similar helical antennas of decreasing size that are nested inside one another on a cylindrical surface of radius r_A (see Fig. 2c).

The TE wave under consideration is excited by the azimuthal component of the antenna current. In the spectrum of the TE wave in the azimuthal wavenumbers, the first mode, which runs in the azimuthal direction in the sense of the ion gyration, plays the most important role because this is the only mode that excites the electric field whose left-polarized component $E_+ = \dfrac{E_r + iE_\theta}{\sqrt{2}}$ is nonzero at the cylinder axis (see, e.g., [1–6]). It is precisely this electric field component that heats the ions under the ICR conditions. For the antenna current distribution shown in Fig. 2b, the first azimuthal mode is described by the expression

$$
J_\theta(\theta, z) = \frac{2}{\pi}J_{0\theta}\Big((A + 1)\sin\Big((A + 1)\frac{\pi}{2}\frac{z}{L} - \theta\Big)
$$

$$
+ (A - 1)\sin\Big((A - 1)\frac{\pi}{2}\frac{z}{L} - \theta\Big) \tag{1}
$$

$$
- 2A\cos\Big(\frac{\pi}{2}\frac{L'}{L}\Big)\sin\Big(A\frac{\pi}{2}\frac{z}{L} - \theta\Big)\Big).
$$

Here, $J_{0\theta}$ is the density of the surface current in the portions of the antenna conductors where it flows in the azimuthal direction, the coordinate z varies within the interval $-L' \le z \le L'$, and $A = a/b$.

The current density given by expression (1) has components that are even and odd in z (see Fig. 3). In the direction of the angular coordinate θ, they are shifted by an angle of $\pi/2$; the even component is proportional to $\sin\theta$ and the odd component is proportional to $\cos\theta$. It is easy to see that the z-averaged value of $J_\theta(\theta, z)$ is equal to zero. In fact, if this were not the case, the current continuity condition would fail because of the azimuthal modulation of the current and a charge would be accumulated.

For further analysis, it is necessary to expand the current density in a Fourier series in the z coordinate. The family of functions into which the current density should be expanded is determined by the boundary conditions. The simplest boundary conditions can be formulated by adopting one of the two diametrically opposite assumptions: that the rf fields are completely reflected from the chamber ends or that they are completely absorbed at the ends. In the first case, standing waves with a discrete wavelength spectrum are established in the system; the maximum wavelength can be twice as large as the system length. In the second case, as in an infinite space, there exist running waves of arbitrary wavelength, having a continuous spectrum. It is under this assumption that the problem of the excitation of electromagnetic fields in a plasma column was analyzed in [5, 6]. In [4], both types of the boundary conditions were considered.

In the frequency range under consideration, it is difficult to make the chamber ends completely absorbing. The assumption that the ends are reflecting seems to be more realistic. There are various possible boundary conditions corresponding to the complete reflection. It will be shown below that the specific form of the boundary conditions depends on the nature of the electric coupling between the plasma and the chamber ends. When the coupling is perfect, the electric field component tangential to the surfaces of the ends should be assumed to vanish, $\mathbf{E}_t = 0$. When the chamber ends are completely insulated from the plasma, it is necessary to use the boundary condition $\partial\mathbf{E}_t/\partial z = 0$. These boundary conditions will be satisfied automatically if, in the first case, the even component of the current density will be expanded into a Fourier series in the functions $\cos\Big(\big(k + \frac{1}{2}\big)\pi\frac{z}{L_1}\Big)$ and the odd component will be expanded in the functions $\sin\Big(k\pi\frac{z}{L_1}\Big)$; in the second case, it is necessary to use the functions $\cos\Big(k\pi\frac{z}{L_1}\Big)$ and $\sin\Big(\big(k + \frac{1}{2}\big)\pi\frac{z}{L_1}\Big)$, respectively.

The electric contact between the plasma and the chamber ends implies that there should be an electric current. Since we are interested in alternating electric

fields, we must regard the chamber ends as emitting ones (see below). Usually, in systems for ICR ion separation, no special means are used to initiate the emission current from the ends. It is for these reasons that the model of insulated ends seems to conform better to the actual conditions.

It will be shown below that the electric current density and left-polarized electric field are expanded in Fourier series in the same functions.

The rf fields generally extend outside of the ICR heating system along the magnetic field. Consequently, the length of the interval $(-L_1, L_1)$ on which the functions are expanded in Fourier series cannot be less than $2L$. Note, however, that the region occupied by rf fields can be made shorter by introducing well-conducting grids (transparent to the plasma) into a separation system (as was proposed by V.A. Zhil'tsov).

With allowance for these considerations and the assumption that the chamber ends are insulated from the plasma, we obtain

$$
J_\theta(\theta, z) = \frac{2}{\pi^2} J_{0\theta} \left[\cos\theta \sum_{k=-\infty}^{\infty} P_k(L') \sin\left(\left(k+\frac{1}{2}\right)\pi\frac{z}{L_1}\right) \right.
$$
$$
\left. - \sin\theta \sum_{k=-\infty}^{\infty} Q_k(L') \cos\left(k\pi\frac{z}{L_1}\right) \right], \tag{2}
$$

where

$$
P_k(L') = \frac{k+\frac{1}{2}}{k+\frac{1}{2}+a_0}\left(\frac{1}{k+\frac{1}{2}+a_-}\sin\left[\left(k+\frac{1}{2}+a_-\right)\pi\frac{L'}{L}\right]\right.
$$

$$
\left. + \frac{1}{k+\frac{1}{2}+a_+}\sin\left[\left(k+\frac{1}{2}+a_+\right)\pi\frac{L'}{L}\right]\right),
$$

$$
Q_k(L') = \frac{k}{k+a_0}\left(\frac{1}{k+a_-}\sin\left[(k+a_-)\pi\frac{L'}{L}\right]\right.
$$

$$
\left. - \frac{1}{k+a_+}\sin\left[(k+a_+)\pi\frac{L'}{L}\right]\right), a_0 = \frac{A}{2}\frac{L_1}{L}, a_\pm = \frac{(A\pm1)}{2}\frac{L_1}{L}.
$$

In expression (2), it has been convenient to switch from summation over the positive integer values of k to summation over all integer values of k. In the case of conducting ends, k should be replaced with $k + 1/2$ in the first sum in expression (2), and vice versa in the second sum.

An analysis shows that, even with a small number of harmonics ($k = 10$), the Fourier series expansion makes it possible to reconstruct current density (1) with good accuracy. When there is a need to use actual current density distributions, which are combinations of distributions (1) with different values of L' and exhibit shorter spatial scales (see below), it is necessary to take a larger number of Fourier harmonics.
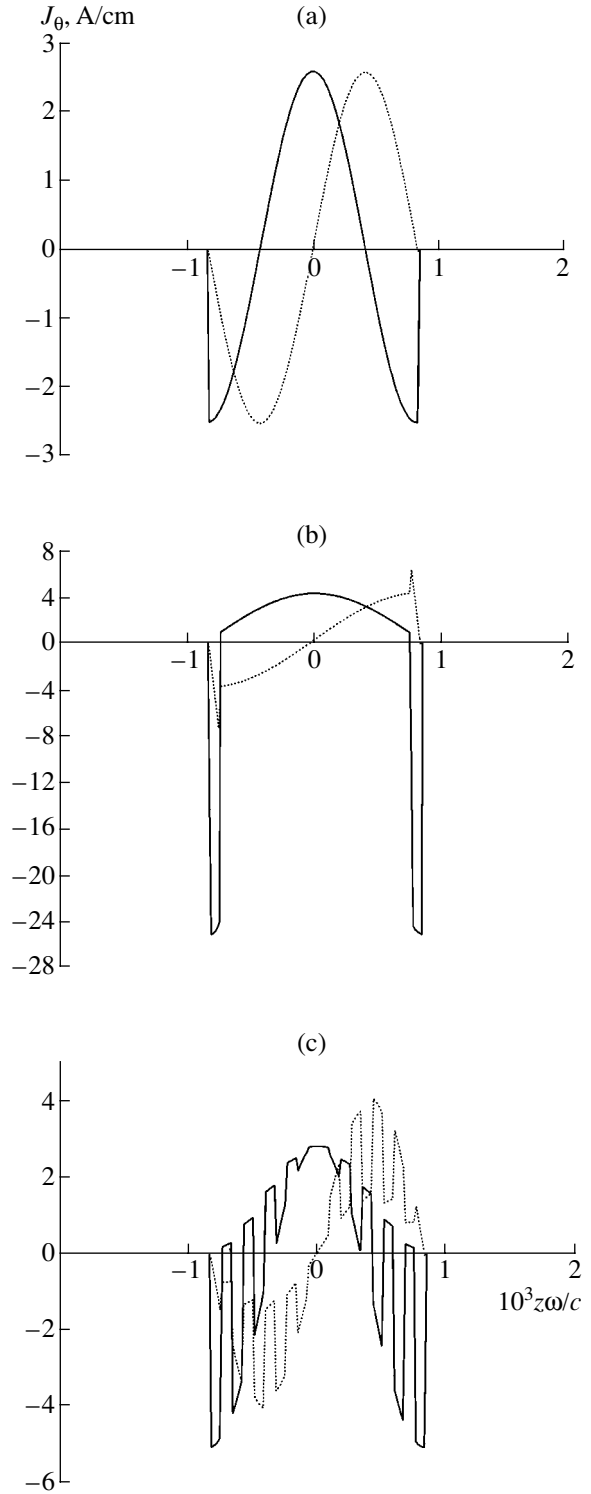
Fig. 3. Longitudinal (along the z axis) profiles of the density of the azimuthal current component rotating in the azimuthal direction in the sense of the ion gyration ($m = -1$) within half-wave antennas: (a) spiral antenna ($n = 10$) with a continuous current density distribution, (b) helical antenna ($n = 1$), and (c) spiral antenna ($n = 5$). In all three figures, the solid curves are for the azimuthal current component that is even in z, and the dotted curves are for the component that is odd in the longitudinal coordinate.

$|J_{\theta,\,ev}/n|^2$, arb. units   (a)

$|J_{\theta,\,od}/n|^2$, arb. units
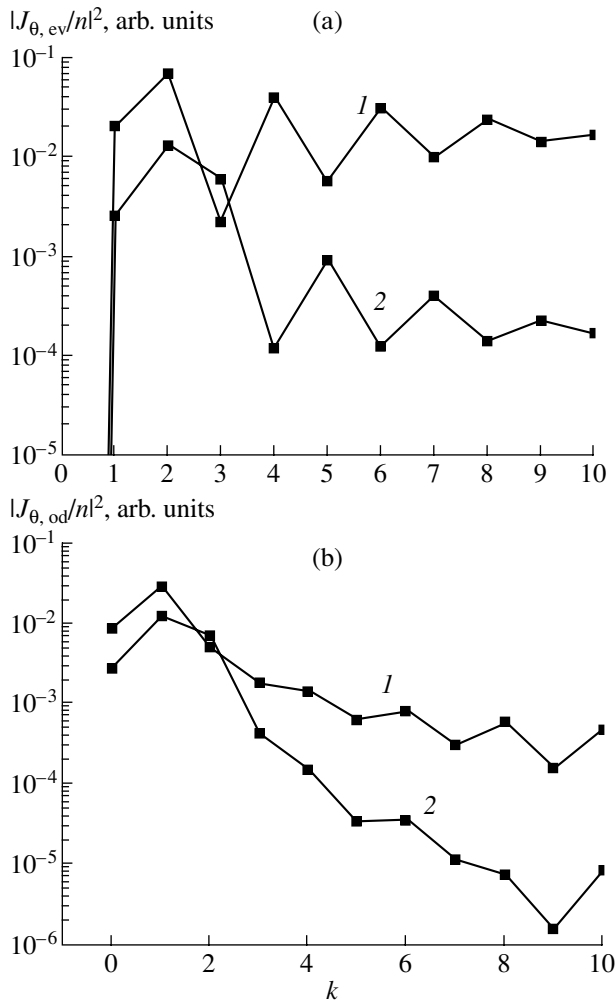
Fig. 4. Spectra of the azimuthal current density in the longitudinal wavenumbers in a helical ($n = 1$) and a spiral ($n = 5$) half-wave antennas for $L_1 = 2L$: (a) even and (b) odd current density components. In both figures, spectra *1* and *2* refer, respectively, to a helical and a spiral antenna.

If the current density varies in time according to the law $\propto \cos(\omega t)$, then, for waves rotating in the azimuthal direction in the sense of the ion gyration, it is described by the expression

$$J_\theta(\theta, z, t)$$

$$= \frac{1}{\pi^2} J_{0\theta} \left[\cos(\theta + \omega t) \sum_{k=-\infty}^{\infty} P_k(L') \sin\left(\left(k + \frac{1}{2}\right)\pi \frac{z}{L_1}\right) \right.$$

$$\left. - \sin(\theta + \omega t) \sum_{k=-\infty}^{\infty} Q_k(L') \cos\left(k\pi \frac{z}{L_1}\right) \right]. \tag{3}$$

By summing expressions (3), first, with $L' = \frac{p}{n}L$ over the range $1 \le p \le n$ and, second with $L' = \left(\frac{p}{n} - \Delta\right)L$ over the same range and by taking the difference

between the first and the second sums, it is possible to construct the current density distributions in the antenna types under consideration with an arbitrary number of conductors. In other words, in order to obtain the spectrum of a spiral antenna, the coefficients $P_k(L')$ and $Q_k(L')$ in expression (3) should be replaced

with the sums $R_k = \sum_{p=1}^{n} \left\{ P_k\left(\frac{p}{n}L\right) - P_k\left(\left(\frac{p}{n} - \Delta\right)L\right) \right\}$

and $S_k = \sum_{p=1}^{n} \left\{ Q_k\left(\frac{p}{n}L\right) - Q_k\left(\left(\frac{p}{n} - \Delta\right)L\right) \right\}$, respectively, where n is the number of conductors in a spiral antenna. A helical antenna can be treated as a limiting case of a spiral antenna with $n = 1$.

The spectra of the current density in spiral and helical half-wave antennas carrying the same total current are compared in Fig. 4. In the model developed here, namely, that in which a spiral antenna is composed of individual conductors, the current in each conductor of the spiral antenna is n times lower than that in the only conductor of the helical antenna. The spectra shown in Fig. 4 were calculated for $L_1 = 2L$. As expected, the spectrum of the current density in a helical antenna is far wider than that of a spiral antenna: its width is determined by the width of the conductor, $\Delta = L/10$. Accordingly, the amplitudes of the Fourier harmonics with numbers of up to $k \approx 20$ are essentially the same. The oscillatory nature of the spectrum is explained by the fact that the antenna size is a multiple of the length of the interval used for Fourier series expansions.

In the case of an $n = 5$ spiral antenna, the contributions of individual conductors to the Fourier coefficients have different phases, so the total contribution is significantly smaller than that of an individual conductor. The only exception to this is Fourier harmonics with the smallest numbers k (in this case, the corresponding contributions of the conductors differ moderately) and also harmonics with the numbers $k \approx 2nq$, where q is an integer (in this case, the periodic character of the positions of the conductors comes into play).

3. SPATIAL STRUCTURE OF RF FIELDS

3.1. Radial Field Structure and Screening of the TM Mode

In determining the spatial structure of the rf fields excited by a current-carrying antenna in a plasma waveguide, it is necessary to take into account the plasma inhomogeneity and the complicated shape of the antenna (see above). In some cases, it is reasonable to supplement the natural assumption that the plasma column is azimuthally and axially uniform. The rf fields in such systems can be conveniently represented as a superposition of the components that are harmonic functions of the longitudinal coordinate z. (That the first azimuthal harmonic plays a special role in analyzing the ICR interaction process was pointed out above.)

Evaluation of the radial dependence of each of the components, as well as the calculation of their sum, can be carried out only numerically (see, e.g., [4, 6]), so it becomes more difficult to reveal the qualitative regular features of the excitation of rf fields in a plasma waveguide. The analysis can be made much simpler by referring to the long-known idea that the transverse electric field of an rf antenna is amplified as a result of plasma response to the antenna longitudinal field. This idea was employed in [2, 3], where the antenna electromagnetic field was represented as a superposition of the modes that are known as TM and TE modes in vacuum. In a plasma, these modes become the so-called slow waves (Trivelpiece–Gould and hybrid modes) and fast waves (Alfvén and magnetosonic modes).

The effect of the plasma on the TM mode becomes important even at a low plasma density if the condition $|\varepsilon_\parallel| \geq 1$ (where $\varepsilon_\parallel$ is the longitudinal permittivity of the plasma) is satisfied. For systems with the parameters mentioned in the Introduction, the electron thermal velocity is higher than the characteristic phase velocity of rf oscillations along the magnetic field, $\omega \ll k_\parallel v_{Te}$. In this case, the longitudinal dielectric function is

$$\varepsilon_\parallel \approx \frac{1}{k_\parallel^2 d_e^2}\left(1 + i\sqrt{\pi}\frac{\omega}{k_\parallel v_{Te}}\right), \text{ where } d_e = \frac{v_{Te}}{\sqrt{2}\,\omega_{pe}} \text{ is the}$$

Debye radius and $v_{Te} = \sqrt{\dfrac{2T_e}{m_e}}$.

In a plasma, the TM mode transforms into potential oscillations. The short-wavelength potential oscillations satisfy the dispersion relation

$$k_\perp^2 \varepsilon_\perp + k_\parallel^2 \varepsilon_\parallel = 0. \tag{4}$$

Here, $\varepsilon_\perp \approx \dfrac{\omega_{pi}^2}{\omega_i^2 - \omega^2} + i\dfrac{\sqrt{\pi}}{2}\dfrac{\omega_{pi}'^2}{\omega k_\parallel v_{Ti}'}W(\zeta_i')$, where $\zeta_i' =$

$\dfrac{\omega - \omega_i'}{k_\parallel v_{Ti}'}$, $v_{Ti}' = \sqrt{\dfrac{2T_i'}{m_i'}}$, and W is the probability integral of the complex argument. With the ion separation problem in mind, we assume that (i) the ion plasma component consists of two ion species, namely, lighter ions (with a mass number of $A = 100$) and heavier ions (with a mass number of $A = 200$), and (ii) the gyrofrequency of the lighter ions is close to the rf field frequency, $\omega \approx \omega_i' = 2\omega_i$. In what follows, the primed quantities will characterize the lighter ions.

When the concentration of lighter ions is so low that their contribution to the dielectric function can be ignored, dispersion relation (4) yields

$$\omega^2 \approx \omega_i^2 + k_\perp^2 V_s^2\left(1 - i\sqrt{\pi}\frac{\omega}{k_\parallel v_{Te}}\right). \tag{5}$$

In this case, the TM mode transforms into ion acoustic oscillations modified by the presence of a magnetic field. However, for the parameters of the system that were mentioned in the Introduction, the governing contribution to $\varepsilon_\perp$ comes from the lighter ions. In its interaction with these ions under the ICR conditions, the TM mode rapidly loses its energy and is strongly damped on short spatial scales when penetrating from the plasma boundary deeper into the plasma.

As an equation for $k_\perp$, dispersion relation (4) has the solution

$$k_\perp \approx e^{i\pi/4}\left(\frac{4}{\pi}\right)^{1/4}\frac{(\omega k_\parallel v_{Ti}')^{1/2}}{d_e \omega_{pi}'}. \tag{6}$$

The longitudinal electric field of the TE mode is weak (in vacuum, it vanishes), so the plasma responds to it to a lesser extent. Under the condition $N_\parallel^2 \gg \varepsilon_\perp$, the effect of the plasma on the TE mode can be ignored and the fields of the mode can be described by the vacuum equation (see, e.g., [3])

$$\frac{1}{r}\frac{d}{dr}r\frac{dB_\parallel}{dr} + \left(\left(\frac{\omega}{c}\right)^2 - k_\parallel^2 - \frac{m^2}{r^2}\right)B_\parallel = -\frac{4\pi}{c}\frac{1}{r}\frac{d}{dr}rJ_\theta. \tag{7}$$

According to [2, 3], the total transverse electric field is expressed in terms of $B_\parallel$ and $E_\parallel$ through the relationship

$$\mathbf{E}_\perp = \frac{i}{1 - N_\parallel^2}\frac{c}{\omega}(\nabla \times (\mathbf{b}B_\parallel) + N_\parallel\nabla_\perp E_\parallel), \tag{8}$$

which yields

$$E_+ = \frac{1}{1 - N_\parallel^2}\frac{1}{\sqrt{2}}\frac{c}{\omega}\left(\frac{d}{dr} - \frac{m}{r}\right)(B_\parallel + iN_\parallel E_\parallel). \tag{9}$$

If, in accordance with what was said above, the TM mode is localized near the plasma boundary and does not penetrate deep into the plasma, then, for the central region of the plasma column, we can set $E_\parallel = 0$. In the central region, the transverse electric field coincides with the electric field of a TE mode in a vacuum waveguide:

$$E_+ = \frac{1}{1 - N_\parallel^2}\frac{1}{\sqrt{2}}\frac{c}{\omega}\left(\frac{d}{dr} - \frac{m}{r}\right)B_\parallel. \tag{10}$$

It should be noted that, under the condition $k_\parallel r_A \ll 1$ and under vacuum conditions, the quantities $B_\parallel$ and $iN_\parallel E_\parallel$ in expression (9) nearly cancel one another (their sum is approximately $(k_\parallel r_A)^2$ times smaller than each of them). As a result, the screening of the TM mode by the plasma leads to an increase in the transverse electric field due to the "liberation" of the electric field of the TE mode. This additional transverse electric field is potential because it is generated by the charges that are induced near the plasma boundary in the interaction with the TM mode. The amplification of the transverse electric field in the plasma was thoroughly discussed in [2, 3].

n_0, j_0, arb. units
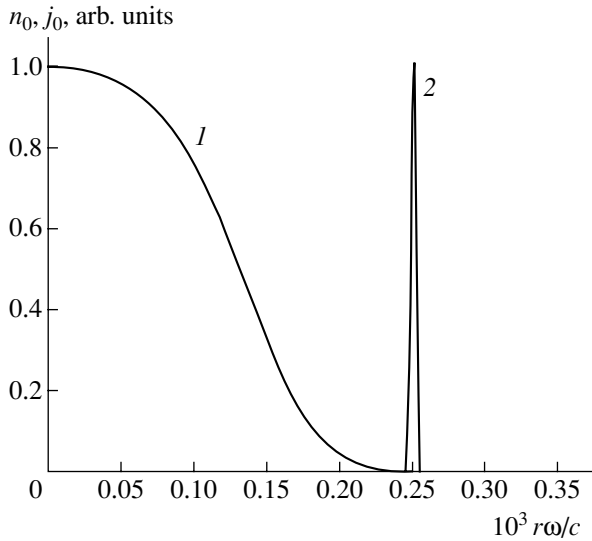
Fig. 5. Radial profiles of (*1*) the plasma density and of (b) the current density in the antenna.

The above considerations of the spatial structure of the rf field are confirmed by the results of calculations carried out by the method described in [3]. In these calculations, an analysis was made of the fields excited by an individual axial Fourier harmonic of the current. The current distribution was approximated by the expression (see Fig. 5)

$$\mathbf{j(r)} = \left(0, 1, -\frac{m}{rk_\parallel}\right)\frac{1}{\sqrt{\pi}\Delta_A}$$

$$\times \exp\left(-\left(\frac{r-r_A}{\Delta_A}\right)^2\right)J_\theta(k_\parallel)\exp(im\theta + ik_\parallel z),$$

where $k_\parallel = \pi/L$, $L = 50$ cm is the half-length of the antenna, $r_A = 15$ cm, $\Delta_A = 10^{-2}r_A$, and $r_B = 20$ cm is the radius of a perfectly conducting wall. In accordance with Section 2 of the present paper, the azimuthal wavenumber was set equal to $m = -1$.

The radial plasma density profile was taken to be

$$n_0(r) = n_0(0)\left(1 - \tanh\left(\frac{r^2 - r_{Pl}^2}{2\Delta_{Pl}r_{Pl}}\right)\right)\left(1 + \tanh\left(\frac{r_{Pl}}{2\Delta_{Pl}}\right)\right)^{-1},$$

where Δ_{Pl} is a parameter characterizing the steepness of the density profile. Here, we set $\Delta_{Pl} = r_{Pl}/2 = 5$ cm.

The remaining parameter values used in calculations have been mentioned in the Introduction.

The rf fields were calculated from Maxwell's equations with the following expressions for the current density components:

$$\mathbf{j}^{(i)} = -\frac{i\omega}{4\pi}((\varepsilon_\perp^{(i)} - 1)\mathbf{E}_\perp + ig^{(i)}\mathbf{E}\times\mathbf{b}),$$

$$\left.\begin{aligned}
\mathbf{j}_\perp^{(e)} &= \frac{\omega_{pe}^2}{4\pi\omega_e}\mathbf{b}\times\mathbf{E} + \frac{c}{4\pi}\nabla\times(\mathbf{b}(Q_1B_\parallel - iN_\parallel Q_2E_\parallel)) \\
j_\parallel^{(e)} &= \frac{\omega}{4\pi}N_\parallel Q_2\left(-B_\parallel + 2i\frac{\omega_e}{\omega}N_\parallel\zeta_e^2 E_\parallel\right)
\end{aligned}\right\},$$

where

$$\varepsilon_\perp^{(i)} = \frac{1}{2}(\varepsilon_+^{(i)} + \varepsilon_-^{(i)}), \quad g^{(i)} = \frac{1}{2}(\varepsilon_+^{(i)} - \varepsilon_-^{(i)}),$$

$$\varepsilon_+^{(i)} = 1 - \frac{\omega_{pi}^2}{\omega(\omega - \omega_i)} + \frac{\omega_{pi}'^2}{\omega k_\parallel v_{Ti}'}i\sqrt{\pi}W(\zeta_i'),$$

$$\varepsilon_-^{(i)} = 1 - \frac{\omega_{pi}^2}{\omega(\omega + \omega_i)} - \frac{\omega_{pi}'^2}{\omega(\omega + \omega_i')},$$

$$\mathbf{b} = \mathbf{B}_0/B_0, \quad Q_1 = -2\left(\frac{\omega_{pe}}{\omega_e}\right)^2\frac{T_e}{m_ec^2}i\sqrt{\pi}\zeta_e W(\zeta_e),$$

$$Q_2 = -\frac{\omega_{pe}^2}{\omega\omega_e N_\parallel^2}(1 + i\sqrt{\pi}\zeta_e W(\zeta_e)), \quad \zeta_e = \frac{\omega}{k_\parallel v_{Te}}.$$

The longitudinal component of the ion current was ignored because of its smallness in comparison to the longitudinal electric current.

Calculations show that, in the presence of plasma, the longitudinal electric field is markedly lower than that in vacuum (see Fig. 6a; curves *1*, *2*). The radial scale length on which this field decays is about several centimeters, which agrees in order of magnitude with expression (6) for $\mathrm{Im}k_\perp$. In a plasma without resonant (lighter) ions, the oscillations manifest themselves as ion acoustic waves (see relationship (5)). This is evidenced by the oscillatory structure of the longitudinal electric field, which becomes more pronounced as the electron temperature is increased (see Fig. 6b). In accordance with expression (6), the higher the electron temperature, the longer the wavelength and, simultaneously, the weaker the resonant interaction of the longitudinal electric field with the electrons, which leads to an increase in the field amplitude. In Fig. 6a, the longitudinal electric field is seen to have a maximum in the boundary region, where the plasma density is low. The maximum is due to the plasma resonance, which occurs under the condition $\omega^2 = \omega_{pi}^2 + \omega_i^2$.

The TE mode is characterized by the longitudinal magnetic field. Figure 6c shows that the plasma with the above parameters has essentially no effect on the TE mode—the radial profile of the longitudinal magnetic field in Fig. 6c is the same as that in vacuum. At the same time, the left-polarized electric field in a plasma is stronger than that in vacuum (cf. curves *1* and *2* in Fig. 6d). It follows from the aforesaid that, in the central plasma region, this field coincides with the field of the TE mode in vacuum (see Fig. 6d, curve *3*). There is
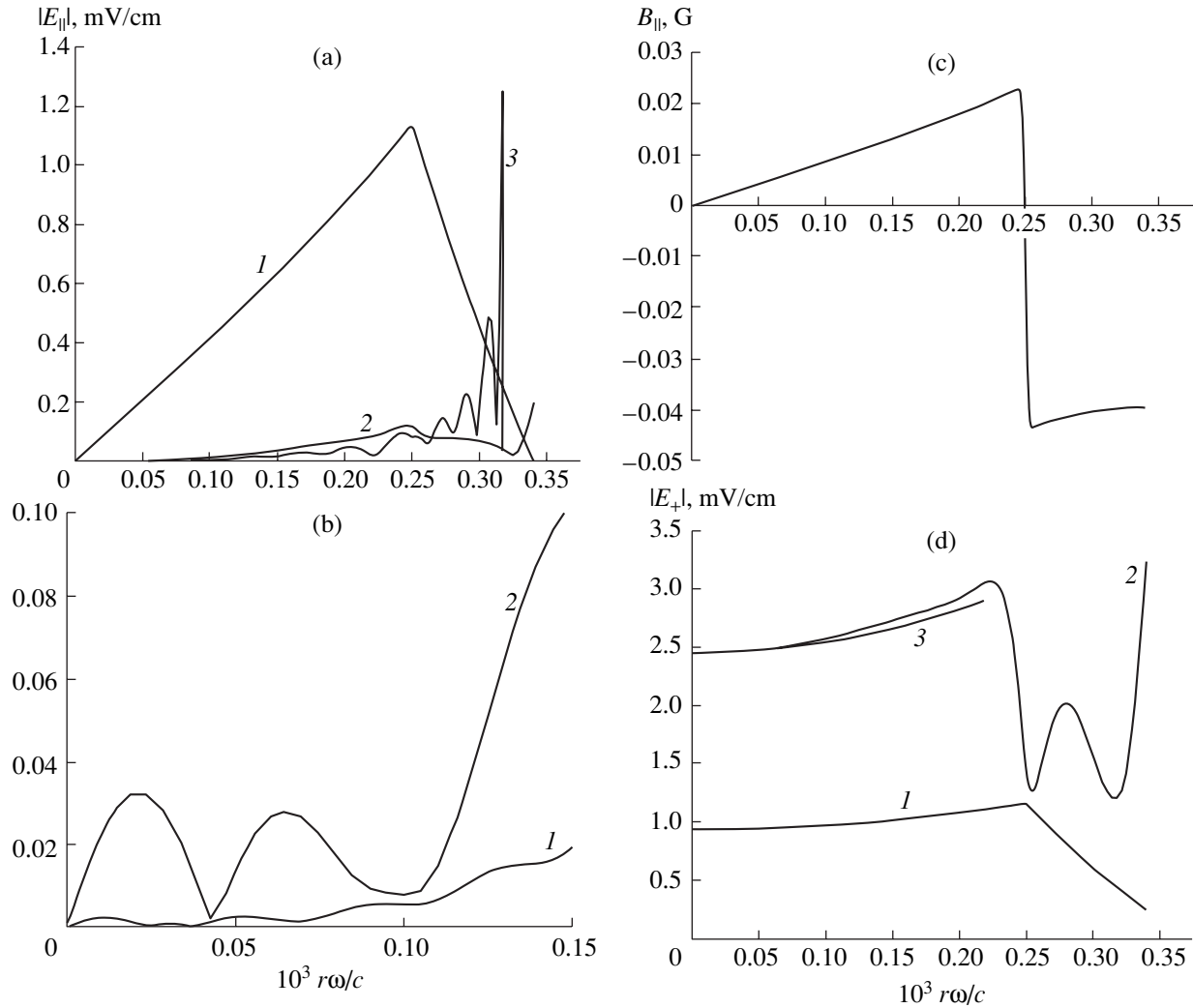
Fig. 6. Radial profiles of the rf fields: (a) longitudinal electric field in vacuum (curve *1*), in a plasma having a density of 10^{12} cm^{-3} and containing 3% of light (resonant) ions (curve *2*), and in a plasma of the same density without resonant ions (curve *3*); (b) longitudinal electric field in the central region of a plasma of density 10^{12} cm^{-3} without resonant ions for T_e = (*1*) 5 and (*2*) 50 eV; (c) longitudinal magnetic field in a plasma of density 10^{12} cm^{-3}; and (d) left-polarized electric field in vacuum (curve *1*) and in a plasma of density 10^{12} cm^{-3} (curve *2*) and TE mode field in vacuum (curve *3*). All of the profiles were calculated for $k_\parallel = 6.3 \times 10^{-2}$ cm^{-1} and for an antenna current of 1 A.

a sharp jump in the vacuum field of the TE mode at the surface on which the current-carrying conductors of the antenna are wound. Since, however, the equations used to analyze the rf fields are inapplicable to this region, Fig. 6d shows only a portion of the radial profile of the left-polarized electric field amplitude.

The transverse electric field is independent of the plasma density and, under the conditions $\varepsilon_\parallel \gg 1$ and $\varepsilon_\perp \ll N_\parallel^2$, coincides with the transverse electric field of the TE mode. In the case under examination, these conditions correspond to the density range $10^5 \le n_0 \le 10^{14}$ cm^{-3}. The plasma with a density above the upper limit has a substantial influence on the TE mode: in par-

ticular, it reduces the left-polarized component of the electric field of the mode. It should be noted that, if the concentration of resonant ions is low and if the transverse dielectric function is governed by nonresonant ions, then there is an Alfvén resonance in the plasma, provided that $\varepsilon \ge N_\parallel^2$. In the vicinity of this point, the TE and TM modes interact closely with one another to convert into a single plasma mode, thereby strengthening the rf fields. A further increase in the plasma density is accompanied by a displacement of the Alfvén resonance toward the plasma boundary and by a weakening of the left-polarized electric field in the main part of the plasma column.

The above analysis is qualitatively consistent with that used in [4] to obtain the dependence of the left-polarized electric field on the plasma density. Note, however, that the plateau in this dependence, which reflects the excitation of the vacuum TE mode, terminates at a lower plasma density ($n_0 \approx 10^{12}$ cm^{-3}) in comparison to that indicated above. This may be attributed to a different ion composition of the plasma. In [4] (see also [5, 6]), the plasma was considered to contain a mixture of ion isotopes of the same chemical element. The isotopes were assumed to have almost the same mass; consequently, under the ICR conditions for the target isotope (i.e., the isotope to be heated), the waste (main) isotope turned out to be in a nearly resonant state. As a result, the transverse dielectric function $\varepsilon_\perp$ of the plasma increased and, therefore, the Alfvén resonance conditions were easier to satisfy. In [5, 6], the excitation of electromagnetic fields in a plasma column was attributed to the Alfvén resonance, and this point of view was, in particular, promoted by using the continuous $k_\parallel$-spectrum approximation without imposing any restrictions on the longitudinal wavenumber $k_\parallel$ from below.

3.2. Axial Field Structure

In order to find out how the rf field depends on the longitudinal coordinate z, it is necessary to take the sum of Fourier series that are analogous to those in expression (3) and have Fourier coefficients that are analogous to those shown in Fig. 6. The corresponding numerical procedure is fairly laborious. With the above considerations, however, it is possible to construct a simpler procedure on the basis of the analytic expressions for $B_\parallel$ and E_+ that derive from Eq. (7) and relationship (10).

Since the antenna conductors are thin, the current distribution in the antenna can be approximated by a distribution in the form of a δ function. In this case, Eq. (7) yields

$$B_\parallel(r, k_\parallel)$$
$$= -\frac{\rho_A}{I'_m(\rho_B)} \Phi''_{m;\, \rho_A, \rho_B}(\rho_A, \rho_B) I_m(\rho) \frac{4\pi}{c} J_\theta(k_\parallel), \quad (11)$$

where J_θ is the surface current density, $\Phi_m(\rho_A, \rho_B) = I_m(\rho_A)K_m(\rho_B) - K_m(\rho_A)I_m(\rho_B)$, $\rho = (N_\parallel^2 - 1)^{1/2}r\omega/c$, I_m is a modified Bessel function, and K_m is a Bessel function.

Expression (11) implies that only long-wavelength modes such that $k_\parallel r_A \lesssim 1$ reach the central region of the plasma column. As a result, the spectrum of $B_\parallel$ in the longitudinal wavenumbers in this region becomes depleted of higher harmonics.

The left-polarized electric field E_+ can be obtained from expression (10). For the mode in question,

namely, that with $m = -1$, the field has the form

$$E_+(r, k_\parallel)$$
$$= -\frac{2\sqrt{2}\pi}{c^2} \frac{\omega r_A}{I'_1(\rho_B)} \Phi''_{1;\, \rho_A, \rho_B}(\rho_A, \rho_B) I_0(\rho) J_\theta(k_\parallel). \quad (12)$$

Expression (12) shows that the contribution of the higher harmonics to the Fourier expansion of the left-polarized electric field is even smaller than that to the Fourier expansion of the longitudinal magnetic field. The Fourier spectra of the density of the currents in a helical and a spiral antenna are strikingly different (see Fig. 4). As for the Fourier spectra of the rf fields excited by these antennas, the difference between them is less pronounced because of the suppression of the higher harmonics (see Fig. 7).

In the central region of the plasma column, which is of most interest to us, the longitudinal magnetic field depends linearly on the radius and the left-polarized electric field is constant. Consequently, the axial profiles of these fields can be characterized by the quantities $B_{\parallel, 0}(z) = B_\parallel(r, z)|_{r = r_A/2}$ and $E_{+, 0}(z) = E_+(r, z)|_{r = 0}$. Since the amplitudes of the higher Fourier harmonics of the fields $B_\parallel$ and E_+ are smaller than those of J_θ, the axial profiles of these fields are smoother. In particular, for $L_1 > L$, these fields extend outside the antenna (see Figs. 8, 9). According to Fig. 8, the higher Fourier harmonics make a contribution to the axial profile of the longitudinal magnetic field; this is why, in Fig. 7, the magnetic fields of the helical and the spiral antenna are seen to differ from one another. However, the left-polarized electric fields of these antennas are virtually indistinguishable (see Fig. 9).

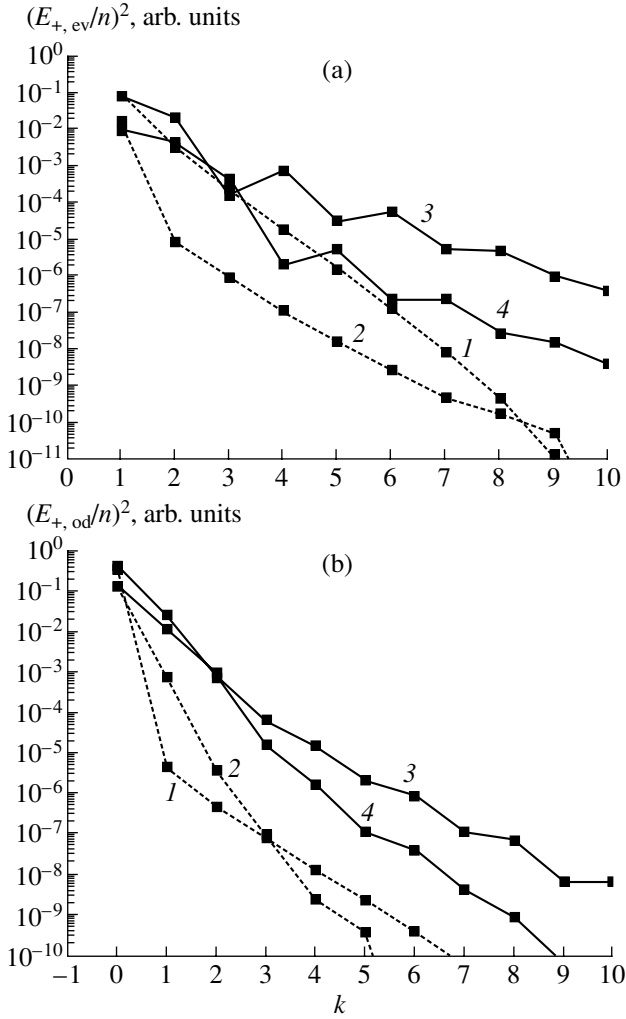## 4. POTENTIAL APPROXIMATION AND BOUNDARY CONDITIONS

The vacuum equations for the TE and TM modes provide the basis for an even simpler approximate method for calculating the rf fields. Let us assume that the plasma density is high enough for the electric charge that neutralizes the TM mode to be localized in a thin surface plasma layer. If the distance from the antenna to the plasma surface is small, then, roughly speaking, the screening layer can be assumed to coincide with the surface of the antenna cylinder.

Poisson's equation makes it possible to express the jump in the radial electric field in terms of the surface current density:

$$E_r\big|_{r_A^-}^{r_A^+} = 4\pi\sigma. \quad (13)$$

On the other hand, Eq. (7) gives

$$B_\parallel\big|_{r_A^-}^{r_A^+} = -\frac{4\pi}{c} J_\theta, \quad (14)$$

$(E_{+, \text{ev}}/n)^2$, arb. units

(a)

$(E_{+, \text{od}}/n)^2$, arb. units

(b)

k

Fig. 7. Spectra of the left-polarized electric field of a helical ($n = 1$) and a spiral ($n = 5$) half-wave antenna: (a) even and (b) odd components. The profiles in both figures refer to a helical antenna such that (*1*) $L_1 = L$ and (*3*) $L_1 = 2L$ and to a spiral antenna such that (*2*) $L_1 = L$ and (*4*) $L_1 = 2L$.

$B_{\parallel, \text{ev}}/n$, G

(a)

$10^3 \, z\omega/c$

$B_{\parallel, \text{od}}/n$, G

(b)

$10^3 \, z\omega/c$

Fig. 8. Axial profiles of the longitudinal rf magnetic field of a half-wave antenna: (a) even and (b) odd components. The profiles in both figures refer to (*1*) a helical antenna ($n = 1$), (*2*) a spiral antenna ($n = 5$), and (*3*) a spiral antenna ($n = 10$) with a continuous current density distribution for $L_1 = 2L$. The total antenna current is 100 A.
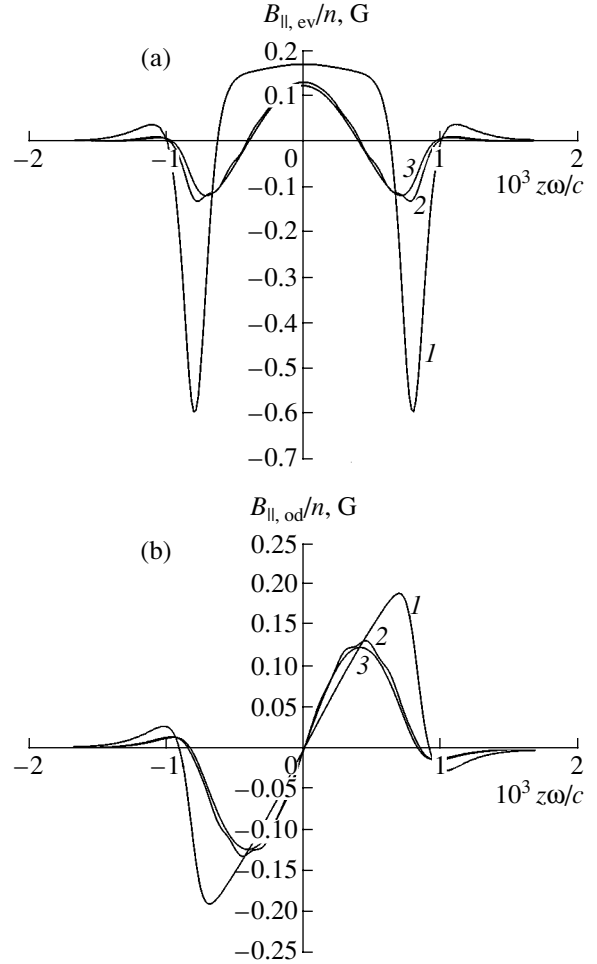
where J_θ is the surface density of the azimuthal current flowing in the antenna.

Expressions (8), (13), and (14) yield the following relationship between the screening charge density and the azimuthal current density in the antenna:

$$\sigma = \frac{1}{1 - N_\parallel^2} \frac{1}{\omega} \frac{m}{r} J_\theta.$$

The vacuum equation for the TM mode (see, e.g., [3]),

$$\frac{1}{r} \frac{d}{dr} r \frac{dE_\parallel}{dr} + \left(\left(\frac{\omega}{c} \right)^2 - k_\parallel^2 - \frac{m^2}{r^2} \right) E_\parallel$$
$$= -\frac{4\pi i}{\omega} (J_\parallel - cN_\parallel \rho), \quad (15)$$

implies that this mode is not excited when the longitudinal current and electric charge both oscillate at the antenna surface. In Eq. (15), the surface density of the longitudinal current is given by the expressions
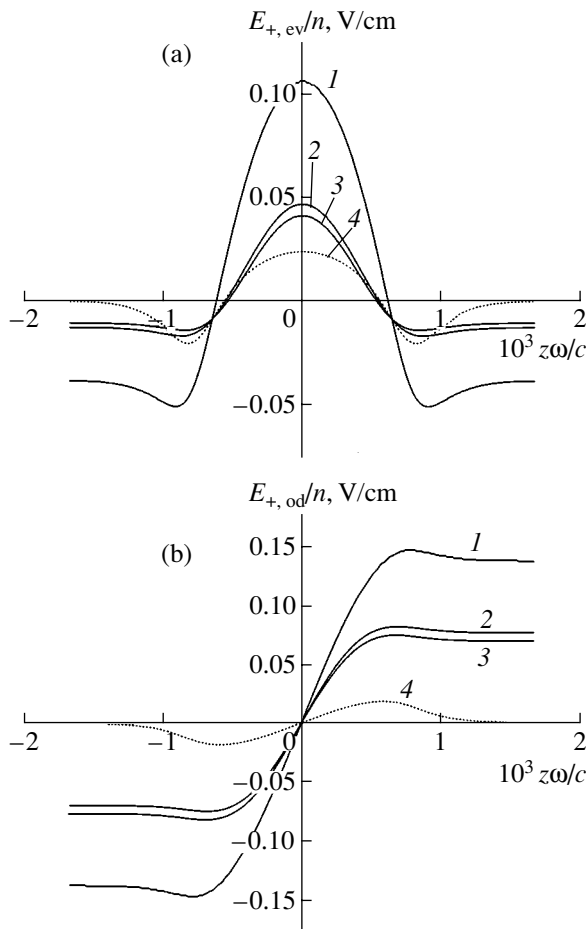
$$J_\parallel' = cN_\parallel \sigma = \frac{N_\parallel}{1 - N_\parallel^2} \frac{c}{\omega} \frac{m}{r} J_\theta. \quad (16)$$

A differential analogue of the first equality in expressions (7) is the equation

$$\frac{\partial J_\parallel'}{\partial t} = c^2 \frac{\partial \sigma}{\partial z}. \quad (17)$$

The longitudinal current density $J_\parallel'$ differs from that in the antenna, $J_\parallel = -\frac{m}{r_A k_\parallel} J_\theta$, by a small amount

$$\delta J_\parallel = \frac{1}{N_\parallel^2 - 1} J_\parallel.$$

Fig. 9. Axial profiles of the left-polarized electric field of a half-wave antenna: (a) even and (b) odd components. The profiles in both figures refer to (*1*) a helical antenna ($n = 1$), (*2*) a spiral antenna ($n = 5$), and (*3*) a spiral antenna ($n = 10$) with a continuous current density distribution for $L_1 = 2L$. Curves *4* show the field profiles in vacuum. The total antenna current is 100 A.

This additional current is carried by electrons in their motion along the magnetic field; the result is the onset of the screening charge,

$$\sigma = \frac{k_\parallel}{\omega}\delta J_\parallel.$$

The above relationships provide an approximate calculation of the electric field of the simplest (helical) antenna. In the region $|z| < L$, the distribution of the longitudinal current density in such an antenna is given by the expression

$$J_\parallel = \left[\delta\left(\theta - \frac{\pi}{2} - \alpha\frac{z}{L}\right) - \delta\left(\theta + \frac{\pi}{2} - \alpha\frac{z}{L}\right)\right] \\ \times \cos(\omega t)\frac{1}{r_A}I^{(0)}, \quad (18)$$

where $\alpha = A\pi/2$ and $I^{(0)}$ is the current in each of the two helical conductors (which are assumed to be infinitely thin).

According to Eq. (17), the distribution of the screening charge is described by a discontinuous function, which has jumps at the antenna surface. At a fixed coordinate z, the longitudinal currents flowing in the conductors on the opposite sides of the antenna cylinder have opposite signs; consequently, the screening charges also have opposite signs there. Such charges generate a transverse electric field. The left-polarized electric field at the center of the chamber is determined by the first azimuthal harmonic of the electric current. This harmonic, which runs in the direction of the ion gyration (see above), makes the following contribution to the longitudinal current density given by expression (18):

$$J_\parallel = \sin\left(\theta + \omega t - \alpha\frac{z}{L}\right)\frac{1}{\pi r_A}I^{(0)}.$$

The density of the charge that screens the TM mode can be found from Eq. (17):

$$\sigma = f(t, \theta, z)\frac{\omega}{\alpha\pi}\frac{L}{r_A c^2}I^{(0)}, \quad (19)$$

where the small difference between $J_\parallel$ and $J_\parallel'$ has been ignored.

For convenience in further calculations, the factor $f(t, \theta, z) = \sin\left(\theta + \omega t - \alpha\frac{z}{L}\right)$, which accounts for the spatiotemporal structure of the charge, can be represented as

$$f(t, \theta, z) = \sin(\theta + \omega t)f_{ev}(z) - \cos(\theta + \omega t)f_{od}(z).$$

The electric potential generated by a charge with density (19) is described by Poisson's equation,

$$\frac{1}{r}\frac{\partial}{\partial r}r\frac{\partial}{\partial r}\varphi - \frac{1}{r^2}\varphi = -4\pi\rho, \quad (20)$$

where $\rho = \delta(r - r_A)\sigma$, the azimuthal wavenumber being $m = -1$.

In Eq. (20), the longitudinal structure of the electric field is taken into account parametrically because the screening effect under discussion is important for antennas whose length in the magnetic field direction is sufficiently large, $L \gg r_A$.

Using expression (19), we find

$$E_+ = -\frac{1}{\sqrt{2}}\frac{\omega}{c}\left(\frac{\partial}{\partial r} + \frac{1}{r}\right)\varphi = -2\sqrt{2}\pi\sigma\left(1 - \left(\frac{r_A}{r_B}\right)^2\right). \quad (21)$$

By derivation, expression (21) is valid only for the region $|z| < L$.

Let us now consider the question about the boundary conditions. The boundary conditions of the first

kind, in which $E_+(z_b) = 0$, admit that $\left.\dfrac{\partial E_+}{\partial z}\right|_{z=z_b} \neq 0$. In this case, by virtue of relationships (17) and (21), there should be an electric current that flows across the plasma boundary. Consequently, the boundary conditions of the first kind imply that the ends the vacuum chamber should be conducting. By similar reasoning, the boundary conditions of the second kind, in which $\left.\dfrac{\partial E_+}{\partial z}\right|_{z=z_b} = 0$, are valid for the chamber ends insulated from the plasma.

In order to satisfy the first-kind boundary conditions (which imply conducting ends), the even component of the electric field should be expanded in a Fourier series in the functions $\cos\left(\left(k+\dfrac{1}{2}\right)\pi\dfrac{z}{L_1}\right)$ and the odd electric field component should be expanded in the functions $\sin\left(k\pi\dfrac{z}{L_1}\right)$. For the second-kind boundary conditions (which imply insulated ends), it is necessary to use the functions $\cos\left(k\pi\dfrac{z}{L_1}\right)$ and $\sin\left(\left(k+\dfrac{1}{2}\right)\pi\dfrac{z}{L_1}\right)$, respectively. The electric current should be expanded in the same functions. In fact, the derivatives of the parameters of the oscillations in question with respect to z are calculated by multiplying their Fourier transforms by $-ik_\parallel$. From expression (12), it is seen that the operator relating the azimuthal antenna current density J_θ and the left-polarized electric field E_+ contains the derivatives that are even in the z coordinate and does not contain odd derivatives.

We continue the electric field to the plasma boundary, assuming initially that the ends of the plasma column are insulated. We take into account that the space charge, whose density is independent of the z coordinate, does not generate a TM mode (see Eq. (15)). It is for this reason that Eq. (17) determines the charge density to within a constant. Adding a constant to expression (19) and, accordingly, to expression (21) does not violate the boundary conditions. The additive constants can be different for different intervals along the z coordinate; in any case, the charge density should be continuous. Taking into account this continuity condition, we arrive at the following expression for the function f_{od}, which describes the distribution of the odd part of the charge density:

$$f_{od} = \begin{cases} \sin\left(\alpha\dfrac{z}{L}\right) & (|z| < L) \\ \sin(\alpha)\,\mathrm{sgn}(z) & (|z| > L). \end{cases} \tag{22}$$

For the even part of the charge density, it is also necessary to take into account the condition that the electron charge be conserved along each magnetic field line

(for the odd part, this conservation condition is satisfied automatically):

$$f_{ev} = \begin{cases} \cos\left(\alpha\dfrac{z}{L}\right) - \cos(\alpha) + \dfrac{L}{L_1}\left(\cos(\alpha) - \dfrac{1}{\alpha}\sin(\alpha)\right) \\ \quad (|z| < L) \\ \dfrac{L}{L_1}\left(\cos(\alpha) - \dfrac{1}{\alpha}\sin(\alpha)\right) \quad (|z| > L). \end{cases} \tag{23}$$

In the case of conducting ends, the continuity conditions at $z = \pm L$ and the condition for the left-polarized electric field to vanish at $z = \pm L_1$ will be satisfied for the even part of the charge density if we set

$$f_{ev} = \begin{cases} \cos\left(\alpha\dfrac{z}{L}\right) - \cos(\alpha) & (|z| < L) \\ 0 & (|z| > L). \end{cases} \tag{24}$$

In order to satisfy the boundary conditions for the odd part of the charge density, it is necessary to assume that an alternating longitudinal current flows across the surface plasma layer (which screens the TM mode) and that this current is independent of the z coordinate. This current is not incorporated into Eq. (7) for the TE mode and enters only into its solutions through the boundary conditions. According to Eq. (17), the required longitudinal current is screened by a charge whose density changes linearly with the z coordinate. By introducing the corresponding term into the equation for the odd part of the charge density, it is possible to satisfy the boundary conditions at the ends:

$$f_{od} = \begin{cases} \sin\left(\alpha\dfrac{z}{L}\right) - \sin(\alpha)\dfrac{z}{L_1} & (|z| < L) \\ \sin(\alpha)\left(\mathrm{sgn}(z) - \dfrac{z}{L_1}\right) & (|z| > L). \end{cases} \tag{25}$$

Expressions (22)–(25) describe the longitudinal profile of the space charge density. The left-polarized electric field, which is of most interest to us, can be found from expressions (19) and (21).

The approximate expressions for the left-polarized electric field provide a quite satisfactory description of the field of the TE mode in the cases of conducting and insulated ends. To see this, Fig. 10 presents the fields of a helical half-wave antenna ($A = 1$). The odd component of these fields extends outside the antenna to the region $|z| > L$. In the case of a one-wave antenna ($A = 2$), the fields in this region are far weaker. In fact, in such an antenna, each generatrix of the antenna cylinder is intersected by both helical conductors. The conductors carry equal currents whose densities $J_\parallel(z)$ have

E_+, V/cm

(a)

(b) E_+, V/cm
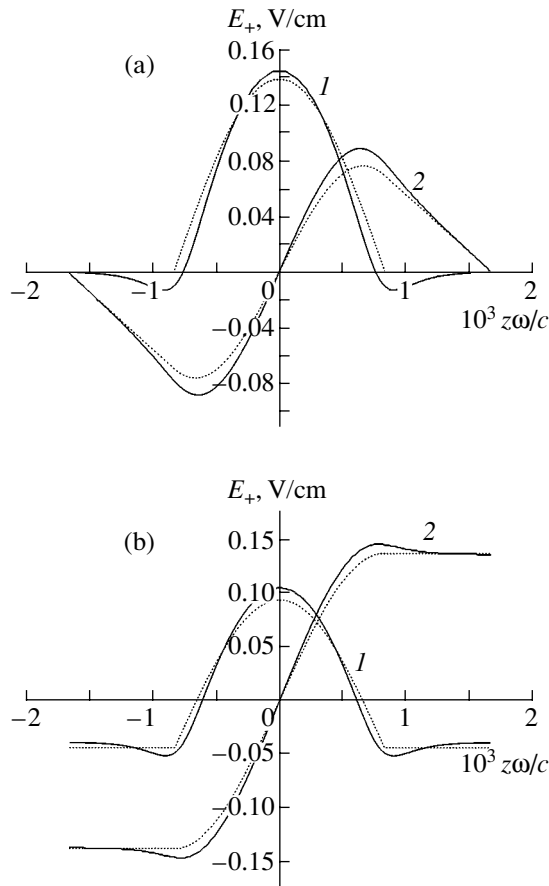
Fig. 10. Axial profiles of the left-polarized electric field of a helical half-wave antenna with (a) conducting and (b) insulated ends for $L_1 = 2L$. Curves *1* and *2* refer to the even and odd field components, respectively; the solid curves are for the total left-polarized electric field; and the dashed curves are for the potential component of this field. The total antenna current is 100 A.

E_+, V/cm
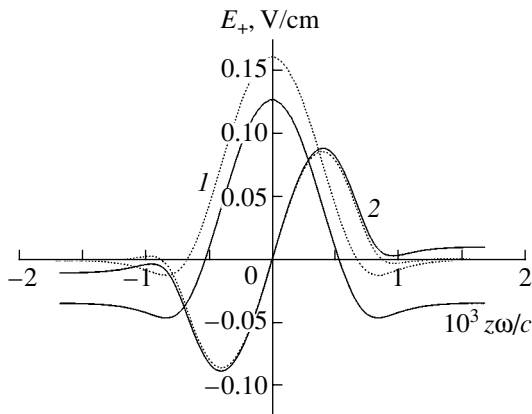
Fig. 11. Axial profiles of the left-polarized electric field of a helical one-wave antenna ($A = 2$) for $L_1 = 2L$: (*1*) even and (*2*) odd field components. The solid curves refer to an antenna with insulated ends, and the dotted curves refer to an antenna with conducting ends. The total antenna current is 100 A.

opposite signs; consequently, the jumps in the screening charge density near the conductors also have opposite signs (see Eq. (17)). This is confirmed by the results of numerical calculations shown in Fig. 11.

Note that, according to [7, 8], the electric field also is "confined" to the antenna surface, provided that the plasma density is high enough to satisfy the condition $N_\parallel^2 \geq \varepsilon_\perp$.

To conclude this section, we estimate the rf field amplitudes. For this purpose, we describe the rf fields by their lowest axial harmonics, which remain essentially undamped when they penetrate into the central region of the plasma column. In doing so, in expressions (11) and (12), we can set ρ_A, $\rho_B \leq 1$. Consequently, in order of magnitude, we have

$$B_{\parallel, 0} \approx \frac{4\pi I^{(0)}}{c \, L},$$

$$E_{+, 0} \approx \frac{1}{N_\parallel^2} \frac{c}{\omega r_A} B_{\parallel, 0} \approx \frac{4}{\pi} \frac{L_1^2}{L r_A} \frac{\omega I^{(0)}}{c^2},$$

where $I^{(0)}$ is the total antenna current. We set this current equal to $I^{(0)} = 100$ A. For a system with the parameter values mentioned in the Introduction, we obtain the estimates $B_{\parallel, 0} \approx 1$ G and $E_{+, 0} \approx 1$ V/cm. The estimates obtained in numerical calculations are about one order of magnitude smaller (see Figs. 8–11).

5. ICR INTERACTION

When the rf field frequency is close to the ion gyrofrequency, the equation of motion of an ion interacting with the left-polarized electric component of this field can be written approximately as

$$\dot{v}_+ + i\omega_i v_+ = \frac{e}{m_i} E_+(z(t), t), \tag{26}$$

where $v_+ = (v_x + i v_y)/\sqrt{2}$.

The transverse electric field of the TE mode is essentially uniform in the central region of the chamber, which is occupied by the bulk plasma. This is why, in Eq. (26) and in the subsequent formulas, the radial dependence of the field component E_+ is ignored.

Using Eq. (26), we find that, for the ions that have passed through the ICR heating system, the quantity $v_+(t)$ is described by the expression

$$v_+(t) = \left(\frac{v_{\perp 0}}{\sqrt{2}} e^{i\varphi_0} \right.$$

$$\left. + \frac{e}{m_i} \int_{-L_1/v_\parallel}^{L_1/v_\parallel} dt' E_+(z(t'), t') e^{i\omega_i t'} \right) e^{-i\omega_i t}, \tag{27}$$

where $v_{\perp 0}$ and φ_0 are the initial velocity and initial phase of the ion gyration. As in Sections 3 and 4, the electric field in expression (27) is represented in a complex form,

$$E_+(z, t) = \frac{2\sqrt{2}}{\pi} \frac{r_A \omega}{c^2} J_{0\theta}$$

$$\times \sum_{k = -\infty}^{\infty} \left\{ R_k \Psi_{k+1/2} \sin\left(\left(k + \frac{1}{2}\right)\pi \frac{z}{L_1}\right) \right. \tag{28}$$

$$\left. - i S_k \Psi_k \cos\left(k\pi \frac{z}{L_1}\right) \right\} e^{-i\omega t},$$

where $z = z_0 + v_\parallel t$, $\Psi_p = \Phi''_{1; \rho_{A,p}, \rho_{B,p}}(\rho_{A,p}, \rho_{B,p})/I'_1(\rho_{B,p})$, $\rho_{A,p} = (N^2_{\parallel,p} - 1)^{1/2} r_A \omega/c$, $\rho_{B,p} = (N^2_{\parallel,p} - 1)^{1/2} r_B \omega/c$, and $k_{\parallel,p} = \pi p/L_1$.

Expression (27) implies that, in the interaction of the ions with the rf field, the increment Δv_+ is independent of $v_{\perp 0}$ and φ_0. In this case, by the symmetry properties of the antenna, the function $E_+(z, t)$ is such that, in a frame of reference rotating with the left-polarized electric field, the plane $v_x 0 v_y$ is displaced uniformly as a single entity due to the ICR interaction. In this plane, it is convenient to direct the $0 v_x$ axis along the displacement. In this case, we obtain

$$\Delta v_x = -\frac{8}{\pi} \frac{e\omega r_A L_1}{m_i c^2 v_\parallel} J_{0\theta}$$

$$\times \left\{ \cos(\Omega') \sum_{k = -\infty}^{\infty} (-1)^k R_k \Psi_{k+1/2} \alpha_k(\Omega') \right. \tag{29}$$

$$\left. + \sin(\Omega') \sum_{k = -\infty}^{\infty} (-1)^k S_k \Psi_k \beta_k(\Omega') \right\},$$

where $\Omega = \omega_i - \omega$, $\Omega' = \dfrac{\Omega L_1}{v_\parallel}$, $\alpha_k(\Omega') = \dfrac{\Omega'}{\Omega'^2 - ((k + 1/2)\pi)^2}$, and $\beta_k(\Omega') = \dfrac{\Omega'}{\Omega'^2 - (k\pi)^2}$.

If the system were infinite in the direction of the main magnetic field, then the longitudinal velocity of the ions that take part in the ICR interaction process would satisfy the condition

$$\omega = \omega_i + k_\parallel v_\parallel. \tag{30}$$

Since the length of the actual systems is finite, the ICR lines are broadened if the longitudinal wavenumber $k_\parallel$ is understood to take the values $k_\parallel = k\pi/L_1$, $(k + 1/2)\pi/L_1$ (see above).

In the model under consideration, an ion flies through the heating system over the time $\tau = 2L_1/v_\parallel$. As

a result, the resonance line acquires a finite width, $\delta\omega = 2\pi/\tau$ (the time-of-flight broadening). Of course, in a finite time, an ion acquires a finite velocity increment. The intensity of the ICR interaction is characterized by the factors $\gamma_1 = \cos(\Omega')\alpha_k(\Omega')$ and $\gamma_2 = \sin(\Omega')\beta_k(\Omega')$. In the "resonant" case ($\Omega\tau \leq 1$), these factors are equal in order of magnitude to $\gamma_{1,2} \approx \tau$. If the rf field frequency is far from being resonant ($\Omega\tau \geq 1$), then, as Ω increases, the factors $\gamma_{1,2}$ oscillate in such a way that their amplitude decreases according to a power (Lorentzian) law, $\gamma_{1,2} \approx \dfrac{1}{\Omega^2\tau}$.

The time-of-flight broadening, i.e., the broadening of the ICR line by $\delta\omega = 2\pi/\tau$, is, in principle, unavoidable. As for the Lorentzian law of decrease of the factors $\gamma_{1,2}$ at $\Omega\tau \geq 1$, the model under consideration attributes it to the sharp boundary of the ICR heating system: behind this boundary, the left-polarized electric field vanishes, whereas, at the boundary, the z-derivative of this field undergoes a jump. It is well-known that the Fourier spectra of nonanalytic functions have pronounced (power-law) tails at large wavenumbers. Consequently, for any value of the quantity Ω and of the longitudinal ion velocity, there always exists a component in the Fourier expansion of the function $E_+(z)$ that satisfies resonance condition (30). It is the amplitude of this harmonic that determines the ICR interaction intensity. Since, in the case at hand, the derivative dE_+/dz has a jump at the plasma boundary, we arrive at the law $E_+(k_\parallel) \underset{k_\parallel \to \infty}{\propto} k_\parallel^{-2}$, which corresponds to the Lorentzian law of decrease of the factors $\gamma_{1,2}$ in the limit $|\Omega| \longrightarrow \infty$.

By applying a nonuniform magnetic field, the ICR interaction region can be localized to a zone where $E_+(z) \neq 0$. In this case, the wings of the ICR line are determined by the characteristic magnetic field gradient at the boundary of the ICR heating region. For instance, when the magnetic field at the boundaries of the system decreases on a characteristic spatial scale L_B ($L_B < L_1$), the ICR line has broadened only by an amount of $\delta\omega \approx v_\parallel/L_B$.

The cyclotron resonance at $k_\parallel = 0$ (i.e., the fundamental resonance) has its specific features. Under the condition

$$\omega = \omega_i, \tag{31}$$

all of the ions, independently of their longitudinal velocities, take part in the resonant interaction, which itself is not associated with the time-of-flight broadening effect. Because of the uniform motion of the ions along the magnetic field, the ICR interaction intensity is determined by the averaged strength of the left-polarized electric field, $\Delta v_x \propto \langle E_+(z)\rangle_z \propto E_+(k_\parallel)|_{k_\parallel = 0}$ (see expression (29)). For insulated ends, we have $\langle E_+(z)\rangle_z = 0$ (see Sections 3, 4). This conclusion corre-

lates with the conservation condition for the screening electron charge. In such systems, the ions for which condition (31) is not satisfied slip out of the ICR interaction process.

In the case of conducting ends, the charge from them can enter the system, so we have $\langle E_+(z)\rangle_z \neq 0$. That the ions in such systems can be heated under condition (31) follows from the expression for the increment in the velocity of ion gyration,

$$\Delta v_x = -\frac{8}{\pi}\frac{e\omega r_A L_1}{m_i c^2 v_\parallel} J_{0\theta}$$

$$\times\left\{\sin(\Omega')\sum_{k=-\infty}^{\infty}(-1)^k R_k \Psi_{k+1/2}\alpha_k'(\Omega')\right. \tag{32}$$

$$\left. + \cos(\Omega')\sum_{k=-\infty}^{\infty}(-1)^k S_k \Psi_k \beta_k'(\Omega')\right\},$$

where the quantities $\alpha_k'(\Omega') = \dfrac{(k+1/2)\pi}{\Omega'^2 - ((k+1/2)\pi)^2}$ and

$\beta_k'(\Omega') = \dfrac{k\pi}{\Omega'^2 - (k\pi)^2}$ do not vanish at $\Omega' = 0$, in contrast to the quantities α_k and β_k.

The characteristic increment in the ion gyration velocity can be determined based on the approximate estimate for the left-polarized electric field that was derived at the end of previous section. Using expression (29), we find

$$\frac{|\Delta v_x|}{v_{Ti}} \approx \frac{L_1}{v_{Ti}^2}\frac{e}{m_i}E_{+,0} \approx \frac{L_1^3}{L\rho_i}\frac{I^{(0)}}{cr_A B_0},$$

where ρ_i is the mean ion gyroradius. This estimate shows that the antenna current $I^{(0)} = 10$ A is sufficient to provide efficient ion heating, $\left(\dfrac{|\Delta v_x|}{v_{Ti}} \approx 10\right)$. The current obtained in numerical calculations is several times higher (see below).

6. ENERGY DISTRIBUTION OF THE ION FLOW

The ion flow that is injected into the ICR heating system is produced in a gas-discharge source. The velocity of such flows at the exit from the source is equal in order of magnitude to the ion acoustic velocity. The normalized (to unity) distribution of the ions in the flow over longitudinal velocities has the form

$$F_0(u_\parallel) = 2A_0^{-1}u_\parallel\exp(-(u_\parallel - U_0)^2), \tag{33}$$

where $A_0 = e^{-U_0^2} + \sqrt{\pi}U_0(1 + \mathrm{erf}(U_0))$ (with $\mathrm{erf}(U_0) = \dfrac{2}{\sqrt{\pi}}\int_0^{U_0}du\,e^{-u^2}$) is the normalizing factor, $u_\parallel = v_\parallel/v_{Ti} > 0$ and $U_0 = V_0/v_{Ti}$. If $V_0 = \sqrt{T_e/m_i}$, then, for $T_e = 10T_i$, we have $U_0 = 2.24$.

The resonant (heated) ions and the nonresonant ions (which remain cold) can be separated out by various methods. The separation method described in [1] is based on the fact that the gyroradii of the heated and cold ions are different. Since the increment in the transverse ion energy is considerably higher than their initial transverse energy, the ion distribution over this energy component is close to that over the total energy. An analysis shows that, in the case of ion separation in a curvilinear magnetic field [9, 10], the distribution over the degrees of freedom (i.e., over transverse and longitudinal energies) plays a minor role. With these circumstances in mind, we will analyze the ion distribution over the total energy.

Using expressions (29) and (33), we can find out how the ions that have passed through the ICR heating system are distributed over the absolute value of the total velocity. Assuming that the ion flow at the entrance to the heating system obeys velocity distribution (33), we obtain

$$F(u) = \frac{4}{\pi A_0}u\int d\mathbf{u}\,u_\parallel\exp(-(u_x - \Delta u_x(u_\parallel))^2 - u_y^2$$
$$- (u_\parallel - U_0)^2)\delta(u^2 - u_x^2 - u_y^2 - u_\parallel^2). \tag{34}$$

Integrating over the azimuthal angle in velocity space and over the transverse velocity, we reduce expression (34) to

$$F(u) = \frac{4}{A_0}u\exp(-u^2 - U_0^2)\int_0^u du_\parallel u_\parallel \tag{35}$$

$$\times \exp(-(\Delta u_x(u_\parallel))^2 + 2u_\parallel U_0)I_0(2\sqrt{u^2 - u_\parallel^2}\Delta u_x(u_\parallel)).$$

For systems with parameters close to those mentioned in the Introduction, the most important of the full set of axial harmonics are the largest scale ones, whose wavenumbers k are on the order of unity, or, more precisely, on the order of L_1/L (see Sections 3, 4). These largest scale harmonics interact efficiently with an ion flow when the rf field frequency satisfies the relationship $\Omega \approx \pi V_0/L$. The ions whose velocity is substantially higher than V_0 are accelerated because of the time-of-flight broadening of the ICR line: as the longitudinal ion velocity $v_\parallel$ increases, the factors $\gamma_{1,2}$, which describe the ICR interaction efficiency, decrease comparatively gradually, according to a power law ($\gamma_1 \propto v_\parallel^{-2}$, $\gamma_2 \propto v_\parallel^{-1}$). Note that, in distribution (33), the fraction of ions with longitudinal velocities $v_\parallel \gg V_0$ is

exponentially small. As for the slow ions ($v_\parallel \ll V_0$), the model under consideration implies that they are accelerated in the same manner as resonant ions with $v_\parallel \approx V_0$ because of the broadening of the ICR line due to a jumplike decrease in the rf field at the ends of the system. In systems with a nonuniform magnetic field, this acceleration mechanism is less pronounced (see above), and so the ion energy distribution at the exit from the ICR heating system can be enriched with ions of low longitudinal velocities $v_\parallel$ in the low-energy range.

The ions that move slowly along the magnetic field stay in the ICR heating system for the longest time. It is these ions that form the high-energy tail of the ion distribution at the exit from the system. The fraction of slow ions in the distribution over longitudinal velocities is largest when the mean velocity of the directed ion motion is zero, $V_0 = 0$. In this case, the tail in the ion distribution is most pronounced (see Fig. 12a). The higher the directed ion velocity V_0, the smaller the relative spread of the ions in their longitudinal velocities and, accordingly, the narrower the energy distribution function of the ions at the exit from the ICR heating system. Since the heating time also decreases with increasing V_0, the rf field amplitude has to be increased in order to provide efficient separation of the resonant and nonresonant ions.

In the PS-1 device, the electron temperature is expected to be about ten times higher than the initial ion temperature; this corresponds to $U_0 = 2.24$. It is for this value of U_0 that the distribution functions presented in Figs. 12b and 12c were calculated. Figure 12b shows that, in the ICR interaction process, the ion acceleration is governed by the fundamental harmonic of the rf field: the ions interact resonantly with this harmonic under the condition $\Delta\omega_i \approx -\pi V_0/L$ ($L_1 = 2L$). Because of the presence of other harmonics in the spectrum of the rf field and because of the time-of-flight broadening effect, the corresponding resonant line is broadened. As $|\Delta\omega_i|$ decreases, the ions that move slowly along the magnetic field are heated more efficiently, and so the distribution function acquires a tail. Simultaneously, the efficiency with which fast ions are heated decreases, with the result that the maximum of the distribution function is displaced toward lower energies. An increase in $|\Delta\omega_i|$, in fact, causes the slow ions to drop out of the ICR interaction process. In this case, the distribution function in the low-energy range becomes close to its initial shape but acquires a low hump.

The heating asymmetry with respect to the sign of $\Delta\omega_i$ is associated with the direction along which the antenna conductors are wound on a cylindrical surface: this direction corresponds to a right-hand screw (see Figs. 1, 2). Consequently, the current density component that runs in the azimuthal direction in the sense of the ion gyration (i.e., to the left for $B_0 > 0$) is dominated by the waves propagating in the positive direction of the
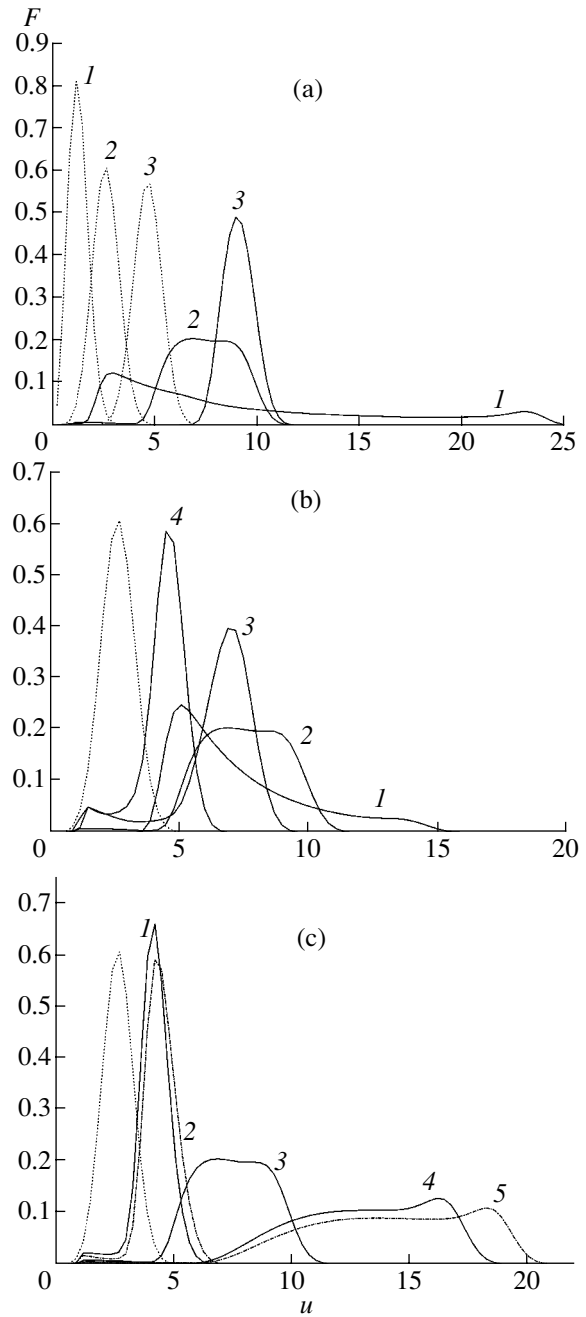
Fig. 12. Distribution functions $F(u)$ of the ion flow over the total velocity at the exit from the ICR heating system. (a) Dependence on the flow velocity along the magnetic field for (*1*) $U_0 = 0$, $I^{(0)} = 50$ A, and $\Omega'_T = \Omega L_1/v_{Ti} = -1.2$; (*2*) $U_0 = 2.24$, $I^{(0)} = 100$ A, and $\Omega'_T = -6$; and (*3*) $U_0 = 4.48$, $I^{(0)} = 200$ A, and $\Omega'_T = -12.5$. (b) Frequency dependence for $U_0 = 2.24$, $I^{(0)} = 100$ A, and $\Omega'_T = (1)$ –4, (*2*) –6, (*3*) –8, and (*4*) 6. (c) Dependence on the scale length and amplitude of an rf field for (*1*) $L_1 = 2L$ and $I^{(0)} = 50$ A, (2) $L_1 = L$ and $I^{(0)} = 100$ A, (*3*) $L_1 = 2L$ and $I^{(0)} = 100$ A, (*4*) $L_1 = 4L$ and $I^{(0)} = 100$ A, and (*5*) $L_1 = 2L$ and $I^{(0)} = 200$ A. In plots (a) and (b), the distributions were calculated for a helical half-wave antenna such that $L_1 = 2L$. The dotted curves are for the initial distribution function.

z axis. In accordance with condition (30), such waves will interact resonantly with the ion plasma component, provided that their frequency is higher than ω_i. In formula (29), which was used in numerical calculations, the asymmetry with respect to the sign of Ω stems from the summation of the first term (which is even in Ω) and the second (odd) term.

Although the increment in the ion gyration velocity depends in a fairly complicated manner on the length of the ICR heating system (see expression (29)), the main effect of variation of L_1 is associated with the time the ions stay in the system. Figure 12c shows that the effect of variations in the system length can be compensated for by variations in the rf field amplitude in such a way that the product E_+L_1 remains approximately constant.

In this section, we have calculated ion distribution function (35) under ICR heating conditions in systems with insulated ends. The main distinguishing feature of systems with conducting ends is the possibility of ICR heating under fundamental cyclotron resonance condition (31). If, in this case, we set $V_0 = 0$, then we arrive at the following simple analytic expression for the ion distribution function:

$$F(u) \approx \frac{2(\Delta u_0)^2 u^5}{\left((\Delta u_0)^2 + u^4\right)^2} \exp\left(-\left(\frac{\Delta u_0}{u}\right)^2\right),$$

where the values of Δu_0 are determined by the relationship $\Delta u_x = \Delta u_0/u_\parallel$. This expression agrees well with the results of numerical calculations by formulas (32) and (35) in the range $\Delta u_0 \geq 1$.

7. CONCLUSIONS

An analysis of the ICR heating process in ion separation systems requires consideration of a number of issues, each of which is the subject of a separate section of the present paper. A central problem in this analysis is the calculation of electromagnetic fields excited by an rf antenna in a plasma column. This was done by representing the rf field as a superposition of the independent solutions to Maxwell's equations that describe the modes known as TM and TE modes in vacuum. In a plasma, the TE mode transforms into the so-called fast waves (Alfvén and magnetosonic modes) and the TM mode transforms into the so-called slow waves (lower-hybrid and electron modes). Under the conditions adopted in the present study, the TM mode does not penetrate deeply into the plasma, while the TE mode is only slightly affected by the plasma and can thus be treated in the "vacuum" approximation. These characteristic properties of the problem under consideration provide a comparatively simple description of the spatial structure of an rf electromagnetic field and make it possible to calculate the energy distribution of an ion flow at the exit from the ICR heating system. Calculations show that the selective ICR heating of a small additive of ions with a mass very different from that of the bulk ions may be possible in systems with fairly moderate parameters.

REFERENCES

1. A. I. Karchevskiĭ and Yu. A. Muromkin, in *Isotopes*, Ed. by V. Yu. Baranov (IzdAT, Moscow, 2004) [in Russian].

2. A. V. Timofeev, Fiz. Plazmy **25**, 232 (1999) [Plasma Phys. Rep. **25**, 207 (1999)].

3. A. V. Timofeev, Fiz. Plazmy **30**, 795 (2004) [Plasma Phys. Rep. **30**, 740 (2004)].

4. A. Compant La Fontaine and V. G. Pashkovsky, Phys. Plasmas **2**, 4641 (1995).

5. A. L. Ustinov, Fiz. Plazmy **22**, 170 (1996) [Plasma Phys. Rep. **22**, 156 (1996)].

6. A. Compant La Fontaine, P. Louvet, P. Le Gourrierec, and A. Pailloux, J. Phys. D **31**, 847 (1998).

7. I. A. Kotel'nikov and S. G. Kuz'min, Fiz. Plazmy **25**, 1095 (1999) [Plasma Phys. Rep. **25**, 1010 (1999)].

8. S. G. Kuz'min, Fiz. Plazmy **25**, 1105 (1999) [Plasma Phys. Rep. **25**, 1020 (1999)].

9. M. I. Belavin, A. V. Zvonkov, and A. V. Timofeev, RF Patent No. 742900 (July 5, 1993).

10. V. I. Volosov, I. A. Kotel'nikov, I. I. Churkin, *et al.*, At. Énerg. **88**, 370 (2000).

Translated by O.E. Khadin

Plasma Opening Switch for the MOL Generator

A. A. Altukhov, G. I. Dolgachev, D. D. Maslennikov, A. S. Fedotkin, and I. A. Khodeev

Russian Research Centre Kurchatov Institute, pl. Kurchatova 1, Moscow, 123182 Russia
Received September 15, 2004; in final form, May 11, 2005

Abstract—Problems related to creating a superpower pulsed current generator (Baikal project, $\approx$10 MV, $\approx$50 MA, $\approx$150 ns) for inertial confinement fusion are considered. In order to test the circuit design of the generator, the MOL unit (3.7 MA, 5 MV, 150 ns), in which a plasma opening switch (POS) is proposed for use as an output power sharpener, is now under construction. Results are presented from experimental testing of a number of proposals enabling the POS operation under the MOL conditions: (i) plasma guns were employed to connect the POS to the inductive storage circuit, (ii) a separating discharger was used to avoid a POS reclosure and to switch the current to a load whose impedance was initially low and increased with time, and (iii) a programmable filling of the POS gap with plasma was implemented in order for the POS to pass a long current prepulse with parameters close to those in actual systems. © 2005 Pleiades Publishing, Inc.

1. INTRODUCTION

The Baikal project is aimed at creating a superpower pulsed current generator ($\approx$10 MV, $\approx$50 MA, $\approx$150 ns) for inertial confinement fusion [1]. A distinctive feature of the project is that, instead of rather expensive capacitors, a shock-excited generator with several cascades for power sharpening will be used as a primary energy storage. A plasma opening-switch (POS) is proposed for use as the final sharpening cascade. The MOL unit, which models the main elements of the future generator, is now under construction [2]. Figure 1 shows a schematic diagram of the connection of the sharpening POS$_1$ to the MOL circuit.[1] After several sharpening cascades, the energy of the shock-excited generator in the form of a high-current pulse is fed to a magnetic compressor, whose primary circuit is a rectangular loop, one side of which is movable and is made of a metal foil. When the pulse current I_{in} flows through the primary loop, its inductance L_3 increases due to the foil acceleration by the magnetic field.

In the initial stage of the foil acceleration, the magnetic flux through the secondary loop of the magnetic compressor is produced with the help of auxiliary capacitor C_2. The foil is the common conductor of both the primary and secondary loops of the magnetic compressor. As the foil is being accelerated, the secondary loop shrinks and its inductance L_4 decreases. After POS$_1$ (which is switched to the magnetic compressor circuit through switch S_7) becomes conducting, the foil is efficiently decelerated by the compressed magnetic field. Step-up transformer T_1 serves to match the parameters of the magnetic compressor and POS$_1$. The load (liner) is imitated by POS$_2$, whose impedance (like that of the liner) is initially low and increases with time. Since a real liner is a very complicated system with

properties that are not known in advance, the substitution of such imitator for the liner simplifies the problem of studying and adjusting the main switch (POS$_1$). To increase the efficiency of energy transfer to a low-impedance load, it was proposed to use separating discharger POS$_2$ between POS$_1$ and the load [3]. The calculated shape of the POS current pulse formed by the magnetic compressor is shown in Fig. 2. The POS$_1$ conduction phase is thought to terminate after the current reaches its maximum. The calculated current pulse can be conventionally divided into two phases: a prepulse ($\sim$38 μs), during which a major fraction of the charge ($\sim$80%) is passed, and the main pulse, which lasts over $\sim$2 μs and carries most of the energy ($\sim$70%). The total duration of the current pulse is about 40 μs. In order to pass such a long current pulse, it was proposed that the filling of the POS gap be programmable, i.e., that an additional plasma be injected as the POS plasma is being eroded [4].

As was shown in [5], a POS can efficiently interrupt the current only if an external axial magnetic field is applied and the linear (along the circumference of the POS outer electrode) density q_{lin} of the charge passed
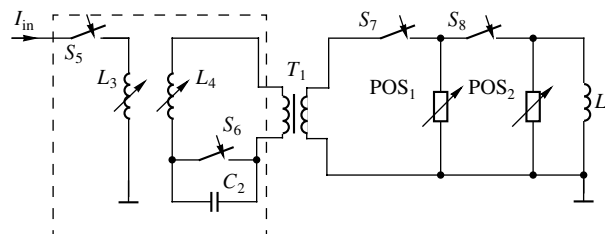

Fig. 1. Circuit diagram of connecting the POS to the power supply of the MOL unit.

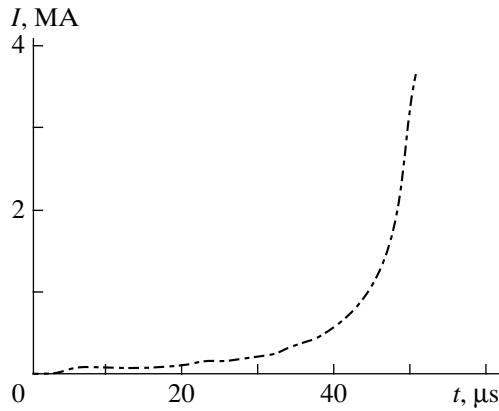[1] A detailed description of the MOL is given in [2].

Fig. 2. Calculated waveform of the POS current.

through the POS is lower than 5 mC/cm. To reduce the density of the current passed through a POS, a multi-module POS scheme (Fig. 3) was proposed in [3].

In order to justify the proposed scheme of a POS, the following problems were considered:

(i) designing a POS module,

(ii) connecting the POS to the inductive storage circuit with the help of plasma guns,

(iii) preventing the POS from reclosure when the load impedance is low,

(iv) transferring the stored energy to a load whose impedance is initially low and increases with time and evaluating the efficiency of energy transfer,

(v) determining the current distribution along the POS and the minimum possible POS length, and

(vi) implementing a programmable filling of the POS gap with plasma in order for the POS to pass a long prepulse with parameters close to those in actual systems.

2. POS MODULE AND SCHEME OF THE EXPERIMENT

The POS module (Fig. 4a) is designed as a prototype module of the MOL generator and is intended for full-scale tests at a current of ≈600 kA and passed charge of ≈5 C on the 1/6-MOL stand, which was specially created on the basis of the RS-20 machine. The module design allows such modules to be compactly packed without disturbing the external magnetic field produced by the solenoid of the module. The solenoid is wound on the inner high-voltage POS electrode (anode). Such a design allows one, first, to more efficiently use the volume occupied by each module and, second, to concentrate a major part of the magnetic energy in the POS gap due to the skinning of the solenoid magnetic field by a copper cathode (see Fig. 4b). Near the end faces of the copper cathode, magnetic field lines diverge from the anode, thus preventing the leakage of the electron current along the field lines from the cathode to the

anode. Under the MOL operating conditions, the surfaces of the POS electrodes will be bombarded by intense fluxes of charged particles accelerated in the electrode gap. Therefore, it was proposed that the metallic surfaces of the electrodes be protected by a ≈7-mm-thick, partially (≈20%) pyrolyzed multilayer carbonic material.[2] The material is highly resistive to the action of high-power pulsed fluxes [6]; possesses the high mechanical strength; and has the optimal conductivity, which allows one, on the one hand, to operate with high current densities (≈10 kA/cm^2) and, on the other hand, to avoid the skinning of the external magnetic field. The high energy density (≈10 J/cm^2) needed to evaporate and ionize the material reduces the probability of an uncontrolled plasma generation when a long current prepulse is passed through the electrodes. In this study, we used a copper cathode coated with carbon. The thickness of the stainless-steel anode was chosen such that the magnetic field of the solenoid could penetrate through it. Flashboard plasma guns had ten gaps, in which plasma was sequentially produced, and an accumulating volume [7], from which the plasma entered the POS gap through holes in the cathode (Fig. 5). These guns are rather compact, and the dielectric (acrylic plastic) forming the plasma is protected from fluxes of charged particles accelerated in the POS. Moreover, the guns allow one to produce a slightly pulsed plasma flux for the programmable filling of the gap with plasma when passing a prepulse [7].

The electric circuit of the stand comprises prepulse battery C_1 and main-pulse battery C_2 (see Fig. 6), as well as a magnetic-field battery and a four-section battery supplying the plasma guns. The magnetic-field battery was controlled by two ignitrons: one switched the battery on, and another shunted the solenoid after the first half-period of the current. The half-period of the quasi-steady magnetic field ($B = 3$–6 kG) was $T/2 = 100$ μs. Each section of the plasma-gun battery had an individual trigger. The load was separated from the POS by a discharger, which was a set of stainless-steel plates insulated by a 1-mm vacuum gap [8]. The duration of the voltage pulse applied to the gap between plane stainless-steel electrodes was determined by the formation time of the explosive-emission plasma. The gap operated as a discharger if the electric field on the surface of a plane cathode exceeded the threshold for explosive electron emission, i.e., if $E > 100$ kV/cm. For a linearly increasing gap voltage, the voltage pulse duration is equal to $\tau_{pulse} = 20/(E - 100)$ μs, where E (in kV/cm) is the strength of the uniform electric field in the gap. The duration of the discharger short-circuiting was about 10 ns and did not depend on the number of gaps. In our experiments, the number of the discharger gaps was varied from 2 to 4, so the breakdown voltage was ≈30–60 kV.

---

[2] The material is fabricated at TsNIIMMASh (OAO Avionika, Khot'kovo, Moscow oblast, Russia).
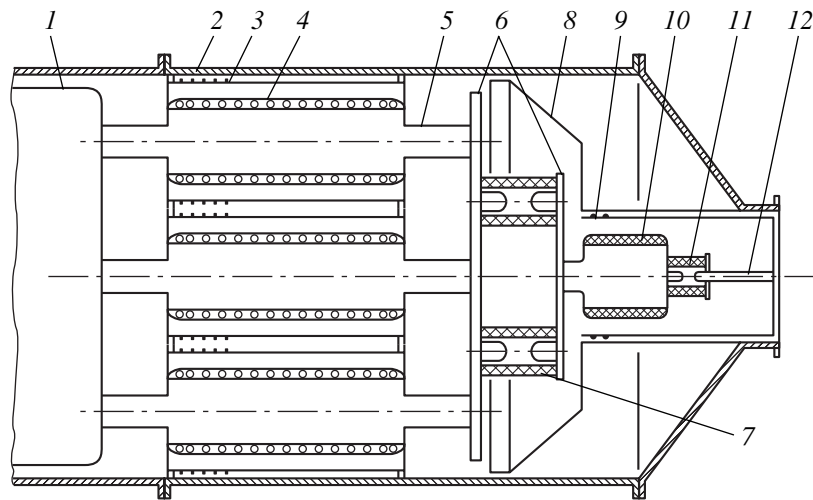
Fig. 3. Schematic of the multimodule POS$_1$ of the MOL unit: (*1*) transformer output, (*2*) vacuum chamber, (*3*) POS$_1$ cathode with plasma guns, (*4*) POS$_1$ anode with a solenoid, (*5*) anode electrodes, (*6*) connecting plate, (*7*) separating discharger, (*8*) return-current conductor, (*9*) POS$_2$ cathode, (*10*) POS$_2$ anode, (*11*) POS$_2$ separating discharger, and (*12*) low-inductance load.
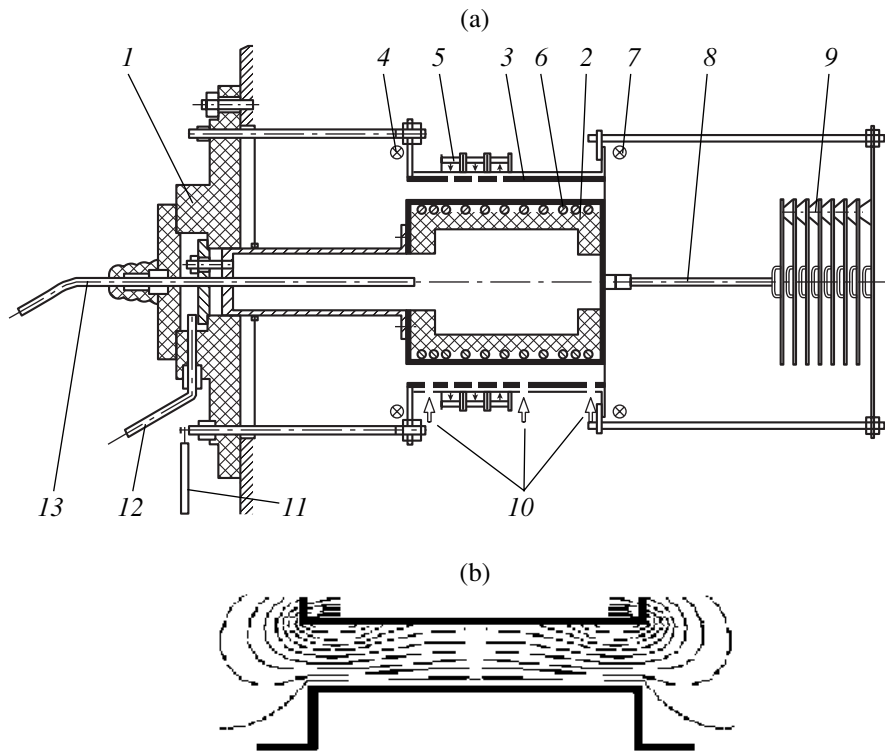
Fig. 4. (a) Schematic of a POS module: (*1*) insulator; (*2*) POS anode; (*3*) cathode; (*4*) Rogowski coil for measuring the input POS current; (*5*) plasma guns; (*6*) solenoid; (*7*) Rogowski coil for measuring the output POS current; (*8*) inductive load; (*9*) separating discharger; (*10*) ion collectors *1, 2,* and *3* (from left to right); (*11*) gun power supply; (*12*) high-voltage conductor; and (*13*) solenoid power supply. (b) Pattern of the lines of the external magnetic field in the POS gap.

As a load with an initially low and, then, increasing impedance, we used 1.6-μF capacitor C_1 (U_{max} = 100 kV, L_{C1} = 0.3 μH). The voltage across such a load increases with time as the current flows. This results in a reclosure of the POS, and the load capacitor discharges through it. In our experiments, we measured
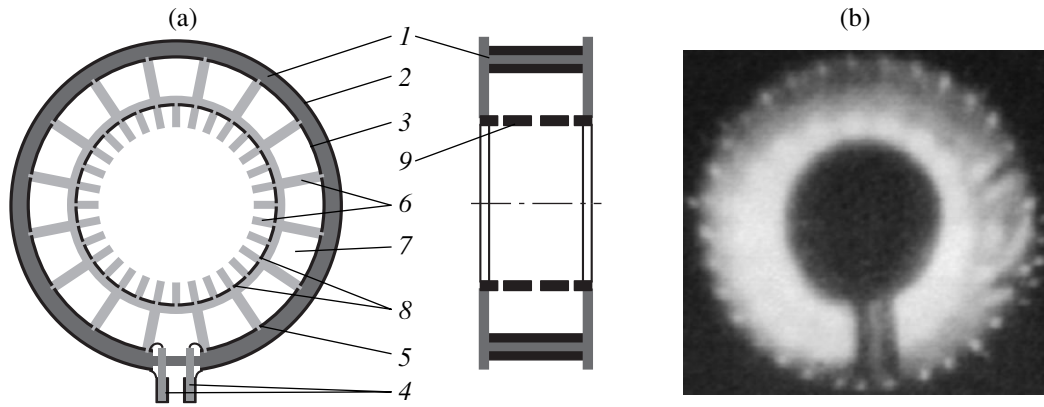
Fig. 5. (a) Schematic of a plasma gun with an accumulating volume: (*1*) dielectric ring, (*2*) outer electrode, (*3*) inner electrodes, (*4*) power supply cables, (*5*) discharge gaps, (*6*) injected plasma, (*7*) accumulating volume, (*8*) output apertures in the conducting ring (POS cathode), and (*9*) conducting ring with output apertures. (b) Image-tube photographs of the plasma glow at 3 μs after the beginning of the discharge (the exposure time is 200 ns).

the input and output currents of the POS (by Rogowski coils and shunts), the voltages across the POS and the capacitive load (by dividers), the voltage across an inductive load (by a loop), and the distribution of the ion current along the POS (by three ion collectors). The plasma gun currents and the magnetic field were also monitored.

3. EXPERIMENTAL RESULTS

3.1. Connecting the POS to the Storage Circuit with the Help of Plasma Guns

The possibility of connecting a POS to the inductive storage circuit with the help of plasma guns was considered in [7]. The design of the MOL generator is appreciably simplified if the POS itself turns the inductive circuit on. There is a keep-alive voltage ($\approx$10 kV) across the POS electrodes, so the current begins to run through the storage circuit after the POS gap is shorted by plasma. While the plasma crosses the gap, the electrons emitted from the plasma surface bombard the anode,
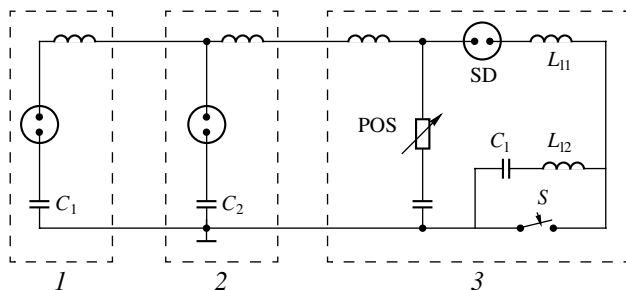
thereby producing the secondary plasma (the so-called "active phase"). Estimates show that, under the MOL operating conditions, the energy deposited by electrons at the anode during the active phase would be about 5 J/cm^2, which is close to the threshold for plasma production. Applying a quasi-steady external magnetic field of about 2 kG allows one to significantly suppress the plasma electron current and to reduce the energy deposited by electrons at the anode. Estimates show that, in this case, the deposited energy is as low as 1 J/cm^2; i.e., the magnetic field does suppress plasma production in the initial stage of the POS operation.

The connection of the POS to the inductive storage circuit by plasma guns is illustrated in Fig. 7a. When the time delay between the discharges of the fast battery and the guns is short enough, the separating discharger breaks down and the increasing current flows through the load, bypassing the POS gap. Due to the inductive voltage drop, the voltage across the gap is about 6 kV. The plasma then closes the POS gap and shunts the load. The increase in the current flowing through the POS plasma leads to the opening of the POS, and the current switches to the load. Such an experiment allows one to determine the optimal time delay between triggering the guns and the POS battery. With this time delay (Fig. 7b), the most advantageous regime of POS operation is observed. The proposed method of experimentally determining the optimal time delay between triggering the guns and the POS may be used in generators with a low "rate of fire."

Fig. 6. Circuit diagram of a POS module: (*1*) prepulse battery, (*2*) main-pulse battery, (*3*) POS with separating discharger *SD* and an inductive or a capacitive load connected through switch *S*.

3.2. Influence of a Separating Discharger when Operating with a Low-Inductance Load

After the POS current is switched to a low-impedance load, the POS is usually reclosed by the plasma existing in the POS gap. As a result, the load is disconnected from the inductive energy storage, because two
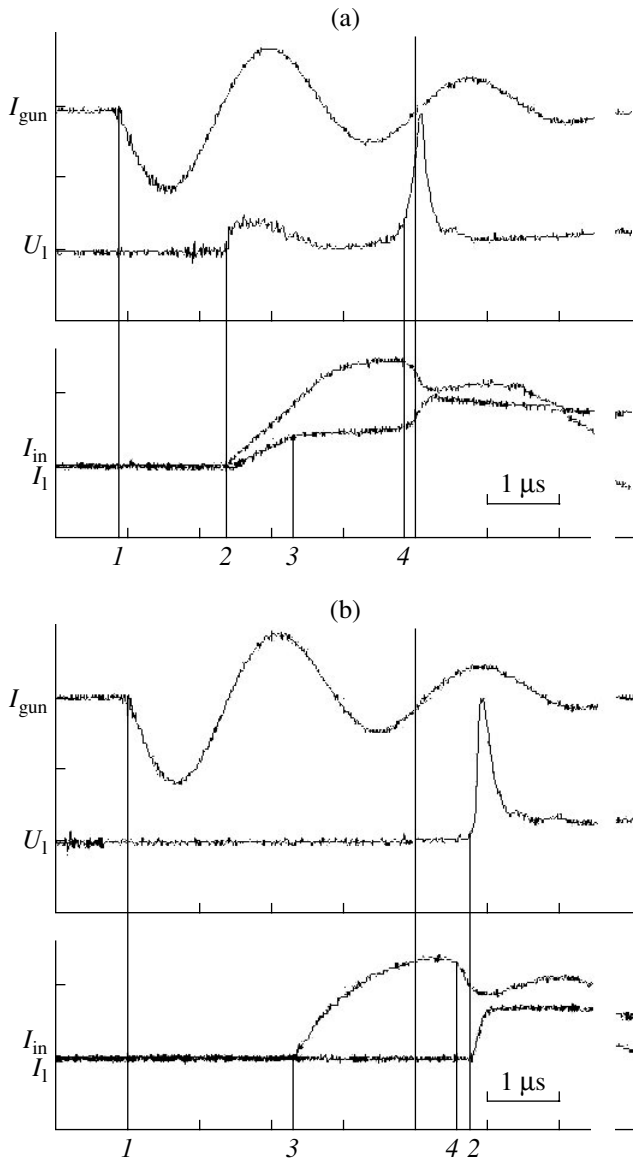
Fig. 7. (a) Connection of the POS to the storage circuit with the help of plasma guns and (b) POS breaking after the time delay chosen using plot (a) for $H_z = 2$ kG. The times indicated correspond to (1) the switching-on of the plasma guns, (2) the breakdown of the separating discharger, (3) the POS closure by the plasma, and (4) the POS breaking. The scales are 2 kA/division for the gun current I_{gun}, 15 kV/division for the load voltage U_l, and 60 kA/division for the POS input current I_{in} and the load current I_l.

independent currents flow through the POS. One of them is the current that flows through the POS–load circuit, whose decay time is equal to L_l/R_l (where L_l and R_l are the inductance and resistance of the circuit), and another is the oscillating current that flows through the POS–Marx generator (MG) circuit (the period of this current is determined by the inductance of the circuit L_0 and the MG capacitance C_0). The use of a separating discharger allows one to achieve a more complete ero-
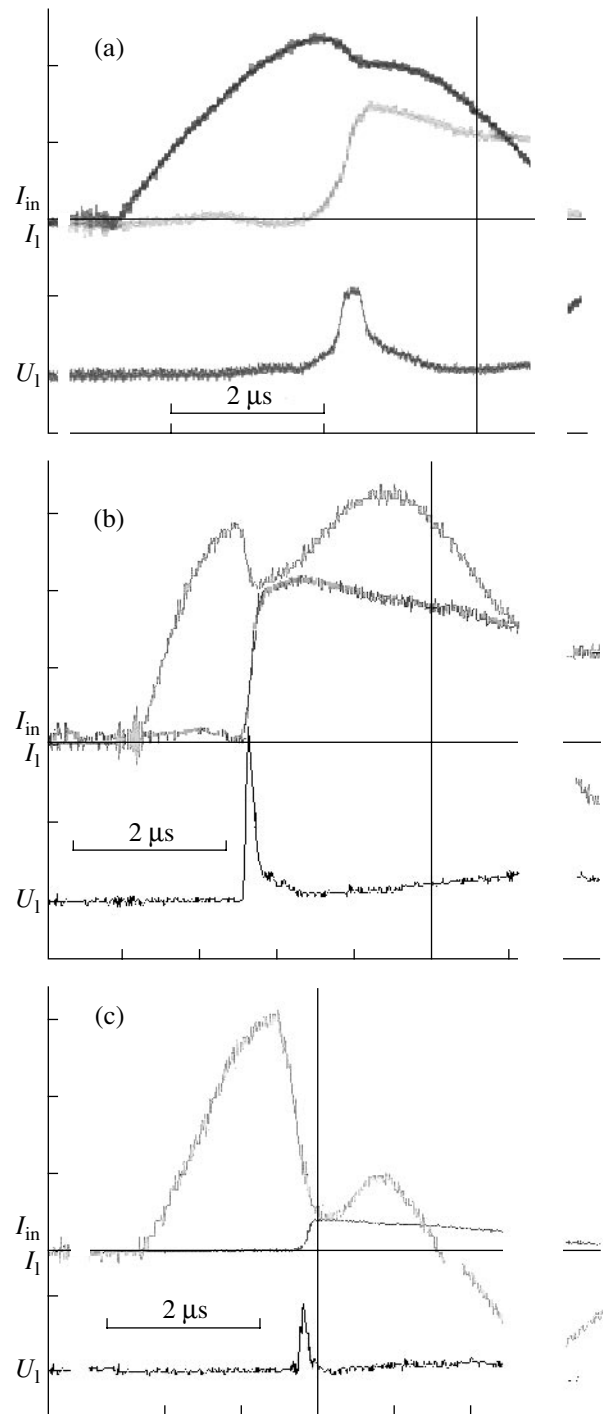

Fig. 8. Effect of the separating discharger: (a) short-circuited discharger, (b) discharger with one gap, and (c) discharger with four gaps for $H_z = 2$ kG. The scales are 60 kA/division for the POS input current I_{in} and the load current I_l and 15 kV/division for the load voltage U_l.

sion of the POS plasma, i.e., to produce a wider vacuum gap between the anode and cathode plasmas. With an external magnetic field, this makes it possible to substantially prolong the high-resistance phase of the POS.
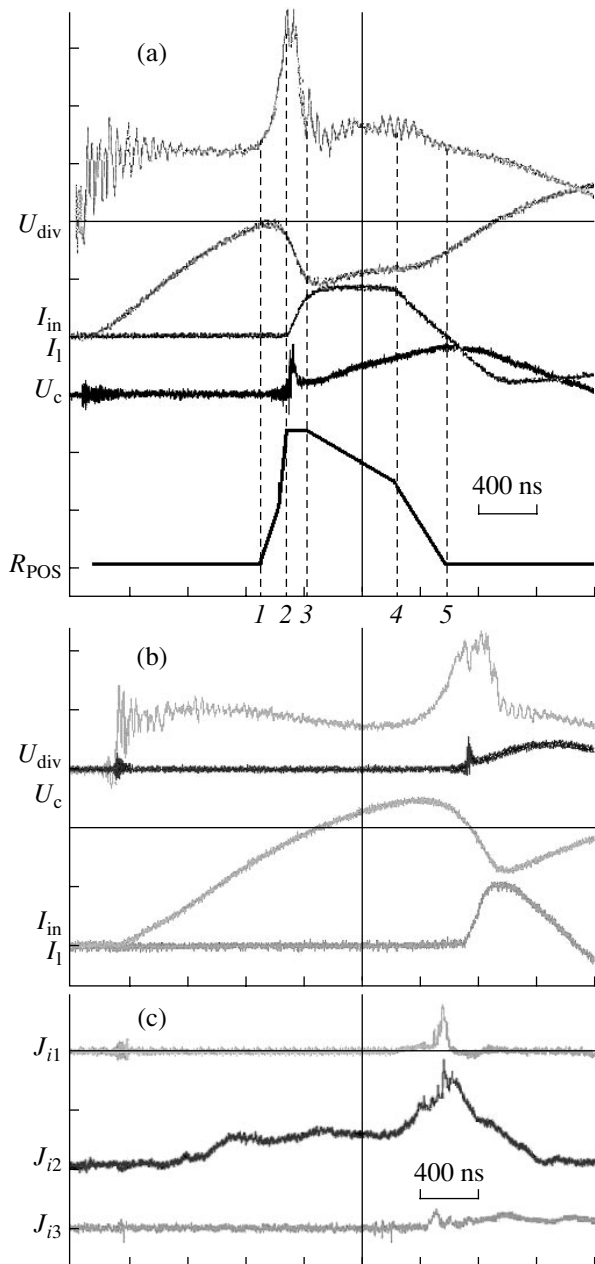
Fig. 9. Energy transfer to a capacitive load: (a) at the front of the current pulse and (b) near the peak of the current for $H_z = 2$ kG. (c) Distribution of the ion currents for the case corresponding to plot (b). The times indicated in plot (a) correspond to (*1*) the beginning of the current interruption, (*2*) the breakdown of the separating discharger and the beginning of the capacitor charging (peak on the U_C waveform corresponds to the inductive voltage), (*3*) the end of energy transfer from the inductive storage and the beginning of energy transfer from the capacitive storage, (*4*) the passage of the capacitive load current into an oscillatory mode, and (*5*) the POS reclosure and the beginning of the discharge of the capacitive load. The scales are 0.5 Ω/division for the POS resistance R_{POS}; 60 kA/division for the POS input current I_{in} and the current through a capacitive load I_l; 15 kV/division for the voltages at the capacitive load, U_C, and at the input divider, U_{div}; and 10 (A/cm^2)/division for the ion current densities J_{i1}, J_{i2}, and J_{i3} at ion collectors *1*, *2*, and *3*, respectively.
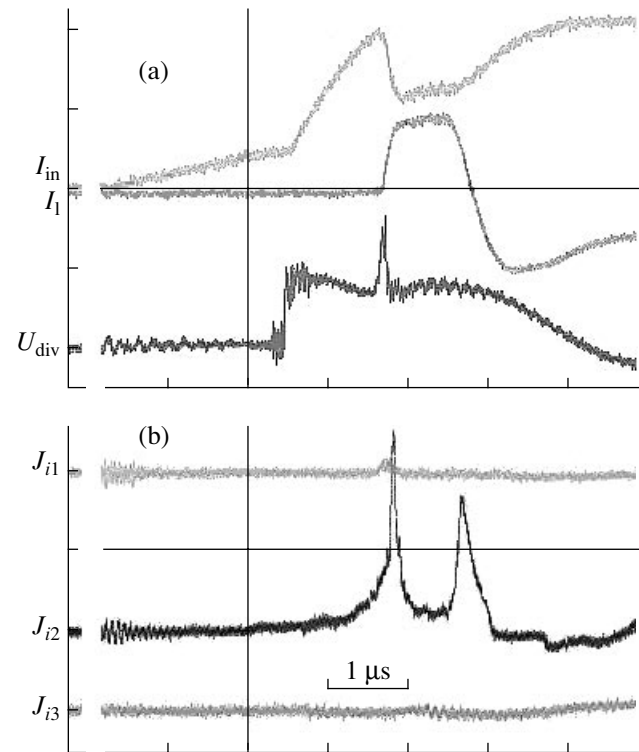
Fig. 10. POS operation with a short current prepulse and a capacitive load for $H_z = 3$ kG: (a) waveforms of the POS input current I_{in} (60 kA/division), the current through a capacitive load I_l (60 kA/division), and the voltage at the input divider U_{div} (15 kV/division) and (b) waveforms of the ion current densities J_{i1}, J_{i2}, and J_{i3} at ion collectors *1*, *2*, and *3*, respectively (10 (A/cm^2)/division).

The breakdown strength of the separating discharger (or the number of the discharger gaps) significantly affects the instant of its breakdown and the rise rate of the current transferred to the inductive load, i.e., the voltage across the load and the value of the current itself (see Fig. 8). If the discharger is closed (Fig. 8a), the POS reclosure by the plasma limits the current switched to the low-inductance load. When four gaps are used (Fig. 8c), the energy is almost entirely released in the POS and no more than 12% of the current is transferred to the load. There is an optimal breakdown strength of the discharger (one to two 1-mm gaps; see Fig. 8b) at which 60–70% of the current is transferred to a 50-nH load at a current rise rate of ~10^{12} A/s. In this case, the POS reclosure occurs ≈0.5 μs after the current is switched to the load. As is usually observed in POS experiments, the generated voltage and the duration of the POS current pause increase with increasing external magnetic field and current rise rate. The reproducibility of the results is fairly high: in about 80% of shots, the scatter in the rise rate of the load current is at a level of 20%.
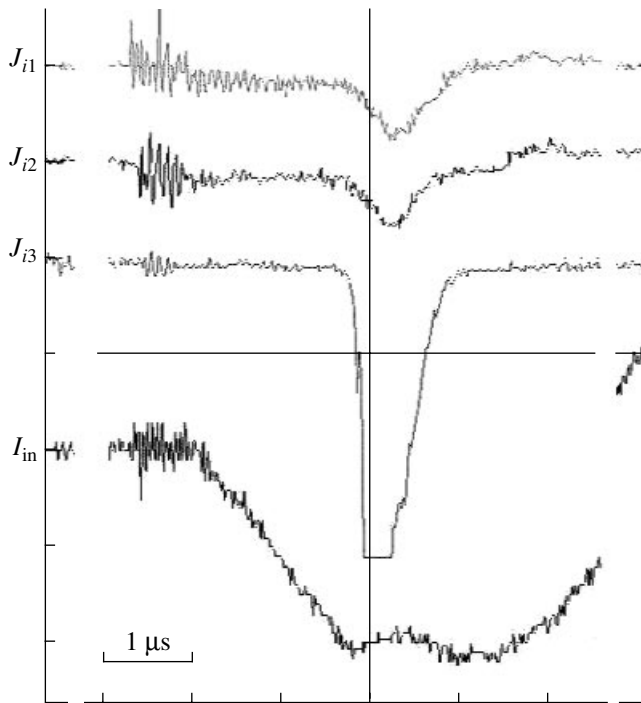
Fig. 11. Distribution of the ion currents in the absence of an external magnetic field. The scales are 60 kA/division for the POS input current I_{in} and 10 (A/cm^2)/division for the ion current densities J_{i1}, J_{i2}, and J_{i3} at ion collectors *1*, *2*, and *3*, respectively.

3.3. POS Operation with a Capacitive Load

We used a capacitive load as an analogue of a load whose impedance is initially low and, then, increases with time. As the capacitor is being charged, its voltage increases. This allows one to evaluate the quality of the POS operation and to trace variations in its resistance R_{POS} (Fig. 9a). At a capacitive storage energy of $W_0 =$ 6.6 kJ and an inductive storage energy of $W_H = 2$ kJ, the energy released in the POS is $W_{POS} = 1.6$ kJ and the energy transferred to the capacitive load is $W_C = 0.5$ kJ. The efficiencies of energy transfer of the inductive storage energy and the capacitive storage energy to the load are $W_C/W_H = 25\%$ and $W_C/W_0 = 7.5\%$, respectively. After the capacitor has been charged (over about 1 µs), the POS gap closes again. By the instant at which the current is interrupted, $\approx 25\%$ of the energy accumulated in the inductive storage is transferred to the capacitor. If the current is interrupted near the peak of the current (Fig. 9b), when the inductive storage energy increases by 1.5–2 times, then the efficiency of energy transfer from the inductive storage to the load decreases to $\approx 10\%$. In this case, the efficiency of energy transfer from the capacitive storage to the load remains at a level of 7%.

3.4. Distribution of the Ion Current along the POS

As was shown in [9], without a magnetic field, there is a minimum length of a POS at which it operates efficiently. For the current ≈ 100 kA and the duration of the conduction phase ≈ 1 µs, the minimum length was found to be ≈ 40 cm, i.e., about three POS diameters. Experiments showed that, in the presence of an external magnetic field, the POS can efficiently operate when its length is approximately equal to (or, in some cases [10], even substantially less than) its diameter (see, e.g., [5]). Nevertheless, the choice of the POS length remains a pressing problem for the MOL generator, which has a long conduction phase. Measurements with the help of three ion collectors *10* (see Fig. 4) showed that the ion current flows mainly through collector *2*, located near the guns, on the load side. The ion current at a level of ~10 A/cm^2 begins to flow long before the drop in the current (Fig. 9c). As was pointed out in [11], this indicates the start of plasma erosion. At the instant of the
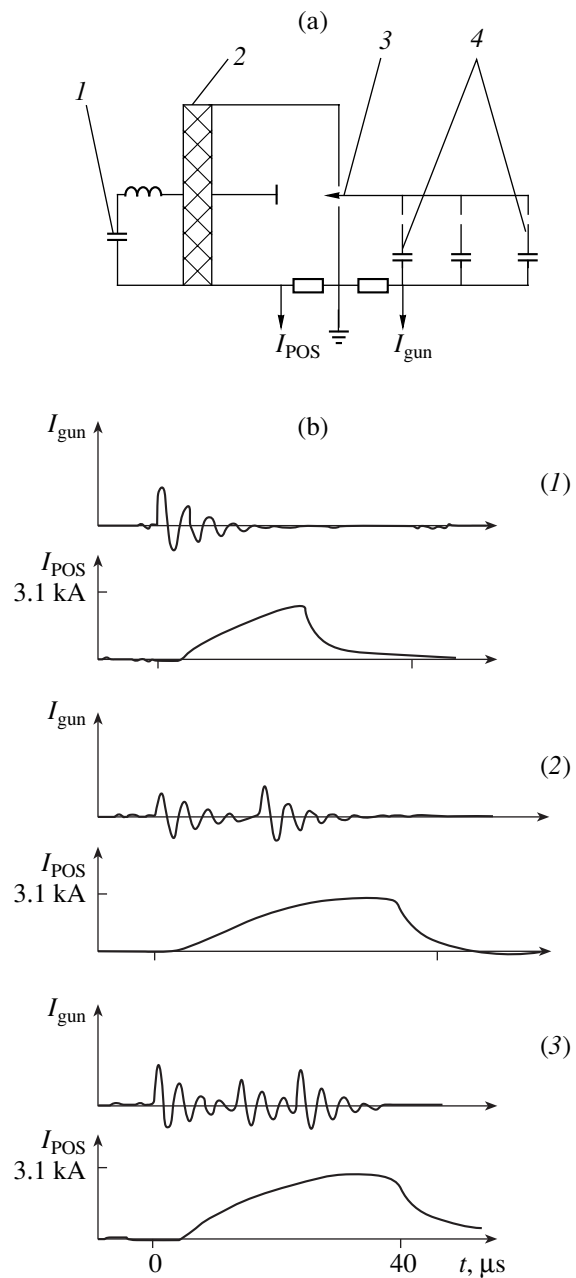

(a)

(b)
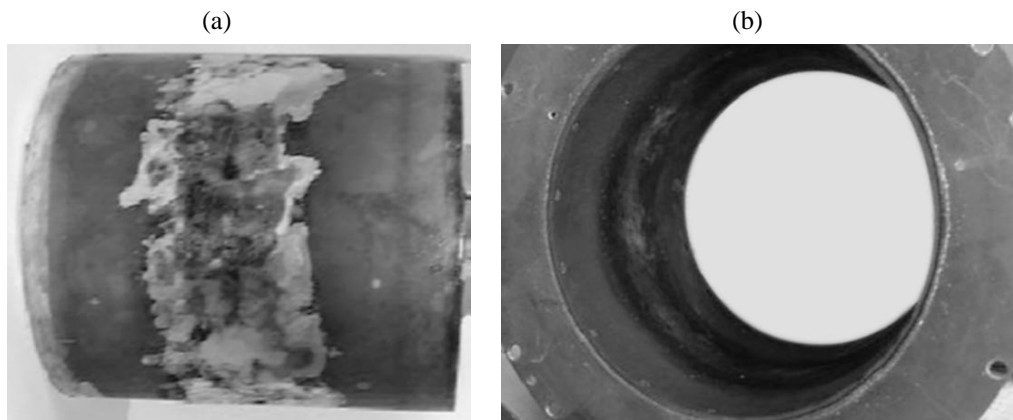
Fig. 12. (a) Anode coated with stainless steel (the power was supplied to the left end; a ring-shaped region exposed to electrons is seen) and (b) cathode coated with carbon (the power was supplied to the front end; a ring-shaped region exposed to ions is seen).
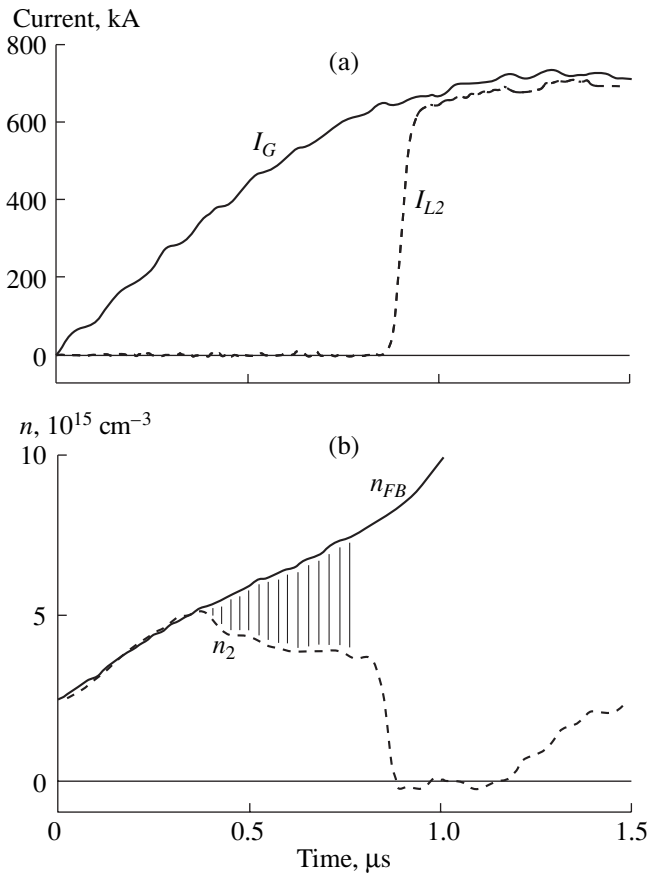
Fig. 13. Change in the plasma density in the POS gap during the current interruption: (a) time evolutions of the generator current I_G and the current I_{L2} switched to the load; (b) time evolution of the plasma density n_{FB} produced by the guns in the POS gap and the time evolution of the plasma density in the course of the generator operation.

Fig. 14. (a) Scheme of the experiment on the programmable filling of the POS gap with plasma: (*1*) battery (6 μF, 50 kV), (*2*) shunt, (*3*) plasma gun, and (*4*) capacitors of the gun power supply. (b) Waveforms of the POS and gun currents for (*1*) one, (*2*) two, and (*3*) three feeding pulses of the plasma guns.

current interruption, the ion current at collector *2* reaches its maximum (≈ 20 A/cm^2) and a narrow peak at a level of 5–10 A/cm^2 is observed in the signal from collector *1*. The signal from collector *3* does not exceed 2 A/cm^2. Similar results were also obtained when operating with a prepulse (Fig. 10). The only difference was that the current at collector *2* had two sharp peaks: one at the instant of the current interruption and another at the instant of the POS reclosure. Without an external magnetic field, the situation was quite different: at the instant of a small decrease in the current, the ion current at a level of more than 30 A/cm^2 was observed only at collector *3* (Fig. 11), whereas at collectors *1* and *2*, it was as low as 2 A/cm^2. Thus, in the presence of an external magnetic field, the ion current at the POS cathode is mainly observed in the plasma gun region at the instant of the current interruption. This is confirmed by traces of the accelerated particles bombarding the POS electrodes (Fig. 12). These results prove the conclusion drawn in [5] that the external magnetic field significantly decreases the velocity of the axial plasma expan-

sion. The axial expansion is related to the stretching of the plasma along the axis due to the axial plasma drift in the magnetic field of the current under the action of the electric field of the electron space charge. Applying an external magnetic field turns the axial drift into the azimuthal one. As a result, the charge separation along the axis and, accordingly, the axial plasma acceleration vanish almost completely.
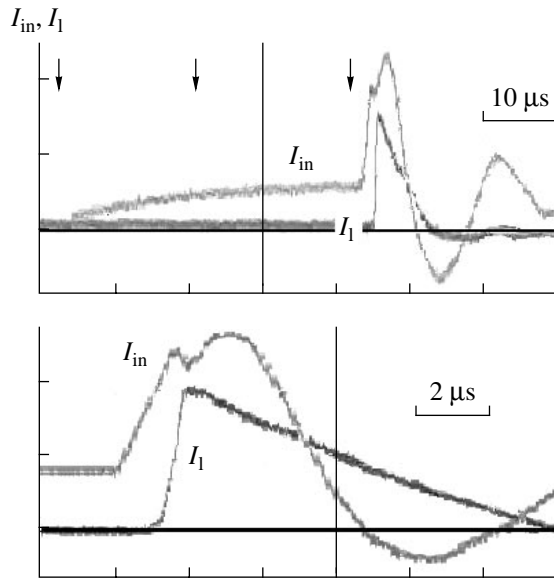
Fig. 15. Waveforms of the current with a prepulse (the separating discharger is short-circuited, $H_z = 6$ kG). The arrows show the instants at which the plasma guns are switched on. The scales of the POS input current I_{in} and the current through an inductive load I_l are 120 kA/division).

3.5. POS Operation with a Current Prepulse

In order for a POS to pass a long current prepulse, a programmable filling of the POS gap by plasma was proposed in [4]. The proposal is based on the ion current measurements, which indicate that the plasma erosion occurs long before the interruption of the POS current [11]. Later on, the dynamics of the plasma density during the conduction phase was studied in [12] (Fig. 13). It can be seen that the plasma density in the POS gap changes appreciably when the current flows through it: the hatched area in Fig. 13b corresponds to the slow preliminary plasma erosion, which is followed by the fast erosion and the interruption of the POS current. The programmable filling of a POS with plasma is intended to partially balance plasma losses during the phase of slow plasma erosion and, thereby, to prolong the conduction phase. The feasibility of this idea was demonstrated in [4, 7]: when two or three feeding pulses were applied to plasma guns filling the POS gap with plasma, the charge passed through the POS increased two- or threefold, respectively, as compared to the case with one feeding pulse (Fig. 14).

The use of plasma guns with an accumulating volume allows one to partially balance plasma losses during the passage of the current and to increase the duration of the conduction phase (including the prepulse phase) to 5–7 µs (Fig. 10). In this case, the waveform of the passed current has the same shape as that without a prepulse and up to 30% of the inductive storage energy is transferred to the capacitor.

It should be noted that the modeling of the MOL current pulse by the sum of two POS currents imposes more stringent requirements upon a POS: whereas the MOL prepulse transfers ≈80% of the charge and ≈20% of the energy, the modeled prepulse transfers ≈80% of both the charge and energy. Probably, it is for this reason that, with a metal-coated anode, the production of the secondary plasma did not allow us to achieve a fairly sharp interruption of the current when the guns were multiply switched on.

When we used a carbon-coated anode, the POS efficiently switched the current to the load after passing the prepulse (Fig. 15). In this case, the linear density of the passed charge reached 20 mC/cm.

4. CONCLUSIONS

It has been shown that a POS can be connected to the inductive storage circuit with the help of plasma guns. By applying a magnetic field and by using a separating discharger, it is possible to maintain the high POS resistance over ~1 µs and to transfer up to 20–30% of the stored energy to a load whose impedance increases with time. Applying an external magnetic field appreciably reduces the axial plasma velocity and decreases the length of the energy deposition region on the POS electrodes to less than 10 cm. The programmable filling of the POS with plasma allows the POS to operate after passing a long (≈40 µs) current prepulse. In this case, the linear density of the passed charge reaches 20 mC/cm. It may be expected that, under the conditions of a real MOL pulse with an increasing current growth rate, the efficiency of the POS operation will be appreciably higher.

REFERENCES

1. V. A. Glukhikh, V. G. Kuchinsky, O. P. Pechersky, *et al.*, in *Proceedings of the 12th International Conference on High-Power Particle Beams, Haifa, 1998*, Vol. 1, p. 71.

2. É. A. Azizov, S. G. Alikhanov, E. P. Velikhov, *et al.*, Vopr. At. Nauki Tekh., Ser. Termoyadernyĭ Sintez, No. 3, 3 (2001).

3. A. S. Altukhov, P. I. Blinov, G. I. Dolgachev, *et al.*, Fiz. Plazmy **29**, 722 (2003) [Plasma Phys. Rep. **29**, 664 (2003)].

4. N. U. Barinov, D. D. Maslennikov, and G. I. Dolgachev, in *Proceedings of the 13th International Conference on High-Power Particle Beams, Nagaoka, 2000*, Vol. 2, p. 583.

5. N. U. Barinov, S. A. Budkov, G. I. Dolgachev, *et al.*, Fiz. Plazmy **28**, 202 (2002) [Plasma Phys. Rep. **28**, 177 (2002)].

6. N. U. Barinov, S. A. Budkov, S. A. Dan'ko, *et al.*, Prib. Tekh. Eksp., No. 2, 112 (2002).

7. G. I. Dolgachev, D. D. Maslennikov, and D. V. Ryzhov, *29th Zvenigorod Conference on Plasma Physics and Controlled Nuclear Fusion, Zvenigorod, 2002*, Abstracts of Papers, p. 237.

8. G. I. Dolgachev, D. D. Maslennikov, and A. G. Ushakov, Prib. Tekh. Eksp., No. 5, 82 (2004).

9. G. I. Dolgachev, A. S. Kingsep, and A. G. Ushakov, Fiz. Plazmy **27**, 64 (2001) [Plasma Phys. Rep. **27**, 62 (2001)].

10. N. U. Barinov, G. S. Belenki, and G. I. Dolgachev, in *Proceedings of the 10th IEEE International Pulsed Power Conference, Albuquerque, 1995*, Vol. 2, p. 1098.

11. G. I. Dolgachev, L. P. Zakatov, and A. G. Ushakov, Fiz. Plazmy **17**, 1171 (1991) [Sov. J. Plasma Phys. **17**, 679 (1991)].

12. B. V. Weber, J. R. Boller, R. J. Commisso, *et al.*, in *Proceedings of the 9th International Conference on High-Power Particle Beams, Washington, 1992*, Vol. 1, p. 375.

Translated by V.I. Bugarya

Neutron Emission Generated in the Collision of Plasma Flows in the Presence of an External Magnetic Field

**G. N. Dudkin[1], B. A. Nechaev[1], V. N. Padalko[1], V. M. Bystritsky[2], V. V Gerasimov[2],
R. V. Kublikov[2], S. S. Parzhitsky[2], V. L. Stolupin[2], J. Vozniak[3],
V. I. Veretel'nik[4], and É. G. Furman[5]**

[1]*Nuclear Physics Institute, Tomsk Polytechnic University, pr. Lenina 2a, Tomsk, 634050 Russia*
[2]*Joint Institute for Nuclear Research, Dubna, Moscow oblast, 141980 Russia*
[3]*Faculty of Physics and Nuclear Engineering, Academy of Mining Engineering and Metallurgy, Krakow, Poland*
[4]*Faculty of Natural Sciences and Mathematics, Tomsk Polytechnic University, Tomsk, 634050 Russia*
[5]*Research Institute of High Voltages, Tomsk Polytechnic University, Tomsk, 634050 Russia*
Received July 22, 2004; in final form, January 12, 2005

Abstract—Results are presented from experimental studies of the neutron emission generated in the collision of deuterium plasma flows produced in discharges in crossed $\mathbf{E} \times \mathbf{H}$ fields and propagating in opposite directions in a neutral gas across an external magnetic field. It is shown that the interaction of oppositely propagating deuterium plasma flows gives rise to the generation of soft X-ray emission and neutron emission from the *dd* reaction ($dd \longrightarrow {}^3\mathrm{He} + n$) and is accompanied by an almost complete depolarization of the flows and rapid variations in the magnetic field (at a rate of $\sim 10^{11}$ G/s). The measurements were performed at energies and velocities of the flows of up to 600 J and 3.5×10^7 cm/s, respectively. The plasma density in each flow was $\sim 10^{15}$ cm^{-3}. The upper estimates for the astrophysical *S* factor and the effective cross sections of the *dd* reaction obtained from our measurements are compared to theoretical calculations and to the results of experiments performed in the MIG high-current accelerator (Institute of High-Current Electronics, Russian Academy of Sciences, Tomsk). © *2005 Pleiades Publishing, Inc.*

1. INTRODUCTION

Investigation of strong interactions between light nuclei in the range of ultralow energies (from a few electronvolts to a few kiloelectronvolts) is of interest for verifying fundamental symmetries (such as charge symmetry and isotopic invariance) [1] and for solving some astrophysical problems [2–4]. It was found, for example, that stars and the Galaxy contain fewer light nuclei (except for $^4\mathrm{He}$) than predicted by conventional star models and by the theory of fusion reactions under conditions of thermodynamic equilibrium. To explain this phenomenon, the authors usually modify the star models by assuming that there are no nuclear or plasma resonances or other anomalies related to collective processes in plasma [5]. In this way, the cross sections for nuclear reactions measured in the range of high energies are extrapolated to the astrophysical energy range for which experimental data are lacking [6].

Experimental investigations of reactions between light nuclei (*dd*, *pd*, *dt*, *d*He, etc., reactions) in the range of ultralow energies require that there be high-intensity flows of accelerated ions, because cross sections for these processes at such energies are very small (10^{-35}–10^{-43} cm^2).

In experimental studies of the *dd* reaction at collision energies of 0.5–3.7 keV (in the center-of-mass frame), high-intensity ion flows were used that were produced in the SGM high-current accelerator (Institute of High-Current Electronics, Russian Academy of Sciences, Tomsk) during the formation of direct and reverse Z-pinches [7–12]. At high energy densities, however, fast nonlinear processes occurring in the liner are accompanied the background emission (neutrons and γ rays), which substantially complicates measurements of the nuclear reaction yield and the interpretation of experimental results. These difficulties have stimulated the search for alternative methods for generating intense low-energy flows of light nuclei.

In [13], results were presented from experimental studies of the formation and interaction of two long (~10 μs) deuterium plasma flows propagating in opposite directions across a magnetic field. Based on these results, preliminary estimates were obtained for the energy parameters of discharges capable of generating oppositely propagating deuterium plasma flows in crossed electric and magnetic fields for studying the *dd* reaction. The use of oppositely propagating plasma flows was expected to substantially lower the device power; to decrease the plasma and energy densities in the flows; and, consequently, to reduce the background emission intensity.

The present paper describes further attempts to determine experimental conditions under which the *dd*
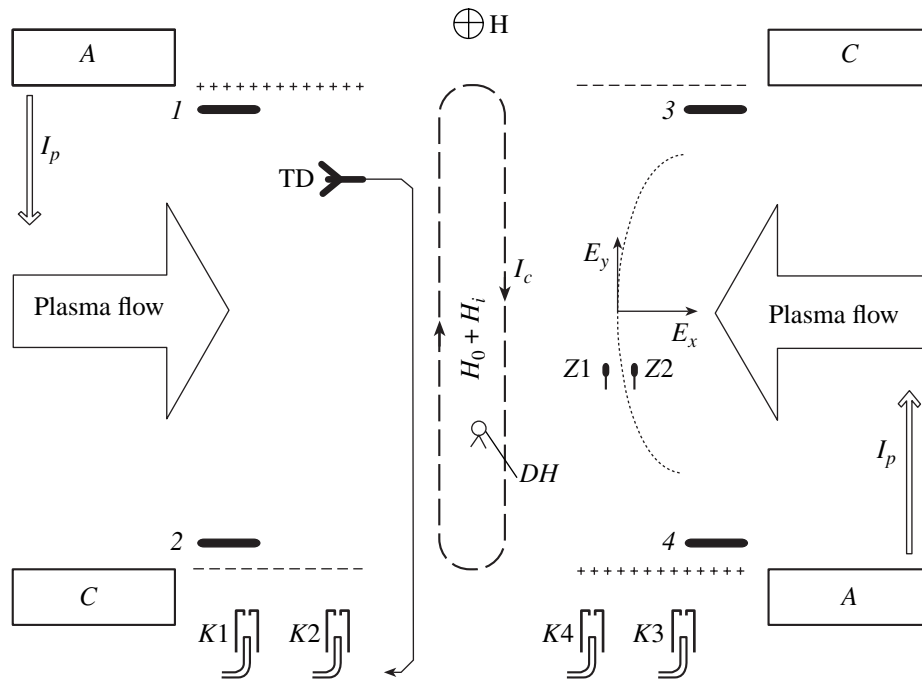
Fig. 1. Arrangement of detectors in the propagation region of the plasma flows: (*A*) anode, (*C*) cathode, (H_0) initial magnetic field, (H_i) field produced by the depolarization current I_c (*DH*) magnetic probe, (*1–4*) electrodes for measuring the potential difference across the flows, (*K1–K4*) collimators of the optical detectors, (*Z1, Z2*) floating probes, and (I_p) discharge current.

reaction can be studied by using two oppositely propagating deuterium plasma flows.

2. EXPERIMENT

2.1. Experimental Setup

Experiments were carried out in a device described in [13]. Figure 1 shows the arrangement of the optical detectors and other diagnostics. Two oppositely propagating plasma flows were formed in a ceramic chamber (18 cm in diameter and ≈150 cm in length) placed in a solenoidal magnetic field with a mirror ratio of ≈1.4. The initial magnetic field in the discharge region was $H_0 \approx 10^4$ G. Two pairs of electrodes were placed in the chamber so that the distance between their centers was 10 cm (the electrode length along the chamber axis being 24 cm, and the interelectrode gap being $D \approx$ 2 cm). After the working gas (deuterium) was fed into the preliminary evacuated chamber, discharges were initiated in the discharge gaps. The discharges were powered in parallel through strip-line conductors from a capacitive storage with a capacitance of $C \approx 18$ μF. An IPT-4 ignitron was used as a switch. An approximate equality of the currents in two discharges was achieved by adjusting the profiles of the discharge gaps. The time interval between the leading edges of the discharge current pulses, as well as between those of signals from optical detectors (*LD1, LD3*), whose collimators (*K1, K3*) were located near the exits of the discharge gaps (see Fig. 1), was less than 100 ns.

The current I_p in both discharge gaps flowed across the magnetic field in opposite directions (see Fig. 1). The plasma in the discharge gaps was accelerated under the action of the electrodynamic force. Outside the discharge gaps, the polarization of the plasma flows [13–16] led to the formation of the electric field $E_y \sim VH/c$ perpendicular to the external magnetic field. As a result, the plasma flows drifted in opposite directions in the crossed E_y and *H* fields and collided at the center of the chamber. The free-propagation distance of each flow until they collided was $L \approx 3$ cm. From the measured voltages between electrodes *1–2* and *3–4* (Fig. 1), we determined the field E_y in the flows propagating across the magnetic field. In addition, these electrodes were used to determine the time and degree of depolarization of the flows during their collision, when the field rapidly decreased. Optical detectors *LD1–LD4* with a spatial resolution of ~1 mm were used to measure the propagation velocities of the flow fronts and the velocity distribution of the liner ions. The detectors measured the intensity of the H_α line of deuterium. Each detector consisted of a collimator, quartz fiber, and filtered photomultiplier. For each flow, we used individual pairs of optical filters, *LD1–LD2* and *LD3–LD4*, with collimators *K1–K2* and *K3–K4*, respectively. The collimators in each pair were separated by a distance of 2.2 cm along the propagation direction of the flows. Variations in the magnetic field in the flow interaction region were measured by one-turn loops *DH* with an area of ≈7 × 10^{-2} cm². The energies of the flows were measured by
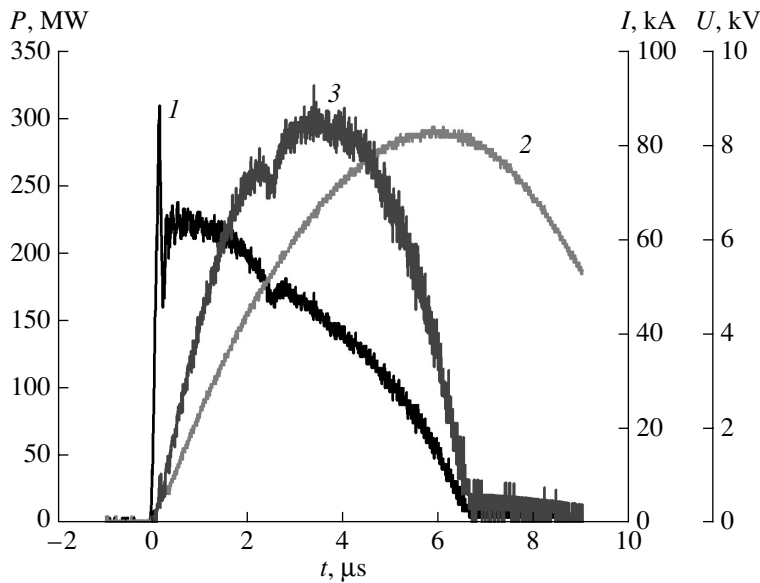
Fig. 2. Energy characteristics of the discharge: waveforms of the (*1*) voltage, (*2*) current, and (*3*) power.

calorimeters *TD*, which were calibrated in the evacuated working chamber by discharging a capacitor with a known energy through a manganin spiral wound on the copper cone of the calorimeter. All these detectors were mounted on a platform that could be displaced along the magnetic field and along the propagation direction of the flows. The discharge current I_p was measured by a Rogowski coil. The potential of the field E_x was measured with the help of floating probes *Z1* and *Z2*, placed at a distance of 0.5 cm from one another. In measuring electric signals, we used optical decoupling.

Neutrons from the $d + d \longrightarrow {}^3\text{He} + n$ reaction were measured by plastic scintillation detectors *S1–S3*, placed at a distance of 150 cm from the flow interaction region, behind a 5-cm-thick lead wall. The dimensions of scintillators *S1* and *S2* were $10 \times 10 \times 80$ cm. The scintillator *S3* was 16 cm in diameter and 20 cm thick. The plastic scintillator of the soft X-ray (SXR) detector (3 mm thick and 30 mm in diameter) was separated from the evacuated volume by a 40-μm beryllium foil and was placed at the chamber axis outside the magnetic field at a distance of 1 m from the flow interaction region. The SXR and neutron detectors are not shown in Fig. 1. All signals from the optical detectors and diagnostic probes were recorded using Tektronix TDS-2014 digital oscilloscopes.

2.2. Energy Characteristics

The energy characteristics of the discharge are shown in Fig. 2. It can be seen from waveform *1* that the discharge voltage decreases rapidly at $t > 6$ μs. The reason for this is that the plasma propagating along the magnetic field reaches the region where magnetic field lines passing through the discharge volume intersect the chamber wall. In this case, the discharge current flowing along the magnetic field lines becomes closed through the chamber wall and the discharge voltage drops to a value characteristic of an arc discharge. The distance from the center of the discharge to the region where the magnetic field lines intersect the chamber wall is ≈40 cm.

Figure 3 shows the energy density distribution in each flow. The measurements were performed by moving calorimeters *TD* along the fronts of the flows (along the electrodes). Based on these measurements, the effective width of the flow along the magnetic field was estimated at $l \approx 10$ cm.

The energy density measured by calorimeters *TD* placed over (and under) the flow was nearly one-seventh of the energy density in the flow. From these measurements, the thickness of the plasma flow was estimated at $d \approx 3$ cm. The total energy of each flow was up to ≈600 J. Comparing the energy parameters of the discharge and the plasma flows, we found that the conversion efficiency of the discharge energy into the flow energy was ≈0.45. The conversion efficiency depended on the initial pressure of the neutral gas (deuterium) in the working chamber. Under our experimental conditions, the optimal deuterium pressure was ≈0.5 torr.

2.3. Collision of the Flows

The first effective collision event occurs 2.0–2.5 μs after the beginning of the discharges. Over the time interval from 0 to 2.0 μs, the flow energy is expended on the ionization of the neutral gas at the fronts of the flows in the field E_x, on the formation of the drift channels (the charging of the plasma capacitors) [13–16],

W, J/cm²
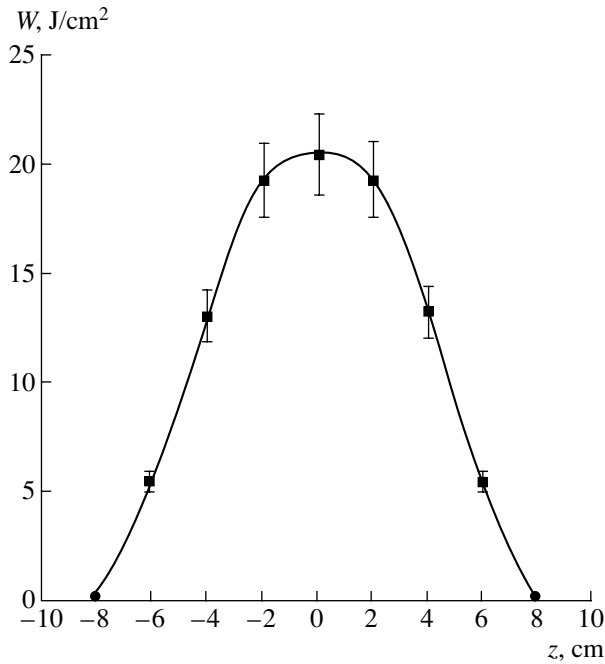
Fig. 3. Energy density distribution in the flow along the magnetic field.

E_y, V/cm; U_{DH}, arb. units
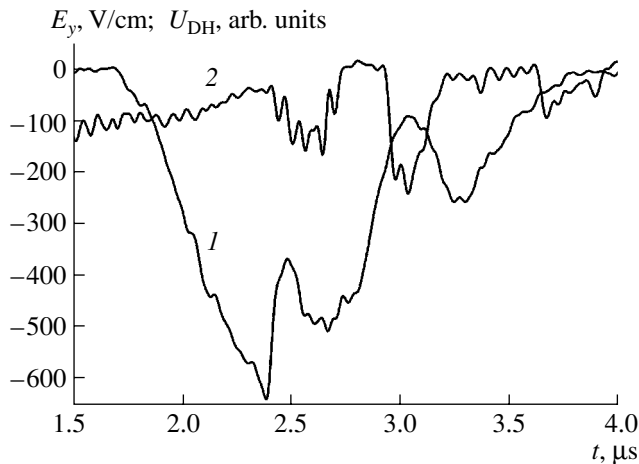
Fig. 4. (*1*) Variations in the electric field strength E_y between electrodes *3* and *4* during the interaction of two plasma flows and (*2*) the magnetic probe signal U_{DH}.

and on the entrainment of the ionized gas into drift motion.

Before the collision, the flows propagate in the formed drift channels. As the colliding flows penetrate into one another to a depth equal to the length of their fronts, they undergo volume depolarization. Hence, the size (along the propagation direction of the flows) of the region where the flows efficiently interact with one

another is on the order of the double length of the flow fronts.

After the flows have been completely depolarized ($E_y \longrightarrow 0$), the drift velocity in the collision region (and near it) decreases to zero ($V \longrightarrow 0$) [13, 16], i.e., the flows stop penetrating into the collision region. Then, the flows emerging from the discharge gaps again form drift channels and a new collision occurs, and so on. The periodicity of collisions can be judged from the periodicity of the magnetic field peaks (Figs. 4, 5). In one shot, we observed up to seven collision events of the oppositely propagating flows. The interaction time of the colliding portions of the flows is on the order of $\tau = 200$–300 ns. Hence, the total effective time of the interaction of the oppositely propagating flows is $T = n\tau$.

The collision of the plasma flows with oppositely directed polarization electric fields is characterized by a rapid decrease in the field strength E_y in the flows (Fig. 4, curve *1*), i.e., the flows become depolarized. The field strength E_y was measured between electrodes *3* and *4* (Fig. 1), located at a distance of ≈2 cm from the center of the collision region. The process of depolarization, which occurs when the plasma capacitors are discharged by the current I_c of (Fig. 1), is accompanied by variations in the magnetic field in the flow collision region (Fig. 4, curve *2*). From the relationship $V = nAdH/dt$ (where V is the detector voltage in volts, $n = 1$ is the number of turns of the magnetic coil, and $A \approx 7 \times 10^{-6}$ m² is the turn area), we could estimate the rate at which the magnetic field varied. It turned out that this rate was higher than 10^{11} G/s. By using magnetic probes, we estimated the effective longitudinal (along the flow propagation direction) size of the interaction region. The measurements showed that, as the magnetic probes were displaced by 1 cm toward the flows from the positions corresponding to the maximum amplitudes of the DH signals, the signal amplitude rapidly dropped (by a factor of about 5). From this, the longitudinal size of the collision region was found to be *2* cm.

The collision of the oppositely propagating deuterium plasma flows was accompanied by the generation of neutrons and SXR emission (Fig. 5; curves *1*, *3*).

3. RESULTS AND DISCUSSION

In none of 30 shots (acts of flow generation) did scintillation detectors $S1$–$S3$ show the presence of neutrons within the time interval 0–2 μs. On the other hand, 20 neutrons were detected within the time interval 2–6 μs (see table). It is this time interval within which up to seven collisions of the flows occurred. The collision period can be roughly estimated by assuming that the time between collisions is determined by the charging time of the plasma capacitor, whose size along the flow is equal to the distance through which the flows freely propagate until they collide ($L \approx 3$ cm). Taking into account ohmic losses caused by the charging current
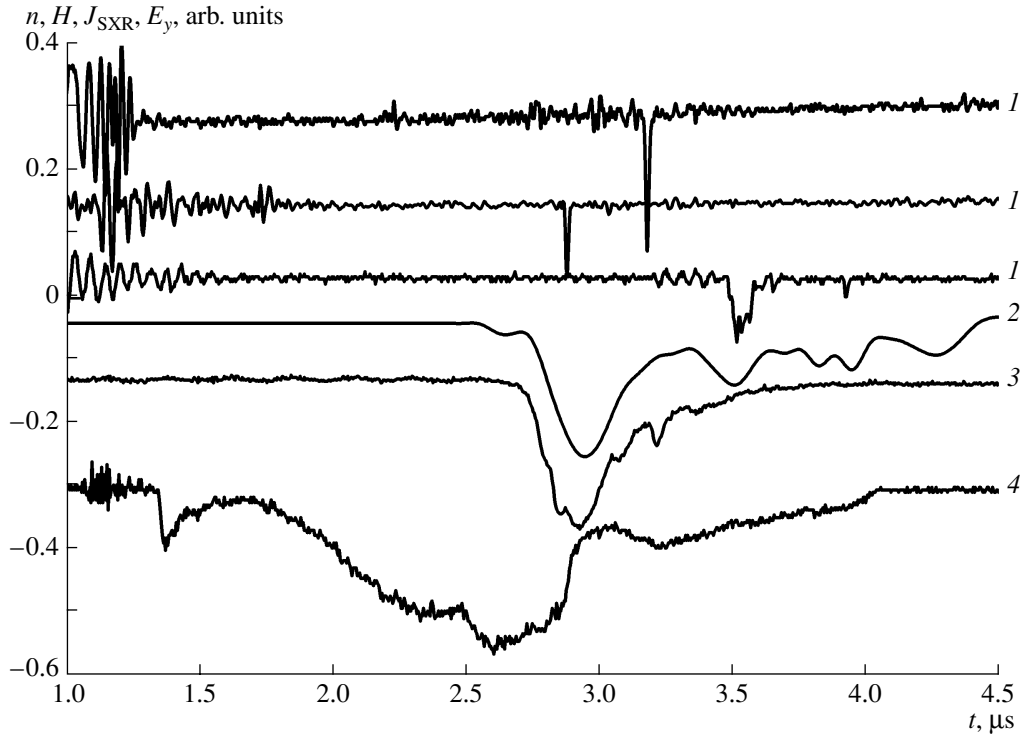
Fig. 5. Signals from (*1*) neutron detectors, (*2*) magnetic probes, (*3*) SXR detectors, and (*4*) detectors measuring the potential difference (field E_y) in the colliding plasma flows.

flowing through the flow front, we find that the time between collisions is equal to [16]

$$T \approx \frac{L}{V}\left[\exp\left(\frac{2eHL}{McV\beta} \right) \right]^{0.5}, \tag{1}$$

where $\beta = \omega_e/\nu_{ie} \approx E_x/E_y$ is the degree of magnetization of electrons, with ω_e and ν_{ie} being the electron cyclotron frequency and the frequency of binary collisions, respectively [15]. The ratio of the fields E_x and E_y at the flow front was measured to be $\approx$2–4. Hence, for $H = 10^4$ G, $V = 3 \times 10^7$ cm/s, $L = 3$ cm, and $\beta = 2$, we find that $T \approx 1$ μs. The higher the electron temperature and the flow velocity, the shorter the collision period.

An analysis of the experimental data shows that the neutron yield is maximum during the first collision. In subsequent collisions (except for some specific cases), both the neutron yield and the amplitude of the magnetic field peaks decrease (Fig. 4). At the same time, the flow parameters after the first collision change only slightly. To clear up the nature of this phenomenon, it is necessary to carry out additional investigations.

In fifteen test shots with only one plasma flow, when collisions were absent, no neutrons were observed.

The table presents the flow front velocity calculated using the data from the optical detectors (Fig. 6) and the values of the velocity (in brackets) and density n_d calculated from the continuity equations for the mass and energy flows in the discharge [13] for the time intervals within which neutrons were observed.

Table

Shot no.	1	9	11	16	17	18	20	25	27	28	30
*S*1	+	+++		+	+	+			+	+	+
*S*2	–	–	–	–	–	–	–	++		+	+
*S*3	+		+++			+	+	–	–	–	–
$V \times 10^7$ cm/s	2.8 (2.8)	3.2 (2.9)	2.8 (2.8)	3.5 (3.7)	3.2 (3.6)	3.2 (3.3)	3 (3)	3.2 (2.9)	3.5 (3.4)	3.5 (3.5)	3.5 (2.5)
$n_d \times 10^{15}$ cm^{-3}	0.9	0.62	0.9	0.85	1	1.3	1	0.65	0.75	0.8	0.6
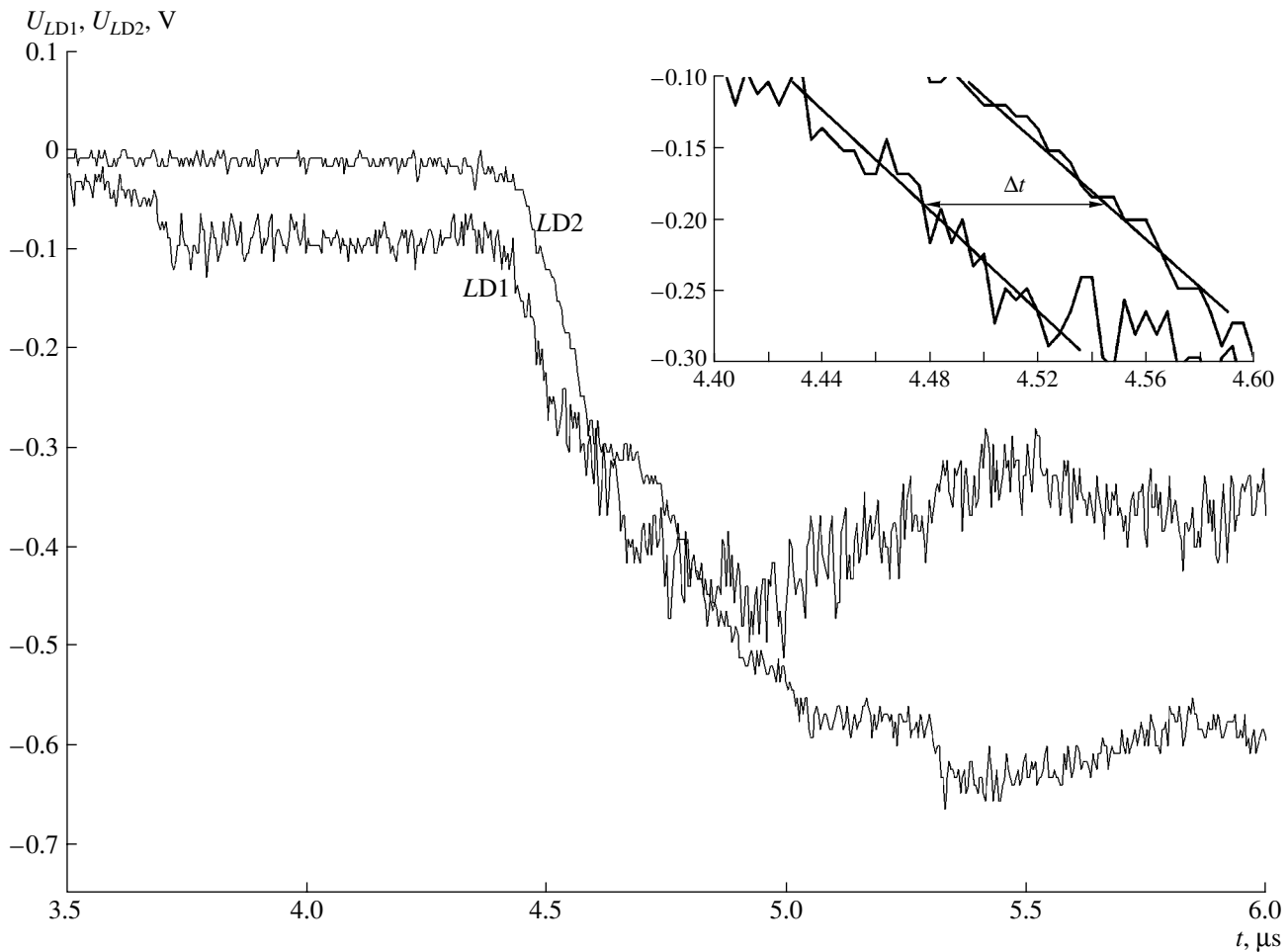
Fig. 6. Signals from optical detectors $LD1$ and $LD2$ and the magnified fragment of the signal fronts. The distance between detector collimators $K1$ and $K2$ along the flow propagation direction is ≈ 2.2 cm; Δt is the time during which the flow travels this distance.

The continuity equations for the mass and energy flows in the discharge are

$$VMn_dS = V_0M_0n_0S_0, \qquad (2)$$

$$P(t) = \frac{MV^2}{2K}Vn_dtS, \quad \frac{KP(t)}{S} = \frac{MV^2(t)}{2}V(t)n_d, \quad (3)$$

where $P(t)$ is the time-varying electric power of the discharge; M_0, V_0, and n_0 are the mass of molecular deuterium and the velocity (at room temperature) and density of the neutral gas particles entering the discharge gap through the cross section S_0; M, V, and n_d are the mass, velocity, and density of deuterium ions in the plasma flow escaping from the discharge gap through the cross section S; and $K = 0.45$ is the conversion efficiency of the discharge electric energy into the flow kinetic energy. The results of previous studies of the current distribution in a discharge in crossed electric and magnetic fields [17] show that the current surface at the entrance to the discharge gap has the shape of a semicylinder. It is assumed that the neutral gas flows into the discharge gap through this surface. In this case, the cylinder diameter D is equal to the electrode gap length and the surface ratio is $S_0/S \approx 0.5\pi$.

From Eqs. (2) and (3), we find

$$V(t) = \sqrt{\frac{2KP(t)}{\pi MV_0n_0S}}, \quad n_d(t) = \sqrt{\frac{\pi^3V_0^3n_0^3SM}{2KP(t)}}. \quad (4)$$

For each shot, the value of the discharge power $P(t)$ (see Fig. 2, curve *3*) corresponded to the time $t \approx t_n - t_{del}$, where t_n is the time at which a neutron is detected and t_{del} is the sum of the following times: the time during which the plasma flow travels the distance (≈ 3 cm) from the discharge gap to the collision region, the time a 2.5-MeV neutron takes to fly from the flow collision region to the neutron detector (the flight base being ≈ 150 cm), and the delay time of the photomultiplier.

An analysis of the temporal distributions of the signals from light detectors $K1$ and $K2$ (or $K3$ and $K4$) positioned at a distance of 2.2 cm from one another allowed us to recover the ion energy distribution in the oppositely propagating flows.

U_{LD1}, U_{LD2}, arb. units
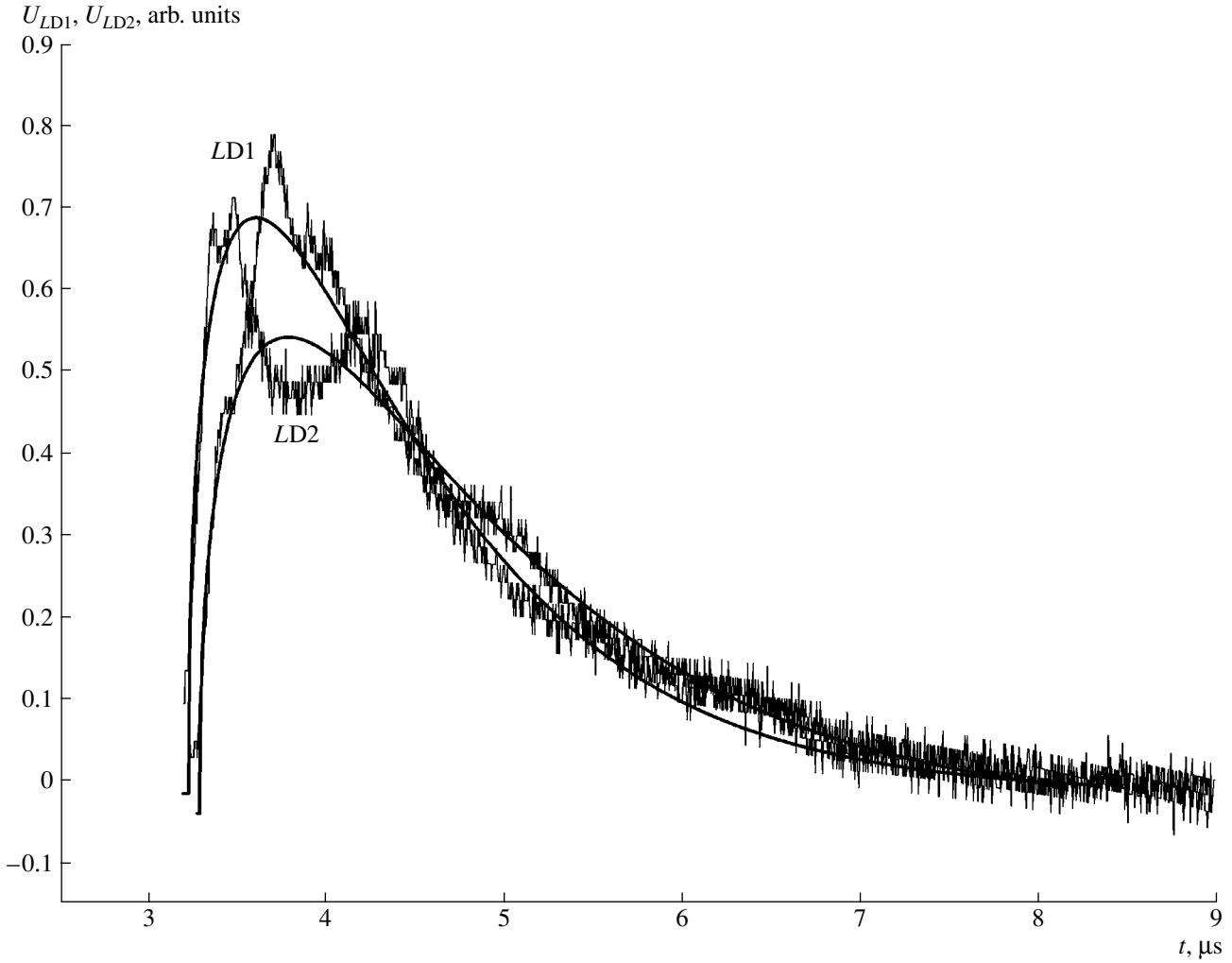
Fig. 7. Signals from optical detectors $LD1$ and $LD2$ in shot no. 18 and the approximating curves (solid lines).

As an example, Fig. 7 shows waveforms of the signals from optical detectors $LD1$ and $LD2$ for shot no. 18. The voltages $U(t)$ at the outputs of the optical detectors were approximated by the function

$$U = U_0 + A\left(1 - e^{-\frac{t-t0}{t1}}\right)^p e^{-\frac{t-t0}{t2}},$$ (5)

where A, U_0, $t1$, $t2$, and $t0$ are variable parameters.

The procedure of recovering the ion energy distribution in the plasma flow by analyzing the shapes of the optical detector signals is described in [10–12].

Figure 8 shows the deuteron distribution (averaged over several shots) over the collision energy in the center-of-mass frame, $f(E_{dd})$.

At present, a generally accepted conception of the interaction of oppositely propagating deuterium plasma flows is still lacking. For this reason, we used the following model to estimate the astrophysical S factor and the effective cross section for the dd reaction.

$f(E_{dd})$, arb. units
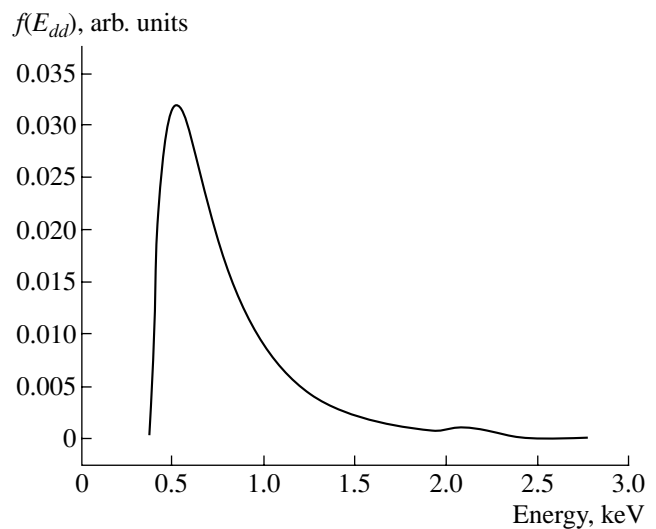
Fig. 8. Average deuteron energy distribution in the plasma flow.

The total number of deuterons (per one shot) in a plasma flow colliding with an oppositely propagating flow is

$$N_d = n_d l d \bar{V} k \tau, \tag{6}$$

where $n_d = 0.85 \times 10^{15}$ cm^{-3} is the deuteron density in the flow, $l = 10$ cm is the flow size along the magnetic field (in the direction perpendicular to the flow propagation direction), $d = 3$ cm is the flow thickness, $\bar{V}$ is the average plasma flow velocity, k is the number of collisions of the flows in one shot, and $\tau = 200$–300 ns the interaction time of the colliding flows.

The total number N_d of deuterons per one shot is on average $N_d = 2 \times 10^{18}$.

Using the above model of oppositely propagating deuterium plasma flows, formulas (13) and (14) from [10], and the measured deuteron energy distribution, we determined the upper estimates for the astrophysical S_{dd} factor and the effective cross section $\tilde{\sigma}_{dd}$ for the *dd* reaction:

$$S \leq 68 \text{ barn keV}, \quad \tilde{\sigma}_{dd}^{\text{exp}} \leq 5 \times 10^{-33} \text{ cm}^2,$$

$$\tilde{\sigma}_{dd}^{\text{cal}} \leq 4 \times 10^{-33} \text{ cm}^2,$$

where $\tilde{\sigma}_{dd}^{\text{cal}}$ is the effective cross section for the *dd* reaction calculated for the astrophysical S factor equal to $S = 53$ barn keV [6, 18] and corresponding to the measured energy distribution of deuterons $f(E_{dd})$ in the plasma flow.

The upper estimates for the S factor and the effective cross sections for the *dd* reaction were calculated for $N_d = 2 \times 10^{18}$, $n_d = 0.85 \times 10^{15}$ cm^{-3}, and the efficiency of neutron detection by the experimental device $\varepsilon_n = 2.4 \times 10^{-3}$ (calculated by the Monte Carlo method).

The above estimates for the S factor and $\tilde{\sigma}_{dd}^{\text{exp}}$ agree with both the results of experiments performed in the SGM high-current plasma accelerator [7, 11, 12] and results of theoretical calculations [19].

4. CONCLUSIONS

The results of our experiments on the interaction of oppositely propagating deuterium plasma flows across the magnetic field can be formulated as follows.

(i) Conditions required for experiments on measuring the characteristics of the *dd* reaction with the required statistical accuracy have been achieved.

(ii) The efficient interaction of oppositely propagating deuterium plasma flows and the associated emission of 2.5-MeV neutrons have been found to be pulsed in character.

(iii) The measured boundary value of the astrophysical S factor and the effective cross section for the *dd* reaction agree with those calculated from the measured deuteron energy distribution in the oppositely propagating plasma flows.

In order to correctly interpret the data that will be obtained in future experiments on studying the *dd* reaction with the use of oppositely propagating deuterium plasma flows, it is necessary to study in detail the generation of two oppositely propagating deuterium plasma flows in discharges in crossed $\mathbf{E} \times \mathbf{H}$ fields, the propagation of these flows in a neutral gas, the formation of drift channels, and the depolarization and collision of such flows.

Furthermore, it is necessary to study how the deuteron energy distribution is affected by the electric fields arising in the flow collision region due to rapid variations in the magnetic field.

It should be noted that measurements of SXR emission generated in the collision of oppositely propagating plasma flows can provide additional information on the influence of strong electric fields on the electron energy distribution in the plasma.

REFERENCES

1. S. P. Merkuriew, A. A. Kvitsinsky, V. V. Kostrykin, *et al.*, in *Proceedings of the International Conference on Theory of Few Body and Quark–Hadronic Systems, Dubna, 1987*, p. 6.

2. C. Rolfs, in *Proceedings of the International Enrico Fermi School on Physics, Course C.3, Villa Monastero, 1987*, p. 48.

3. M. Arnould and M. Forestini, in *Proceedings of the 3rd International Summer School, La Rabida, 1988*, p. 48.

4. V. B. Belyaev, A. Bertin, Vit. M. Bystritskii, *et al.*, Nukleonika **40**, 3 (1995).

5. V. N. Tsytovich, R. Bingham, U. de Angelis, and A. Forlani, Usp. Fiz. Nauk **166**, 113 (1996) [Phys. Usp. **39**, 103 (1996)].

6. A. Krauss, H. W. Becker, H. P. Trautvetter, and C. Rolps, Nucl. Phys. A **465**, 150 (1987).

7. V. M. Bystritsky, Vit. M. Bystritskii, V. M. Grebenyuk, *et al.*, Laser Part. Beams **18**, 325 (2000).

8. V. M. Bystritsky, Vit. M. Bystritskii, V. M. Grebenyuk, *et al.*, Nucl. Instrum. Meth. A **455**, 706 (2000).

9. Vit. M. Bystritskii, Vyach. M. Bystritsky, J. Vozniak, *et al.*, Zh. Tekh. Fiz. **72** (9), 29 (2002) [Tech. Phys. **47**, 1098 (2002)].

10. V. M. Bystritsky, Vit. M. Bystritskii, G. N. Dudkin, *et al.*, Yad. Fiz. (to be published).

11. V. M. Bystritsky, V. V. Gerasimov, A. R. Krylov, *et al.*, Yad. Fiz. **66**, 1731 (2003).

12. Vit. M. Bystritskii, V. M. Bystritsky, S. A. Chaikovsky, *et al.*, Yad. Fiz. **64**, 920 (2001).

13. G. N. Dudkin, B. A. Nechaev, V. N. Padalko, *et al.*, Fiz. Plazmy **29**, 714 (2003) [Plasma Phys. Rep. **29**, 657 (2003)].

14. A. G. Belikov and N. A. Khizhnyak, Fiz. Plazmy **21**, 723 (1995) [Plasma Phys. Rep. **21**, 685 (1995)].

15. G. N. Dudkin, B. A. Nechaev, and V. N. Padalko, Fiz. Plazmy **23**, 258 (1997) [Plasma Phys. Rep. **23**, 237 (1997)].

16. G. N. Dudkin, B. A. Nechaev, V. N. Padalko, and É. G. Furman, Fiz. Plazmy **27**, 599 (2001) [Plasma Phys. Rep. **27**, 563 (2001)].

17. B. A. Nechaev and A. V. Peshkov, Zh. Tekh. Fiz. **63** (8), 181 (1993) [Tech. Phys. **38**, 725 (1993)].

18. R. E. Brown and N. Jarmie, Phys. Rev. C **41**, 1391 (1990).

19. V. M. Bystritsky and F. M. Pen'kov, Yad. Fiz. **66**, 77 (2003).

Translated by N.F. Larionova

BEAMS
IN PLASMA

Relativistic Diamagnetic Equilibrium of a Thin-Walled Annular Electron Beam in an External Magnetic Field

A. F. Aleksandrov[1], M. V. Kuzelev[1], and A. A. Rukhadze[2]

[1]*Moscow State University, Vorob'evy gory, Moscow, 119899 Russia*

[2]*Prokhorov Institute of General Physics, Russian Academy of Sciences,
ul. Vavilova 38, Moscow, 119991 Russia*

Abstract—A self-consistent equilibrium state of a thin-walled annular electron beam in an external magnetic field is investigated with allowance for diamagnetic effect and relativistic effects in the beam rotational motion. An equation for the relativistic angular velocities of the beam rotation is derived in the hydrodynamic approximation. The main parameters of the beam equilibrium state are obtained analytically and are calculated numerically. The parameters of a longitudinally homogeneous, relativistic diamagnetic high-density electron beam are determined. © 2005 Pleiades Publishing, Inc.

High-current relativistic electron beams found widespread use in various fields of science, engineering, and technology soon after physicists learned to produce them in the 1960s. It is not surprising, therefore, that a host of works were devoted to studying the equilibrium configurations of such beams and to determining the maximum possible values of their parameters. This research was so extensive not only because of the wide variety of applied problems associated with high-current beams but also because of the large number of parameters involved in the equilibrium equations for such beams (see below). The latter circumstance makes the beam equilibrium problem far more difficult to examine mathematically and even complicates its formulation. The problem can be successfully analyzed only under certain, often unrealistic, simplifying assumptions. Essentially all of the equilibrium problems for high-current beams to which more or less complete solutions have ever been obtained are described in the well-known monographs [1–7] (see also the original literature cited therein).

Here, we investigate the equilibrium problem for a particular type of beam under specific conditions, namely, the equilibrium of a longitudinally homogeneous, annular relativistic beam with an infinitely thin wall in an external magnetic field. The physics of such a beam constitutes the basis of the theory of relativistic plasma microwave electronics—a theory that provides a good qualitative description of experiments [8].

We consider an axisymmetric, longitudinally homogeneous, electron beam propagating along an external uniform magnetic field. In the hydrodynamic approximation, the states of such a beam are determined from the following familiar balance equation for the radial forces [2]:

$$
\gamma_b(r)\omega_e^2(r) + \frac{1}{r^2}(1 - f - \beta_0^2)\int_0^r \omega_b^2(r')r'dr'
$$
$$
+ \frac{1}{c^2}\omega_e(r)\int_r^\infty \omega_e(r')\omega_b^2(r')r'dr' - \Omega_e\omega_e(r) = 0. \tag{1}
$$

Here, $\omega_e(r)$ is the angular velocity of the beam rotation, $\omega_b(r)$ is the Langmuir frequency of the beam electrons, $f \leq 1$ is the coefficient of neutralization of the beam charge by the immobile ion background, and Ω_e is the electron gyrofrequency in the external magnetic field. Equation (1) is written under the assumption that the longitudinal velocity of the beam electrons is constant over the entire beam cross section and is equal to $v_\parallel(r) = u = \beta_0 c = \text{const}$. The relativistic factor of the beam electrons, $\gamma_b(r)$, is given by the formula

$$
\gamma_b(r) = \left(1 - \frac{v_\parallel^2(r)}{c^2} - \frac{v_\perp^2(r)}{c^2}\right)^{-1/2}
$$
$$
= \left(1 - \beta_0^2 - \frac{\omega_e^2(r)r^2}{c^2}\right)^{-1/2}. \tag{2}
$$

The first term in Eq. (1) stems from the repulsive nature of the centrifugal force, the term proportional to $1 - f$ arises from the repulsive nature of the electrostatic force, the term proportional to $-\beta_0^2$ accounts for the magnetic compression force exerted on the beam by its

own azimuthal magnetic field, and the last term is due to the compressive force of the external magnetic field.

Equation (1) can be analyzed using two approaches [2, 4]: the first is to find the corresponding Langmuir frequency $\omega_b(r)$, i.e., to determine the radial electron density profile, assuming that the angular velocity $\omega_e(r)$ of the beam rotation is known, and the second is to determine the angular rotation velocity $\omega_e(r)$ from a given Langmuir frequency $\omega_b(r)$, assuming that the parameters f, β_0, and Ω_e are known. In either case, the analysis of integral equation (1) runs into difficulties when account is taken of the diamagnetic effects, as well as of the dependence of the relativistic factor $\gamma_b(r)$ of the beam on its angular rotation velocity. Such difficulties, however, do not arise in the case of an annular electron beam with a thin (or, more precisely, an infinitely thin) wall. This case, which is of practical importance, is the subject of the present paper.

The squared Langmuir frequency of the electrons of an annular beam with an infinitely thin wall is given by the formula

$$\omega_b^2(r) = \omega_{0b}^2 \Delta_b \delta(r - r_b), \qquad (3)$$

where Δ_b is the beam wall thickness, r_b is the mean beam radius, and ω_{0b} is a constant. The product $\omega_{0b}^2 \Delta_b$ determines a measurable quantity—the density of the beam electrons per unit area of the beam wall. It is obvious that, in the case of distribution (3), Eq. (1) is meaningful only for the radius $r = r_b$, although it is formally valid for the radii r at which the electron density is zero.

We rewrite radial force balance equation (1) in the form

$$\gamma_b(r)\omega_e^2(r) + \int_0^\infty G(r, r')\omega_b^2(r')r'dr' - \Omega_e\omega_e(r) = 0, \quad (4)$$

where

$$G(r, r') = \begin{cases} \dfrac{1}{r^2}(1 - f - \beta_0^2), & r' < r \\[2mm] \dfrac{\omega_e(r)\omega_e(r')}{c^2}, & r' > r. \end{cases} \qquad (5)$$

Multiplying Eq. (4) by $\delta(r - r_b)$, integrating the resulting equation over r in the vicinity of the radius $r = r_b$, and taking into account distribution (3), we obtain the equation

$$\gamma\omega_e^2 + \omega_{0b}^2\Delta_b\int_0^\infty G(r_b, r')\delta(r' - r_b)r'dr' - \Omega_e\omega_e = 0, \quad (6)$$

where $\omega_e = \omega_e(r_b)$, and $\gamma = \gamma_b(r_b) = (1 - \beta_0^2 - \omega_e^2 r_b^2/c^2)^{-1/2}$.

In calculating the integral in Eq. (6), we must keep in mind that the function $G(r_b, r')$ at the point $r' = r_b$ is discontinuous because of the discontinuity in the components of the self-field of a beam with a δ-shaped distribution of the charge density. The main property of the δ function, $\int f(x)\delta(x)dx = f(0)$, can be naturally generalized as follows:

$$\int f(x)\delta(x)dx = \frac{1}{2}[f(x - 0) + f(x + 0)]. \qquad (7)$$

Using this generalization and performing integration in Eq. (6), we obtain the following equation for the angular rotation velocity ω_e of a thin-walled annular beam:

$$\omega_e^2\left(\gamma + \frac{1}{2}\Delta_b r_b\frac{\omega_{0b}^2}{c^2}\right)$$
$$+ \frac{1}{2}\frac{\Delta_b}{r_b}\omega_{0b}^2(1 - f - \beta_0^2) - \Omega_e\omega_e = 0. \qquad (8)$$

In deriving Eq. (6) and, accordingly, basic equation (8), we did not address the question of the discontinuity in the function $\omega_e(r)$ due to the shear of the rotation velocity of an annular beam with an infinitely thin wall. This question, however, is quite important because, in deriving local equation (6) from integral equation (4), it is necessary to calculate the integrals

$$\int\omega_e(r)\delta(r - r_b)dr,$$
$$\int\gamma_b(r)\omega_e^2(r)\delta(r - r_b)dr. \qquad (9)$$

In order to investigate the structure of the function $\omega_e(r)$ and to eliminate problems associated with its discontinuity, instead of distribution (3), we use the following distribution for the squared Langmuir frequency of the beam electrons:

$$\omega_b^2(r) = \omega_{0b}^2\Delta_b\delta_\varepsilon(r - r_b),$$
$$\delta_\varepsilon(x) = \begin{cases} (2\varepsilon)^{-1}, & x \in [-\varepsilon, \varepsilon], \\ 0, & x \notin [-\varepsilon, \varepsilon], \end{cases} \qquad (10)$$

where $\varepsilon \ll r_b$. In the limit $\varepsilon \longrightarrow 0$, distribution (10) passes over to distribution (3). Note that the quantities Δ_b and 2ε are equivalent in meaning to one another. In taking the limit $\varepsilon \longrightarrow 0$, however, the beam density per unit wall area, which is proportional to $\sim\omega_{0b}^2\Delta_b$, should be treated as an independent constant. Integrals (9) should be calculated over the interval $r \in [r_b - \varepsilon, r_b + \varepsilon]$.

If we ignore both diamagnetic effects and relativistic effects in the beam rotation, then, using Eq. (1), we obtain from distribution (10) the following familiar dis-
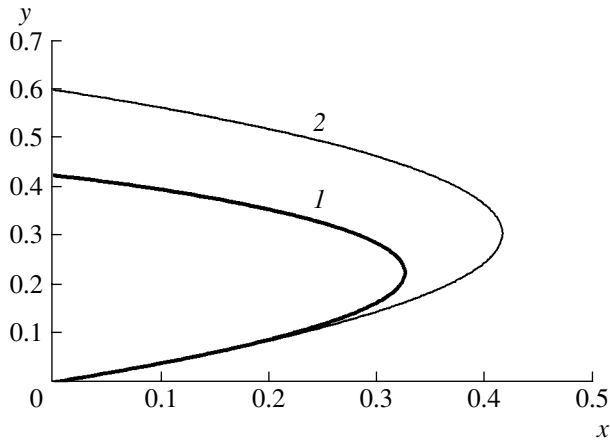
Fig. 1. Dimensionless angular rotation velocity $y = \omega r_b/c$ of a thin-walled annular beam in an external magnetic field for $z = \Omega_e r_b/c = 1$ and $\beta_0 = 0.8$, calculated (*1*) with and (*2*) without allowance for the diamagnetism of the beam and relativistic effects in its rotation.
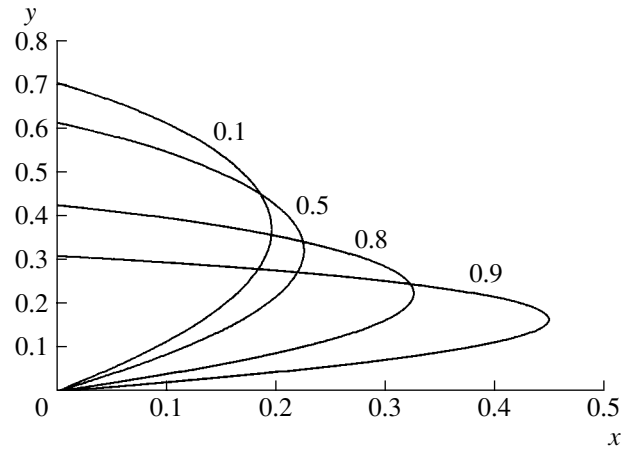
Fig. 2. Dimensionless angular rotation velocity $y = \omega r_b/c$ of a thin-walled annular beam in an external magnetic field for $z = \Omega_e r_b/c = 1$ and $\beta_0 = 0.1, 0.5, 0.8,$ and 0.9.

tributions of the angular rotation velocity of the beam [2]:

$$\omega_e(r) = \omega_e^{(\pm)}(r) \tag{11}$$
$$= \frac{\Omega_e}{2\gamma_0}\left[1 \pm \left(1 - \frac{2\gamma_0\omega_{0b}^2}{\Omega_e^2}\frac{\Delta_b}{r_b}(1 - f - \beta_0^2)\left(1 + \frac{r - r_b}{\varepsilon}\right)\right)^{1/2}\right],$$

where $\gamma_0 = (1 - \beta_0^2)^{-1/2}$. In the limit $\varepsilon \longrightarrow 0$, function (11) has a discontinuity at the point $r = r_b$. It is easy to see that integrals (9) with distribution (11) are independent of ε. In particular, we have

$$\omega_e = \omega_e(r_b) = \omega_e^{(\pm)}(r_b)$$
$$= \frac{\Omega_e}{2\gamma_0}\left[1 \pm \left(1 - \frac{2\gamma_0\omega_{0b}^2}{\Omega_e^2}\frac{\Delta_b}{r_b}(1 - f - \beta_0^2)\right)^{1/2}\right]. \tag{12}$$

When the diamagnetism of the beam and relativistic effects in its rotation have to be taken into account, formula (12) is of course invalid. In this case, the angular rotation velocity ω_e should be determined from Eq. (8). Hence, the quantity ω_e in Eq. (8) is the angular velocity of rotation at a certain point inside the beam, i.e., the angular velocity averaged over the shear of the rotation.

Let us now proceed to the investigation of Eq. (8). In this way, the main difficulty is introduced by relativistic effects in the beam rotational motion, i.e., by the fact that the relativistic factor γ is a nonlinear function of ω_e. As for the diamagnetic effects, they lead to only a simple correction—the second term in the coefficient in front of ω_e^2. Equation (8) can generally be solved only

numerically. In obtaining numerical solutions, it is convenient to use the dimensionless variables

$$y = \frac{\omega_e r_b}{c}, \quad x = \frac{1}{2}\Delta_b r_b \frac{\omega_{0b}^2}{c^2}, \quad z = \frac{\Omega_e r_b}{c}, \tag{13}$$

in terms of which Eq. (8) has the form

$$y^2((1 - \beta_0^2 - y^2)^{-1/2} + x) + (1 - f - \beta_0^2)x - zy = 0. \tag{14}$$

Let us consider the results of solving Eq. (14) numerically, restricting ourselves to the case of a completely unneutralized electron beam, $f = 0$. Figure 1 shows the dimensionless frequencies $y(x)$ calculated for $\beta_0 = 0.8$ and $z = 1$. Curve *1* in the figure was obtained from Eq. (14), while curve *2* was obtained from an equation in which relativistic effects in the beam rotational motion and diamagnetic effects were ignored. In dimensionless variables (13), the latter equation has the form

$$y^2(1 - \beta_0^2)^{-1/2} + (1 - f - \beta_0^2)x - zy = 0. \tag{15}$$

For $f = 0$, the solutions to Eq. (15) are given by the formulas

$$y = y^{(\pm)} \pm \frac{z}{2\gamma_0}\left(1 \pm \sqrt{1 - \frac{4x}{z^2\gamma_0}}\right). \tag{15a}$$

As might be anticipated, in conventional variables, these formulas coincide with expressions (12) (with $f = 0$).

From Fig. 1, it is clear that relativistic effects in the beam rotational motion substantially decrease the higher angular velocity $\omega_e^{(+)}$. We can also see that the range of dimensionless densities x at which the beam
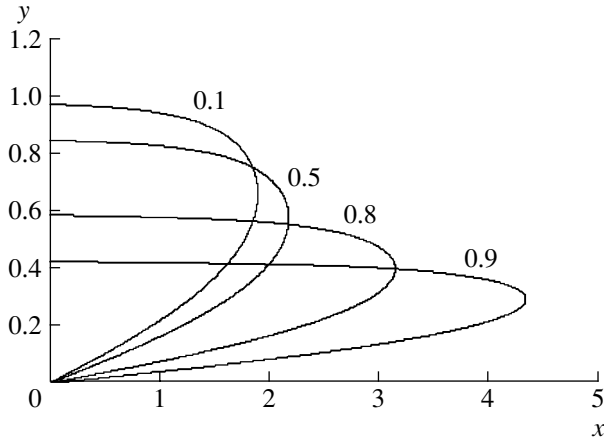
Fig. 3. Dimensionless angular rotation velocity $y = \omega r_b/c$ of a thin-walled annular beam in an external magnetic field for $z = \Omega_e r_b/c = 5$ and $\beta_0 = 0.1, 0.5, 0.8,$ and 0.9.
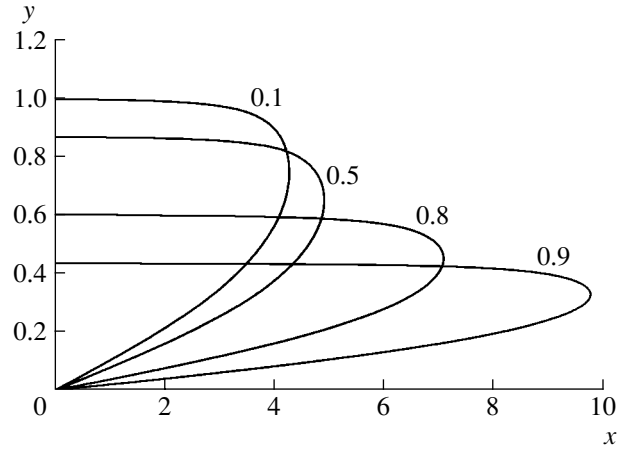
Fig. 4. Dimensionless angular rotation velocity $y = \omega r_b/c$ of a thin-walled annular beam in an external magnetic field for $z = \Omega_e r_b/c = 10$ and $\beta_0 = 0.1, 0.5, 0.8,$ and 0.9.

can be in a steady state is narrower, primarily because of the diamagnetic effect. Figure 2 shows the dimensionless angular velocities $y(x)$ calculated for $z = 1$ and for different values of β_0 (see the numerals by the curves $y(x)$). We see that the higher the longitudinal velocity, the lower the two rotation velocities $\omega_e^{(\pm)}$. Figure 3 also shows the dimensionless angular velocities, but calculated for a stronger magnetic field, $z = 5$. The angular velocities $\omega_e^{(+)}$ and $\omega_e^{(-)}$ are seen to become asymmetric with respect to their half-sum. The higher angular velocity $\omega_e^{(+)}$ depends more weakly on the beam density than does the lower angular velocity $\omega_e^{(-)}$. The stronger the external magnetic field and the less pronounced the relativistic effects in the beam longitudinal motion, the larger the asymmetry (Fig. 4).

Figure 5 shows the maximum values of the dimensionless density of the beam electrons, x_{max}, as functions of the dimensionless magnetic field z for different β_0 values. A beam with a dimensionless density in the range $x > x_{max}$ cannot be in the steady state in which we are interested here. This result is quite obvious: the stronger the external magnetic field and the more pronounced the relativistic effects in the beam longitudinal motion, the wider the range of densities at which the beam can be in a steady state. Note that such a result does not contradict the data presented in Fig. 1. Curve 2 in Fig. 1 was calculated from Eq. (15), which does not apply to the parameter values adopted above. As for Fig. 5 and subsequent figures, they were obtained from the correct equation (14).

Let us now consider some of the results obtained by solving Eqs. (8) and (14) analytically for a particular case of $f = 0$. The maximum dimensionless densities at

which the beam can be in a steady state are given by the approximate formulas

$$x_{max} \approx \begin{cases} \dfrac{1}{4}\gamma_0 z^2, & z \ll 1 \\[2mm] \dfrac{1}{2}\gamma_0 z, & z \gg 1, \end{cases} \tag{16}$$

which agree satisfactorily with the data presented in Fig. 5. For $x \ll x_{max}$, Eq. (14) yields the following two expressions for the dimensionless angular velocities:

$$y = \begin{cases} y^{(+)} \approx \dfrac{1}{\gamma_0}\dfrac{z}{\sqrt{1+z^2}}, \\[3mm] y^{(-)} \approx \dfrac{x}{\gamma_0^2 z}, \end{cases} \quad x \ll x_{max}. \tag{17}$$

According to these expressions, we always have $y^{(+)} \geq y^{(-)}$; here, the equality sign refers only to the case $x = x_{max}$, to which formulas (17) are inapplicable, and, moreover, the maximum $y^{(+)}$ is reached only for $x = 0$ (see Figs. 2–4). This is why the maximum dimensionless angular velocity of an annular beam is given by the quantity $y^{(+)}$ from formulas (17). On the other hand, the beam rotational motion is nonrelativistic when $y^2 \ll 1 - \beta_0^2$ (see formula (2)). Consequently, with allowance for formulas (17), we find that relativistic effects in the beam rotational motion are unimportant under the inequality

$$z = \frac{\Omega_e r_b}{c} \ll 1. \tag{18}$$

This condition, however, applies only to a beam rotating at a high frequency. As for the rotation at a low fre-
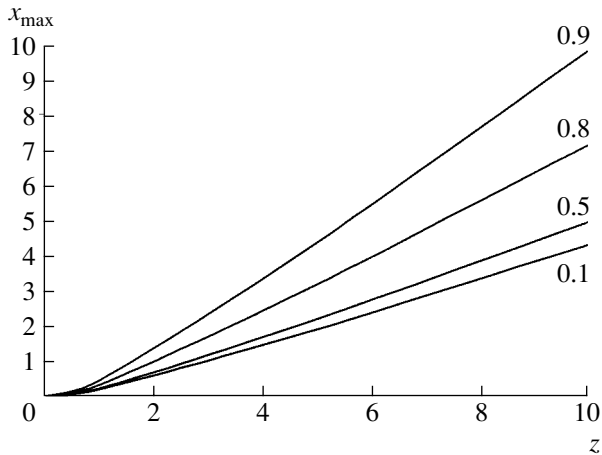
Fig. 5. Maximum dimensionless beam density $x = \Delta_b r_b \omega_b^2 /(2c^2)$ as a function of the dimensionless external magnetic field $z = \Omega_e r_b/c$ for $\beta_0 = 0.1$, 0.5, 0.8, and 0.9.
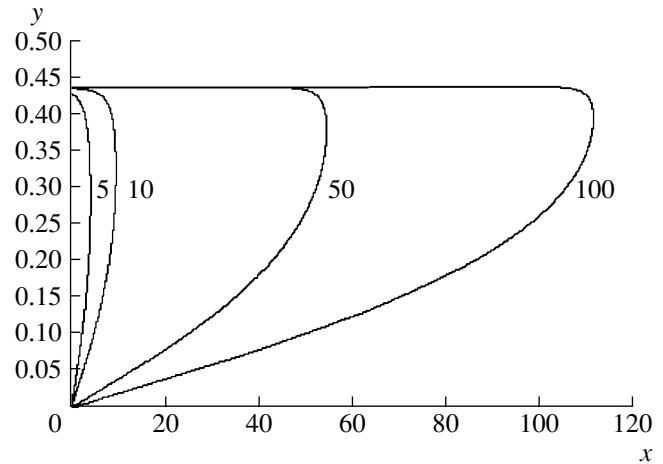
Fig. 6. Dimensionless angular rotation velocity $y = \omega r_b/c$ of a thin-walled annular beam in a strong external magnetic field for $\beta_0 = 0.9$ and $z = \Omega_e r_b/c = 5$, 10, 50, and 100.

quency $y^{(-)}$ for $x \ll x_{max}$, it is always nonrelativistic, as follows from formulas (17).

In dimensional variables, angular velocities (17) are given by the expressions

$$\omega_e^{(+)} = \frac{c}{r_b \gamma_0} \frac{z}{\sqrt{1 + z^2}} \approx \begin{cases} \dfrac{\Omega_e}{\gamma_0}, & z \ll 1 \\[2mm] \dfrac{c}{r_b \gamma_0}, & z \gg 1, \end{cases} \tag{19}$$

$$\omega_e^{(-)} = \frac{\Delta_b}{r_b} \frac{\omega_{0b}^2}{2\gamma_0^2 \Omega_e}.$$

These expressions imply that, in a weak external magnetic field, $z \ll 1$ (when the beam rotational motion is nonrelativistic), the frequency $\omega_e^{(+)}$ coincides with the relativistic electron gyrofrequency Ω_e/γ_0; in this case, only the axial motion of the beam electrons is relativistic. For a strong external magnetic field $z \gg 1$ (the case of relativistic beam rotation), the frequency $\omega_e^{(+)}$ differs qualitatively from that in the previous case and can be obtained by equating the total relativistic factor of an electron, $\gamma_b = (1 - \beta_0^2 - y^2)^{-1/2}$, to infinity. Accordingly, the angular velocity of the beam rotation cannot in principle be higher than $c/(r_b\gamma_0)$. The frequency $\omega_e^{(-)}$ exhibits qualitatively the same structure (see the second of expressions (19)) as its nonrelativistic analogues and has the same physical meaning (see [2]). Generally, relativistic effects in the beam rotation at a low frequency $\omega_e^{(-)}$ are unimportant as long as $x \ll x_{max}$.

Let us determine the conditions under which diamagnetic effects do (or do not) play a role. Equation (8) implies that the diamagnetism of an electron beam is insignificant for $x \ll \gamma_b$. This yields the condition under which diamagnetic effects can be ignored:

$$x = \frac{1}{2}\Delta_b r_b \frac{\omega_b^2}{c^2} \ll \gamma_0 \sqrt{1 + z^2}. \tag{20}$$

We see from condition (20) and formulas (16) that, for $z \ll 1$, diamagnetic effects are always small and that, for $z \gg 1$, the diamagnetism of high-density beams should always be taken into account. The diamagnetic effects of the beam rotation at a low frequency $\omega_b^{(-)}$ are unimportant as long as $x \ll x_{max}$.

For large z values and arbitrary x values, Eq. (14) is quite difficult to investigate analytically. Since the case of a strong external magnetic field is of considerable interest, we again turn to the results of numerical calculations. Figure 6 presents the dimensionless frequency $y(x)$ calculated for $\beta_0 = 0.9$ and for different values of z (see the numerals by the curves). An analysis of Fig. 6 and Eq. (14) shows that, for a strong external magnetic field, the following approximate expressions are valid:

$$y = \begin{cases} y^{(+)} \approx \dfrac{1}{\gamma_0} \\[2mm] y^{(-)} \approx \dfrac{x}{\gamma_0^2 z}, \end{cases} \quad \omega_e = \begin{cases} \omega_b^{(+)} \approx \dfrac{c}{r_b \gamma_0} \\[2mm] \omega_b^{(-)} \approx \dfrac{\Delta_b}{r_b} \dfrac{\omega_b^2}{2\gamma_0^2 \Omega_e}. \end{cases} \tag{21}$$

We thus see that, when $z \gg 1$, formulas (17) and (19) are approximately valid for sufficiently large x values; however, the closer the dimensionless beam density x to x_{max}, the worse the validity of the formulas.

Formulas (21) can help us to answer the question of whether the above equilibrium states can be achieved in practice. In terms of γ and γ_0, the dimensionless angular velocity y has the form

$$y^2 = \gamma_0^{-2} - \gamma^{-2}. \tag{22}$$

The total relativistic factor of the beam, γ, should be considered as a given quantity determined by the accelerating voltage of a high-current diode. The longitudinal relativistic factor can take on values from 1 to γ: for $\gamma_0 = 1$, the beam can execute only rotation motion and, for $\gamma_0 = \gamma$, the beam does not rotate at all.

If we substitute $y = y^{(+)}$, with $y^{(+)}$ being defined in formulas (21), into expression (22), then we obtain $\gamma \gg 1$ (or, more precisely, $\gamma \longrightarrow \infty$). Consequently, in a strong external magnetic field, equilibrium rotation of an annular electron beam at a high frequency $\omega_e^{(+)}$ is possible only when the energy of the beam electrons is sufficiently high. Substituting $y = y^{(-)}$, with $y^{(-)}$ being defined in formulas (21), into expression (22), we arrive at the relationship

$$x = z\gamma_0\sqrt{1 - \frac{\gamma_0^2}{\gamma^2}}. \tag{23}$$

From Fig. 5 we see that, for $z > 1$, this relationship can easily be satisfied for a certain value of the dimensionless density lying in the range $x < x_{\max}$.

Finally, we determine the parameters of a relativistic diamagnetic annular beam of maximum possible density, $x = x_{\max}$, in a strong external magnetic field, $z \gg 1$. To do this, we substitute the corresponding value of $x_{\max}$ from formulas (16) into relationship (23). As a result, we obtain the following beam parameters:

$$\gamma_0 = \frac{\sqrt{3}}{2}\gamma, \quad \omega_e = \frac{1}{2}\frac{c}{r_b\gamma_0}. \tag{24}$$

We see from Fig. 6 that the ω_e value given by formulas (24) is several times less than that calculated numerically. This circumstance is a consequence of the fact that relationship (23) is inapplicable to the limit $x \longrightarrow x_{\max}$. However, the above formulas predict the correct orders of magnitude of the quantities and provide their correct dependence on the main parameters of the problem.

ACKNOWLEDGMENTS

REFERENCES

1. A. N. Didenko, V. P. Grigor'ev, and Yu. P. Usov, *High-Power Electron Beams and Their Application* (Atomizdat, Moscow, 1977) [in Russian].

2. R. C. Davidson, *Theory of Nonneutral Plasmas* (Benjamin, New York, 1974; Mir, Moscow, 1978).

3. J. D. Lawson, *The Physics of Charged-Particle Beams* (Clarendon, Oxford, 1977; Mir, Moscow, 1980).

4. A. A. Rukhadze, L. S. Bogdankevich, S. E. Rosinskii, and V. G. Rukhlin, in *Physics of High-Current Relativistic Electron Beams* (Atomizdat, Moscow, 1980) [in Russian].

5. R. B. Miller, *Introduction to the Physics of Intense Charged Particle Beams* (Plenum, New York, 1982; Mir, Moscow, 1984).

6. E. A. Abramyan, B. A. Al'terkop, and G. D. Kuleshov, *Intense Electron Beams* (Énergoatomizdat, Moscow, 1984) [in Russian].

7. A. S. Chikhachev, *Kinetic Theory of Quasi-Steady Charged Particle Beams* (Fizmatlit, Moscow, 2001) [in Russian].

8. M. V. Kuzelev, A. A. Rukhadze, and P. S. Strelkov, *Plasma Relativistic Microwave Electronics* (Mosk. Gos. Tekhn. Univ. im. N.É. Baumana, Moscow, 2002) [in Russian].

Translated by I.A. Kalabalyk

<div align="center">

PLASMA
DIAGNOSTICS

</div>

Hilbert–Huang Transform in MHD Plasma Diagnostics

A. M. Kakurin and I. I. Orlovsky

Russian Research Centre Kurchatov Institute, pl. Kurchatova 1, Moscow, 123182 Russia

Received February 9, 2005; in final form, April 7, 2005

Abstract—A new method for processing experimental data from MHD diagnostics is discussed that provides a more detailed study of the dynamics of large-scale MHD instabilities. The method is based on the Hilbert–Huang transform method and includes an empirical mode decomposition algorithm, which is used to decompose the experimental MHD diagnostic signals into a set of frequency- and amplitude-modulated harmonics in order to construct the time evolutions of the amplitudes and frequencies of these harmonics with the help of the Hilbert transform. The method can also be applied to analyze data from other diagnostics that measure unsteady oscillating signals. © 2005 Pleiades Publishing, Inc.

1. INTRODUCTION

The development of novel approaches to studying the dynamic parameters of large-scale MHD perturbations in tokamaks is important since, in recent years, interest has renewed in neoclassical tearing modes and resistive wall modes (RWMs) caused by the finite conductivity of the chamber wall. An analysis of the characteristic features of these instabilities is required to understand the physical mechanisms governing their behavior and to elaborate methods for controlling them.

Detailed investigation of the dynamic properties of MHD instabilities requires further development of the methods for MHD diagnostics of tokamak plasmas. An efficient path in this direction is to refine methods for processing experimental data. MHD diagnostics usually provide information in the form of signals from numerous magnetic probes that are arranged near the plasma boundary and measure the magnetic field perturbations driven by MHD instabilities. The recorded signals have the form of oscillations whose parameters change throughout the discharge. The oscillations have both regular and stochastic components, whose intensity ratio depends on the discharge regime. It should be noted that, in modern tokamaks, the diagnostic complexes operate under the conditions of high-level noises that are introduced by the plasma and the power electrotechnical equipment and mask the desired signals from MHD instabilities.

The unsteady (and sometimes nonlinear) character of oscillations limits the possibilities of the standard spectral methods in investigating the dynamics of instabilities. However, limitations imposed by the unsteady character of oscillations can be removed by applying the time–frequency distribution (TFD) methods [1], which make it possible to follow the time evolution of the signal spectrum. At present, such methods as the windowed Fourier transform, the wavelet transform [2], and the Choi–Williams distribution [3] have already found application in MHD plasma diagnostics.

It should be noted that, however, that the TFD methods do not provide simultaneous precise measurements of the spectral and temporal parameters of the signals because of the restrictions imposed by the uncertainty relation. These restrictions can be removed by using an approach in which the experimental data to be analyzed are converted into a so-called analytic signal [4]. It was recently proposed to use this approach in studying the characteristic properties of the dynamics of MHD perturbations in tokamaks [5]. This approach was successfully applied in experiments on studying the effect of the control electromagnetic system on MHD instability in the HBT-EP tokamak [6].

In contrast to the TFD methods, which involve a formal decomposition of the nonlinear oscillatory process into individual harmonics, the approach based on the analytic signals allows one to interpret the nonlinearity of oscillations as a variation in the instantaneous frequency during the oscillation period [7, 8]. Such an interpretation was used in studying the dynamics of a tearing mode in a tokamak [9]. The approach in question, however, is subject to a serious restriction: it requires that the basic oscillating function be monocomponent; i.e., the number of local extremes of the function and the number of its zeros should differ by no more than unity and the upper and lower envelopes of the oscillating function should be symmetric with respect to its zero level [7].

The latter (symmetry) requirement is often not satisfied for MHD diagnostic signals because of the presence of externally induced signals from the electrotechnical equipment, plasma noises, and measurement instruments and also because of the simultaneous development of several MHD modes that exhibit different time behaviors. This drawback can be overcome by using the recently developed Hilbert–Huang transform
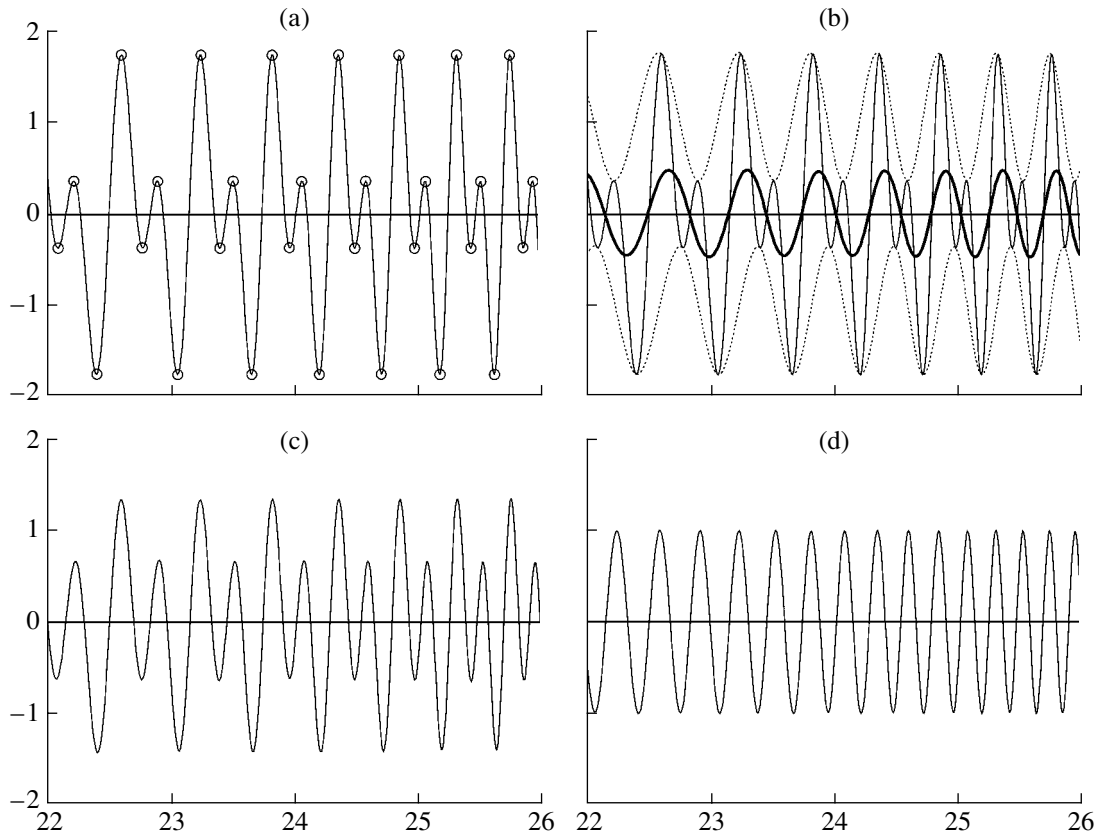
Fig. 1. (a) Original signal $f(t)$ with the indicated extremes; (b) envelopes calculated by interpolating between the extremes of $f(t)$ (dashed curves) and the mean $m(t)$ of the envelopes (heavy curve); (c) difference between the original signal and the mean of the envelopes, $f(t) - m(t)$; and (d) monocomponent function $f_0(t)$.

(HHT) method, which is based on the decomposition of the original function $f(t)$ into a set of monocomponent harmonics $f_i(t)$ and the construction of the corresponding analytic signal for each of them [7, 8]. The HHT method makes it possible to determine such time-dependent spectral parameters of the monocomponent harmonics $f_i(t)$ as the amplitude, phase, and instantaneous frequency, i.e., to follow the dynamic parameters of the object described by the original function $f(t)$. It is worth noting that the monocomponent harmonics of the signal analyzed by means of MHD diagnostics often come from individual (generally unsteady) nonlinear oscillatory processes related to MHD plasma instabilities.

The decomposition method under consideration, which was called the empirical mode decomposition (EMD) method, consists in successive calculations of the harmonics $f_i(t)$ having the shape of amplitude- and frequency-modulated oscillations. The EMD method is suitable for processing signals from magnetic probes in a tokamak because they are oscillations with time-varying amplitude and frequency. In our earlier paper [10], this method was successfully applied to analyze the spatial structure of large-scale MHD perturbations.

2. HILBERT–HUANG TRANSFORM ALGORITHM

In the initial step of the EMD method, the basic oscillating function $f(t)$ with $t \in [a, b]$ is decomposed into monocomponent harmonics by an algorithm that was proposed by Huang *et al.* [7] and is based on the following idea. All extremes of the function $f(t)$ on the interval $[a, b]$ are found. The upper, $u(t)$, and lower, $d(t)$, envelopes of the function $f(t)$ are calculated by interpolating between its local maxima and minima, respectively, in terms of periodic cubic splines, as is shown in Fig. 1a. The mean of the envelopes, $m(t) = (u(t) + d(t))/2$, is calculated and is subtracted from the original function $f(t)$ in order to eliminate the local trend (Fig. 1b). The function $f(t) - m(t)$ (Fig. 1c) is then regarded as the original function, and the above procedure for eliminating the local trend is applied to it. The cycle of these iterations is continued until the mean of the envelopes at a certain iteration step becomes small enough to satisfy a stopping criterion on the interval $[a, b]$. The iterative process yields a monocomponent function (harmonic) $f_0(t)$ (Fig. 1d). The monocomponent harmonic so calculated is subtracted from the original signal, and the above cycle of iterations is applied to the
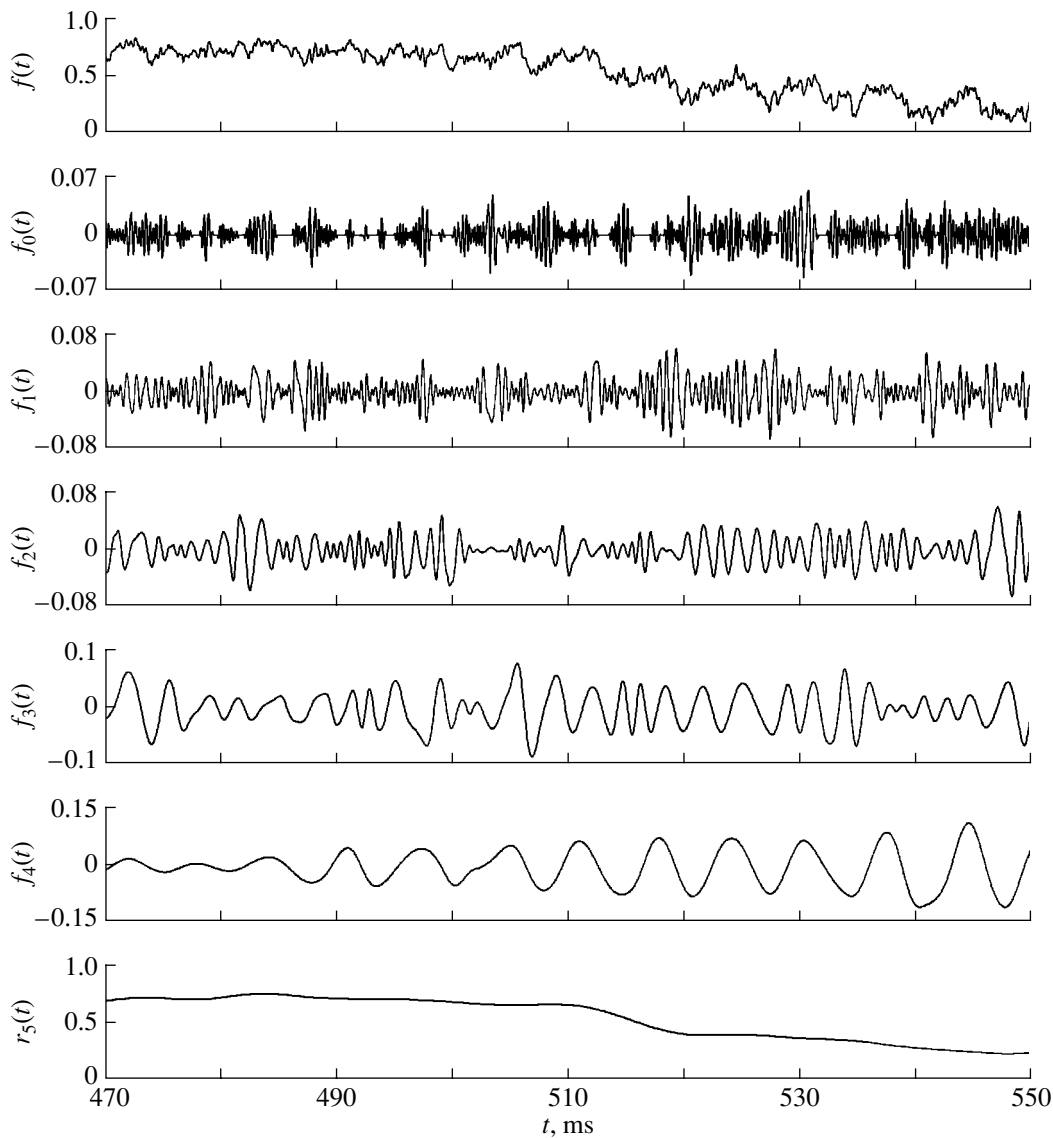
Fig. 2. Decomposition of the signal $f(t)$ showing the intensity of the deuterium D_β spectral line into a set of monocomponent harmonics $f_0(t) - f_4(t)$ and the global trend $r_5(t)$.

remainder $f(t) - f_0(t)$ to obtain the second monocomponent harmonic $f_1(t)$. This second harmonic and the first one are subtracted from the original signal and the above cycle of iterations is again applied to the remainder $f(t) - f_0(t) - f_1(t)$ to obtain the third monocomponent harmonic $f_2(t)$. This procedure is continued until the remainder becomes a global trend nonoscillating on the interval $[a, b]$ or satisfies the condition that the deviation of the mean $m(t)$ of the envelopes from zero be small. Hence, the EMD method decomposes the original function into the sum of monocomponent harmonics plus the remainder in the form of either a nonoscillating trend or a trend whose oscillation amplitude is less than a prescribed threshold value. As an example of how to apply the EMD algorithm, Fig. 2 shows the

decomposition of an experimental signal from a photomultiplier that recorded the evolution of the intensity of the D_β spectral line emitted from the T-10 plasma.

The EMD method can formally be described as the following, easily implemented, numerical algorithm for decomposing the function $f(t)$ with $t \in [a, b]$.

(i) Initialization: $i = 0$, $r_i(t) = f(t)$, $t \in [a, b]$.

(ii) Initialization: $j = 0$, $g_j(t) = r_i(t)$, $t \in [a, b]$.

(iii) Determination of the extremes of $g_i(t)$.

(iv) Calculation of the upper and lower envelopes $u_j(t)$ and $d_j(t)$ by spline interpolation using the extremes obtained.
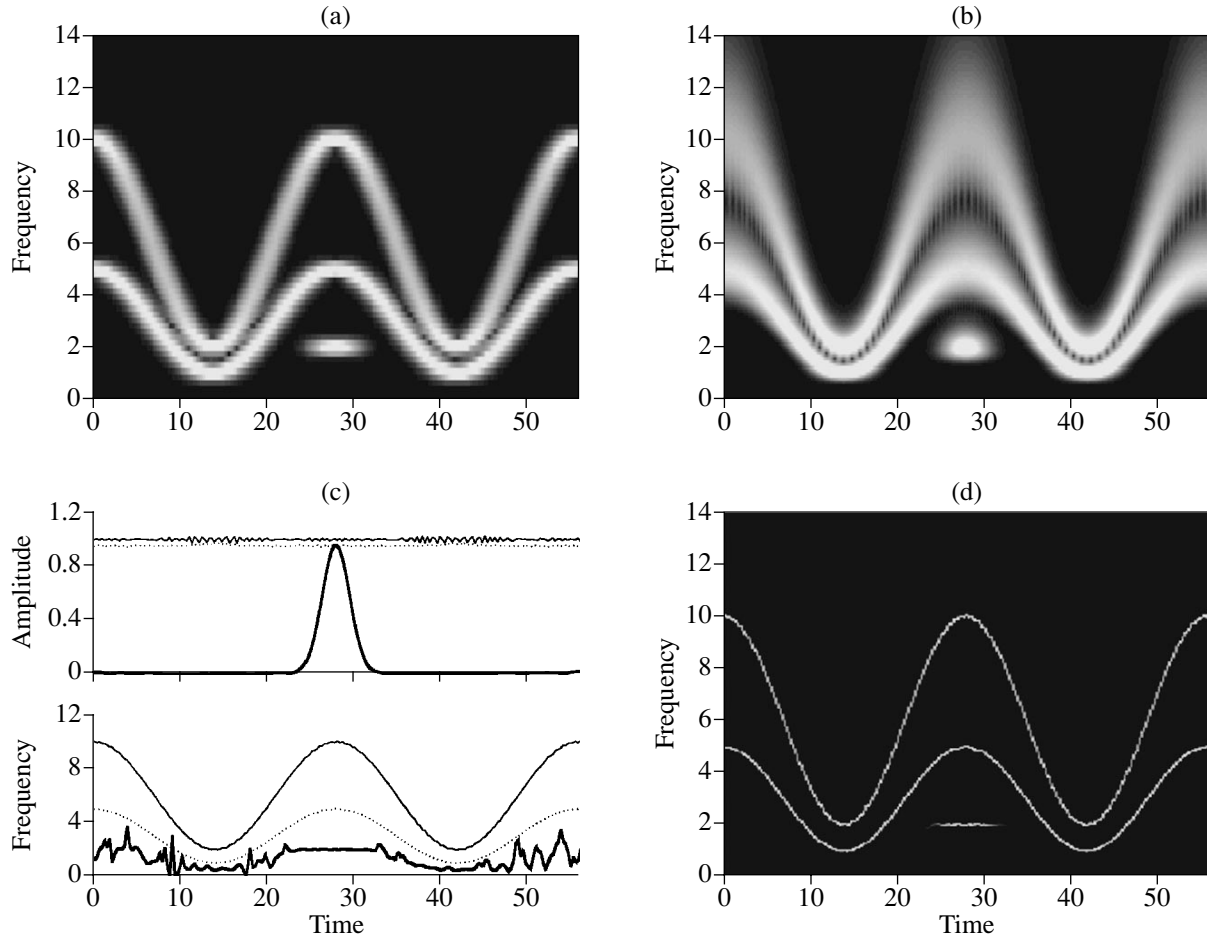
Fig. 3. Results from a temporal–frequency analysis of a test signal $x(t)$: (a) spectrogram; (b) scalogram; (c) time evolutions of the amplitudes and frequencies of the monocomponent harmonics calculated by the HHT algorithm (the first harmonic is shown by the light curves; the second, by the dotted curves; and the third, by the heavy curves); and (d) Hilbert spectrum.

(v) Calculation of the mean of the envelopes (the local trend): $m_j(t) = (u_j(t) + d_j(t))/2$.

(vi) Elimination of the local trend: $g_{j+1}(t) = g_j(t) - m_j(t)$.

(vii) Determination of whether or not $g_j(t)$ satisfies a *stopping criterion*. If not, the $j = j + 1$ iterate is taken and step (iii) is repeated.

(viii) Extraction of the monocomponent harmonic: $f_i(t) = g_j(t)$.

(ix) Elimination of the extracted harmonic: $r_{i+1}(t) = r_i(t) - f_i(t)$.

(x) If the oscillation amplitude $r_{i+1}(t)$ is above the threshold level, the $i = i + 1$ iterate is taken and step (ii) is repeated.

The algorithm yields the decomposition

$$f(t) = \sum_{i=0}^{n-1} f_i(t) + r_n(t), \qquad (1)$$

where the remainder $r_n(t)$ is the global trend of the function $f(t)$. The stopping criterion (in step (vii)) checks whether the function $g_j(t)$ is monocomponent; different authors have formulated it in different ways [7, 8, 11–13]. We are using here the criterion in the formulation by Flandrin *et al.* [13]: the function $g_j(t)$ is considered monocomponent if the inequality $g_j(t) < \delta_1$ is satisfied for 95% of the interpolation points in the interval $t \in [a, b]$ and the inequality $g_j(t) < \delta_2$ is satisfied for the remaining 5% of the points; the quantities $\delta_1 < \delta_2$ in these inequalities are specified in advance. If the function $g_j(t)$ satisfies this criterion, the harmonic $f_i(t) = g_j(t)$ is considered to be singled out. As a result, each function $f_i(t)$ in decomposition (1) is monocomponent and oscillates on its own characteristic time scale, which decreases as the number i of the function increases. The process of the calculation of the function is thus reduced to the elimination of the local trend corresponding to the time scale on which the function oscillates.
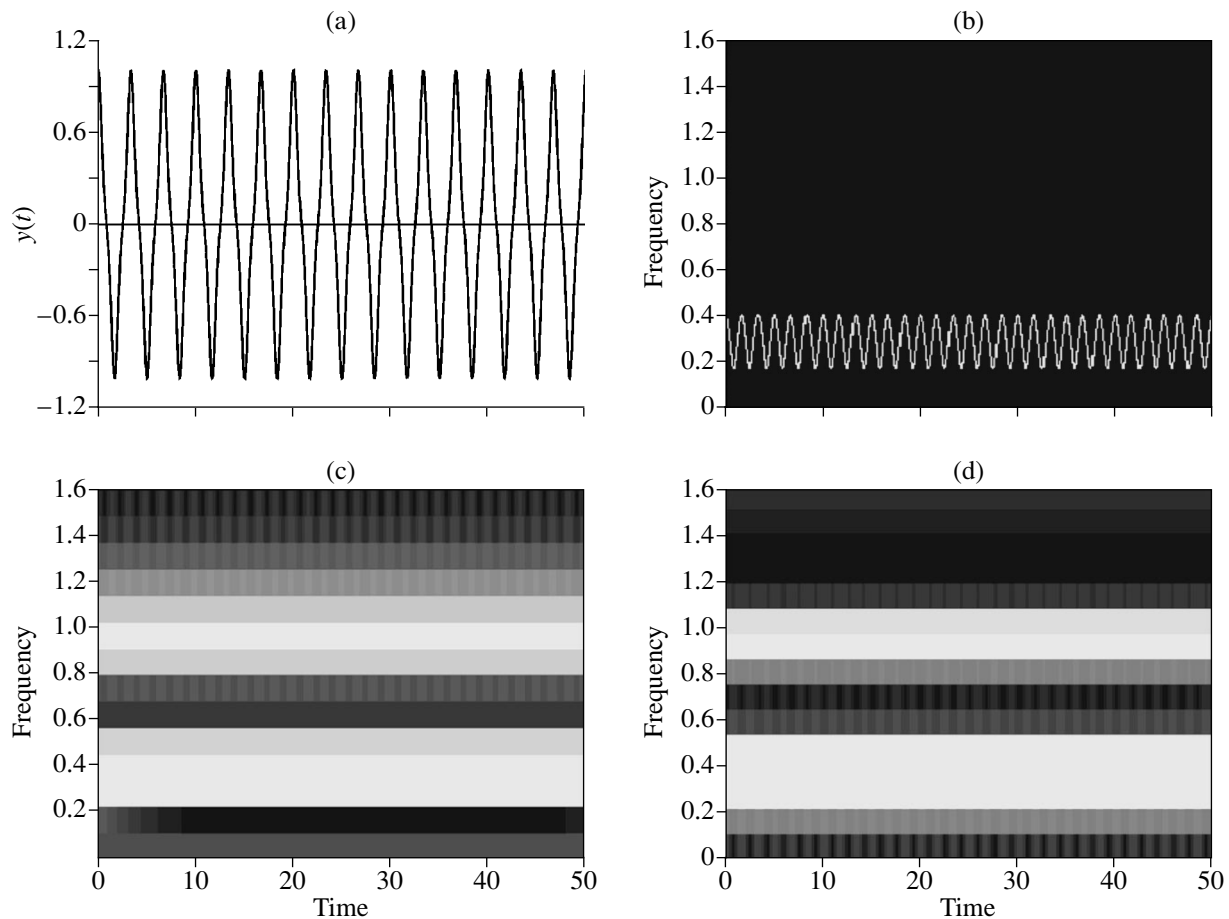
Fig. 4. (a) Original signal $y(t)$, (b) Hilbert spectrum, (c) spectrogram, and (d) scalogram.

A serious problem in the practical implementation of the EMD algorithm is that, in calculating the upper and lower envelopes by spline interpolation, the iteration procedure diverges in the end portions of the interval on which the oscillating function is defined. As the algorithm operates, these end portions expand more deeply into the interval, thereby distorting the shapes of the harmonics that are being singled out. For functions defined on short intervals, this can lead to a wrong result. This problem can be overcome in different ways, e.g., by smoothing the functions over the end portions of the interval or by extrapolating the functions beyond the interval in question by means of a mirror image reflection or by the method of neuronets [13–15]. In our case, the duration of the experimental signal substantially exceeded the time interval of interest to us. This is why we extended the interval by an amount of 5% in both directions, smoothed the signal over the end portions of the extended interval, and linearly extrapolated the functions at these portions when applying spline interpolation. As a result, each of the end portions in which the iteration procedure diverged did not exceed 5% of the entire extended interval. After the decomposition process was completed, the end portions by which the original time interval was extended were discarded, so the behavior of the functions on them did not affect the signal on the time interval of interest to us.

In comparing the EMD technique to spectral methods, it should be noted that, in the first case, the decomposition is carried out in the space of time realizations, whereas, in the second case, it is carried out in the space of spectral representations. In the EMD method, there is no need to utilize a predetermined set of basis functions for decomposition, whereas the spectral methods make use of harmonic functions as the basis for decomposition. Hence, the EMD method does not make any a priori assumptions regarding the shape of the oscillations of the individual harmonics, the only exception being a rather weak condition that the harmonics be monocomponent. In [7, 8], it was shown that the monocomponent harmonics yielded by the EMD method are mutually orthogonal with sufficient accuracy. This circumstance makes it possible to consider the EMD as a decomposition into the basis functions that are determined by the character of the signal itself; i.e., the basis for decomposition is in a sense adaptive.
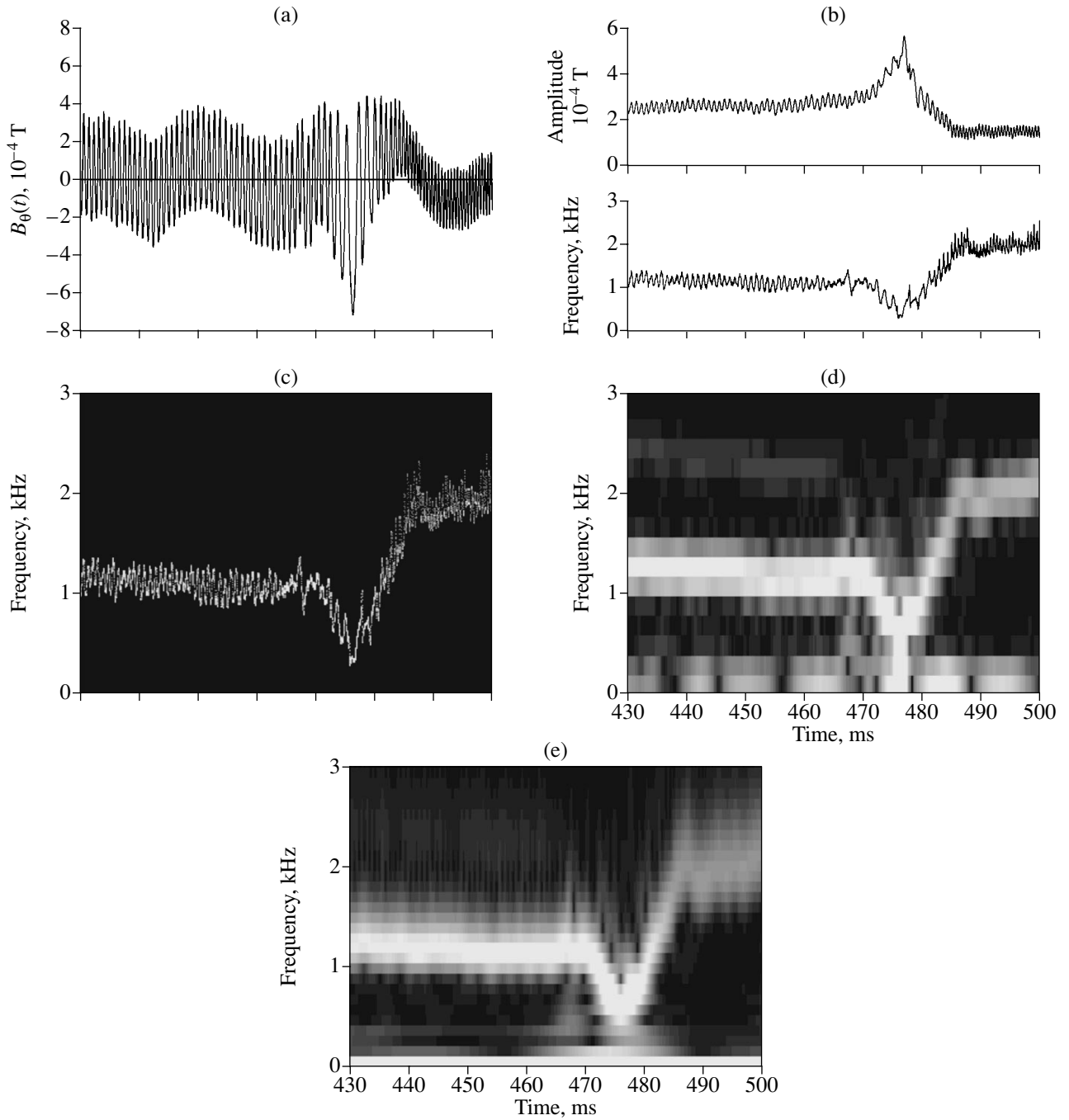
Fig. 5. Experimental data from T-10 shot no. 21576: (a) time evolution of the poloidal magnetic field perturbation $B_\theta(t)$; (b) time evolutions of the amplitude and frequency of the $m = 2$ spatial mode, calculated by the HHT method; (c) Hilbert spectrum; (d) spectrogram; and (e) scalogram.

For each of the harmonics $f_i(x)$, with the help of the Hilbert transform

$$H[x(t)] = v.p. \int_{-\infty}^{+\infty} \frac{x(\tau)}{\pi(t-\tau)} d\tau, \qquad (2)$$

it is possible to construct the analytic signal $z_i(t)$,

$$\hat{f}_i(t) = H[f_i(t)],$$
$$z_i(t) = f_i(t) + i\hat{f}_i(t), \qquad (3)$$
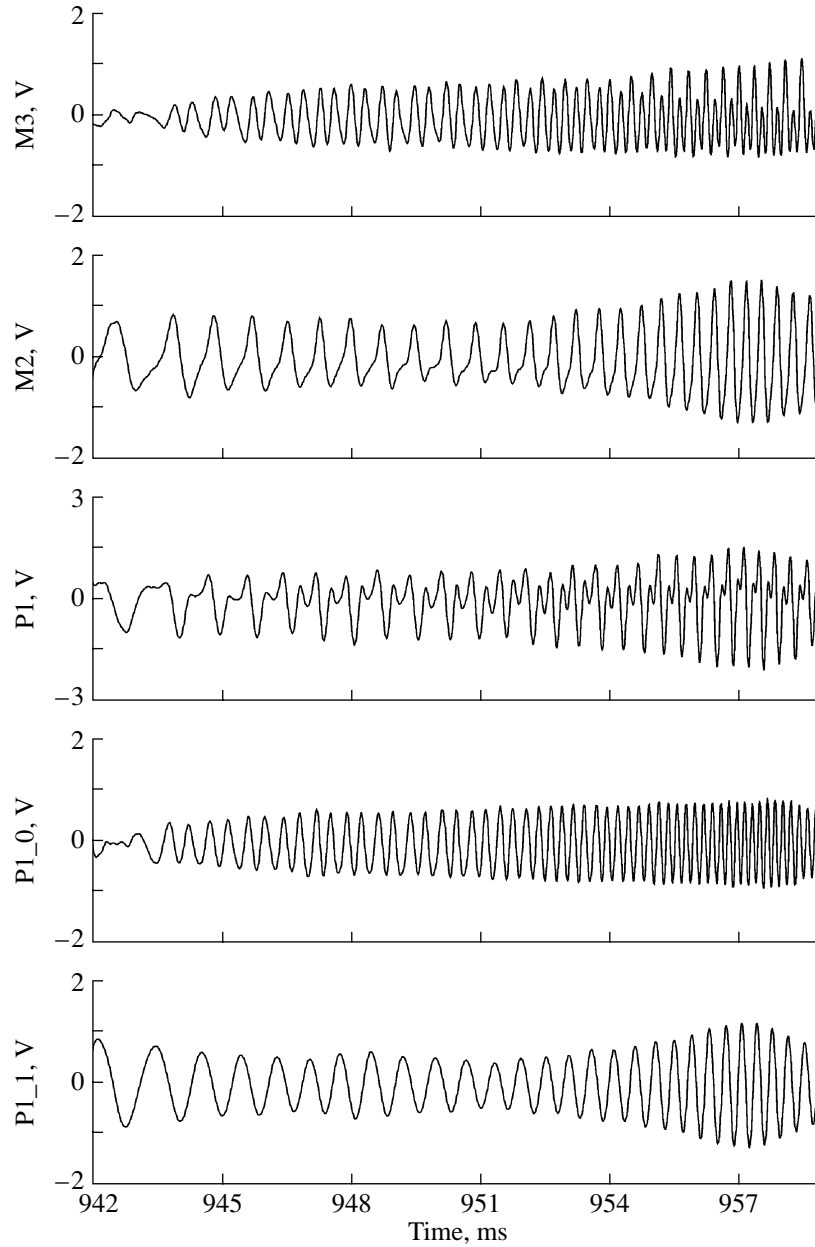
Fig. 6. Experimental data from T-10 shot no. 34 397: the experimental signals from the $m = 3$ (M3) and $m = 2$ (M2) spatial modes measured by a solitary probe P1 and the monocomponent harmonics P1_0 and P1_1 of the signal P1, which were singled out by the EMD method.

with uniquely defined amplitude $A_i(t)$, phase $\psi_i(t)$, and instantaneous frequency $\omega_i(t)$:

$$A_i(t) = |z_i(t)| = \sqrt{f_i^2(t) + \hat{f}_i^2(t)},$$

$$\psi_i(t) = \arg z_i(t) = \arctan\frac{\hat{f}_i(t)}{f_i(t)}, \tag{4}$$

$$\omega_i(t) = \frac{d\psi_i(t)}{dt} = \frac{f_i(t)\hat{f}_i'(t) - f_i'(t)\hat{f}_i(t)}{f_i^2(t) + \hat{f}_i^2(t)}.$$

With the resulting sets of $A_i(t)$ and $\omega_i(t)$, it is possible to construct the time–frequency distribution for the function $f(t)$, also known as the Hilbert spectrum $H(\omega, t) = \sum A_i(\omega_i, t)$.

Let us consider how the HHT method is used to analyze several different test signals. As an example, we examine a signal that is a superposition of two frequency-modulated sinusoidal components and one amplitude-modulated component (a Gaussian wave packet):

$$x(t) \;=\; \sin\!\left[2\pi\!\left(6t + \frac{5.6}{\pi}\sin\!\left(\frac{\pi t}{14}\right)\right)\right]$$

$$+ \sin\!\left[2\pi\!\left(3t + \frac{2.8}{\pi}\sin\!\left(\frac{\pi t}{14}\right)\right)\right] \qquad (5)$$

$$+ \exp(-0.2(t-28)^2)\sin(4\pi t).$$

Figures 3a and 3b present the spectrogram (the windowed Fourier transform) and scalogram (the wavelet transform in the frequency–time plane) of the signal $x(t)$, and Fig. 3c presents the results obtained by the HHT method, namely, the time evolutions of the amplitude and instantaneous frequency of the monocomponent harmonics of the signal $x(t)$.

The Hilbert spectrum displayed in Fig. 3d clearly shows that the HHT method makes it possible to remove the frequency–time uncertainty typical of the spectrogram and scalogram and to exactly depict the evolution of the frequencies and amplitudes of the harmonics of the test signal $x(t)$ in the time–frequency plane with a resolution limited only by the discrete representation of the signal.

In order to illustrate how the HHT method can be used to analyze a nonlinear oscillatory process, we choose a test function $y(t)$ describing a Stokes wave (Fig. 4a):

$$y(t) \;=\; \cos(0.6\pi t + 0.3\sin(1.2\pi t)). \qquad (6)$$

Figure 4b presents the frequency–time parameters of the signal $y(t)$ that were obtained using the HHT method. We clearly see the frequency modulation of the signal, which manifests itself in the anharmonicity of the oscillations (Fig. 4a). In contrast to the Hilbert spectrum, the spectrogram and scalogram (see Figs. 4c and 4d, respectively) do not reveal internal modulation, i.e., variation in the instantaneous frequency during the oscillation period, because of the limited frequency–time resolution; in this case, the nonlinearity manifests itself as the presence of an additional harmonic.

3. APPLICATION OF THE HHT METHOD TO THE EXPERIMENTAL DATA FROM MHD DIAGNOSTICS

The HHT method was used to analyze signals from the MHD diagnostic complex in investigating the dynamic behavior of large-scale MHD perturbations in the T-10 tokamak. The corresponding HHT algorithm was implemented as an individual program module and was integrated into the system for acquisition and analysis of MHD diagnostic data.

Let us consider examples of how the HHT method was applied in practice. Figure 5a displays the time evolution of the perturbed poloidal magnetic field $B_\theta(t)$ of the $m = 2$ unstable MHD mode. Figure 5b clearly demonstrates the behavior of the frequency and amplitude of the mode. Along with the general tendencies,
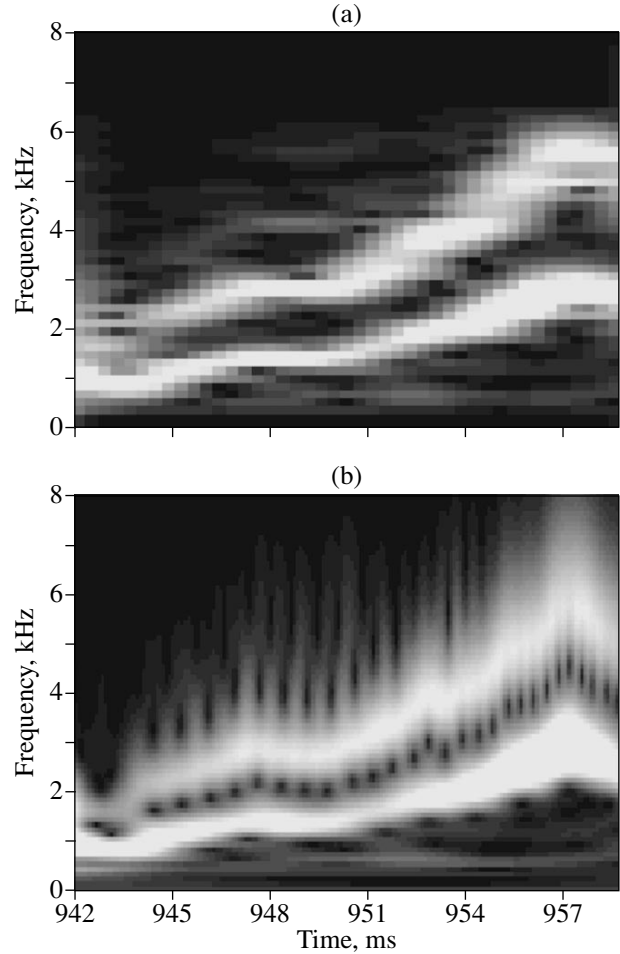
Fig. 7. (a) Spectrogram and (b) scalogram of the experimental signal P1.

we also see that there is internal modulation, which is caused by the nonuniformity of rotation of the magnetic island, as was previously shown in [9]. The spectrogram and scalogram presented in Figs. 5c and 5d reflect the global behavior of the frequency, but the nonuniform rotation of the perturbation manifests itself in the same manner as in the test signal, i.e., as the presence of the second harmonic.

Figure 6 illustrates an analysis of the MHD diagnostic signals from two MHD modes that develop simultaneously and exhibit different dynamic behavior. The figure displays the time evolutions of the M2 and M3 signals, corresponding to the $m = 2$ and $m = 3$ unstable MHD modes; the signal from a solitary magnetic probe P1, which recorded the total perturbation of the poloidal magnetic field at the place where it was positioned; and the monocomponent harmonics P1_0 and P1_1 of the signal P1, which were singled out by the EMD method. The data presented in Fig. 6 show good agreement between the results of the decomposition of the total perturbation of the poloidal magnetic field into the $m = 2$ and 3 MHD modes by the methods of spatial Fou-
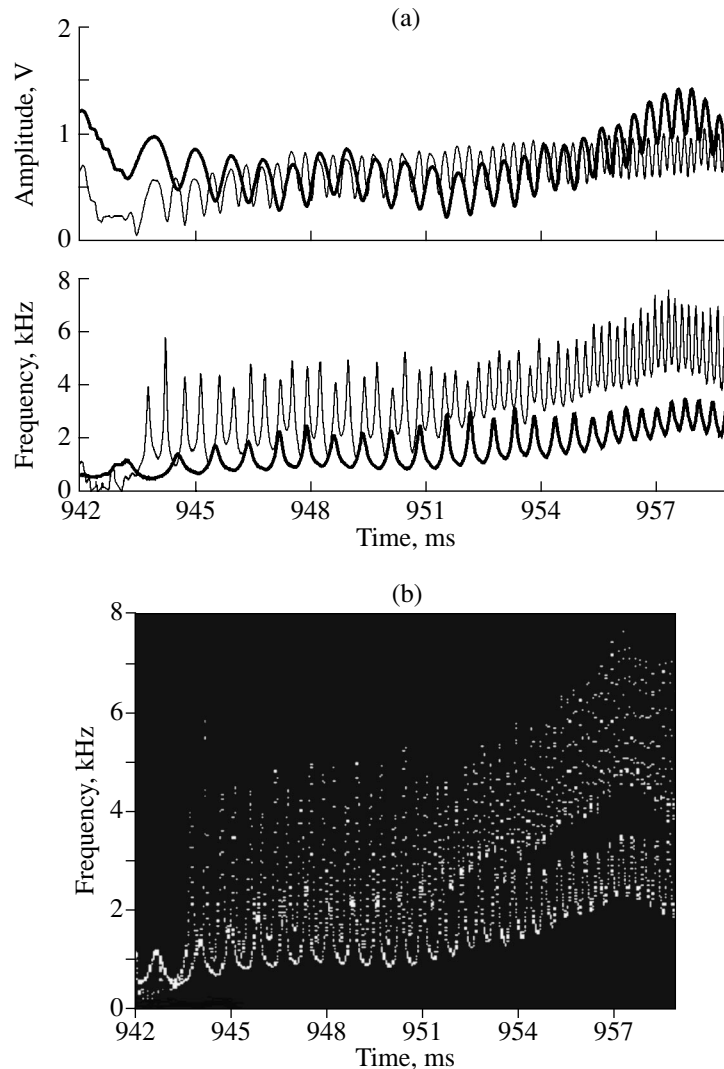
Fig. 8. (a) Time evolution of the amplitude and frequency of the monocomponent signals P1_0 (light curves) and P1_1 (heavy curves) and (b) Hilbert spectrum of the signals P1_0 and P1_1.

rier analysis and the results of the EMD method. The M3 signal and the monocomponent harmonic P1_0 related to it behave in essentially the same manner, as well as the M2 signal and the related P1_1 harmonic. The EMD algorithm first singles out the high-frequency harmonic of the signal P1, which corresponds to the field perturbation associated with the evolution of the $m = 3$ MHD mode, and, then, it singles out the signal harmonic associated with the $m = 2$ mode. This indicates that each monocomponent harmonic in the signal P1 corresponds to its own oscillatory process.

The spectrogram of the signal P1 in Fig. 7a shows the presence of two modes of MHD perturbations. It is, however, difficult to draw any conclusion about the nonuniformity of their rotation because the oscillation frequency of the poloidal magnetic field of the $m = 3$ mode is two times higher than that of the field of the $m = 2$ mode and the plot of the second harmonic of the

$m = 2$ mode oscillations in the frequency–time plane overlaps with that of the first harmonic of the $m = 3$ mode oscillations.

The wavelet transform in Fig. 7b also shows the presence of two oscillatory processes; moreover, the vertical strips in the transform provide qualitative evidence that the oscillations are frequency-modulated, which is a consequence of the nonuniform rotation of the MHD perturbations. For the experimental signals under analysis, the Hilbert–Huang transform (Fig. 8) makes it possible to separate out the oscillation modes and to expand the method that was previously used to investigate the characteristic dynamic properties of an individual tearing mode [10] to the case in which two unstable MHD modes exist simultaneously. It should be noted that time evolutions (see Fig. 8a) are easier to analyze quantitatively than a Hilbert spectrum (see Fig. 8b).

4. CONCLUSIONS

The HHT method raises the temporal–frequency analysis of the MHD diagnostic signals to a qualitatively new level. The HHT algorithm is free of restrictions on the frequency and time resolution, so it allows one to determine how the instantaneous frequency of the signal varies during the oscillation period and thereby to thoroughly investigate the fine structure of the spectral dynamics of unstable MHD perturbations. The HHT method can also be used to analyze the data from other diagnostics that measure unsteady oscillating signals.

ACKNOWLEDGMENTS

REFERENCES

1. L. Cohen, Proc. IEEE **77**, 72 (1989).

2. V. Dose, G. Venus, and H. Zohm, Phys. Plasmas **4**, 323 (1997).

3. A. C. A. Figueiredo and M. F. F. Nave, in *Proceedings of the 30th EPS Conference on Controlled Fusion and Plasma Physics, St. Petersburg, 2003*, Vol. 27A, Paper P-2.141.

4. D. E. Vakman and L. A. Vaĭnshteĭn, Usp. Fiz. Nauk **123**, 657 (1997) [Phys. Usp. **20**, 1002 (1997)].

5. E. D. Taylor, C. Cates, and M. E. Mauel, Rev. Sci. Instrum. **70**, 4545 (1999).

6. G. A. Navratil, C. Cates, and M. E. Mauel, Phys. Plasmas **5**, 1855 (1998).

7. N. E. Huang, Z. Shen, and S. Long, Proc. R. Soc. London, Ser. A **454**, 903 (1998); http://www.keck.ucsf.edu/~schenk.Huang_etal198.pdf.

8. N. E. Huang, Z. Shen, and R. S. Long, Annu. Rev. Fluid Mech. **31**, 417 (1999).

9. A. M. Kakurin and I. I. Orlovsky, Fiz. Plazmy **30**, 406 (2004) [Plasma Phys. Rep. **30**, 370 (2004)].

10. A. M. Kakurin and I. I. Orlovsky, Fiz. Plazmy **30**, 307 (2004) [Plasma Phys. Rep. **30**, 277 (2004)].

11. N. E. Huang, M.-L. C. Wu, and S. R. Long, Proc. R. Soc. London, Ser. A **459**, 1471 (2003).

12. S. T. Quek, P. S. Tua, and Q. Wang, Smart Mater. Struct. **12**, 447 (2003).

13. P. Flandrin, G. Rilling, and P. Goncalves, in *Proceedings of the IEEE–EURASIP Workshop on Nonlinear Signal and Image Processing, Grado-Gorizia, Italy, 2003*, Paper NSIP-03; http://perso.ens-lyon.fr/patrick.flandrin/NSIP03.pdf.

14. J. Zhao, High Technol. Lett. **8** (3), 40 (2002).

15. Y. Deng, W. Wang, and C. Qian, Chin. Sci. Bull. **46**, 954 (2001).

Translated by O.E. Khadin

================== MAGNETOSPHERIC ==================
PLASMA

Configuration of an Inviscid Plasma in the Field of a Rotating Magnetized Central Body

A. O. Soldatkin and Yu. V. Chugunov

Institute of Applied Physics, Russian Academy of Sciences, ul. Ul'yanova 46, Nizhni Novgorod, 603950 Russia
Received December 22, 2004; in final form, March 14, 2005

Abstract—The problem is considered of configurations of a strongly magnetized inviscid plasma around a rotating magnetized central body. Strong plasma magnetization implies that the Hall conductivity is much lower than the transverse conductivity, which in turn is much lower than the longitudinal conductivity. For such conditions, a self-consistent set of equations is derived that describes the conduction current density, the magnetic and electric fields, and the angular frequency of the plasma rotation under the assumptions that the components of the dielectric tensor of the plasma envelope are known functions of height and that the plasma mass velocity has only the azimuthal component. Under the assumption that the transverse conductivity is constant over a magnetic surface, the nonlinear equations derived are solved in quadratures within the class of angular frequency distributions that are symmetric about the equatorial plane. A particular solution for the plasma configurations in a dipole magnetic field is considered that corresponds to a model exponential dependence of the transverse conductivity on the number of the *L*-envelope (or, equivalently, on the number of the unperturbed magnetic surface). © 2005 Pleiades Publishing, Inc.

1. INTRODUCTION

At present, there is a wide variety of models of the Earth's plasmasphere and the plasmaspheres of other planets (see, e.g., [1]). Most of them were developed with the aim of systematizing the experimental data for different plasmasphere regions, and the physical quantities in them are described by analytic functions that were obtained by approximating these data mathematically [2]. The most important task of the models is to provide a quantitative description of plasmaspheric phenomena and an analysis of observations, theoretical investigation often being insufficiently comprehensive. In this context, it is relevant to construct such self-consistent models of the plasmaspheres of magnetized planets in which the main qualitative effects would be derived from first principles and the experimental data would serve as the basis for a quantitative description.

On the other hand, it should be noted that, when investigating the plasmaspheres, most attention is usually focused on the interaction of the plasma envelope with the solar wind [3]. At the same time, the dynamics of the plasmaspheric layers adjacent to the planet's surface is also fairly complicated [4] because it involves electrodynamic and magnetohydrodynamic phenomena, which should generally be described in a self-consistent manner.

The formulation and analysis even of a simplified model of the plasma envelope of a rotating magnetized central body run into significant difficulties. They are associated, first of all, with the nonlinear structure of equations, even in the simplest axisymmetric case, and with the necessity of accounting for the anisotropic conductivity of a viscous plasma in a magnetic and a gravitational fields. Of course, this task touches on a number of important problems in the physics of magnetohydrodynamic flows and plasma configurations in fields of different origin and, consequently, is significant not only for practical applications associated with the description of the planetary plasmaspheres but also from the standpoint of general physics.

In attempting to describe the Earth's plasmasphere self-consistently, Bespalov and Chugunov [5] considered an axisymmetric problem about the steady-state simultaneous rotation of a plasma envelope and a magnetized spherical body in the magnetohydrodynamic approximation. Under the assumption that the conductivity of an inviscid plasma is uniform and isotropic, they described plasma configurations rotating differentially in a dipole magnetic field. They found that the differential (nonrigid) nature of the envelope rotation plays a significant role in the dynamics of the system because it leads to the generation of conduction current at the expense of the unipolar induction effect [6]. For a rotating system, this effect was thoroughly considered in [7–11] using a non-self-consistent approach in which the electric potential and conduction current were calculated from the prescribed profiles of the plasma conductivity and of the angular rotation frequency of the plasma medium.

Papers [12–14] considered a generalization of the self-consistent problem of the plasma envelope to the case of a viscous plasma with a nonuniform and anisotropic conductivity. It was found that, in a wide range of the envelope parameters, perturbations in a differentially rotating layer whose thickness is determined by the magnetic and hydrodynamic viscosity are subject to

a dynamic skin effect. In the approximation used in [12–14], the magnetic field perturbations and conduction current vanish in an inviscid plasma flow. In this case, the higher order terms that can be omitted when viscosity is important should be taken into account in the corresponding equations. The objective of the present paper is to consider the characteristic features of the formation of an inviscid plasma envelope and the generation of magnetic field perturbations within it.

In what follows, we will study the problem of configurations of an inviscid plasma around a rotating magnetized central body under the assumption that the plasma is strongly magnetized, i.e., that the Hall conductivity is much lower than the transverse conductivity, which in turn is much lower than the longitudinal conductivity. This problem is important, e.g., for investigations of the planetary plasmaspheres at considerable heights, where the plasma is rare and is highly magnetized. In Section 2, we formulate the problem and derive a self-consistent set of equations describing a strongly magnetized inviscid plasma. In Section 3, using the assumption that the transverse conductivity is constant over a magnetic surface, we solve this set of nonlinear equations in quadratures to obtain a solution that has a certain symmetry property. In Section 4, we analyze a particular solution for plasma configurations in a dipole magnetic field.

2. FORMULATION OF THE PROBLEM

We consider a time-independent axisymmetric problem of the plasma motion around a rotating magnetized central body under the assumption that the plasma mass velocity $\mathbf{V}$ has only the azimuthal component. In spherical coordinates (r, Θ, φ), the plasma motion can be described in terms of the angular rotation frequency ω,

$$\mathbf{V} = (0, 0, \omega(r, \Theta)r\sin\Theta). \tag{1}$$

The parameters of the plasma envelope, as well as of the fields and currents, can be described by magnetohydrodynamic equations. For a uniform anisotropic plasma conductivity, the problem in question was thoroughly discussed in [12]. In [14], it was generalized to the case of a nonuniform plasma conductivity.

The magnetic field $\mathbf{B}$ can conveniently be described by the vector potential $\mathbf{A}$ in the Coulomb gauge,

$$\mathbf{B} = \nabla \times \mathbf{A}, \quad \nabla \cdot \mathbf{A} = 0.$$

Using Ohm's law for an anisotropic conducting moving medium [15],

$$\mathbf{j} = \Sigma\left(\mathbf{E} + \frac{1}{c}\mathbf{V} \times \mathbf{B}\right) \tag{2}$$

(where Σ is the conductivity tensor and c is the speed of light), we can algebraically obtain the following local expression for the electric field $\mathbf{E}$ in terms of the mag-

netic field, conduction current density $\mathbf{j}$, and mass velocity:

$$\mathbf{E} = \frac{\mathbf{j}}{\tilde{\sigma}_\perp} - \frac{1}{c}\mathbf{V} \times \mathbf{B} - \left(1 - \frac{\tilde{\sigma}_\perp}{\sigma_\parallel}\right)\frac{(\mathbf{j} \cdot \mathbf{B})}{\tilde{\sigma}_\perp B^2}\mathbf{B}$$
$$- \frac{\sigma_H}{\sigma_\perp \tilde{\sigma}_\perp}\frac{\mathbf{B} \times \mathbf{j}}{B}. \tag{3}$$

Here, $\sigma_\parallel, \sigma_\perp$, and σ_H are the longitudinal, transverse, and Hall conductivities, respectively, which are all assumed to be given functions of the coordinates. The quantity

$$\tilde{\sigma}_\perp = \sigma_\perp + \frac{\sigma_H^2}{\sigma_\perp}$$

is the effective Cowling conductivity.

In the steady-state axisymmetric problem, the azimuthal component of the electric field is equal to zero, which yields the following algebraic expression relating the azimuthal current density to the magnetic field and to the current density:

$$j_\varphi = \left(1 - \frac{\tilde{\sigma}_\perp}{\sigma_\parallel}\right)\frac{(\mathbf{j} \cdot \mathbf{B})}{B^2}B_\varphi + \frac{\sigma_H}{\sigma_\perp}\frac{(\mathbf{B} \times \mathbf{j})_\varphi}{B}. \tag{4}$$

In the model of a viscous medium that was considered in [12–14], the second term on the right-hand side of relationship (4) was treated as the main one and the first term was ignored under conditions in which the Hall conductivity predominates over the transverse conductivity. In contrast, in the inviscid plasma flow under examination here, the second term vanishes and the azimuthal component j_φ of the current density is a second-order quantity in the azimuthal magnetic field component B_φ.

Another important fact is that, in the models considered in [12–14], the difference between the electric field and the unipolar field

$$\mathbf{E}^d = -\frac{1}{c}\mathbf{V} \times \mathbf{B} \tag{5}$$

was treated as being insignificant in writing the equations for the angular rotation frequency of the medium and its density. The situation with an inviscid medium is different: for a nonuniform effective Cowling conductivity, this difference can govern the profiles of the angular rotation frequency ω, the conduction current density, and the magnetic field perturbations.

The basic set of equations that was presented in [14] describes the electric and magnetic fields, the conduction current density, and the angular rotation frequency of the medium and its density in the plasma envelope. For an inviscid medium, however, this set can be simplified. In fact, let us assume that the conductivity tensor components satisfy the conditions

$$\sigma_H \ll \sigma_\perp \ll \sigma_\parallel, \tag{6}$$

which imply that the medium is strongly magnetized.

In this way, it is convenient to switch from the vector potential component A_φ to the quantity Φ, which has the meaning of the magnetic flux through a part of a sphere of radius r within the angular intervals from 0 to Θ, and to introduce the quantity I, which is proportional to the total current through the same part of the sphere:

$$\Phi = 2\pi r \sin\Theta \cdot A_\varphi, \quad I = 2r \sin\Theta \cdot B_\varphi.$$

In what follows, we will work in dimensionless variables $f = f^{\text{DIMENSIONAL}}/f_0$. The corresponding normalizing factors are the radius r_0 of the spherical body, the angular rotation frequency of the body ω_0, and the magnetic field strength $B_0 = |B(R, 0)|$ at the pole of the body. The remaining normalizing factors are expressed in terms of the factors just introduced: $\Phi_0 = \pi r_0^2 B_0$, $I_0 = r_0 B_0$, $j_0 = cB_0/4r_0$, and $E_0 = \omega_0 r_0 B_0/c$.

In these dimensionless variables, we have

$$j_\varphi = -\frac{1}{2\pi}\hat{\Lambda}\left(\frac{\Phi}{r\sin\Theta}\right), \tag{7}$$

where $\hat{\Lambda} = \dfrac{\partial^2}{\partial r^2}r + \dfrac{1}{r}\dfrac{\partial}{\partial\Theta}\dfrac{1}{\sin\Theta}\dfrac{\partial}{\partial\Theta}\sin\Theta$ is a second-order differential operator. Under the above assumptions, the azimuthal component of the Navier–Stokes equation for a plasma medium yields (see [14])

$$I = \hat{I}(\Phi). \tag{8}$$

We thus see that the quantity I is an arbitrary function of the magnetic flux Φ. Relationship (8) implies, in particular, that the lines of the meridional component of the conduction current density coincide with the lines of the meridional component of the magnetic field. In this case, the azimuthal component of the Ampère's force should be equal to zero in order to ensure that the plasma can be steady, because there are no other azimuthal forces that act on an inviscid plasma moving only in the azimuthal direction. Note that the approach used here has much in common with the method based on the Grad–Shafranov equation [16] and can be regarded as a generalization of this method to the case of a strongly anisotropic plasma (in a geometry with the corresponding symmetries).

With relationship (8), algebraic relationship (4) can be substantially simplified. Under conditions (6), it takes the form

$$j_\varphi = \frac{1}{2\pi}\frac{\hat{I}}{r\sin\Theta}\frac{\partial\hat{I}}{\partial\Phi}(1+Y),$$

$$Y = \left(1 - \frac{\tilde{\sigma}_\perp}{\sigma_\|}\right)\frac{\hat{I}^2}{\left(\dfrac{\partial\Phi}{\partial r}\right)^2 + \dfrac{1}{r^2}\left(\dfrac{\partial\Phi}{\partial\Theta}\right)^2} - \frac{\tilde{\sigma}_\perp}{\sigma_\|}. \tag{9}$$

We assume that the plasma envelope only slightly distorts the magnetic self-field of the central body, so that

$$I \ll 1. \tag{10}$$

Taking into account conditions (6), we see that the quantity Y is small in comparison to unity and is on the order of the larger of the two quantities—the quantity I^2 and the ratio $\tilde{\sigma}_\perp/\sigma_\|$.

Conditions (6) and (10) enable us to combine Eq. (3) and the equation $\nabla \times \mathbf{B} = 4\pi\mathbf{j}/c$ into the following dimensionless equation (this point was discussed in [14]):

$$Re_M\frac{\partial(\omega, \Phi)}{\partial(r, \Theta)} = \frac{\pi Y}{\sin\Theta}\left\{\frac{\partial^2\hat{I}}{\partial\Phi^2}\left(\left(\frac{\partial\Phi}{\partial r}\right)^2 + \frac{1}{r^2}\left(\frac{\partial\Phi}{\partial\Theta}\right)^2\right)\right.$$
$$\left. - \frac{1}{Re_M}\frac{\partial\hat{I}}{\partial\Phi}\left(\frac{\partial Re_M}{\partial r}\frac{\partial\Phi}{\partial r} + \frac{1}{r^2}\frac{\partial Re_M}{\partial\Theta}\frac{\partial\Phi}{\partial\Theta}\right)\right\}, \tag{11}$$

where $\dfrac{\partial(U, V)}{\partial(r, \Theta)} = \dfrac{\partial U}{\partial r}\dfrac{\partial V}{\partial\Theta} - \dfrac{\partial U}{\partial\Theta}\dfrac{\partial V}{\partial r}$ is the Jacobian and

$$Re_M(r) = 4\pi\frac{\omega_0 r_0^2}{c^2}\tilde{\sigma}_\perp(r) \tag{12}$$

is the radius-dependent magnetic Reynolds number, proportional to the effective Cowling conductivity $\tilde{\sigma}_\perp(r)$.

The above equations should generally be supplemented with the equation of motion in the meridional plane, the equation of state, and the heat balance equation. These three equations determine the density, pressure, and temperature of the plasma. However, in the model proposed here, these plasma parameters are not considered because they do not enter into the equations for the electrodynamic quantities. The components of the conductivity tensor are assumed to be known functions of the coordinates and to be related to an actual plasma density distribution, which is not discussed here. Of course, it is clear that, in a fully self-consistent theory, the conductivity tensor should not be considered to be given but instead should be described self-consistently with allowance for the processes of ion production and ion recombination. If, however, the profiles of the conductivity tensor components form independently of the phenomena that are accounted for in the model, this drawback of the theory seems to be insignificant.

The above set of four equations (7)–(9) and (11) describes four unknown functions j_φ, I, Φ, and ω, because the meridional components of the magnetic field and conduction current are obtained by differentiating the functions I and Φ, respectively, and the electric field is given by expression (3). Hence, this is a closed set of equations for describing the magnetic and electric fields, the conduction current, and the angular rotation frequency of the medium under the conditions adopted here.

3. CLASS OF SOLUTIONS TO THE NONLINEAR EQUATIONS IN THE CASE OF CONSTANT TRANSVERSE CONDUCTIVITY OVER A MAGNETIC SURFACE

The above set of equations contains an arbitrary function $\hat{I}(\Phi)$ of the magnetic flux and function (12), which is assumed to be given. Under conditions (6), the Cowling conductivity is approximately equal to the transverse conductivity.

The fundamental difficulty in solving the set of equations is associated with Eq. (11). It is easy to see, however, that the right-hand side of this equation is a small quantity of the third or higher order in I. It is then clear that, under the conditions adopted here, the angular rotation frequency is approximately constant over a magnetic surface. As follows from Eq. (11), the small deviations of the angular rotation frequency from the distribution $\omega = \omega(\Phi)$ are important in determining the azimuthal component of the magnetic field.

In analyzing the set of equations, the key question is how to specify the function $\sigma_\perp(r, \Theta)$. As a simple example, we consider the case in which the magnetic Reynolds number, like the quantity I, is a function of only Φ,

$$Re_M = Re_M(\Phi), \qquad (13)$$

or, in other words, the transverse conductivity is constant along a magnetic field line. In our opinion, the assumption that the plasma density (and, accordingly, the magnetic Reynolds number) is a function of the magnetic surface seems to be quite realistic, in particular, because it is consistent with the experimental data on the inner plasmaspheres of the Earth and Jupiter. For instance, in terrestrial conditions, the plasma density varies insignificantly (as a power of the number of the L-envelope—the coordinate of the magnetic surfaces that is expressed in Earth radii and is measured from the Earth's center in the magnetic equatorial plane) within the volume enclosed by a certain L-envelope (up to $L \sim 5, 6$) and decreases abruptly at greater heights. It is also clear that, under conditions in which the longitudinal conductivity plays a dominant role, the direction along a magnetic field line is a preferential direction. This justifies the assumption that the magnetic Reynolds number is a function of Φ.

In the expression for Y, we can omit the ratio $\tilde{\sigma}_\perp/\sigma_\parallel$, assuming that it is small in comparison to $\hat{I}^2$. As a result, under conditions (6), we arrive, instead of Eq. (11), at the equation

$$Re_M \frac{\partial(\omega, \Phi)}{\partial(r, \Theta)} = \frac{\pi \hat{I}^2}{\sin\Theta}\left\{\frac{\partial^2 \hat{I}}{\partial \Phi^2} - \frac{\partial \hat{I}}{\partial \Phi}\frac{1}{Re_M}\frac{\partial Re_M}{\partial \Phi}\right\}, \quad (14)$$

which can conveniently be rewritten as

$$\frac{\partial(\omega, \Phi)}{\partial(r, \Theta)} = \frac{X(\Phi)}{\sin\Theta},$$

$$X(\Phi) = \frac{\pi \hat{I}^2}{Re_M}\left\{\frac{\partial^2 \hat{I}}{\partial \Phi^2} - \frac{\partial \hat{I}}{\partial \Phi}\frac{1}{Re_M}\frac{\partial Re_M}{\partial \Phi}\right\}.$$

If the function X, which depends on the magnetic flux Φ, has a nonzero component symmetric with respect to the $\Theta = \pi/2$ plane, then the solution ω contains a nonzero antisymmetric part. For instance, for a dipole magnetic field and for a function $\Phi = \Phi_H$, the solution to Eq. (14) has the form

$$\omega = \cos\Theta\frac{X(\Phi_H)}{\Phi_H^2} + Z(\Phi_H), \qquad (15)$$

where Z is an arbitrary function.

We restrict ourselves to considering only the functions of Φ that are symmetric with respect to the $\Theta = \pi/2$ plane. In this case, if only symmetric distributions of ω are of interest to us, then it is necessary to set $X = 0$. This condition relates the function $\hat{I}(\Phi)$, which was assumed to be arbitrary up to this point, to the magnetic Reynolds number $Re_M(\Phi)$,

$$\frac{\partial^2 \hat{I}}{\partial \Phi^2} - \frac{\partial \hat{I}}{\partial \Phi}\frac{1}{Re_M}\frac{\partial Re_M}{\partial \Phi} = 0,$$

i.e., we have

$$\hat{I} = C_0 \int_{\Phi_0}^{\Phi} Re_M(x)dx, \qquad (16)$$

where C_0 is a constant of integration. In this case, the angular rotation frequency of the envelope is equal to

$$\omega = \hat{\omega}(\Phi), \qquad (17)$$

where $\hat{\omega}$ is an arbitrary function.

Hence, for a class of solutions ω that are symmetric with respect to the $\Theta = \pi/2$ plane, the function $\hat{I}(\Phi)$ is naturally determined by expression (16) and the angular rotation frequency, too, is a function of the magnetic flux. The physical meaning of the resulting solution (17) is that the angular rotation frequency of the medium is constant along a magnetic field line and the rotation of the medium along one magnetic surface is independent of the rotations along the other magnetic surfaces. In this respect, the problem based on the above set of equations differs substantially from the problems considered in [12–14], in which the viscous interaction between the layers in the plasma envelope was fundamentally important for the generation of the electric current and magnetic field perturbations.

Expressions (9), (16), and (17) describe, respectively, the azimuthal component of the conduction current, the conduction current I, and the angular rotation
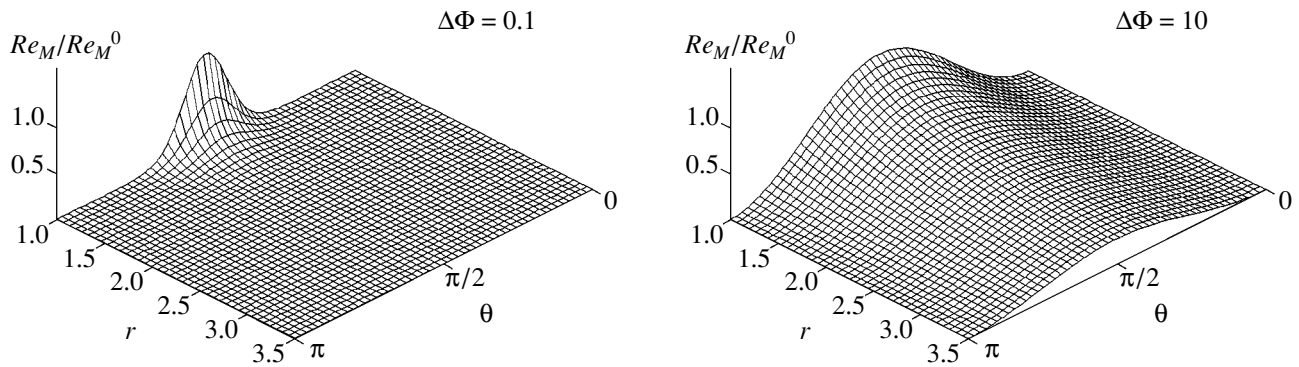
Fig. 1. Normalized model distributions of the magnetic Reynolds number for $\Delta\Phi = 0.1$ and 10.

frequency in terms of the given function (13) and the function Φ, which is to be determined from Eq. (7). Under the above assumptions, this equation can be rewritten as

$$\frac{\partial^2\Phi}{\partial r^2} + \frac{\sin\Theta}{r^2}\frac{\partial}{\partial\Theta}\frac{1}{\sin\Theta}\frac{\partial\Phi}{\partial\Theta}$$
$$= I^0 Re_M(\Phi)\int_{\Phi^0}^{\Phi} Re_M(x)dx, \qquad (18)$$

where Φ^0 is a constant of integration. Equation (18) is in fact analogous to the Grad–Shafranov equation. Hence, under the assumption that the transverse conductivity is constant over a magnetic surface, the problem of finding the sought-for class of solutions to the above set of nonlinear equations is reduced to that of solving partial differential equation (18) with the known right-hand side.

4. PARTICULAR SOLUTION

Now, we apply the approach used in [12–14] and assume that the magnetic flux Φ is the sum of the unperturbed flux Φ_H, associated with the magnetic self-field of a spherical body, and a small perturbation Φ_1, which is to be determined,

$$\Phi = \Phi_H + \Phi_1,$$

where $\hat\Lambda\left(\dfrac{\Phi_H}{r\sin\Theta}\right) = 0$, $|\Phi_1| \ll |\Phi_H|$, $\left|\dfrac{\partial\Phi_1}{\partial r}\right| \ll \left|\dfrac{\partial\Phi_H}{\partial r}\right|$,

and $\left|\dfrac{\partial\Phi_1}{\partial\Theta}\right| \ll \left|\dfrac{\partial\Phi_H}{\partial\Theta}\right|$.

The validity of the above linearization procedure, as well as of the above simplifying assumptions, is checked simply by substituting the solution obtained into the basic set of equations.

We specify dependence (13) by choosing it in a simple form suitable for solving the problem,

$$Re_M = Re_M^0 \frac{\exp\left(-\dfrac{\Phi_H}{\Delta\Phi}\right) - 1}{\exp\left(\dfrac{1}{\Delta\Phi}\right) - 1}, \qquad (19)$$

where

$$\Delta\Phi > 0. \qquad (20)$$

In this case, the following boundary condition is satisfied:

$$Re_M \xrightarrow[\Phi\to 0]{} = 0.$$

It is clear that it is sufficient to consider solely the values $\Phi_H > -1$, because the values $\Phi_H < -1$ are reached only inside the spherical body (at $r < 0$), and that the value $Re_M^0 = Re_M(-1)$ should be regarded as positive. The parameter $\Delta\Phi$ determines the spatial scale on which the distribution Re_M and, accordingly, the complete solution are localized in the radial and polar directions simultaneously. The change in a model distribution of the magnetic Reynolds number with increasing $\Delta\Phi$ is illustrated in Fig. 1, in which the distributions are plotted for two opposite cases: $1 \gg \Delta\Phi = 0.1$ and $1 \ll \Delta\Phi = 10$.

With allowance for the condition

$$I \xrightarrow[\Phi_H\to 0]{} = 0$$

we find from expression (16) the conduction current I:

$$I = I^0 \frac{\exp\left(-\dfrac{\Phi_H}{\Delta\Phi}\right) + \dfrac{\Phi_H}{\Delta\Phi} - 1}{\exp\left(\dfrac{1}{\Delta\Phi}\right) - \dfrac{1}{\Delta\Phi} - 1}. \qquad (21)$$
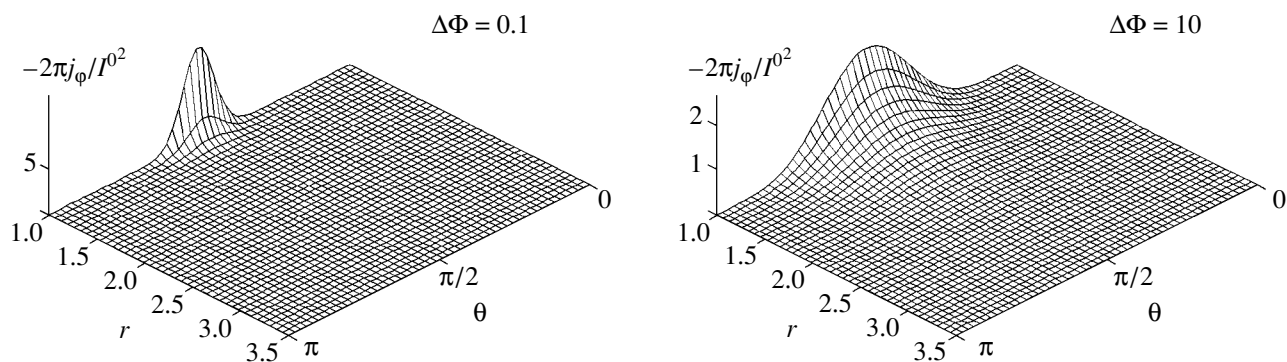
Fig. 2. Distributions of the azimuthal component of the current density that correspond to the model distributions of Re_M for $\Delta\Phi = 0.1$ and 10.

The azimuthal component of the conduction current density can be found from expression (9):

$$j_\varphi = -\frac{1}{2\pi r \sin\Theta} \frac{I^{0^2}}{\Delta\Phi}$$

$$\times \frac{\left(\exp\left(-\frac{\Phi_H}{\Delta\Phi}\right) + \frac{\Phi_H}{\Delta\Phi} - 1\right)\left(\exp\left(-\frac{\Phi_H}{\Delta\Phi}\right) - 1\right)}{\left(\exp\left(\frac{1}{\Delta\Phi}\right) - \frac{1}{\Delta\Phi} - 1\right)^2}, \quad (22)$$

the radial and meridional components being

$$j_r = -\frac{\cos\Theta}{\pi r^3}\frac{\partial I}{\partial \Phi_H}, \quad j_\Theta = -\frac{\sin\Theta}{2\pi r^3}\frac{\partial I}{\partial \Phi_H}. \quad (23)$$

The lines of the meridional component of the conduction current density coincide with the lines of the unperturbed dipole magnetic field; i.e., the conduction current always flows over a magnetic surface.[1] The value of the conduction current density at each of the magnetic surfaces is determined by the function $\partial I/\partial\Phi_H$, which is proportional to Re_M. Note that, according to condition (20), the meridional current flows along the magnetic field lines in a direction opposite to that of the magnetic field. A comparison between expressions (9) and (23) shows that the azimuthal current is much lower than the meridional current: the absolute value of the meridional current density, $(j_r^2 + j_\Theta^2)^{1/2}$, is a first-order quantity in the parameter I, whereas the azimuthal current density j_φ is a second-order quantity in this parameter.

The azimuthal current density is negative, which indicates that the azimuthal current flows in a direction opposite to that of the plasma motion. The distributions of the azimuthal current density for $1 \gg \Delta\Phi = 0.1$ and $1 \ll \Delta\Phi = 10$ are shown in Fig. 2.

---

[1] It is assumed that the current loops in the envelope are closed in its lower layers, which are characterized by a sufficiently high quasi-isotropic conduction.

For

$$r\Delta\Phi \ll 1, \quad (24)$$

we obtain the following estimate of the half-width of the interval of the angles Θ that corresponds to the current jet:

$$\alpha_\varphi = \sqrt{\frac{r\Delta\Phi}{4}}, \quad (25)$$

the scale on which the azimuthal current density j_φ varies in the radial direction being estimated by

$$\Delta r_\varphi = \frac{\Delta\Phi r^2}{2\sin^2\Theta}. \quad (26)$$

These two estimates were obtained under the assumption that condition (24) is satisfied for the r values under consideration. Estimates (25) and (26) imply that, when the parameter $\Delta\Phi$ is sufficiently small, the corresponding solution is strongly localized near the circle $\{r = 1, \Theta = \pi/2\}$.

The total current in the jet,

$$J_\varphi^{sum} = \int_0^\infty r\,dr \int_0^\pi j_\varphi\,d\Theta, \quad (27)$$

can be obtained by numerically integrating expression (22) for the azimuthal current density. For instance, for the two cases under discussion, we have $J_\varphi^{sum}(\Delta F = 0.1) \approx 0.037 I^{0^2}$, and $J_\varphi^{sum}(\Delta F = 10) \approx 0.16 I^{0^2}$.

The distribution of the azimuthal component of the magnetic field, $B_\varphi = I/(2r\sin\Theta)$, is symmetric with respect to the equatorial plane. It is clear that this distribution is topologically equivalent to distributions (19) and (17).

Above, we have considered a steady solution to the problem. The question of the stability of the solution is very complicated and is not discussed here. However, there are some experimental and theoretical arguments supporting the conclusion that such axisymmetric flows can indeed occur in nature. First, note that, although the axis of the Earth's magnetic field deviates from the vec-

tor of the angular velocity of the Earth's rotation (this deviation manifests itself as periodic perturbations in the plasma envelope), the structure of the plasmasphere does not change, thereby providing evidence of its stability. The second argument is that any perturbation distorts the electric field and causes it to deviate from being equilibrium. This process is accompanied by the corresponding redistribution of charges. However, since the system under consideration is dissipative, it should be subject to relaxation processes on characteristic time scales on the order of $1/4\pi\sigma$, where σ is the effective conductivity. This is why the perturbed charge density should relax to an equilibrium distribution. Finally, that magnetohydrodynamic flows similar to those considered above can be stable follows from the experimental investigations of pinches [17].

5. CONCLUSIONS

The problem of configurations of an inviscid plasma in the field of a rotating magnetized spherical body has been formulated in the strongly anisotropic conductivity approximation, $\sigma_H \ll \sigma_\perp \ll \sigma_\parallel$. For such conditions, the corresponding simple set of equations has been derived under the assumption that the transverse conductivity is constant along a magnetic field line and a class of solutions to these nonlinear equations has been found by solving them in quadratures. We have considered a model dependence of the transverse conductivity on the magnetic flux Φ. For this dependence, which was chosen satisfy the natural boundary conditions, the distributions of the conduction current and dipole magnetic field perturbations have been obtained under the assumption that the magnetic self-field of the central body is only slightly distorted by the plasma envelope.

It has been shown that, in the geometry chosen to solve the problem, the angular rotation frequency of an inviscid plasma is an arbitrary function of the magnetic flux Φ, so that the electrodynamic quantities are independent of the angular rotation frequency, provided that it is constant along the magnetic field.

In the geometry chosen to describe an inviscid plasma flow such that the plasma mass velocity has only the azimuthal component, the conduction current flows over a magnetic surface. In this case, the azimuthal component of the conduction current density is a second-order quantity in the azimuthal component B_φ of the perturbed magnetic field of the central body, in contrast to the case of a viscous plasma medium, in which it is a first-order quantity in B_φ and is proportional to the Hall conductivity.

Under conditions of strongly anisotropic conductivity of an inviscid medium such that the longitudinal conductivity is very high, the form of the solution is determined by the geometry of the unperturbed magnetic field of the central body: the transverse conductivity, the angular rotation frequency, and the quantity $I = 2B_\varphi r \sin\Theta$ are constant over a magnetic surface and the

conduction current flows over it. In the case of a dipole magnetic field, the solution varies in accordance with the number of the magnetic surface, i.e., it is localized in the radial and polar directions simultaneously.

REFERENCES

1. G. Ganguli, M. A. Reynolds, and M. W. Liemohn, J. Atmos. Sol.–Terr. Phys. **62**, 1647 (2000).
2. D. L. Gallagher, P. D. Craven, and R. H. Comfort, J. Geophys. Res. **105**, 18 819 (2000).
3. Y. Kamide, J. Atmos. Sol.-Terr. Phys. **62**, 1659 (2000).
4. *Physics of the Earth's Upper Atmosphere*, Ed. by C. O. Hines, I. Paghis, T. R. Hartz, and J. A. Fejer (Prentice-Hall, Englewood Cliffs, NJ, 1965; Gidrometizdat, Leningrad, 1971).
5. P. A. Bespalov and Yu. V. Chugunov, Planet. Space Sci. **32**, 365 (1984).
6. I. E. Tamm, *The Principles of Electricity Theory* (Nauka, Moscow, 1989) [in Russian].
7. P. A. Bespalov, Yu. V. Chugunov, and S. S. Davydenko, J. Atmos. Terr. Phys. **58**, 605 (1996).
8. P. A. Bespalov, Yu. V. Chugunov, and S. S. Davydenko, J. Atmos. Electr. **16** (2), 69 (1996).
9. D. E. Malov and Yu. V. Chugunov, Izv. Vyssh. Uchebn. Zaved., Radiofiz. **40**, 232 (1997).
10. A. O. Soldatkin and Yu. V. Chugunov, Izv. Vyssh. Uchebn. Zaved., Radiofiz. **44**, 778 (2001).
11. A. O. Soldatkin and Yu. V. Chugunov, J. Atmos. Sol.–Terr. Phys. **65**, 821 (2003).
12. A. O. Soldatkin and Yu. V. Chugunov, Fiz. Plazmy **29**, 72 (2003) [Plasma Phys. Rep. **29**, 65 (2003)].
13. A. O. Soldatkin and Yu. V. Chugunov, Adv. Space Res. **31**, 1407 (2003).
14. A. O. Soldatkin and Yu. V. Chugunov, Izv. Vyssh. Uchebn. Zaved., Radiofiz. **47**, 181 (2004).
15. B. N. Gershman, *Dynamics of the Ionospheric Plasma* (Nauka, Moscow, 1974) [in Russian].
16. L. D. Landau and E. M. Lifshitz, *Electrodynamics of Continuous Media* (Gostekhizdat, Moscow, 1953; Pergamon, Oxford, 1960).
17. R. C. Davidson, *Theory of Nonneutral Plasmas* (Benjamin, New York, 1974; Mir, Moscow, 1978).

Translated by O.E. Khadin

TRANSPORT PROCESSES

Theory of Heat Transport in a Magnetized High-Temperature Plasma

V. Yu. Zaburdaev

Russian Research Centre Kurchatov Institute, pl. Kurchatova 1, Moscow, 123182 Russia
e-mail: zaburd@dap.kiae.ru
Received April 22, 2004; in final form, March 24, 2005

Abstract—The transport of charged particles across a strong magnetic field with a small random component is studied in the double diffusion approximation. It is shown that the density of the particles whose initial distribution is stretched along the field satisfies a subdiffusion equation with fractional derivatives. A more general initial particle distribution is also considered, and the applicability of the solutions obtained is discussed. © 2005 Pleiades Publishing, Inc.

1. In this paper, we consider the diffusion of magnetized charged particles in a strong time-independent longitudinal magnetic field with a small random transverse component. Such a situation often occurs in systems in which there is a preferential direction of the magnetic field, e.g., in tokamaks, open magnetic traps, and other types of magnetic confinement systems. A stochastic magnetic field can be described in the simplest diffusion approximation [1–3]. Although this well-known approach has a long history and is widely used in studying the problems of heat transport in plasma, it is expedient to briefly outline its main aspects in order to provide a better insight into the phenomenon in question. The geometry of the problem is as follows. The magnetic field **B** points preferentially in the z direction. This indicates that the component of the magnetic field that is parallel to the z axis is much stronger than its random transverse component δB, $B_\parallel \gg \delta B$. An important point is that the magnetic field is nondivergent, $\nabla \cdot \mathbf{B} = 0$. A flux tube of such a field is shown in the figure, which is borrowed from the excellent review by Isichenko [4]. In a certain plane $z = z_0$, we choose a contour that encloses a bundle of magnetic field lines. In moving in the longitudinal (positive or negative) direction, we see that individual magnetic field lines move away from one another and the contour is deformed: it becomes more and more curved, but the area enclosed by it is conserved because of the conservation of the magnetic flux. As a result, the distance d between the walls of the magnetic flux tube decreases exponentially. When moving away from the $z = z_0$ plane, we see that the contour fills the perpendicular plane more and more uniformly. After averaging over the tube cross-sectional area, we can say that the averaged density b of the magnetic field lines decreases so as to satisfy the diffusion equation in which the role of time is played by the z coordinate (or, in a more general case, the superdiffusion equation in which the role of

the Laplacian is played by its fractional power $\Delta_\perp^\beta$, with $\beta < 1$),

$$\frac{\partial b}{\partial z} = D_B \Delta_\perp b. \qquad (1)$$

Here, D_B is the effective diffusion coefficient [5] and z is the absolute distance from the initial position of the contour. Let us briefly comment on this equation. In the problem as formulated, the mean magnetic field is generally the same over the entire space and has a certain constant strength B_0. However, if we wish to trace the behavior of the density of a bundle of magnetic field lines marked by the particles moving along them, then we see that, because of the magnetic field fluctuations,
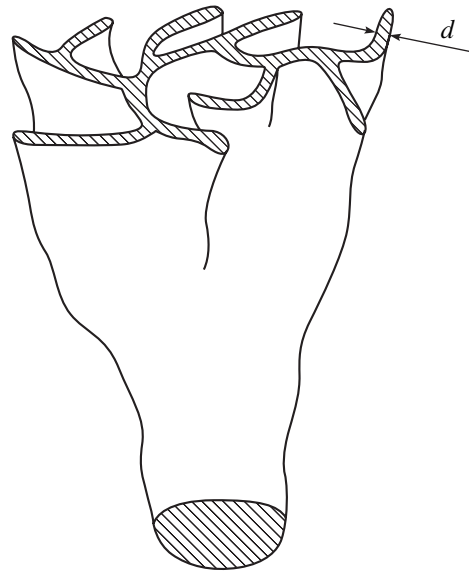
Magnetic flux tube in a magnetic field with a random component.

this density behaves according to a diffusion law, as is implied by Eq. (1). In other words, by the quantity b satisfying Eq. (1), we mean the density of the marked magnetic field lines. As was said above, this approach implies that, before applying the averaging procedure, we must choose a certain contour enclosing magnetic field lines in order to trace its deformation and expansion in moving along the z axis. At this point, it is useful to mention other approaches to describing a stochastic magnetic field. The equation for an individual magnetic field line can be written as

$$\frac{d\mathbf{r}'}{dz} = \frac{\delta\mathbf{B}_\perp}{B_0}, \qquad (2)$$

where $\mathbf{r}'$ is the coordinate in the plane perpendicular to the z axis. The corresponding averaging procedure, which inevitably involves certain assumptions about the behavior of the random magnetic field component $\delta\mathbf{B}_\perp$, reduces Eq. (2) to Eq. (1). The form of Eq. (2) clearly points to the analogy with the problem of a random two-dimensional incompressible flow with a time-dependent velocity field and with the problem of Hamiltonian chaos [6]. An analogous result on the diffusion of magnetic field lines can also be obtained in terms of quasilinear theory (see, e.g., [7]). The above behavior of the magnetic field may stem from different reasons, primarily from various plasma instabilities (see the papers cited above and also [8]).

We thus have determined how the magnetic field should be described in the model developed here. The next step is to describe the behavior of charged particles. It is well known that the squared ratio of the particle gyrofrequency to the collision frequency determines the ratio between the longitudinal and transverse transport coefficients in a magnetic field. We assume that the magnetic field is strong and, accordingly, that the particles are magnetized, $(\omega_B/\nu)^2 \propto D_{n\parallel}/D_{n\perp} \gg 1$. In the limit in which this ratio tends to infinity, the particles move exactly along the magnetic field lines and do not jump from one line to another (the questions of the transverse transport and about the applicability limit of this approximation will be discussed in more detail below). The density distribution of the particles along a magnetic field line is determined by collisions among them and by their collisions with other plasma particles. This distribution is also described by a diffusion equation,

$$\frac{\partial n_b}{\partial t} = D_n \frac{\partial^2 n_b}{\partial l^2}, \qquad (3)$$

where l is the coordinate along the magnetic field line and the longitudinal diffusion coefficient D_n is assumed to be constant and to be the same for all particles (hereafter, we omit the subscript indicating that the diffusion is in the longitudinal direction). Since the magnetic field fluctuations are small, we can set $l \simeq z$.

Hence, we have described the model with which we will study the transport of charged particles in a stochastic magnetic field. All the simplifying assumptions of the model are well known and seem to be suitable for providing an adequate description of the physical picture of heat transport. Note again that, in the above simplified model, the magnetic field is time-independent and the magnetized particles take a random walk exactly along the magnetic field lines, without jumping from one line to another. Thus, if a randomly moving particle returns to its initial position, its transverse displacement is zero. The task now is to give a rigorous derivation of the equations that describe transverse diffusion in the problem as formulated.

2. Although the diffusion equations describing the magnetic field evolution and the evolution of the particles are simple and well studied, their simultaneous solution in the model under consideration is a nontrivial task. From the formal (mathematical) point of view, Eqs. (1) and (3) are not coupled to one another: Eq. (3) describes the particle transport as a function of time and the z coordinate, while Eq. (1) describes the expansion of the magnetic field lines in the transverse direction as a function of the same z coordinate. It is easy to see, however, that, when the stochastic behavior of a magnetic field line and the particle diffusion along it are taken into account simultaneously, the result is effective transport in the transverse direction (for simplicity, one can consider ballistic motion of the particles along the field; in this case, the transverse particle transport will occur in accordance with the diffusion of the magnetic field lines). Simple scaling estimates based on the set of Eqs. (1) and (3) yield the following self-similar relationship between the variables in the problem, or equivalently, the following new relationship between the spatial and the time scales: $\bar{r} \propto t^{1/4}$. The most likely candidates that possess this self-similarity property and that can be used to describe the diffusion of passive particles (i.e., the particles that have no effect on the medium) are, e.g., equations with the squared Laplacian on the right-hand side and equations with a time-dependent diffusion coefficient. However, equations of the first type represent an unphysical situation because their Green's function is not of fixed sign, whereas equations of the second type imply that the problem is spatially inhomogeneous. These preliminary considerations show that the answer should be sought in another class of equations. It should be emphasized that, in what follows, the desired equations will be rigorously derived based on a precise formulation of the problem.

In constructing the most general solution for the particle distribution step by step, we consider a simple problem in which the particles are initially localized at the point $(\mathbf{r}_0, \zeta)$, i.e., $n_0(\mathbf{r}) = n_0\delta(\mathbf{r}' - \mathbf{r}_0)\delta(z - \zeta)$. The radius vector $\mathbf{r}$ is defined by the pair $(\mathbf{r}', z)$, where $\mathbf{r}'$ is the position vector in the plane that is perpendicular to the z axis and passes through the point z. In this case, the solution is quite evident—it is simply a product of

the solutions to Eqs. (1) and (3) with the initial conditions B_0 and n_0/B_0, respectively:

$$n(\mathbf{r}, t) = n_0 \frac{e^{-\frac{(z-\zeta)^2}{4D_n t}}}{\sqrt{4\pi D_n t}} \frac{e^{-\frac{(\mathbf{r}'-\mathbf{r}_0)^2}{4D_B|z-\zeta|}}}{4\pi D_B|z-\zeta|}. \quad (4)$$

The same solution can be obtained in a mathematically more precise way. For simplicity, we consider a planar problem in which the position vector $\mathbf{r}'$ has only one component, $\mathbf{r}' \longrightarrow x$ (with this simplification, we will arrive at the same final result but after far more illustrative manipulations). The probability density for the occurrence of a particle at a given point is equal to

$$\delta[\mathbf{r} - \mathbf{r}(t)] = \delta[\mathbf{r}' - \mathbf{r}'(t)]\delta[z - z(t)].$$

From the equation of particle motion (see Eq. (2)), we have

$$d\mathbf{r}/dt = V(t)\mathbf{h}, \quad \mathbf{h} = (\mathbf{B}_0 + \delta\mathbf{B}_\perp)/|\mathbf{B}_0 + \delta\mathbf{B}_\perp|,$$

$$z(t) = z_0 + \tilde{z}(t) = z_0 + \int_0^t V(t')dt'.$$

Here, $V(t)$ is a random Gaussian variable with a zero mean, which describes the collision-induced random variations in the velocity of a particle moving along a magnetic field line. The quantity $\tilde{z}(t)$ is the sum of independent random quantities and is therefore a random Gaussian quantity having the probability density function

$$\frac{1}{\sqrt{4\pi D_n t}}e^{-\tilde{z}^2/(4D_n t)}.$$

Analogously, we have

$$x(t) = x_0 + \tilde{x}(t) = x_0 + \int_0^t V(t')\frac{\delta B(z(t))}{B_0}dt'$$

$$= \int_0^{z(t)} \frac{\delta B(z')}{B_0}dz',$$

where $\tilde{x}(t)$, too, is a random Gaussian quantity with the probability density function

$$\frac{1}{\sqrt{4\pi D_B|z(t)|}}e^{-\tilde{x}^2/(4D_B|z(t)|)}.$$

Consequently, the sought-for probability density function is equal to

$$n(x, z, x_0, z_0, t) = \iint \delta(x - x_0 - x')\delta(z - z_0 - z')$$

$$\times \frac{1}{\sqrt{4\pi D_B|z'|}}e^{-x'^2/(4D_B|z'|)} \frac{1}{\sqrt{4\pi D_n t}}e^{-z'^2/(4D_n t)}dz'dx'.$$

Taking the integrals in this function yields formula (4).

The above mathematical procedure corresponds to a random time replacement or to the substitution of one random process for the argument (carrier) of another random process. The resulting random process will be nondiffusive, and, moreover, it will be non-Markovian. In what follows, it will be shown that the random-walk process just considered, namely, the one whose argument is also a random-walk process, obeys a subdiffusion scaling.

To do this, we consider an initial particle distribution that is uniform along the z axis. In experiments, such a distribution can be produced, e.g., with the help of a laser pulse.

It should be kept in mind, however, that, in this situation, particles with different coordinates ζ can occur at the same magnetic field line; in this case, the above initial condition in the form of a delta function for the equation describing the diffusion along this field line is incorrect. However, for a two-dimensional random-walk process, the probability that the trajectory will return to its initial point is zero. This question, which is important for achieving a realistic formulation of the problem of the transverse evolution of particles distributed initially around the z axis in such a manner that the transverse size of the distribution is much less than its longitudinal size, will be discussed below.

In the model formulation of the problem, the solution is obtained by integrating formula (4) over ζ and by setting $\mathbf{r}_0 = 0$:

$$n(\mathbf{r}', t) = 2\int_{-\infty}^{z} n_0 \frac{e^{-\frac{(z-\zeta)^2}{4D_n t}}}{\sqrt{4\pi D_n t}} \frac{e^{-\frac{\mathbf{r}'^2}{4D_B|z-\zeta|}}}{4\pi D_B|z-\zeta|}d\zeta$$

$$= \frac{1}{8\pi^2 D_B\sqrt{D_n t}}G_{03}^{30}\left(\frac{\mathbf{r}'^4}{256D_B^2 D_n t}\bigg|_{0,\ 0,\ 1/2}\right). \quad (5)$$

The integral in formula (5) is expressed through the Meyer's G function, which is defined in terms of a fairly involved contour integral containing Euler's gamma function [9]. The solution obtained, however, can be investigated without reference to the asymptotic expressions of this complicated special function. Let us try to find out what equation function (5) would satisfy. Taking the Fourier transformation of function (5) in the variable $\mathbf{r}'$ and then the Laplace transformation of the resulting function in the time t, we can easily calculate the integral to obtain

$$n_{p,\mathbf{k}} = \frac{1}{\sqrt{pD_n}}\frac{n_0}{\sqrt{p/D_n} + D_B\mathbf{k}^2}. \quad (6)$$

Here, the subscripts p and $\mathbf{k}$ refer to the Laplace and Fourier components of the function and the quantities p and $\mathbf{k}$ themselves are the variables in the Laplace and Fourier representations, respectively. We transform expression (6) by multiplying it by the denominator of

its right-hand side and by applying the inverse Fourier transformation in the coordinate:

$$\frac{n_p\sqrt{p}}{\sqrt{D_n}} = D_B\Delta_\perp n_p + \frac{n_0\delta(\mathbf{r'})}{\sqrt{D_n p}}.$$

To within a factor of $\sqrt{\pi}$, the expression on the left-hand side is nothing more than the fractional time derivative of order 1/2. Finally, in conventional coordinates, the equation satisfied by function (5) is rewritten as

$$\frac{\partial^{1/2}n}{\partial t^{1/2}} = D_B\sqrt{\pi D_n}\Delta_\perp n + \frac{n_0\delta(\mathbf{r'})}{\sqrt{t}}. \tag{7}$$

In order for Eq. (7) to be capable of describing particles that obey a uniform distribution in the longitudinal direction and a given distribution in a direction transverse to the magnetic field, it is sufficient to make the replacement $n_0 \longrightarrow n_0(\mathbf{r'})$. We thus have shown that the expansion of an initial particle distribution stretched along the z axis is described by a subdiffusion equation.

The possibility of using a fractional-derivative subdiffusion equation with an appropriate self-similarity property in analogous problems was pointed out by Balescu [10]. In that paper, the parameters of the equation were chosen to satisfy the dimensional estimates of the characteristic spatial and time scales of the problem and also to be consistent with the results that were obtained for the moments of the distribution function in other models. It was not, however, clearly formulated to what extent this equation is applicable to the physical problem. In a subsequent paper [11] (see also [12]), Vanden Eijnden and Balescu used a hybrid kinetic equation in order to derive an asymptotic expression for the particle density that was analogous to the expression obtained from an equation with fractional derivatives and that provided exactly the same behavior of the moments of the distribution function. An important advantage of [11] is that Vanden Eijnden and Balescu considered the possible mechanisms for collisional transverse transport; this problem, however, is more complicated and goes beyond the scope of the present paper (see [13]). In what follows, a simple and rigorous derivation of an effective transport equation that is valid on arbitrary time scales will be proposed that does not require any additional model assumptions. Moreover, solution (4) applies to any localized initial particle distribution. The solution method proposed here also helps to demonstrate a relationship with the model of random-walk processes in continuous time and to analyze memory effects that are exhibited by subdiffusion equations (see below) and are often fall out of consideration and thereby are not discussed in the literature. It should be noted that there are alternative approaches to solving the problem under consideration, e.g., the approach developed by Kota and Jokipii [14], who used the Kubo formalism, which is based on an analysis of the velocity correlation functions and yields a subdiffusion scaling, too.

At this point, it is also expedient to mention a paper by Zybin and Istomin [15], who studied particle transport in a random magnetic field and considered an analogous model called the "second-order diffusion" model. They asserted that, in such a formulation of the problem, the transverse transport is purely diffusive and the assumption of a subdiffusion scaling is erroneous. Note that the subdiffusion regime in the double diffusion model was proposed as early as 1962 by Getmantsev [16] (see also [17]). A more detailed discussion of the history of this issue, as well as of the relevant numerical and theoretical results, can be found in [4], in a recent review by Bakunin [18], and in a paper by Kota and Jokipii [14]. It is of interest to note that the true derivation of the subdiffusion scaling at the beginning of a paper by Zybin and Istomin [15] was subsequently declared invalid. The main error made by the authors of [15] in considering their model example was that they estimated the rate of diffusion of particles along the magnetic field lines by the particle characteristic velocity. However, this estimate in fact corresponds to switching from the original diffusive motion of the particles to their ballistic unidirectional motion and leads naturally to a diffusion scaling. The use of such an approach can stem from the assumption that the magnetic field is unsteady or from the assumption that the particles can jump from one magnetic field line to another due to collisions. Averaging over the ensemble of realizations of the magnetic field, i.e., switching from a fixed random magnetic field configuration to an averaged configuration, also can yield analogous results, which are erroneous in the model under consideration.

3. Subdiffusion equations have been known for a fairly long time: rich experience has been gained in using them, and their properties, solutions, and asymptotics have been examined in detail [19–21]. However, not all of the papers considering subdiffusion equations were based on a reasonable physical model (or even any model at all) from which they were derived. This is why it is necessary to mention interesting papers [22–24] (see also [25]). It is expedient to point out only the main properties of Eq. (7) (see [26]) because our purpose here is not to consider the general features of subdiffusion equations. The Green's function for Eq. (7) is a self-similar function of the form (see formula (5))

$$G(r, t) = \frac{1}{t^{1/2}}\Phi\left(\frac{r'}{t^{1/4}}\right). \tag{8}$$

In our case, the self-similarity property, which, as a rule, greatly simplifies the analysis of the equations, is attracting in character. This means that any initial particle distribution will asymptotically evolve to the Green's function profile. Recall also that the subdiffusion regime corresponds to a slower expansion of a particle cloud than in the case of conventional diffusion: the characteristic cloud width $\bar{r}$ increases according to the law

$$\bar{r}^2 \propto D_B(D_n t)^{1/2}. \tag{9}$$

Note that this law determines the applicability limit of the model proposed here: on long time scales, the evolution of a particle cloud is governed by the competition between subdiffusion expansion (9) and the slow transverse diffusion $\bar{r}^2 \propto D^* t$, which was ignored up to this point because of the assumption of a strongly magnetized plasma (see above). The determination of the effective transverse diffusion coefficient D^* for particles in a stochastic magnetic field is a fairly complicated task. Following [2, 3], this coefficient can be estimated by the formula $D^* = (\delta B/B)(D_{n\perp}D_n)^{1/2}$; in this case, we have $D_n(\delta B/B)^2 > D_{n\perp}$ (of course, other estimates can also be used, see, e.g., [27]). A comparison of the above expansion rates yields the following estimate for the applicability limit of the model developed here: $t \ll t^* = (D_B^2/D_{n\perp})(B/\delta B)^2$. We see that, for a strongly magnetized plasma and for small magnetic field fluctuations, this time can be fairly long.

All the features mentioned above could also be derived directly from formula (5). For an asymptotic analysis, however, the Laplace–Fourier transformation method makes this derivation somewhat more illustrative. Moreover, in rare cases only, the Green's function can be expressed in terms of tabulated special functions in conventional coordinate space, as in the above analysis.

An important property of subdiffusion equations is that they exhibit memory effects, which were analyzed in [28]. Equation (7) does not possess the property of continuous evolution. In other words, if we consider a state to which the system has evolved by a certain time as a new initial condition, then the continuity of the evolution is violated. Through a special choice of the initial condition, it is also possible to affect the initial stage of the process. For subdiffusion equations of form (7), these effects manifest themselves on macroscopic time scales. In [28], it was shown that, in order to provide an adequate description of the situation, it is necessary to take into account the dependence on the microscopic details of the transport process, as well as of the initial distribution. Presumably, the reason why, in our case, the continuity of the evolution is violated is associated with the averaging of the magnetic field over a small cross-sectional area in formulating the initial condition in the diffusion approximation. This averaging corresponds to a redistribution of the particles over the magnetic field lines in such a way that no two of them have different coordinates and occur at the same field line. In order to preserve the continuity property, it is necessary to take into account the distribution of the particles over the magnetic field lines and to solve the diffusion equations with an initial condition that remembers all information about the prehistory of the evolution. In so doing, however, it is necessary to know the behavior of each magnetic field line and, consequently, to solve exact dynamic equation (2), which is a separate and complicated task. This is why, in what follows, we will again use the above averaged description

tion of the magnetic field but will give an estimate of the extent to which this approach is realistic.

4. In order to demonstrate the consequences of the memory effects, which, in the case at hand, stem from the characteristic features of the initial particle distribution over the magnetic field lines, we consider a problem in which the particles are initially distributed over a cylindrical region Ω of a certain radius and of comparable height. In this problem, we are dealing with two possible situations. In the first situation, the particles are distributed in such a way that no two of them occur at the same magnetic field line and have different coordinates. In this situation, the solution for the particle distribution is obtained by simply integrating formula (4) (the case when the region Ω lies in a plane perpendicular to the z axis also presents no problem because, in this case, each of the particles occurs at its own magnetic field line):

$$n(\mathbf{r}, t) = \int_{\Omega} n_0(\mathbf{r}_0, \zeta) \frac{e^{-\frac{(z-\zeta)^2}{4D_n t}}}{\sqrt{4\pi D_n t}} \frac{e^{-\frac{(\mathbf{r}'-\mathbf{r}_0)^2}{4D_B|z-\zeta|}}}{4\pi D_B|z-\zeta|} d\mathbf{r}_0 d\zeta. \quad (10)$$

In the second situation, the particles are distributed over a cylindrical region Ω in such a way that they obey a certain given distribution along each of the magnetic field lines that cross the cylinder. What are the consequences of such a distribution? Let us consider a magnetic field line such that its portion inside the cylinder coincides with the cylinder axis and has a length a (with such a symmetric model condition, the final result will not change qualitatively, because we will be interested in the behavior of the particles on spatial scales much greater than the dimensions of the region Ω). Let the coordinate origin be at the center of one of the bases of the cylinder. In this case, the particle density is calculated by the formula ($z > a$)

$$n(\mathbf{r}, t) = B(\mathbf{r}', z-a)\int_0^a n_0(\zeta)G(z-\zeta, t)d\zeta \simeq A$$
$$B(\mathbf{r}', z-a)G(z-z_0, t), \quad (11)$$

where $G(z, t)$ and $B(\mathbf{r}', z)$ are the Green's functions of Eqs. (1) and (3), respectively; $A = \int_0^a n_0(\zeta)d\zeta$; and $Az_0 = \int_0^a \zeta n_0(\zeta)d\zeta$. If we use approximation (10) for the chosen magnetic field line, then we arrive at a different solution,

$$n'(\mathbf{r}, t) = \int_0^a n_0(\zeta)G(z-\zeta, t)B(\mathbf{r}', z-\zeta)d\zeta. \quad (12)$$

The main difference between density distributions (11) and (12) is as follows. In formula (11), the particle evolution is described by a single diffusion equation with the initial condition $n_0(z)$ and the diffusive random walk

of a given magnetic field line comes into play at the point $z = a$. In formula (12), we are dealing with point sources producing particles that diffuse along their own magnetic field lines, which, in turn, are distributed diffusively and originate from given points. By subtracting one integral from another, we can estimate the accuracy of the averaged approximate formula (10). We subtract formula (11) from formula (12) and take into account the condition $z \gg a$ to obtain

$$\Delta n_1 \equiv n - n' \simeq \frac{\partial B}{\partial z}(\mathbf{r}', z) \int_0^a n_0(\zeta) G(z - \zeta, t)(a - \zeta) d\zeta \tag{13}$$
$$\simeq A z_0' \frac{\partial B}{\partial z}(\mathbf{r}', z) G(z, t),$$

where $A z_0' = \int_0^a (a - \zeta) n_0(\zeta) d\zeta$ is a certain longitudinal dimension of the region Ω that is averaged over the initial distribution. We thus see that, because of the diffusive character of the function B on long spatial scales $z \gg a$, the discrepancy Δn_1 is small in comparison to the mean value n of the particle density on such spatial scales. This indicates that the particle transport is asymptotically described by subdiffusion equation (7).

Let us now turn to Eq. (7), because it is the equation for which we wish to analyze the influence of the memory effects. As the initial condition, we choose a general particle density distribution whose asymptotic behavior is described by Eq. (7). Let the region Ω be stretched along the z axis and let the characteristic longitudinal dimension of this region be much greater than the spatial scale on which we will follow the evolution of the particle density and which, in turn, substantially exceeds the transverse dimension of the region, $l_\parallel \gg r' \gg l_\perp$. The mean length a' of the portion of the magnetic field line that is inside the region can be estimated from the diffusion scaling: $a' = l_\perp^2 / D_B$. We are thus faced with the situation that was considered above. The only difference is that, in formula (13), we must replace the length a with the estimate a' and integrate over the cross-sectional area S of the region,

$$\Delta n_2 \simeq \int_S \frac{\partial B}{\partial z}(\mathbf{r}' - \mathbf{r}_0, z) G(z, t) \int_0^{a'} n_0(\mathbf{r}_0, \zeta)(a' - \zeta) d\zeta d\mathbf{r}_0$$
$$\simeq \frac{\partial B}{\partial z}(\mathbf{r}', z) G(z, t) \int_S \int_0^{a'} n_0(\mathbf{r}_0, \zeta)(a' - \zeta) d\zeta d\mathbf{r}_0.$$

We denote by $A_0 = \text{const}$ the integral over the region on the right-hand side of this formula. For $n_0 = \text{const}$, the integral is approximately equal to $-S a'^2 n_0 / 2 \sim -l_\perp^2 a'^2 n_0$, which will be used below for estimates. In order to calculate the accuracy of this integral estimate at the point $(\mathbf{r}', z)$, we must take the sum of the contributions from the regions of length on the order of a' and

switch from the sum to an integral over ζ with a weighting function of $1/a'$,

$$\Delta n \simeq \frac{2 A_0}{a'} \int_{-\infty}^{z} \frac{\partial B}{\partial z}(\mathbf{r}', z - \zeta) G(z - \zeta, t) d\zeta.$$

Since the magnetic field satisfies Eq. (1), we can replace the derivative with respect to the z coordinate with the transverse Laplacian operator. Taking into account that the Green's function for the equation describing the particle density is independent of $\mathbf{r}$, we can factor it out of the integral sign. As a result, we arrive at the following final estimate of the order of smallness of the approximation accuracy (see formula (4)):

$$\Delta n \simeq \frac{2 A_0 D_B}{a'} \Delta_\perp \int_{-\infty}^{z} B(\mathbf{r}', z - \zeta) G(z - \zeta, t) d\zeta \tag{14}$$
$$\sim \frac{l_\perp^2}{2} \Delta_\perp n(\mathbf{r}', t) = O\left(\frac{1}{t}\right),$$

where the particle density $n(\mathbf{r}', t)$ satisfies subdiffusion equation (7) and is a self-similar function of form (8).

A more sophisticated problem is that in which the magnetic field lines cross the initial region many times. According to the theory of Brownian motion, the probability that the magnetic field line passes through the initial region in a finite time (a finite value of the z coordinate) is equal to unity. Since the diffusion equation automatically takes into account the contribution of such trajectories, it can be stated that the above diffusion approximation adequately describes the situation under analysis. Let us discuss this problem in more detail. We choose a certain point with the coordinates $(\mathbf{r}_1', z_1)$ in the region Ω. With a probability determined by diffusion, a certain number of the magnetic field lines that pass through the vicinity of this point also pass through the vicinity of a point $(\mathbf{r}_2', z_2)$ lying in the region Ω (for definiteness, we set $z_2 > z_1$). By virtue of the symmetry of the problem (see the comments on Eq. (1) and formula (4)), we can reverse the direction of motion[1] and choose a bundle of magnetic field lines passing through the vicinity of the point $(\mathbf{r}_2', z_2)$ to see that the same number of them should pass through the vicinity of the point $(\mathbf{r}_1', z_1)$. In other words, any two points in the initial region are connected by magnetic field lines whose density depends on the relative positions of the points. The contributions of these points to the density of the magnetic field lines at a certain spatial

---

[1] A similar effect underlies the mechanism of enhanced diffusion in a stochastic magnetic field [2, 3]: a particle that starts from a certain initial point will execute a random walk along a magnetic field line and then, because of the slow transverse diffusion, it will occur at a nearby magnetic field line and will move along it but in the opposite direction; as a result, the particle, on average, moves away over a long distance from the initial point.

point $(\mathbf{r}_3', z_3)$ should be calculated by summing them with the corresponding diffusive weighting functions $B(|\mathbf{r}_1' - \mathbf{r}_3'|, |z_1 - z_3|)$ and $B(|\mathbf{r}_2' - \mathbf{r}_3'|, |z_2 - z_3|)$. By doing this, we automatically and correctly take into account the trajectories that pass through all three of these points (it is obvious that such trajectories always exist). We thereby have shown that the above two approaches to calculating the particle density at a given point are completely equivalent to one another, specifically, the approach based on a correct total initial condition that is formulated for the common magnetic field lines and involves nontrivial density values $n_0(\mathbf{r}_1', z_1)$ and $n_0(\mathbf{r}_2', z_2)$, which should be obtained by calculating the probability for the trajectory to pass through three fixed points (or even through more points, if account is taken of the repeated returns of the trajectory), and the approach based on formula (4) with the same initial conditions on the particle distributions in the form of delta functions but with allowance for the diffusive expansion of the magnetic field lines. Consequently, for an initial particle distribution over a region of finite transverse dimension, the deviation of the evolution of the particle density in the initial stage from that predicted by Eq. (7) can be attributed to the particles moving along the portions of the magnetic field lines that are inside the initial region and have the mean length $a' = l_\perp^2/D_B$. By virtue of estimate (14), the contribution of these particles is small.

5. Thus, in considering the problem of the particle transport in a strong time-independent longitudinal magnetic field with a small random transverse component, a simple method for calculating the particle density has been proposed and the criteria for its applicability have been given. With this method, it has been demonstrated that the evolution of an initial particle distribution stretched along the magnetic field is described by a subdiffusion equation with fractional derivatives that has a self-similar solution consistent with the well-known scaling $\bar{r} \propto t^{1/4}$. It should be noted that the problem considered above constitutes one of the few examples of the rigorous derivation of an equation with fractional derivatives and thereby shows the naturalness and importance of this approach to describing stochastic processes in which the subdiffusive behavior of the particles is an inherent feature of the physical phenomenon.

ACKNOWLEDGMENTS

REFERENCES

1. T. Stix, Phys. Rev. Lett. **30**, 833 (1973).
2. B. B. Kadomtsev and O. P. Pogutse, in *Proceedings of the 7th International Conference on Plasma Physics and Controlled Nuclear Fusion Research, Innsbruck, 1979*, Vol. I, p. 949.
3. A. B. Rechester and M. N. Rosenbluth, Phys. Rev. Lett. **42**, 1247 (1979).
4. M. B. Isichenko, Rev. Mod. Phys. **64**, 961 (1992).
5. M. N. Rosenbluth, R. Z. Sagdeev, J. B. Taylor, and G. M. Zaslavski, Nucl. Fusion **6**, 297 (1966).
6. B. V. Chirikov, Phys. Rep. **52**, 263 (1979).
7. L. A. Artsimovich and R. Z. Sagdeev, *Plasma Physics for Physicists* (Atomizdat, Moscow, 1979) [in Russian].
8. A. A. Galeev and L. M. Zeleny, *Theoretical and Computational Plasma Physics* (IAEA, Vienna, 1978), p. 93.
9. A. P. Prudnikov, Yu. A. Brychkov, and O. I. Marychev, *Integrals and Series* (Nauka, Moscow, 1986; Gordon & Breach, New York, 1989), Vol. 3.
10. R. Balescu, Phys. Rev. E **51**, 4807 (1995).
11. E. Vanden Eijnden and R. Balescu, Phys. Plasmas **3**, 874 (1996).
12. R. Balescu, Plasma Phys. Controlled Fusion **42**, B1 (2000).
13. M. Vlad, F. Spineanu, J. H. Misguich, and R. Balescu, Phys. Rev. E **61**, 3023 (2000).
14. J. Kota and J. R. Jokipii, Astrophys. J. **531**, 1067 (2000).
15. K. P. Zybin and Ya. N. Istomin, Zh. Éksp. Teor. Fiz. **89**, 836 (1985) [Sov. Phys. JETP **62**, 479 (1985)].
16. G. G. Getmantsev, Astron. Zh. **39**, 607 (1962) [Sov. Astron. **6**, 477 (1962)].
17. J. R. Jokipii, Astrophys. J. **146**, 480 (1966).
18. O. G. Bakuninm, Rep. Prog. Phys. **67**, 965 (2004).
19. E. W. Montroll and M. F. Schlesinger, in *Studies in Statistical Mechanics*, Ed. by J. Leibowitz and E. W. Montroll (North-Holland, Amsterdam, 1984), Vol. 2, p. 1.
20. J.-P. Bouchaud and A. Georges, Phys. Rep. **195**, 127 (1990).
21. J. Klafter and R. Metzler, Phys. Rep. **339**, 1 (2000).
22. S. Havlin and D. Ben-Avraham, Adv. Phys. **36**, 695 (1987).
23. L. A. Bol'shov, A. M. Dykhne, and P. S. Kondratenko, Pis'ma Zh. Éksp. Teor. Fiz. **75**, 291 (2002) [JETP Lett. **75**, 246 (2002)].
24. I. A. Lubashevskiĭ and A. A. Zemlyanov, Zh. Éksp. Teor. Fiz. **114**, 1284 (1998) [JETP **87**, 700 (1998)].
25. K. V. Chukbar, Zh. Éksp. Teor. Fiz. **109**, 1335 (1996) [JETP **82**, 719 (1996)].
26. K. V. Chukbar, Zh. Éksp. Teor. Fiz. **108**, 1875 (1995) [JETP **81**, 1025 (1995)].
27. A. A. Galeev and L. M. Zeleniy, Physica D (Amsterdam) **2**, 90 (1981).
28. V. Yu. Zaburdaev and K. V. Chukbar, Pis'ma Zh. Éksp. Teor. Fiz. **77**, 654 (2003) [JETP Lett. **77**, 551 (2003)].

Translated by G.V. Shepekina

Behavior of Small-Scale Density Fluctuations in Discharges with Off-Axis Electron-Cyclotron Resonance Heating in the T-10 Tokamak

D. A. Shelukhin, V. A. Vershkov, and K. A. Razumova

Institute of Nuclear Fusion, Russian Research Centre Kurchatov Institute,
pl. Kurchatova 1, Moscow, 123182 Russia

Received January 25, 2005

Abstract—In experiments on off-axis electron-cyclotron resonance heating in the T-10 tokamak, a steep gradient of the electron temperature was observed to form for a short time at a relative radius of $\rho \approx 0.25$ after the heating power was switched off. Small-scale fluctuations of the electron density were studied with the help of correlation reflectometry. It was found that, in a narrow region near $\rho \approx 0.25$, the amplitude of the density fluctuations was two times lower than that in the ohmic heating phase. Quasi-coherent fluctuations were suppressed over a period of time during which the steep temperature gradient existed. Measurements of the poloidal rotation velocity of turbulent fluctuations show that there is no velocity shear after the heating is switched off. An analysis of the linear growth rates of instabilities shows that the ion-temperature-gradient mode is unstable at $\rho \approx 0.25$ throughout the entire discharge phase. The effect observed can be explained by an increase in the distance between the rational surfaces near the radius at which the safety factor is $q = 1$ due to the temporary flattening of the q profile after the off-axis electron-cyclotron resonance heating is switched off. © *2005 Pleiades Publishing, Inc.*

1. INTRODUCTION

Discharges with off-axis electron-cyclotron resonance heating (ECRH) are of great interest for tokamak studies. First, off-axis ECRH leads to the formation of broader profiles of the electron temperature and plasma current density. As a result, sawtooth oscillations are suppressed, which is convenient for studying the plasma properties in the central region of the plasma column. Furthermore, in accordance with the model of critical gradients [1], the formation of a flat electron-temperature profile in the plasma core should suppress turbulence. Experiments on the T-10 and TEXTOR tokamaks have shown that an electron transport barrier forms in the transient stage of a discharge after off-axis ECRH is switched off [2].

In this paper, we present results from studying small-scale density fluctuations in T-10 discharges with off-axis ECRH. The paper is organized as follows: the scheme of experiment, diagnostics used, and the basic properties of the tokamak plasma are described in Section 2. Section 3 is devoted to measurements of the density fluctuations. The transport coefficients are estimated in Section 4. The experimental results are discussed in Section 5. The main results of the study are summarized in the Conclusions.

2. EXPERIMENTAL PARAMETERS

We carried out measurements of turbulence in experiments with off-axis ECRH in the T-10 tokamak

[2]. The circular-cross-section plasma of the T-10 tokamak has a major radius of $R = 1.5$ m and a minor radius of $a = 0.3$ m. In the main series of experiments, the plasma current was $I_p = 180$ kA and the toroidal magnetic field was $B_T = 2.33$ T. The average electron density varied in the range of $(1.5–2) \times 10^{19}$ m^{-3}. In order to verify the results obtained, we also performed control experiments at different values of the current and the magnetic field. The plasma was heated by two gyrotrons with a frequency of 140 GHz and total power of 0.53 MW. This corresponds to clearly pronounced off-axis (at a relative radius of $\rho = r/a = 0.4$ if the Shafranov shift is taken into account) heating at the second harmonic of the electron-cyclotron frequency. The radial width of the region where the microwave power was absorbed was determined from the experimental data by using the COBRA code and was found to be about 4 cm (at a level of e^{-1}) [3].

The electron temperature was measured by a multichannel radiometer operating at the second harmonic of the electron-cyclotron emission. To find the absolute values of the electron temperature, the radiometer was calibrated by using the signals recorded in the ohmic phase of a discharge with the known electron temperature profile $T_e(r)$, which was calculated from the slope of the X-ray spectra measured by a multichannel X-ray spectrometer. The electron density was measured by an eight-channel radio interferometer and eight-channel HCN-laser interferometer. The radial profile of the
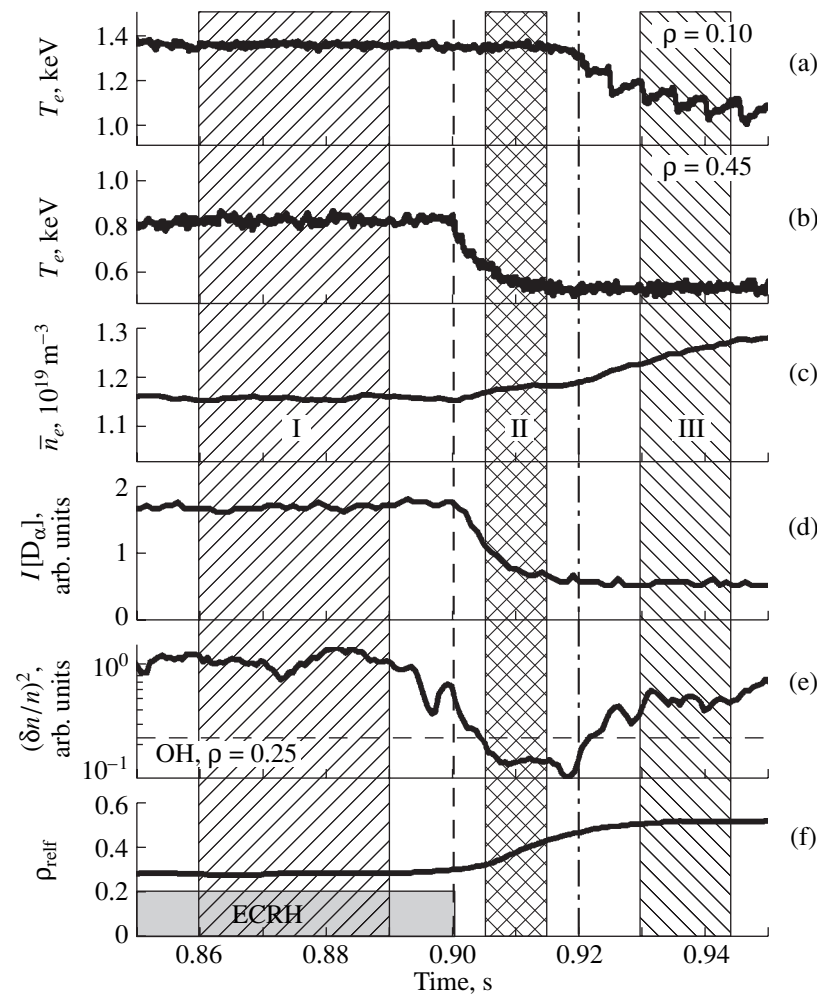
Fig. 1. Time evolution of the plasma parameters in a discharge with off-axis ECRH: (a) central electron temperature, (b) electron temperature in the ECRH region, (c) average electron density, (d) intensity of the D_α line, (e) density fluctuations in the frequency range 50–400 kHz (the horizontal dashed line shows the level of density fluctuations at $\rho \approx 0.25$ in an ohmic discharge), and (f) position of the critical-density surface. The vertical dashed line shows the instant at which ECRH is switched off, and the dashed-and-dotted line shows the start of a decrease in the central electron temperature. Hatched regions I, II, and III show the time intervals over which the plasma parameters were averaged during the ECRH, transient, and ohmic phases of the discharge, respectively.

plasma density $T_e(r)$ was reconstructed using the data from all the 6 vertical channels of both interferometers.

Small-scale fluctuations of the plasma density were measured by an O-mode correlation heterodyne reflectometer [4]. The reflectometer recorded the parameters of a wave reflected from three points located at different poloidal angles. This allowed us to determine the amplitude of electron density fluctuations, as well as their poloidal coherence and velocity.

The discharge scenario was as follows. After both the plasma current and electron density had reached their steady-state values (0.5 s after the beginning of the discharge), off-axis ECRH was switched on and operated over about 0.35 s. ECRH was followed by an ohmic phase, which lasted over about 0.1 s. Typical behavior of the plasma parameters during a discharge is shown in Fig. 1. The characteristic phases of the dis-

charge—the ECRH phase, the transient phase (in which a steep electron temperature gradient forms), and the ohmic phase—are denoted in Fig. 1 by I, II, and III, respectively. It can be seen in Fig. 1b that the electron temperature in the heating region ($\rho \approx 0.45$) decreases immediately after off-axis ECRH is switched off (the dashed vertical line). On the other hand, the central temperature (Fig. 1a) remains unchanged over 10–20 ms after ECRH and then also decreases due to the onset of sawtooth oscillations.

Such plasma behavior leads to the formation of steep electron temperature gradients at radii less than the radius of the heating region. Typical profiles of the electron temperature in discharges with off-axis ECRH are depicted in Fig. 2a (the symbols and curves show the experimental data and their approximations, respectively). Here and in the subsequent figures, the profiles corresponding to the ECRH phase (I), transient phase

(II), and ohmic phase (III) are shown by dashed lines and open triangles, solid lines and semi-closed circles, and dashed-and-dotted lines and closed squares, respectively. One can see that the temperature profile during ECRH (I) is wider than that in the ohmic phase (III). At $\rho \approx 0.2$, the parameter R/L_{Te} (where $L_{Te} = (d\ln T_e/dr)^{-1}$ is the inverse temperature gradient), characterizing the steepness of the electron temperature profile, varies from 4 in the ECRH phase to 6 in the ohmic phase. However, in the transient phase, the electron temperature gradient is very steep, $R/L_{Te} \sim 15$. This value is larger than that predicted by the model of critical gradients. Hence, the onset of strong turbulence and enhanced transport could be expected in this region [1]. Nevertheless, that the central temperature is retained over a long time contradicts this approach. It should also be noted that the region where the electron temperature gradient is steep coincides with the position of the phase reversal of sawtooth oscillations in the ohmic phase of the discharge. It is commonly accepted that this position corresponds to the magnetic surface with $q = 1$.

The behavior of the average electron density in these experiments is typical of ECRH discharges in T-10 (see Fig. 1c). The density begins to grow just after the ECRH is switched off. The reconstruction of the density profile shows that, during ECRH, the profile is additionally peaked at radii less than the radius of the heating region (Fig. 2b, curve I). This allowed us to measure density fluctuations in the plasma core. Such a narrow peak in the density profile persists for a while after ECRH is switched off (Fig. 2b, curve II) and then relaxes to that shown by curve III in Fig. 2b. Special investigations showed that the peak was not an artifact; it was also observed in the raw data of the interferometer. The influx of neutrals from the rail limiter of T-10 was monitored by the intensity of the D_α line (Fig. 1d). It was found that the influx highly increased during ECRH and then rapidly decreased.

3. MEASUREMENTS OF TURBULENCE

Plasma turbulence was analyzed by measuring small-scale fluctuations of the electron density with the help of an O-mode correlation heterodyne reflectometer [4]. Since the reflectometer frequency was fixed during a tokamak discharge, the radial profiles of density fluctuations were measured in a series of similar discharges with different reflectometer frequencies. To measure the radial profiles of turbulence more accurately, we also varied the average electron density. Since the position of the reflecting layer changed during a discharge, the point of reflection was determined from the reconstructed radial profile of the electron density. The time evolution of the position of the reflection point during a discharge are illustrated in Fig. 1f. The amplitude of fluctuations was calculated from the data obtained by the quadrature (vector) detection of
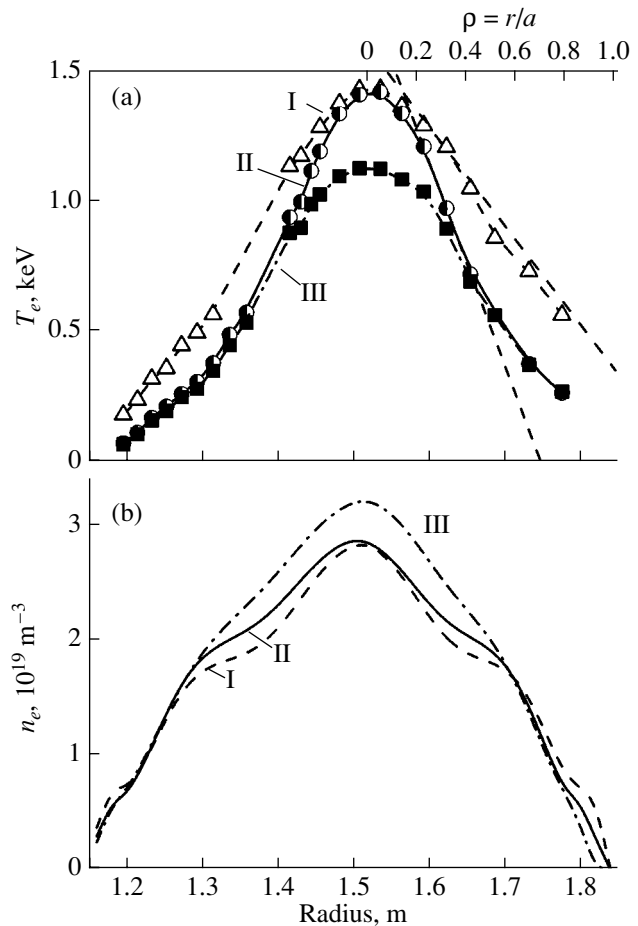
Fig. 2. Radial profiles of (a) the electron temperature and (b) the reconstructed electron density in phases I, II, and III. The symbols and curves show the experimental data and their approximations, respectively. The normalized minor radius is plotted on the upper abscissa in plot (a).

the electric field of the reflected wave. A correction for the nonlocal character of reflectometric measurements was made using a 1D geometrical approach [5].

Typical behavior of electron density fluctuations in the frequency range of 50–400 kHz is shown in Fig. 1e. The fluctuation level during ECRH is much higher than that in the ohmic phase and decreases substantially over about 10 ms after ECRH is switched off. Moreover, within this time interval, the fluctuation level is about two times lower than that in the same region of the plasma column in the ohmic phase (light horizontal dashed line).

The radial profile of the amplitude of density fluctuations was measured as was described above and was averaged over the data from three measurement channels. The results of these measurements are presented in Fig. 3a. It can be seen that, in the ohmic phase, the level of density fluctuations (curve III) is nearly constant in the gradient region. During ECRH, the fluctuation level is two to four times higher throughout the
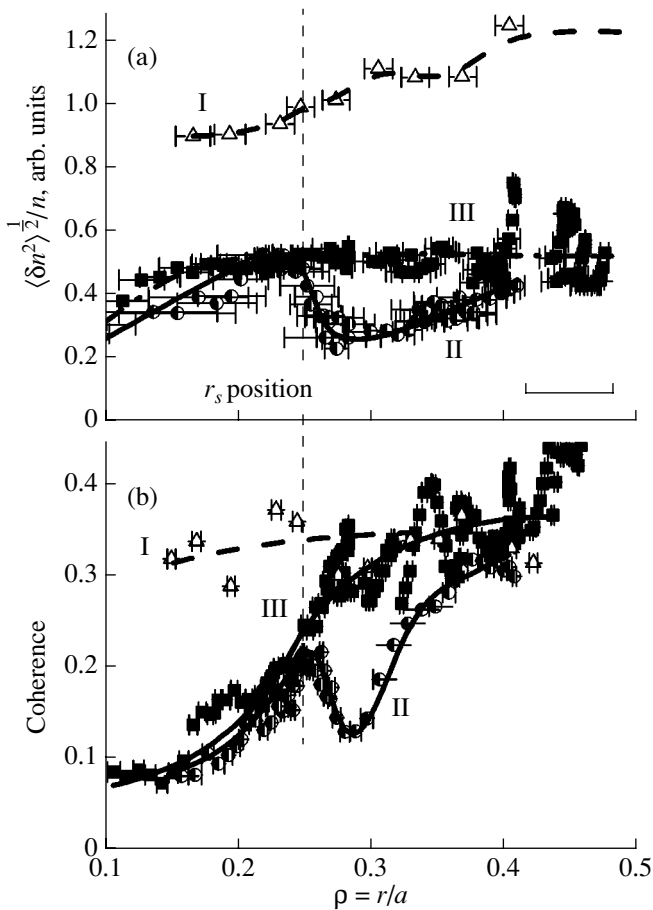
Fig. 3. Radial profiles of (a) the relative amplitude of density fluctuations and (b) the poloidal coherence of oscillations within time intervals I, II, and III. The symbols and curves show the experimental data and their approximations, respectively. The vertical dashed line shows the radial position of the phase reversal of sawtooth oscillations in the ohmic stage of a discharge.
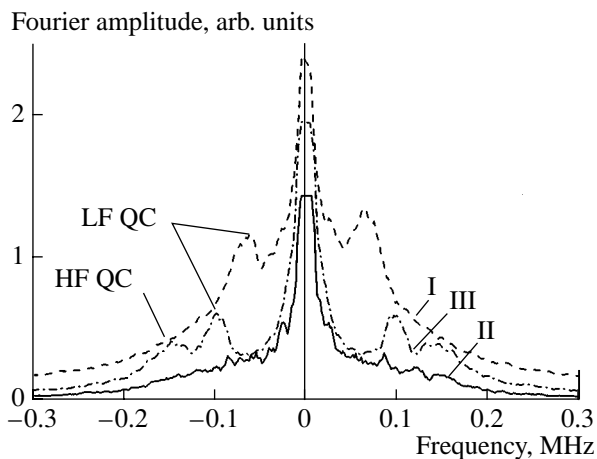
Fig. 4. Fourier spectra of the reflectometer signal within time intervals I, II, and III. The arrows show the peaks corresponding to LF and HF QC oscillations (shot no. 35960).

plasma column (curve I). This means that, even in the region in which the electron temperature gradient is low, the level of turbulence is higher than that in the ohmic phase. Such behavior contradicts the model of critical gradients. Over 5–15 ms after ECRH, the level of density fluctuations (curve II) decreases to the ohmic level at all radii under analysis, except for a narrow region near $\rho \approx 0.3$, where it becomes two times lower than that in the ohmic phase. The position of this region agrees well with the position of the steep electron temperature gradient, because the radial position of the reflection point is determined with an error of about 2 cm due to an uncertainty in reconstructing the radial electron density profile.

Correlation measurements also showed that the level of poloidal coherency in the region where the oscillations were suppressed for 5–20 ms after ECRH was four times lower than that during ECRH (Fig. 3b; curves II and I, respectively). This indicates that the poloidal correlation lengths decrease after ECRH. The correlation level in the ohmic phase is somewhat higher than that during ECRH.

A thorough study of the turbulence spectra gives additional information on the mechanisms of the effects observed. Figure 4 shows typical Fourier spectra of turbulence measured near $\rho \approx 0.3$ during ECRH (curve I), 5–15 ms after ECRH (curve II), and in the ohmic phase (curve III). It can be seen that the level of broadband (BB) density fluctuations during ECRH is rather high. There is also a peak of low-frequency (LF) quasi-coherent (QC) oscillations around a frequency of 0.1 MHz. As was shown in [6], such spectra are typical of regimes with high particle fluxes. After ECRH is switched off, the turbulence level at high frequencies decreases and LF QC oscillations disappear. This indicates that the instability is suppressed in the region of a steep temperature gradient. After the steep temperature gradient disappears, the level of BB oscillations increases. In this phase of the discharge, both LF and high-frequency (HF) QC oscillations are present in the spectrum.

The suppression of density fluctuations has been frequently observed in transport barriers in other tokamaks [7]. Such suppression is often attributed to the stabilization of turbulence by the velocity shear [8]. In our experiments, the poloidal velocity was measured by determining the poloidal time delay of density fluctuations from the cross-correlation function. Since the poloidal angle between the reflection points is known, we can find the angular velocity of fluctuations. The results obtained are presented in Fig. 5. In the ohmic phase (curve III), the angular rotation velocity throughout the plasma core is constant and exceeds the velocity in the outer region of the plasma column. The region with a nonzero velocity gradient lies inside the $q = 2$ magnetic surface (the position of this surface is shown by the vertical dashed-and-dotted line). Outside the $q = 2$ surface, the rotation velocity is about two times slower. The velocity profile during ECRH (curve I) is

similar to that in the ohmic phase, but the location of the high velocity gradient is shifted toward the center of the plasma. Such behavior may be explained as follows. The electron transport in plasma highly increases during ECRH, so the absolute value of the plasma potential decreases. As a result, the electric field decreases, which leads to a decrease in the velocity of $\mathbf{E} \times \mathbf{B}$ rotation. After ECRH is switched off (curve II), the rotation velocity decreases at all radii under analysis and a flat profile of the rotation velocity is established. This means that the stabilization by the velocity shear cannot explain the effects observed. In order to verify these results, we performed additional experiments at different values of the plasma current and magnetic field. Reflectometric measurements showed that the behavior of density fluctuations in these regimes was similar to that in the base discharges.

4. STUDY OF TRANSPORT IN DISCHARGES WITH OFF-AXIS ECRH

Transport coefficients in discharges with off-axis ECRH in T-10 have been previously investigated by different methods. An analysis of the cooling-pulse propagation shows that, after ECRH is switched off, the electron thermal diffusivity χ_e at $\rho \approx 0.3$ decreases to lower than 0.3 m^2/s [9]. A more sophisticated model that takes into account the temporal behavior of the temperature [3] shows that χ_e is about 0.25 m^2/s at radii less than the radius of the heating region and that there is a narrow layer ($\Delta\rho \approx 0.05$) within which the thermal diffusivity is minimal (about 0.15 m^2/s).

Both methods allow the effective electron thermal diffusivity χ_e to be accurately estimated but cannot distinguish between the heat fluxes due to heat conduction and to particle transport. On the other hand, as was noted above, the shape of the turbulence spectrum may indicate the existence of high fluxes of charged particles during ECRH. In order to verify this assumption, we analyzed the transport coefficients by using the heat balance equation. The total heat flux can be written in the form

$$\Gamma_e = -n_e\chi_e\frac{\partial T_e}{\partial r} + \frac{3}{2}\Gamma_n T_e$$

$$= -n_e[\chi_e + \chi_e^{\text{diff}}]\frac{\partial T_e}{\partial r} = -n_e\chi_e^{\text{eff}}\frac{\partial T_e}{\partial r},$$

where χ_e^{diff} is the effective thermal diffusivity due to particle transport,

$$\chi_e^{\text{diff}} = \frac{3}{2}\frac{\Gamma_n T_e}{n_e}\left(\frac{\partial T_e}{\partial r}\right)^{-1},$$

with Γ_n being the particle flux. It should be noted that the coefficient 3/2 in front of the term corresponding to the heat flux is not commonly accepted, and some authors prefer 5/2. Estimates obtained with both these
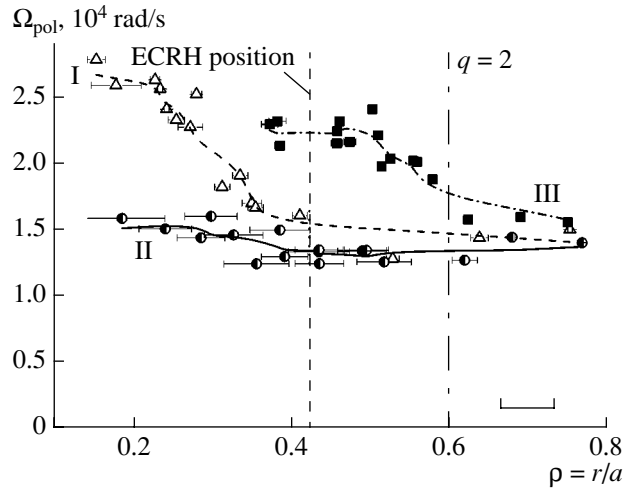
Fig. 5. Radial profiles of the angular rotation velocity of density fluctuations within time intervals I, II, and III. The symbols and curves show the experimental data and their approximations, respectively. The vertical dashed line shows the radial position of the heating region, and the vertical dashed-and-dotted line shows the position of the $m/n = 2/1$ MHD island in the ohmic stage of a discharge.

coefficients differ insignificantly. Experimental data were analyzed with the 1.5D ASTRA code [10]. In the computations, we used the experimental data on the profiles of the electron temperature and density, the loop voltage, and the total ECRH power. The profile of the absorbed ECRH power determined by Andreev *et al.* [3] was used. The time dependence of the neutral influx was determined from the intensity of the D_α line. The absolute value of the neutral influx was chosen such that the ratio of the heat diffusivity to the diffusion coefficient was $\chi_e/D_e \approx 2$ for the ohmic phase of a discharge [11]. The obtained value of the particle influx does not contradict previous measurements. The neoclassical resistivity was used to compute the ohmic power and the diffusion of the current. The ion temperature was determined under the following assumptions: the rate of electron-to-ion heat transfer and the profile of the ion thermal diffusivity were both neoclassical, but the diffusivity profile was multiplied by a factor of 2–3 to adjust the calculated values of the ion temperature and neutron flux to the measured ones. It was found that the effective thermal diffusivity obtained from the analysis of the balance equation was close to that obtained by other methods.

Interesting data can be obtained from an analysis of the heat-flux structure. Figure 6 compares the total effective thermal diffusivity χ_e^{eff} (curve *1*) and the effective thermal diffusivity due to particle transport χ_e^{diff} (curve *2*) in the region with a steep gradient of the electron temperature. One can see that, during ECRH, a major fraction of the heat flux is transferred by the particle flux. This is due to the large influx of neutrals

χ_e, m²/s
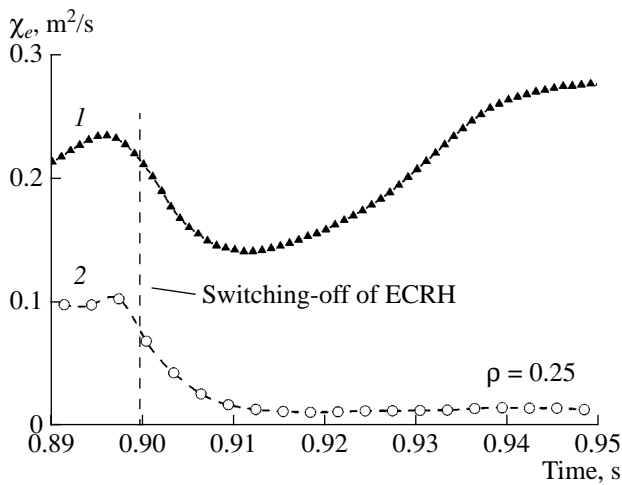
Fig. 6. Time evolution of (*1*) the total effective thermal diffusivity and (*2*) the thermal diffusivity due to particle transport. The vertical dashed line shows the instant at which ECRH is switched off.

χ_e, m²/s
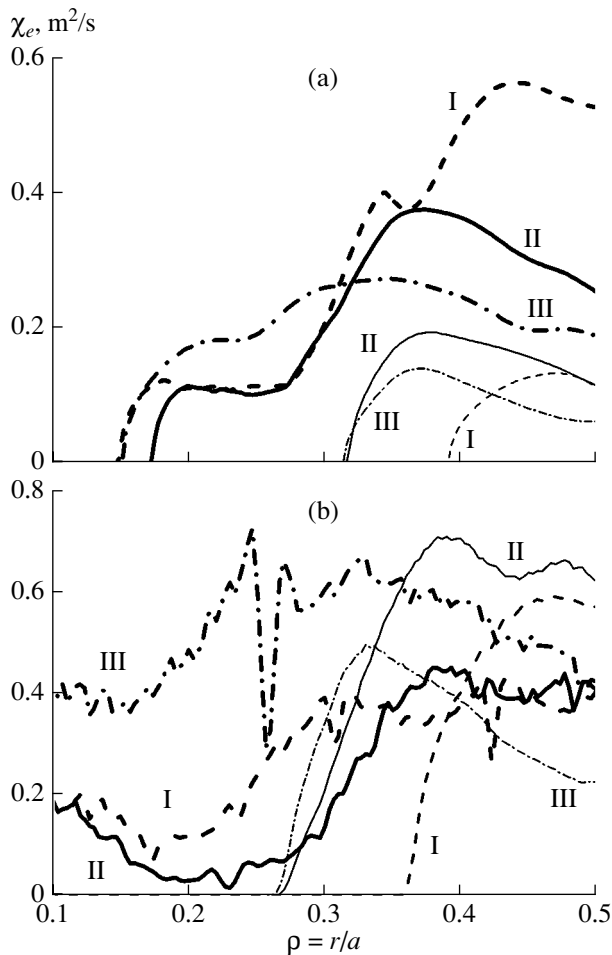
Fig. 7. Radial profiles of the effective thermal diffusivity obtained (a) from a linear theory and (b) with allowance for the magnetic configuration for time intervals I, II, and III. The heavy and light curves correspond to ITG and DTE modes, respectively.

arriving from the wall and the rail limiter during ECRH and to the deep penetration of these neutrals into the discharge. After ECRH is switched off, both the neutral influx and χ_e^{eff} decrease. In the ohmic phase, the effective thermal diffusivity increases again.

5. DISCUSSION

Our experiments demonstrate that the following effects take place after ECRH is switched off: (i) the formation of a steep electron temperature gradient, (ii) the suppression of small-scale density fluctuations, and (iii) a decrease in the electron transport coefficients. All this indicates the formation of an inner transport barrier (ITB). The question naturally arises as to the mechanism for the formation of such a barrier. As was discussed above, the suppression of plasma instability by the velocity shear is impossible because of the flat profile of the angular rotation velocity.

A possible mechanism for the stabilization of fluctuations is a decrease in the growth rates of instabilities. We estimated the thermal diffusivity from the measured profiles of the electron temperature and density and from the calculated profiles of q and the ion temperature by using a linear theory. Previous experiments showed that the main sources of turbulence in the plasma core are the ion-temperature-gradient (ITG) mode and the dissipative trapped-electron (DTE) mode [12]. The thermal diffusivity for the ITG mode was calculated according to [13], and the contribution from the DTE mode was estimated using [14].

Figure 7a presents the results of calculations for three phases of the discharge: during ECRH (curve I), 5–15 ms after ECRH (curve II), and in the ohmic phase (curve III). The heavy and light curves correspond to the ITG and DTE modes, respectively. It can be seen that, in the plasma core, the ITG-driven transport prevails throughout the discharge. After ECRH is switched off, the thermal diffusivity in the barrier region changes only slightly. Such behavior is expectable because both the ion temperature and the density profile, which determine transport, change insignificantly in this region. It is interesting that, after ECRH is switched off, the region dominated by the DTE mode shifts toward the center. This correlates with the onset of HF QC oscillations in the plasma core in the ohmic phase (Fig. 4, curve III).

Thus, the linear theory of instabilities fails to explain the entire set of the experimental data. Experiments with off-axis ECRH show that the formation of an ITB is very sensitive to the profile of q [2]. Therefore, we used an approach based on the analysis of transport coefficients with allowance for the magnetic field configuration [15]. The plasma transport in this model results from the interaction among radially localized modes having large poloidal (m) and toroidal

(n) numbers. The contribution from each mode located at the radius r_m^n to the plasma transport is defined as

$$\chi_{sp}^{n,m}(r) = \chi_0(r_m^n)\exp\left[-\frac{(r-r_m^n)^2}{4\rho_i^2}\right],$$

where χ_0 is the thermal diffusivity determined from the linear theory of instability and ρ_i is the ion Larmor radius. The authors of [15] suggested that the transport be calculated by summing over all modes m and n. This, however, leads to a substantial increase in the transport at the plasma periphery, so that the calculated values of the thermal diffusivity considerably exceed the measured ones. On the other hand, a nonlinear analysis of the instability dynamics that was performed with the help of 3D gyrokinetic simulations showed that the transport was caused by the coupling of modes having equal toroidal numbers n and that, at each instant, there was only one m mode with the corresponding value of n [16]. Therefore, the method proposed in [15] was modified to take into account the coupling of modes with different poloidal but equal toroidal numbers. The resulting transport was computed by averaging over all the possible toroidal numbers,

$$\chi^n(r) = \sum_m \chi_{sp}^{n,m}(r), \quad \chi(r) = \sum_n \chi^n(r)/n_{\max}(r).$$

The maximum poloidal and toroidal numbers are determined by the appropriate instabilities. The value of $k_\perp\rho_i$ was chosen to be equal to 0.3 for the ITG mode and 1 for the DTE mode. Accordingly, the maximum poloidal and toroidal numbers were taken to be

$$m_{\max}(r) = k_\perp r, \quad n_{\max}(r) = m_{\max}(r)/q(r).$$

This corresponds to the maximum poloidal number in the gradient region of about 20–40 for the ITG mode and 60–120 for the DTE mode. In this approach, the rate of plasma transport is proportional to "the density of the excited modes," which has the meaning of the average number of rational magnetic surfaces with equal toroidal numbers n within a given radial interval. The computed densities of the excited modes for three phases of the discharge are presented in Figs. 8a–8c. The profile of q (Fig. 8d) needed for these calculations was taken from [2]. One can see that the density of rational magnetic surfaces is almost constant throughout all radii of interest in both the ECRH (curve I) and ohmic (curve III) phases. However, 12 ms after the ECRH is switched off (curve II), the density of magnetic surfaces has a minimum at $\rho \approx 0.2$, which corresponds to the region with a low q gradient. The reason for this is that the number of rational surfaces with high numbers m and n decreases in a region corresponding to low rational values of q. If the gradient of q is low in this region, then the magnetic surfaces are separated from one another by a distance that exceeds their radial
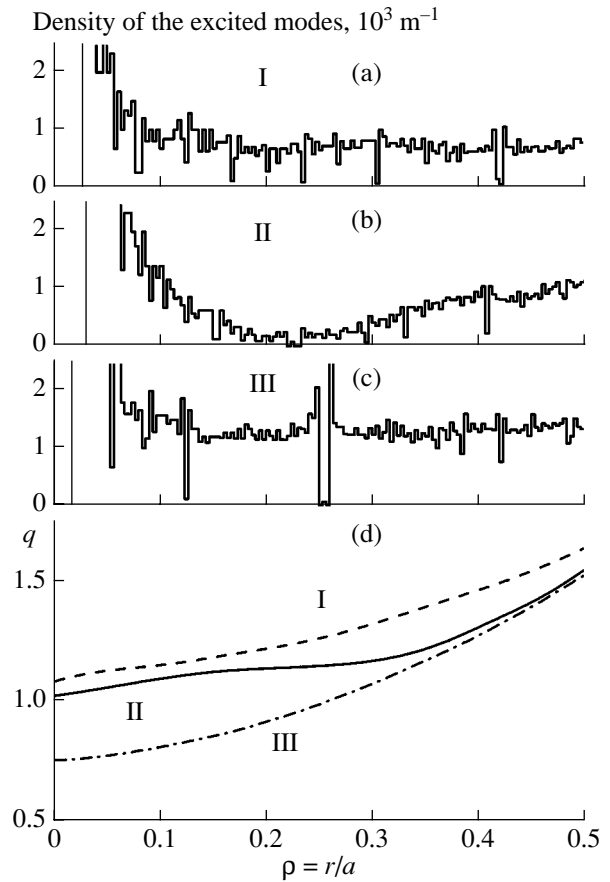
Fig. 8. Radial profiles of the densities of the excited modes within time intervals (a) I, (b) II, and (c) III. (d) Radial profile of q within time intervals I, II, and III (taken from [2]).

size, so coupling between them becomes impossible. This leads to a reduction in transport. It should be noted that a similar conclusion was drawn in [17].

The calculated thermal diffusivities are shown in Fig. 7b. It can be seen that the thermal diffusivity decreases substantially after ECRH is switched off. This approach also explains the disappearance of QC oscillations after ECRH. The formation of radially stretched structures that manifest themselves as QC oscillations is related to the toroidal coupling of the excited modes with large rational numbers. If the coupling is broken (e.g., due to the velocity shear or to the long radial distance between modes), the QC oscillations disappear. Thus, the reduction in transport in this regime is related to a break in the toroidal coupling of the excited modes, rather than to a decrease in the linear growth rates of instabilities.

6. CONCLUSIONS

The formation of a steep gradient of the electron temperature has been observed in T-10 experiments after off-axis ECRH was switched off. It has been found that the transport coefficients in the steep-gradi-

ent region are rather low (about 0.15–0.3 m²/s) and the density fluctuations are suppressed. This allows us to interpret these results as the formation of a temporary ITB in these discharges. It has been shown that the mechanism for stabilization of instabilities by the velocity shear does not operate under these conditions. The formation of the barrier is attributed to a decrease in the number of rational magnetic surfaces with high numbers of m and n around the surfaces with low m and n. This concept, however, requires a more accurate analysis.

ACKNOWLEDGMENTS

REFERENCES

1. F. Ryter, G. Tardini, F. De Luca, *et al.*, in *Proceedings of the 19th IAEA Fusion Energy Conference, Lyon, 2002*, Paper CN-94/EX/C4-2Ra.

2. K. A. Razumova, A. J. H. Donne, V. F. Andreev, *et al.*, Nucl. Fusion **44**, 1067 (2004).

3. V. F. Andreev, Yu. N. Dnestrovskij, M. V. Ossipenko, *et al.*, Plasma Phys. Controlled Fusion **46**, 319 (2004).

4. V. A. Vershkov, V. V. Dreval, and S. V. Soldatov, Rev. Sci. Instrum. **70**, 1700 (1999).

5. E. Mazzucato and R. Nazikian, Phys. Rev. Lett. **71**, 1840 (1993).

6. V. A. Vershkov, D. A. Shelukhin, and K. A. Razumova, in *Proceedings of the 30th EPS Conference on Controlled Fusion and Plasma Physics, St. Petersburg, 2003*; ECA **27A**, P3-115 (2003).

7. G. D. Conway, D. N. Borba, B. Alper, *et al.*, Phys. Rev. Lett. **84**, 1463 (2000).

8. C. M. Greenfield, D. P. Schissel, B. W. Stallard, *et al.*, Phys. Plasmas **4**, 1596 (1997).

9. S. V. Neudatchin, A. Ya. Kislov, D. A. Kislov, *et al.*, in *Proceedings of the 30th EPS Conference on Controlled Fusion and Plasma Physics, St. Petersburg, 2003*; ECA **27A**, P3-116 (2003).

10. G. V. Pereverzev and P. N. Yushmanov, Report No. IPP 5/98 (Max-Planck Inst. for Plasma Physics, Garching, 2002).

11. V. M. Leonov, V. G. Merezhkin, V. S. Mukhovatov, *et al.*, in *Proceedings of the 8th International Conference on Plasma Physics and Controlled Nuclear Fusion Research, Brussels, 1980* (IAEA, Vienna, 1981), Vol. 1, p. 393.

12. V. A. Vershkov for T-10, TEXTOR, and FTU Teams, in *Proceedings of the 31st EPS Conference on Controlled Fusion and Plasma Physics, London, 2004*; ECA **28G**, P-1-172 (2004).

13. M. Z. Tokar, J. Ongena, and B. Unterberg, Phys. Rev. Lett. **84**, 895 (2000).

14. J. Weiland and H. Nordman, Nucl. Fusion **31**, 390 (1991).

15. A. D. Beklemishev and W. Horton, Phys. Fluids **4**, 200 (1992).

16. Z. Lin, T. S. Hahm, W. W. Lee, *et al.*, Science **281**, 1835 (1998).

17. F. Romanelli and F. Zonka, Phys. Fluids **5**, 4081 (1993).

Translated by V.I. Bugarya

================================ **TOKAMAKS** ================================

On the Ablation Models of Fuel Pellets

V. A. Rozhansky and I. Yu. Senichenkov

St. Petersburg State Polytechnical University, Politekhnicheskaya ul. 29, St. Petersburg, 195251 Russia
Received October 20, 2004; in final form, March 3, 2005

Abstract—The neutral gas shielding model and neutral-gas–plasma shielding model are analyzed qualitatively. The main physical processes that govern the formation of the shielding gas cloud and, consequently, the ablation rate are considered. For the neutral gas shielding model, simple formulas relating the ablation rate and cloud parameters to the parameters of the pellet and the background plasma are presented. The estimates of the efficiency of neutral gas shielding and plasma shielding are compared. It is shown that the main portion of the energy flux of the background electrons is released in the plasma cloud. Formulas for the ablation rate and plasma parameters are derived in the neutral-gas–plasma shielding model. The question is discussed as to why the neutral gas shielding model describes well the ablation rate of the pellet material, although it does not take into account the ionization effects and the effects associated with the interaction of ionized particles with the magnetic field. The reason is that the ablation rate depends weakly on the energy flux of hot electrons; as a result, the attenuation of this flux by the electrostatic shielding and plasma shielding has little effect on the ablation rate. This justifies the use of the neutral gas shielding model to estimate the ablation rate (to within a factor of about 2) over a wide range of parameters of the pellet and the background plasma. © *2005 Pleiades Publishing, Inc.*

1. INTRODUCTION

Pellet injection into tokamak and stellarator plasmas is one of the most promising methods for fueling reactors. It is this circumstance that stimulates interest in studying the interaction of pellets with plasmas in tokamaks and stellarators. Pellets are also used to diagnose the tokamak plasma and to control its parameters.

The main parameter that determines the fueling efficiency of a tokamak reactor is the ablation rate of the pellet material. This is why the physical mechanisms that govern the ablation rate have been studied in many theoretical and experimental papers.

The pellet injected into the tokamak plasma evaporates due to heat fluxes carried by electrons and ions of the background plasma, producing a neutral gas cloud around it, which then ionizes (see figure). This cloud shields the pellet from the plasma particle flux, thereby governing the plasma particle energy loss and the ablation rate.

The first attempt to describe the ablation of a pellet was made by Parks *et al.* [1, 2], who developed the neutral gas shielding (NGS) model in studying the deceleration of the background plasma electrons in an expanding spherical neutral gas cloud. This model makes it possible to obtain simple formulas for the dependence of the ablation rate $\dot{N}$, cloud temperature T_N, and cloud density n_N on the pellet radius r_p, the temperature T_0 and density n_0 of the background plasma, and the atomic mass M_I of the pellet material [2]. The NGS model was later refined by many authors [3–11]. Although the NGS model is based on simple assumptions, it satisfactorily describes the ablation rates of the pellets and their

lifetimes in experiments on various fusion devices [12]. This is why the model is widely used to estimate the pellet penetration depths [13, 14]. On the other hand, the NGS model (at least, in [2]) does not take into account such factors as the shielding by the secondary (ablated) plasma, which expands preferentially along the magnetic field; the effects of the electrostatic shielding of the cloud [15–17]; and the two-dimensional character of neutral gas expansion. It is therefore surprising that the NGS model is capable of satisfactorily describing the experiment.

Because of the above internal contradictions of the pellet ablation model, attempts have been made to improve it. There are several possible ways of doing so.

First, it can be improved by a more accurate description of the deceleration of the background electrons with allowance for their energy distribution [3, 18]. For a hydrogen (or deuterium, or tritium) pellet, the sublimation energy is negligibly low, so that only an insignificant portion of the heat flux carried by the electrons that are in the tail of the distribution function reaches the pellet. Macaulay [7] showed that, in a model with a Maxwellian electron distribution function, the ablation rate is four times higher than that in a model with a monoenergetic electron beam.

The second way is to account for the geometric effects associated with the fact that hot electrons move along the magnetic field while the expansion of neutral gas is essentially spherical [3]. This approach makes it possible to incorporate the two-dimensional distribution of the ablation rate over the pellet surface and leads to a coefficient of about 2 in the expression for the ablation rate [3].
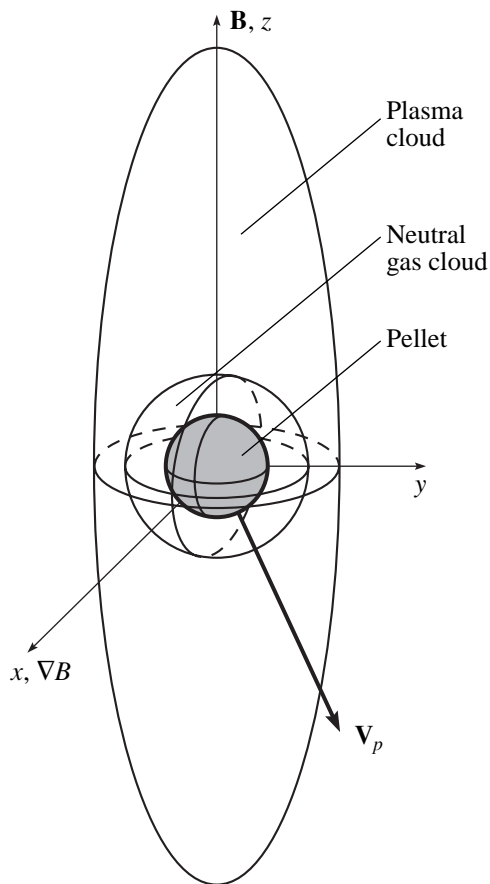
Schematic representation of the cloud surrounding a pellet.

Third, it was proposed to take into account the following circumstance. After ionization, the particles expand along the magnetic field rather that across it. This provides a description of the pellet shielding with allowance for the contribution of ionized particles. This approach (which also accounts for the Maxwellian distribution of the background electrons) was called the neutral-gas–plasma shielding (NGPS) model [18]; it was further developed in [6–10].

The fourth way to improve the model is to take into account atomic processes occurring at the pellet surface (the sublimation and dissociation of molecules [19]) and in the cloud (radiation emission and ionization), as well as the possible change in the shape of the pellet [4, 8, 11].

Fifth, it was pointed out that a cold cloud surrounding the pellet is charged negatively with respect to the background plasma. Parks *et al.* [2] considered the formation of an electric field inside the cloud that is necessary for the conduction current to balance the influx of hot electrons. This potential was found to be low in comparison to the energy of the hot electrons, so the formation of the electric field in the cloud was not incorporated into the NGS model [2]. In [15–17], it was

shown that, in one-dimensional geometry, the ambipolarity constraint and quasineutrality condition at the interface between the hot background plasma and the cold cloud lead to the onset of an electrostatic potential on the order of the temperature of the background plasma, $\Delta\Phi \approx (1\text{--}2)T_0/e$, which indicates a decrease in the energy flux by a factor of $\exp(\Delta\Phi)$. This effect was called electrostatic shielding. Its influence on the ablation rate was investigated, e.g., in [8–10].

Finally, the expansion dynamics of the cloud and its shape are highly sensitive to the plasma polarization in a nonuniform magnetic field and to the particle drift in crossed electric and magnetic fields [20]. The effect of the drift on the ablation rate is associated with the fact that the plasma is blown away from the cloud toward the low-field side of the torus. In [21], it was shown that this process occurs primarily with the plasma at the ends of a cigar-shaped cloud, so the shielding efficiency of the ionized part of the cloud changes only slightly. The particle drift influences not only the shielding efficiency but also the distribution of the material ablated from the injected pellet [22, 23]: the ablated material is displaced a long distance toward the low-field side of the torus. This displacement was observed in many experiments on present-day tokamaks [13, 14, 24, 25]. When the particle drift is taken into account, the problem of the ablation of the pellet material becomes three-dimensional.

The above effects were incorporated in various numerical [7–11, 21, 26] and analytical [3, 10] models of pellet ablation and pellet cloud evolution. There is now no model, however, capable of providing a sufficiently complete description of all of the above effects, because the ablation of the pellet material is a rather complicated process.

In the present paper, based on elementary physical estimates, we propose simple scalings describing the ablation rate of the pellet material as a function of the parameters of the pellet and the background plasma, as well as the cloud parameters. We estimate the relative contributions of the neutral gas cloud and plasma cloud to the shielding of the pellet. We also discuss the question of why the results of calculations based on the NGS model agree satisfactorily with the experimental data.

2. NEUTRAL GAS SHIELDING MODEL

The NGS model provides a simple physical pattern of the ablation of a pellet in a homogeneous plasma. In the model, it is assumed that the neutral gas cloud around the pellet (see figure) expands in a spherically symmetric fashion and is heated by the background plasma electrons that are decelerated within it. Let us show how a simple analysis can lead us to the sought-for scalings describing the ablation rate of the pellet and the cloud parameters as functions of the pellet radius r_p, the temperature T_0 and density n_0 of the background

plasma, and the atomic mass M_I of the material of the injected pellet.

Let r_* be the characteristic radius of the neutral gas cloud. Thus, the neutral gas density n_N and the expansion velocity V_* are related by

$$n_N \sim \frac{\dot{N}}{4\pi r_*^2 V_*}. \tag{1}$$

The energy flux of the background electrons and the divergence of this flux are on the order of $q_{\text{inc}} \sim \dfrac{n_0 T_0^{3/2}}{m_e^{1/2}}$ (where m_e is the mass of an electron) and $\nabla \cdot \mathbf{q}_{\text{inc}} \sim \dfrac{n_0 T_0^{3/2}}{r_* m_e^{1/2}}$, respectively. The latter estimate represents the heat that is released within the cloud and goes primarily into the expansion of the cloud, so we have $\nabla \cdot \mathbf{q}_{\text{inc}} \sim n_N T_N \nabla \cdot \mathbf{V}$. Insignificant energy losses by ionization and radiation emission can be ignored. The time derivatives are absent because a steady-state expansion is considered. Using the estimate $\nabla \cdot \mathbf{V} \sim \dfrac{V_*}{r_*}$, we obtain

$$\frac{n_0 T_0^{3/2}}{r_* m_e^{1/2}} \sim \frac{n_N T_N V_*}{r_*}. \tag{2}$$

It is known [27] that the deceleration of a monoenergetic electron beam in the cloud by Coulomb collisions is described by the equation

$$\frac{dV}{dt} = -\frac{4\pi Z(Z+1)e^4 n \Lambda}{m_e^2 V^3} V, \tag{3}$$

where n is the instantaneous neutral density and Λ is the Coulomb logarithm. The factor $Z(Z+1)$ arises because of the following circumstance: along its path, a fast electron collides with Zn electrons (either free or bound), whose contribution to the cross section for Coulomb collisions is equal to $Zne^4 \cdot 1^4$, and with n nuclei, whose contribution is $nZ^2 \cdot 1^2 e^4$ (here, the number of electrons and nuclei is normalized to a unit volume). In our elementary dimensional analysis, we ignore inelastic collisions and the electron distribution over pitch angles.

In Eq. (3), we make the replacement $\dfrac{d}{dt} = V\dfrac{d}{ds}$ (where s is the coordinate along the path of an electron) and integrate over s to obtain

$$\frac{1}{4}V^4 \Big|_{V_0}^{V^{(\infty)}} = \frac{4\pi Z(Z+1)e^4 \Lambda}{m_e^2} \int_{s_0}^{\infty} n\, ds, \tag{4}$$

where s_0 is the coordinate corresponding to the pellet surface, V_0 is the electron velocity at this surface, and

$V^{(\infty)}$ is the initial electron velocity in the background plasma. Since the sublimation energy in hydrogen is small, the shielding should be efficient enough for the energy of the electrons that reach the pellet to be very low. Consequently, we can set $V_0 = 0$. The electrons that reach the pellet have initial velocities higher than the electron thermal velocity $V_T = \sqrt{2T_0/m_e}$ [28]; these are the electrons that are in the tail of the distribution function. In order to take this effect into account, we will use the estimate $V^{(\infty)} = \alpha V_T$ and will retain the factor $\alpha > 1$ in further manipulations. Note that the case $\alpha = 1$ corresponds to the approximation of the Maxwellian electron distribution by a monoenergetic electron beam with an energy equal to the electron temperature. This approach was used in the earliest versions of the NGS model [2].

The integral $\int_{s_0}^{\infty} n\, ds$ can be estimated in order of magnitude by $n_N r_*$, so relationship (4) can be rewritten as

$$\alpha^4 T_0^2 \sim 4\pi Z(Z+1)e^4 \Lambda n_N r_*. \tag{5}$$

This relationship implies that the mean free path of the background electrons should be on the order of the cloud radius r_*.

The set of Eqs. (1), (2), and (5) should be closed by the additional assumption that the cloud expands at the sound speed,

$$V_* = \sqrt{T_N/M_I}, \tag{6}$$

where $M_I = \mu_I m_p$, with m_p being the mass of a proton. In the approach utilized here, supplementing this relationship with the numerical coefficient $\gamma = 7/5$ for hydrogen molecules (deuterium) or with $\gamma = 5/3$ for atoms into which the molecules are dissociated would lead to an excessive accuracy.

With the same accuracy, we can assume that $r_* = r_p$ because the pellet radius is the only characteristic dimension in the problem under consideration (the mean free path of the background electrons is equal in order of magnitude to r_p). After some algebra, from Eqs. (1), (2), (5), and (6) we obtain

$$\dot{N} = \left(\frac{4\pi}{e^8 m_e^{1/2} \Lambda^2 m_p}\right)^{\frac{1}{3}} \alpha^{\frac{8}{3}} (Z(Z+1))^{-\frac{2}{3}} r_p^{\frac{4}{3}} n_0^{\frac{1}{3}} T_0^{\frac{11}{6}} \mu_I^{-\frac{1}{3}}, \tag{7}$$

$$T_N = \left(16\pi^2 e^8 \frac{m_p}{m_e} \Lambda^2\right)^{\frac{1}{3}} \alpha^{-\frac{8}{3}} (Z(Z+1))^{\frac{2}{3}} r_p^{\frac{2}{3}} n_0^{\frac{2}{3}} T_0^{-\frac{1}{3}} \mu_I^{\frac{1}{3}}, \tag{8}$$

$$n_N = \frac{\alpha^4 T_0^2}{4\pi e^4 \Lambda (Z(Z+1)) r_p}. \tag{9}$$

The temperature T_0 of the background plasma is expressed in kiloelectronvolts, the density n_0 of the background plasma in units of 10^{13} cm^{-3}, the pellet radius in millimeters, the ablation rate in reciprocal seconds, the temperature T_N of the neutral gas cloud in electronvolts, and the density n_N of the neutral gas cloud in units of 10^{18} cm^{-3}. We then explicitly evaluate the constants in order to convert expressions (7)–(9) into a form suitable for calculations:

$$\dot{N} = 7.2 \times 10^{23} \alpha^{\frac{8}{3}} (Z(Z+1))^{-\frac{2}{3}} r_p^{\frac{4}{3}} n_0^{\frac{1}{3}} T_0^{\frac{11}{6}} \mu_I^{-\frac{1}{3}}, \quad (10)$$

$$T_N = 2.33 \alpha^{-\frac{8}{3}} (Z(Z+1))^{\frac{2}{3}} r_p^{\frac{2}{3}} n_0^{\frac{2}{3}} T_0^{-\frac{1}{3}} \mu_I^{\frac{1}{3}}, \quad (11)$$

$$n_N = 3.84 \frac{\alpha^4 T_0^2}{(Z(Z+1)) r_p}. \quad (12)$$

These are just the sought-for scalings. They differ from the so-called Parks scalings [2] in the powers of the temperature (the Parks scalings are such that $\dot{N} \sim T_0^{1.64}$, $T_N \sim T_0^{-0.14}$, and $n_N \sim T_0^{1.68}$). This difference arises because, in [2], use was made of the results of more accurate calculations of the cross section for electron scattering by neutral atoms [1], rather than of the simple Rutherford cross section $\sigma \sim V^{-4}$. If we set $\alpha \approx 3$, we see that the numerical coefficients approximately coincide with those presented in [2]. Recall that the fraction of electrons that have passed through the cloud and reached the pellet is equal to $1 - \mathrm{erf}(\alpha)$.

Formulas (7)–(9) describe the qualitative dependence of the ablation rate and cloud parameters on the parameters of the pellet and the background plasma.

The NGS model was further developed by various authors. Kuteev *et al.* [3] and Houlberg *et al.* [18] proposed to take into account the Maxwellian electron distribution function. In [3, 7, 11], two-dimensional models were constructed in which hot electrons were assumed to fly along the magnetic field whereas the expansion of the cloud was assumed to be spherically symmetric (i.e., the cloud expanded exactly in the radial direction).

In carrying out numerical simulations with allowance for sublimation and dissociation, Macaulay [7] analyzed the results of a model supplemented with the assumptions that the electron flow is directed along the magnetic field and that the electrons obey a Maxwellian distribution and compared them to formulas analogous to relationships (7)–(9) and with the Parks scalings [2]. He confirmed the conclusion of the preceding paper by Kuteev *et al.* [3] that accounting for a Maxwellian electron distribution increases the ablation rate by a factor of 4; however, taking into account the geometric effects (the directional character of the electron flow) and atomic processes, in turn, reduces the ablation rate by a

factor of 2. The resulting scalings thereby turn out to be very similar to the Parks scalings [2].

It should be noted, however, that with such improvements, in which only one or several of the above effects influencing the ablation of the pellet material are taken into account, as well as with the original Parks model, there remains an uncertainty in the numerical coefficient. In fact, each of these effects leads to a correction to the numerical coefficient in expression (7) for the ablation rate and to the powers of the parameters in the scalings. However, the other effects lead to a correction of the same order of magnitude and thereby can change this numerical coefficient, as well as the powers of the parameters, by an amount comparable to that introduced by one of them.

The NGS model is incomplete because it does not incorporate a wide class of phenomena, such as the ejection of molecules and clusters from the pellet surface, their dissociation and ionization, their interaction with the tokamak magnetic field, the transition from spherically symmetric expansion of the cloud near the pellet to the expansion preferentially along the magnetic field, the magnetic field inhomogeneity, the pitch angle scattering, inelastic processes, and the details of the electrostatic shielding. The question as to why this model nevertheless provides a successful description of experiments will be discussed below.

3. NEUTRAL-GAS–PLASMA SHIELDING MODEL

In this section, we will apply the above qualitative analysis to the NGPS model, which is a continuation of the NGS model. One of the purposes of Houlberg *et al.* [18]—the originators of the NGPS model—was to take into account the contribution of the plasma cloud surrounding the neutral gas cloud to the shielding of the pellet (see figure).

We again assume that the cloud of neutral particles around the pellet expands in a spherically symmetric fashion. However, calculations [6, 29] show that, when the degree of ionization becomes relatively high (about 5%), the Lorentz force created in the interaction of the diamagnetic currents with the magnetic field becomes strong enough to counterbalance the pressure gradient force and the cloud stops expanding in the direction transverse to the field. The cloud further expands preferentially along the magnetic field (the transverse drift and diffusion are ignored); as a result, it acquires a cigar shape, observed in all pellet injection experiments (see, e.g., [30]). The transverse size of the cloud is precisely (to within a factor on the order of unity [29]) the distance the neutral particles travel before they become ionized. We denote this distance by l_i.

We assume that the background electrons are decelerated both in the neutral gas cloud (with the characteristic density n_N and characteristic temperature T_N) and in the plasma cloud (with the characteristic density n_p

and characteristic temperature T_p). In this section, we ignore electrostatic shielding; its effect on the ablation of the pellet material will be considered below. Since the expansion of neutral atoms is spherically symmetric, we can, as before, use formula (1), in which we replace the expansion velocity V_* with the sound speed $c_{sN} = \sqrt{T_N/M_I}$ corresponding to the temperature of the neutral gas cloud. As a result, we obtain

$$n_N \sim \frac{\dot{N}}{4\pi r_p^2 c_{sN}}. \tag{13}$$

Upon ionization, the ions and electrons, as well as the remaining neutrals, fly along the magnetic field. Under the assumption that they fly within a cylindrical channel of radius l_i, we obtain from the particle conservation law the relationship

$$n_p \sim \frac{\dot{N}}{2\pi l_i^2 c_{sp}}, \tag{14}$$

where $c_{sp} = \sqrt{T_p/M_I}$ is the sound speed in the plasma cloud and the factor 2 reflects the fact that the particles within the cylinder expand in two opposite directions.

Let the fraction of the background electron flux q_{inc} that reaches the neutral gas cloud be β (in this case, the fraction of the background electrons that are decelerated in the plasma cloud is equal to $(1 - \beta)q_{inc}$), and let all the energy released within the neutral gas cloud go into the expansion of the cloud. By analogy with relationship (2), we then obtain

$$\beta \frac{n_0 T_0^{3/2}}{r_* m_e^{1/2}} \sim \frac{n_N T_N c_{sN}}{r_*}. \tag{15}$$

In the plasma cloud, the energy balance equation has the form

$$(1 - \beta)\frac{n_0 T_0^{3/2}}{l_z m_e^{1/2}} \sim \frac{n_p T_p c_{sp}}{l_z} + \frac{n_p E_i c_{sp}}{l_z}, \tag{16}$$

where l_z is the longitudinal size of the cloud and E_i is the ionization energy (for hydrogen, we have $E_i = 13.6$ eV). The second term on the right-hand side of relationship (16) shows that the energy acquired by an originally neutral atom as it travels a distance equal to the cloud's characteristic size is sufficient for its ionization. In the original NGPS model [18], it was proposed to estimate the longitudinal size of the plasma cloud by

$$l_z = c_{sp}\frac{l_i}{V_p}. \tag{17a}$$

This estimate corresponds to the assumption that ionized particles are confined by the magnetic field, so, in the reference frame associated with the pellet, they lag behind the pellet. Accordingly, estimate (17a) gives the distance the particles travel at the sound speed during

the time required for the pellet to move a distance equal to the transverse size of the cloud.

However, for the pellet parameters in present-day tokamaks, a more realistic situation is that in which the drift of ionized particles in a nonuniform magnetic field leads to plasma polarization; as a result, the particles drift toward the low-field side of the torus with the acceleration $g = 2\frac{c_{sp}^2}{R}$, where R is the tokamak major radius.

Hence, as the pellet travels a distance equal to the transverse size of the cloud, the ionized particles travel along the magnetic field a distance of only

$$l_z = \sqrt{l_i R}. \tag{17b}$$

In what follows, we will discuss both of these alternative versions.

The possible effect of the poloidal drift in the radial electric field on the shape of the cloud (and, accordingly, on its longitudinal size) was discussed in [8]. It is likely, however, that the radial electric field should be almost completely shielded by the cloud's self-field (which ensures the common motion of the pellet and of the cloud across the magnetic field, see [20] for details) and should manifest itself only at the edges of the cloud. This is why the effect of the poloidal drift on the ablation rate of the pellet material seems to be quantitatively unimportant and thereby will be ignored in further analysis.

In the case in question, the law by which the hot electrons are decelerated, i.e., relationship (4), remains valid. It is only necessary to represent the integral on its right-hand side as the sum of the integrals over the neutral gas cloud and plasma cloud, $\int_{s_0}^{\infty} n\,ds \approx n_N r_p + n_p l_z$. Substituting this estimate into relationship (4) (and again setting $V_0 = 0$ and $V^{(\infty)} = \alpha\sqrt{2T_0/M_I}$), we obtain

$$\alpha^4 T_0^2 \sim 4\pi Z(Z+1)e^4 \Lambda(n_N r_* + n_p l_z). \tag{18}$$

In order to close the set of equations, we need two more relationships. One of them is derived from the assumption that the cloud expansion is continuous, i.e., is not accompanied by the onset of discontinuities and shock waves; accordingly, the pressures in the neutral gas cloud and in the plasma cloud should be of the same order of magnitude:

$$n_N T_N \sim n_p T_p. \tag{19}$$

Another relationship can be obtained by noting that, since the ionization rate depends strongly on temperature, the temperature of the plasma cloud remains constant from the beginning of ionization until all the neutral atoms have become ionized. Hence, the last of the required relationships has the form

$$T_p = \text{const}. \tag{20}$$

Setting $T_p = 1$ eV, we can ignore the first term on the right-hand side of Eq. (16)—the one that describes the expansion and heating of the cloud—and retain only the second term, which describes energy losses by ionization.

Equations (15), (16), and (19) then yield the following relationships between the parameters of the neutral gas cloud and those of the plasma cloud:

$$\frac{T_N}{T_p} \sim \left(\frac{\beta E_i}{(1-\beta)T_p}\right)^2, \tag{21}$$

$$\frac{n_p}{n_N} \sim \left(\frac{\beta E_i}{(1-\beta)T_p}\right)^2. \tag{22}$$

Using formulas (13), (14), and (22), we obtain the following relationship between the pellet radius and the transverse size of the cloud:

$$\frac{l_i^2}{r_p^2} \sim 2\frac{(1-\beta)T_p}{\beta E_i}. \tag{23}$$

Combining formulas (13), (14), and (18) gives

$$\alpha^4 T_0^2 \sim 4Z(Z+1)e^4\Lambda\dot{N}\left(\frac{1}{4r_p c_{sN}} + \frac{l_z}{2l_i^2 c_{sp}}\right). \tag{24}$$

Using alternative relationships (17a) and (17b) between l_z and l_i, we arrive at the following two alternative sets of equations for $\dot{N}$ and β:

$$\begin{cases} \dfrac{n_0 T_0^{3/2}}{m_e^{1/2}} = \dfrac{\dot{N}T_p\beta E_i^2}{4\pi r_p^2(1-\beta)^2 T_p} \\[2ex] \alpha^4 T_0^2 = \dfrac{4(Z(Z+1))e^4\Lambda\dot{N}}{r_p} \\[2ex] \times\left(\dfrac{(1-\beta)T_p}{4\beta E_i}\sqrt{\dfrac{M_I}{T_p}} + \dfrac{1}{2\sqrt{2}V_p}\sqrt{\dfrac{\beta E_i}{(1-\beta)T_p}}\right), \end{cases} \tag{25a}$$

$$\begin{cases} \dfrac{n_0 T_0^{3/2}}{m_e^{1/2}} = \dfrac{\dot{N}T_p\beta E_i^2}{4\pi r_p^2(1-\beta)^2 T_p} \\[2ex] \alpha^4 T_0^2 = \dfrac{(Z(Z+1))e^4\Lambda\dot{N}}{r_p\sqrt{T_p/M_I}} \\[2ex] \times\left(\dfrac{(1-\beta)T_p}{\beta E_i} + \sqrt{\dfrac{R}{2r_p}}\left(\dfrac{\beta E_i}{(1-\beta)T_p}\right)^{3/4}\right), \end{cases} \tag{25b}$$

respectively. Eliminating the ablation rate $\dot{N}$ in Eqs. (25a) and (25b), we obtain the following two alternative equations for β:

$$A_s = \frac{(1-\beta)^2}{\beta}\left(\frac{1-\beta}{\beta}B_s + \sqrt{\frac{\beta}{1-\beta}}C_s\right), \tag{26a}$$

$$A_d = \frac{(1-\beta)^2}{\beta}\left(\frac{1-\beta}{\beta}\frac{T_p}{E_i} + \sqrt{\frac{R}{2r_p}}\left(\frac{\beta}{(1-\beta)}\frac{E_i}{T_p}\right)^{3/4}\right), \tag{26b}$$

where $A_s = \dfrac{\alpha^4 T_0^{1/2} m_e^{1/2} E_i^2}{16\pi e^4\Lambda(Z(Z+1))r_p n_0 T_p}$, $B_s = \dfrac{T_p}{4E_i}\sqrt{\dfrac{M_I}{T_p}}$,

$C_s = \dfrac{1}{2\sqrt{2}V_p}\sqrt{\dfrac{T_p}{E_i}}$, and $A_d =$

$\dfrac{\alpha^4 T_0^{1/2} m_e^{1/2} E_i^2}{4\pi e^4\Lambda(Z(Z+1))r_p M_I^{1/2} n_0 T_p^{1/2}}.$

Since Eqs. (26a) and (26b) are difficult to solve analytically, we solved them numerically for two sets of plasma and pellet parameters typical of the present-day tokamaks and of the projected ITER device.

For the parameters of the present-day tokamaks, namely, $T_0 = 1$ keV, $T_p = 1$ eV, $Z = 1$, $r_p = 0.1$ cm, $n_0 = 3 \times 10^{13}$ cm^{-3}, $\mu_I = 2$, $V_p = 5 \times 10^4$ cm/s, and $R = 150$ cm, Eq. (26a) has the solution $\beta_s = 0.013$ and Eq. (26b) has the solution $\beta_d = 0.014$. Both these solutions were calculated for $\alpha = 3$.

This numerical analysis shows that the electrons of the background plasma lose a significant portion of their energy in the plasma cloud rather than in the neutral gas cloud. In such circumstances, however, the contributions of the neutral gas and plasma clouds to the shielding of the pellet turn out to be approximately the same (in order to see this, compare the two terms in parentheses in Eqs. (26)).

For the parameters of the future tokamak reactor, namely, $T_0 = 10$ keV, $T_p = 1$ eV, $Z = 1$, $r_p = 0.3$ cm, $n_0 = 10^{14}$ cm^{-3}, $\mu_I = 2$, $V_p = 15 \times 10^4$ cm/s, and $R = 620$ cm, the solutions are $\beta_s = 0.02$ and $\beta_d = 0.38$. Both these solutions were again calculated for $\alpha = 3$.

Using the smallness of the parameter β, we can obtain approximate scalings that relate the ablation rate and the parameters of the neutral gas cloud to the plasma and pellet parameters and are analogous to scalings (7)–(9). In fact, for $\beta \ll 1$, we can assume that

$$\beta = \frac{T_p}{E_i}\sqrt{\frac{T_N}{T_p}}, \tag{27}$$

and, instead of relationship (2), can write

$$\beta\frac{n_0 T_0^{3/2}}{r_* m_e^{1/2}} \sim \frac{n_N T_N V_*}{r_*}. \tag{28}$$

Combining formulas (1), (5), (6), (27), and (28) (in fact, we are considering the neutral gas cloud in the same manner as in Section 2, but with allowance for the fact that, after the background electrons have passed

through the plasma cloud, their energy flux is attenuated by a factor of β), we obtain

$$
\dot{N} = \frac{2\alpha^2}{e^2}\sqrt{\frac{\pi}{\Lambda}}\sqrt[4]{\frac{1}{m_e m_p}}(Z(Z+1))^{-\frac{1}{2}}
$$
$$
\times r_p^{\frac{3}{2}} n_0^{\frac{1}{2}} T_0^{\frac{7}{4}} \mu_I^{-\frac{1}{4}} T_p^{\frac{1}{4}} E_i^{-\frac{1}{2}}, \tag{29}
$$

$$
T_N = 4\pi\Lambda e^4 \sqrt{\frac{m_p}{m_e}}\alpha^{-4}(Z(Z+1)) r_p n_0 T_0^{-\frac{1}{2}} \mu_I^{\frac{1}{2}} T_p^{\frac{1}{2}} E_i^{-1}, \tag{30}
$$

$$
n_N = \frac{\alpha^4 T_0^2}{4\pi\Lambda e^4 (Z(Z+1)) r_p}, \tag{31}
$$

$$
\beta = (4\pi\Lambda)^{\frac{1}{2}}\left(\frac{m_p}{m_e}\right)^{\frac{1}{4}} e^2 \alpha^{-2}(Z(Z+1))^{\frac{1}{2}}
$$
$$
\times n_0^{\frac{1}{2}} T_0^{-\frac{1}{4}} r_p^{\frac{1}{2}} \mu_I^{\frac{1}{4}} T_p^{\frac{3}{4}} E_i^{\frac{3}{2}}, \tag{32}
$$

or

$$
\dot{N} = 0.89 \times 10^{24}\alpha^2 (Z(Z+1))^{-\frac{1}{2}}
$$
$$
\times r_p^{\frac{3}{2}} n_0^{\frac{1}{2}} T_0^{\frac{7}{4}} \mu_I^{-\frac{1}{4}} T_p^{\frac{1}{4}} E_i^{-\frac{1}{2}}, \tag{33}
$$

$$
T_N = 3.54\alpha^{-4}(Z(Z+1)) r_p n_0 T_0^{-\frac{1}{2}} \mu_I^{\frac{1}{2}} T_p^{\frac{1}{2}} E_i^{-1}, \tag{34}
$$

$$
n_N = 3.84\frac{\alpha^4 T_0^2}{(Z(Z+1)) r_p}, \tag{35}
$$

$$
\beta = 1.88\alpha^{-2}(Z(Z+1))^{\frac{1}{2}} n_0^{\frac{1}{2}} T_0^{-\frac{1}{4}} r_p^{\frac{1}{2}} \mu_I^{\frac{1}{4}} T_p^{\frac{3}{4}} E_i^{\frac{3}{2}}. \tag{36}
$$

Here, the temperature T_0 of the background plasma is expressed in kiloelectronvolts, the density n_0 of the background plasma in units of 10^{13} cm^{-3}, the pellet radius in millimeters, the ablation rate in reciprocal seconds, the temperature T_N of the neutral gas cloud and the ionization potential E_i in electronvolts, and the density n_N of the neutral gas cloud in units of 10^{18} cm^{-3}.

For $T_0 = 1$ keV, $T_p = 1$ eV, $Z = 1$, $r_p = 0.1$ cm, $n_0 = 3 \times 10^{13}$ cm^{-3}, and $\mu_I = 2$ (and again for $\alpha = 3$), scalings (33)–(36) yield $\dot{N} = 2.2 \times 10^{24}$ s^{-1}, $T_N = 0.027$ eV, $n_N = 1.51 \times 10^{20}$ cm^{-3}, and $\beta = 0.12$. For comparison, scalings (10)–(12) with the same parameter values give $\dot{N} = 3.3 \times 10^{24}$ s^{-1}, $T_N = 1.53$ eV, and $n_N = 3.0 \times 10^{19}$ cm^{-3} ($\alpha = 2$). Note that formulas (10) and (33) yield approximately the same values of the ablation rate and the values of the density of the neutral gas cloud that are given by formulas (9) and (31) differ by a factor of $Z(Z + 1) = 2$. At the same time, the NGS model

highly overestimates the temperature of the neutral gas cloud: at temperatures higher than 1 eV, the ionization processes and the interaction of the ionized particles with the magnetic field become significant. However, when the plasma shielding is taken into account, the temperature values become more realistic.

4. EFFECT OF THE ELECTROSTATIC SHIELDING

Let us now consider how the electrostatic shielding affects the ablation rate of the pellet material. Recall that the shielding effect occurs at the interface between the background plasma and the cold cloud surrounding the pellet and serves to reduce the electron heat flux and to ensure that the net current flowing into the cloud be zero.

If the potential drop at the interface between the background plasma and the cloud is equal to $\Delta\Phi$, then the energy flux density of the originally Maxwellian electrons after they have passed through the shielding layer is reduced by a factor of $\exp\left(\frac{e\Delta\Phi}{T_0}\right)$, the mean electron energy being unchanged. In other words, the electron distribution function remains Maxwellian with the same temperature but with a density reduced by a factor of $\exp\left(\frac{e\Delta\Phi}{T_0}\right)$. In this case, the mean free path of the background electrons, of course, does not change but their number becomes smaller, indicating a lower energy release in the cloud around the pellet.

Formally, this implies that, in calculating the ablation rate, we must replace the background plasma density n_0 in all the formulas of Section 3 with $n_0 \exp\left(\frac{e\Delta\Phi}{T_0}\right)$.

In a one-dimensional approach, the shielding potential was estimated in [8, 15–17]. Later on, an attempt to take into account the effect of fast ions was made by Kuteev and Kostrukov [9], who showed that this potential is on the order of several units of the background plasma temperature, $e\Delta\Phi \sim T_0$. In their numerical simulations, Garzotti et al. [10] chose the value $e\Delta\Phi = 2T_0$.

Within the cloud, the current of hot electrons to the pellet is neutralized by the conduction current of cold electrons, which is directed outward from the pellet. This conduction current in the cloud also is maintained by a potential drop, which, however, is much lower than the energy of the hot electrons, as follows from the estimates made by Parks [2] and from the results of numerical simulations carried out by Lengyel et al. [26].

Hence, the main effect of the electrostatic shielding is an effective decrease in the background plasma density. Following Garzotti et al. [10], in our simple model,

we can set $e\Delta\Phi = 2T_0$. In this case, formulas (33)–(36) become

$$\dot{N} = 0.33 \times 10^{24} \alpha^2 (Z(Z+1))^{-\frac{1}{2}} r_p^{\frac{3}{2}} n_0^{\frac{1}{2}} T_0^{\frac{7}{4}} \mu_I^{-\frac{1}{4}} T_p^{\frac{1}{4}} E_i^{-\frac{1}{2}}, \quad (37)$$

$$T_N = 0.32 \alpha^{-4} (Z(Z+1)) r_p n_0 T_0^{-\frac{1}{2}} \mu_I^{\frac{1}{2}} T_p^{\frac{1}{2}} E_i^{-1}, \quad (38)$$

$$n_N = 3.84 \frac{\alpha^4 T_0^2}{(Z(Z+1)) r_p}, \quad (39)$$

$$\beta = 0.69 \alpha^{-2} (Z(Z+1))^{\frac{1}{2}} n_0^{\frac{1}{2}} T_0^{-\frac{1}{4}} r_p^{\frac{1}{2}} \mu_I^{\frac{1}{4}} T_p^{\frac{3}{4}} E_i^{\frac{3}{2}}. \quad (40)$$

5. DISCUSSION OF THE RESULTS

In Section 2, we have presented the simplest qualitative estimates of the ablation rate of the pellet material under the assumption that the pellet is surrounded only by a neutral gas cloud. These estimates, which underlie the NGS model, reflect the main processes occurring in the neutral gas cloud around the pellet, specifically, the expansion of the cloud and the heating and deceleration of the background electrons in it.

In Section 3, we have obtained analogous qualitative estimates with allowance for the shielding of the pellet by a plasma cloud produced as a result of the ionization of the neutral particles in the gas cloud. These simple estimates show that only a small portion (about 1–2%) of the energy flux of the background electrons reaches the neutral gas cloud while essentially all the electron energy flux is attenuated within the plasma cloud. This is why the NGS model, which does not take into account the presence of the plasma cloud, is incomplete.

Scalings (29), (33), and (37), which have been obtained for the ablation rate of the pellet material with allowance for the plasma shielding, are very similar to the Parks scalings [1] and to the scalings derived by Garzotti et al. [10]. The similarity concerns the powers of the corresponding parameters of the background plasma and of the pellet. Let us make a more detailed comparison of formula (37) to the following formula from [10]:

$$\frac{dr_p}{dt} = 1.2882 \prod_i P_i^{\alpha_i + \sum_i \beta_{ij} P_i}. \quad (41)$$

This scaling was obtained via numerical simulations of a wide diversity of experiments from the International Pellet Ablation Database (IPADBase) [12] by adjusting the coefficients in the powers of the parameters in a way to provide the best possible description of the experimental results. In the simulations, the electrostatic shielding was taken into account by choosing the shielding potential such that $e\Delta\Phi = 2T_0$. The numerical results and, accordingly, the scalings were shown to agree with the experiments.

Ignoring the cross dependence on the quantities in the powers of the parameters in scaling (41) (the corresponding coefficients are small), we arrive at the following expression for the ablation rate (we have already set $\mu_I = 2$, $R = 1.5$ m, and $B = 2.5$ T):

$$\dot{N} = 1.57 \times 10^{24} r_p^{1.41} n_0^{0.40} T_0^{1.71}, \quad (42)$$

where the temperature T_0 of the background plasma is expressed in kiloelectronvolts, the density n_0 of the background plasma is in units of 10^{13} cm^{-3}, and the pellet radius is given in millimeters. For $T_0 = 1$ keV, $r_p = 0.1$ cm, and $n_0 = 3 \times 10^{13}$ cm^{-3}, formula (42) yields $\dot{N} = 2.5 \times 10^{24}$ s^{-1}.

Substituting the parameter values $\alpha = 3$, $Z = 1$, $T_p = 1$ eV, $E_i = 13.6$ eV, and $\mu = 2$ into scaling (37) gives

$$\dot{N} = 0.47 \times 10^{24} r_p^{\frac{3}{2}} n_0^{\frac{1}{2}} T_0^{\frac{7}{4}}, \quad (43)$$

where the temperature T_0 of the background plasma is also expressed in kiloelectronvolts, the density n_0 of the background plasma is in units of 10^{13} cm^{-3}, and the pellet radius is in millimeters. For $T_0 = 1$ keV, $r_p = 0.1$ cm, and $n_0 = 3 \times 10^{13}$ cm^{-3}, formula (43) yields an ablation rate of $\dot{N} = 0.82 \times 10^{24}$ s^{-1}. For comparison, with the same parameter values, the corresponding Parks scaling [2] gives $\dot{N} = 1.06 \times 10^{24}$ s^{-1}.

We thus see that scaling (37) also agrees satisfactorily with the scaling in the NGS model and is capable of describing the pellet injection experiments.

The remaining cloud parameters calculated from formulas (38)–(40) are as follows: $T_N = 0.037$ eV, $n_N = 7.5 \times 10^{19}$ cm^{-3}, and $\beta = 0.004$. The plasma cloud density estimated from formula (22) is equal to $n_p \approx 5.2 \times 10^{17}$ cm^{-3}. These parameter values agree satisfactorily with the measurement data obtained by Müller et al. [31] (a plasma cloud temperature of (1–4) eV and a plasma cloud density of $(1.0–3.5) \times 10^{17}$ cm^{-3}) and with the numerical results calculated by Pegourie and Picchiotino [6] and Senichenkov et al. [21].

Since the NGS model does not take into account the strong plasma and electrostatic shieldings, the fact that it agrees with formulas (37) and (42) appears at first glance to be surprising. This can be explained as follows.

Let the energy flux of the hot electrons that have passed through the regions of the electrostatic and plasma shielding and have reached the neutral gas cloud just near the pellet be attenuated by a factor of β (this is precisely the above definition of the parameter β—the fraction of the background electrons that reach the neutral gas cloud). In this case, in the analysis car-

ried out in Section 2, we must formally replace n_0 with βn_0. However, the ablation rate $\dot{N}$ depends weakly on the background plasma density n_0, $\dot{N} \sim n_0^{\frac{1}{3}}$; consequently, when the electron energy flux is attenuated by a factor of β, the ablation rate decreases by a factor of only $\beta^{1/3}$, i.e., by a considerably smaller amount.

Our rough estimates (see formula (37)) yield $\beta = 0.004$ and, accordingly, $\beta^{1/3} \approx 0.15$. Hence, when both the electrostatic and plasma shieldings are taken into account, the ablation rate is six to seven times lower than that predicted by the NGS model without allowance for the kinetic effects. However, when the electron distribution function is assumed to be Maxwellian, the ablation rate becomes higher by approximately the same factor ($\alpha = 3$, $\alpha^2 = 9$). This indicates that the coefficient α effectively takes into account the fact that the cloud should be thick enough to stop the hottest electrons from the tail of the Maxwellian distribution function.

In this case, it is important that, for the parameters chosen above (namely, those of the present-day tokamaks), the contributions of the neutral gas cloud and plasma cloud to the shielding of the pellet turn out to be approximately the same; consequently, ignoring the thickness of the plasma cloud leads us to an error of about a factor of 2.

Note that, since the density of the neutral gas cloud is proportional to α^4 (see formula (31)), accounting for the kinetic effects (by introducing the coefficient α) substantially increases the shielding efficiency of the neutral gas cloud, in agreement with the results obtained by Kuteev and Tsendin [28].

As a result, the ablation rates calculated from the Parks scaling and from scaling (37) proposed here differ by a factor of less than 2, so our rough scaling can well be used for estimates. Note finally that numerous improvements and refinements of the NGS model do not lead to a greater reliability of the predictions in comparison to that provided by scalings (7)–(9) because, by accounting for, e.g., the variable shape of the pellet while simultaneously ignoring the plasma shielding, it is impossible to appreciably increase the accuracy of the model.

6. CONCLUSIONS

In this paper, we have qualitatively analyzed the NGS and NGPS models and have indicated the main physical processes that govern the formation of the shielding cloud and, accordingly, the ablation rate of the pellet material. In the NGS model, these are the expansion of the cloud and its heating, as well as the deceleration of the background plasma electrons in it. This model makes it possible to obtain simple analytic formulas relating the ablation rate and cloud parameters to the parameters of the background plasma and pellet parameters. For the NGPS model, we have carried out a similar analysis with allowance for the deceleration of the background electrons in the plasma cloud surrounding the neutral gas cloud. We have considered two cases: that in which ionized particles are stopped by the magnetic field and that in which they drift toward the low-field side of the torus. For both cases, we have compared the estimates of the efficiency of neutral gas shielding and plasma shielding and have shown that the main portion of the energy flux of the background electrons is released in the plasma cloud. We have derived formulas for the ablation rate and plasma parameters in the NGPS model and have found that the ablation rate is approximately the same as that in the NGS model. At the same time, the NGPS model has been found to yield more reasonable parameters of the neutral cloud than does the NGS model.

We have discussed the question of why the NGS model describes well the ablation rate of the pellet material, although it does not take into account the ionization effects and the effects related to the interaction of ionized particles with the magnetic field. The reason is that the ablation rate depends weakly on the density of the hot electrons and, consequently, on their energy flux, which is proportional to their density. As a result, the attenuation of this flux by the electrostatic shielding and plasma shielding has only a slight influence on the ablation rate. This justifies the use of the NGS model to estimate the ablation rate (to within a factor of about 2).

Hence, in spite of its simplicity, the NGS model can be used to estimate the ablation rates of pellets over a wide range of the parameters of the pellet and the background plasma. The NGS model, however, is inapplicable for calculating the parameters of the cloud (especially its temperature), so it is necessary to use more elaborate and accurate models.

REFERENCES

1. P. B. Parks, R. J. Turnbull, and C. A. Foster, Nucl. Fusion **17**, 539 (1977).
2. P. B. Parks and R. J. Turnbull, Phys. Fluids **21**, 1735 (1978).
3. B. V. Kuteev, A. P. Umov, and L. D. Tsendin, Fiz. Plazmy **11**, 409 (1985) [Sov. J. Plasma Phys. **11**, 236 (1985)].
4. S. M. Egorov, B. V. Kuteev, I. V. Miroshnikov, *et al.*, Nucl. Fusion **32**, 2025 (1992).
5. B. Pegourie, J.-M. Picchiotino, H.-M. Drawin, *et al.*, Nucl. Fusion **33**, 591 (1993).
6. B. Pegourie and J.-M. Picchiotino, Plasma Phys. Controlled Fusion **35**, B157 (1993).
7. A. K. MacAulay, Nucl. Fusion **34**, 43 (1994).
8. B. V. Kuteev, Nucl. Fusion **35**, 431 (1995).

9. B. V. Kuteev and A. Yu. Kostrukov, in *Proceedings of the 22nd EPS Conference on Controlled Fusion and Plasma Physics, Bournemouth, 1995*; ECA **19C**, P-I.120 (1995).

10. L. Garzotti, B. Pegourie, A. Geraud, *et al.*, Nucl. Fusion **37**, 1167 (1997).

11. R. Ishizaki, P. B. Parks, N. Nakajima, and M. Okamoto, Phys. Plasmas **11**, 4064 (2004).

12. L. R. Baylor, A. Geraud, W. A. Houlberg, *et al.*, Nucl. Fusion **37**, 445 (1997).

13. L. R. Baylor, T. C. Jernigan, S. K. Combs, *et al.*, Phys. Plasmas **7**, 1878 (2000).

14. T. T. C. Jones, L. R. Baylor, C. D. Challis, *et al.*, in *Proceedings of the 27th EPS Conference on Controlled Fusion and Plasma Physics, Budapest, 2000*; ECA **24B**, 13 (2000).

15. V. A. Rozhanskiĭ, Fiz. Plazmy **15**, 1101 (1989) [Sov. J. Plasma Phys. **15**, 638 (1989)].

16. V. A. Rozhansky, Contrib. Plasma Phys. **34**, 145 (1994).

17. L. L. Lengyel, V. A. Rozhanskij, and I. Yu. Veselova, Nucl. Fusion **36**, 1679 (1996).

18. W. A. Houlberg, S. L. Milora, and S. E. Attenberger, Nucl. Fusion **28**, 595 (1988).

19. F. S. Felber, P. H. Miller, and P. B. Parks, Nucl. Fusion **19**, 1061 (1979).

20. V. Rozhansky, I. Veselova, and S. Voskoboynikov, Plasma Phys. Controlled Fusion **37**, 399 (1995).

21. I. Yu. Senichenkov, I. Yu. Veselova, and V. A. Rozhansky, in *Proceedings of the 29th EPS Conference on Controlled Fusion and Plasma Physics, Montreux, 2002*; ECA **26B**, P-4.081 (2002).

22. P. B. Parks, W. D. Sessions, and R. L. Baylor, Phys. Plasmas, **7**, 1968 (2000).

23. V. Rozhansky, I. Senichenkov, I. Veselova, and R. Schneider, Plasma Phys. Controlled Fusion **46**, 575 (2004).

24. P. T. Lang, K. Büchl, M. Kaufmann, *et al.*, Phys. Rev. Lett. **79**, 1487 (1997).

25. J. de Kloe, E. Noordermeer, N. J. Lopes Cardozo, and A. A. M. Oomens, Phys. Rev. Lett. **82**, 2685 (1999).

26. L. L. Lengyel, K. Büchl, G. Pautasso, *et al.*, Nucl. Fusion **39**, 791 (1999).

27. B. A. Trubnikov, in *Reviews of Plasma Physics*, Ed. by M. A. Leontovich (Gosatomizdat, Moscow, 1963; Consultants Bureau, New York, 1965), Vol. 1.

28. B. V. Kuteev and L. D. Tsendin, Research Report No. NIFS-717 (NIFS, Toki, 2001).

29. L. L. Lengyel and P. N. Spathis, Nucl. Fusion **34**, 675 (1994).

30. S. L. Milora, W. A. Houlberg, L. L. Lengyel, and V. Mertens, Nucl. Fusion **35**, 657 (1995).

31. H. W. Müller, R. Dux, M. Kaufmann, *et al.*, Nucl. Fusion **42**, 301 (2002).

Translated by O.E. Khadin